AEROSOL DEPOSITION IN MODELS OF A HUMAN LUNG BIFURCATION

Thesis by

Karl Ammon Bell

In Partial Fulfillment of the Requirements
for the Degree of
Doctor of Philosophy

California Institute of Technology
Pasadena, California

1974

(Submitted February 7, 1974)

to Joan

ACKNOWLEDGEMENTS

I wish to express my deepest appreciation to my advisor, Professor Sheldon K. Friedlander, whose guidance and encouragement were invaluable to this research. His personal interest and enthusiasm have been an inspiration in my choice of a professional career. Dr. George M. Hidy, who directed the initial phase of my research, deserves much recognition for his continuous support and encouragement. During the incipient period of this research, Professor Lester Lees also provided valuable guidance. Special thanks is given to Dr. David Shaw for his enthusiastic interest and collaboration, and to Dr. Chiu-sen Wang for several helpful discussions.

I am deeply grateful to Mr. Paul Morand for his help in collecting experimental data. Mr. Dennis Loh is also thanked for his measurements of deposition during steady flow in my model.

Technical assistance received from Messrs. Elton Daly and Robert Greenway in the construction of the experimental models is greatly appreciated. Mrs. Carla Willard and Miss Helen Fabel are thanked for the excellent typing of the manuscript.

Other people who contributed to this research through helpful discussions are Drs. Bernard Altshuler, Daniel Chang, Rudolf Husar, Gary Leal, Morton Lippmann, Fredrick Shair, David Swift, and Harold Wayland, and Messrs. Steve Heisler, Dwight Landis, Paul Roberts,

and Richard Schlesinger.

Financial assistance provided by the National Science Foundation, U. S. Public Health Service, National Institute of Environmental Health Sciences, Environmental Protection Agency, and the Ford Foundation is greatly appreciated.

I dedicate this thesis to my wife whose love, support and understanding were essential during the course of this work.

Finally, I thank my parents for their patience, understanding and financial support during these many years of my education.

ABSTRACT

The bifurcations of the human upper respiratory tract are regions in which enhanced local deposition of airborne particles occurs. Existing mathematical models do not characterize these local "hot spots", which may be important in the development of certain respiratory diseases, the setting of air quality standards according to particle size, and the diagnosis and therapy of respiratory diseases by aerosols.

Idealized two-dimensional ("2-D") and three-dimensional ("3-D") models of the first bifurcation of the human lung with parent and daughter branches were used in theoretical and experimental studies designed to characterize local deposition patterns (Bell and Friedlander, 1973). Monodisperse latex aerosols, having diameters from 0.088 to 7.6μm, were passed through the experimental models at unsteady flow rates simulating conditions of rest and moderate exercise in humans. Deposited particles were counted by optical and electron microscopy, and the aerosol concentration was measured either by gravimetry or by light scattering photometry. Deposition patterns of the "3-D" model data are depicted by computer plotted maps having contours of constant transfer coefficients. Steady potential flow around a wedge was employed to model local deposition by impaction, sedimentation and interception. Steady and quasi-steady laminar boundary layer flows along a wedge were used to model deposition by convective diffusion.

In both models data and theory from 0.088 to 7.6μm for transfer coefficients were similar in trend to curves of deposition efficiency for the entire human lung or the collection efficiency for fibrous filters. Although similar average transfer coefficients are observed in the diffusion and impaction sub-ranges, the deposition patterns are strikingly different. Data $< 0.5\mu$m agreed well with theories of convective diffusion and data $> 2\mu$m agreed fairly well with theories of impaction, sedimentation and interception. The 0.5 - 2.0μm data fall between the two theories on account of unsteady boundary layer effects not included in the theories. Effects of secondary flows on particle deposition must be taken into account in estimating local nonuniformities and "hot spots", however, they can be neglected when calculating the deposition efficiency for each branch. "3-D" model theories more accurately approximate the experimental efficiencies than the models of either Landahl or the ICRP Task Group on Lung Dynamics, and all "3-D" model theories and deposition patterns can be used to model deposition in the tracheobronchial trees of humans and animals.

Measurements indicate that the 150,000 epithelial cells lining the lung wall near the carina receive 25.4 times more 5.7μm particles than the average over the branch. The corresponding figure falls to 3.8 as particle size is reduced to the diffusion range. The relative intensity of "hot spots" calculated for cigarette smoke in the

first three generations of the human lung roughly agreed with the frequency that bronchial carcinomas originate in each of these generations. In addition to local deposition rates, the relative rates of dissolution of irritant aerosols are crucial for modeling acute dose-response.

To assure a fairly uniform coating of therapeutic or diagnostic aerosol over > 75% of the surface of human airways, unit density particles with diameters < 1 μm can be inhaled at any flow rate. For maximum nonuniformity, least surface coverage, and maximum collection at bifurcations, unit density particles with diameters $\geq$ 5 μm should be inhaled rapidly.

The 1.1 μm deposition patterns and efficiencies were significantly different for unsteady and steady inhalations at the same time-averaged flow rates, and similar conclusions should be valid for all respirable particles. Therefore, steady flow can not be used in lung models to accurately estimate deposition in the real lung.

Results from the diffusion subrange can be used to estimate local transfer rates of pollutant gases in lung airways, gases and fat molecules at bifurcations in blood vessels, and heat and mass in other flow systems.

TABLE OF CONTENTS

LIST OF TABLES

LIST OF FIGURES

LIST OF MAPS

LIST OF GRAPHS

LIST OF PLOTS

LIST OF MATRIXES

Chapter 1

INTRODUCTION

1.1 Goals of the Study

The bifurcations of the human upper respiratory tract are regions in which enhanced local deposition of airborne particulates occurs (Ermala and Holsti, 1955; Nadel et al., 1970). Chronic bronchitis and lung cancer are diseases of the upper respiratory tract which may be associated with such deposition "hot spots". Auerbach et al. (1961) and Kotin and Falk (1959) have found histological evidence to justify this hypothesis. Cross sections excised from the bifurcation regions of the lungs of humans dying with or without lung cancer had a greater frequency of precancerous and cancerous epithelial changes than sections excised from other regions of the tracheobronchial tree. In recent work by Schlesinger and Lippmann (1972) the experimentally measured mean deposition efficiency and the distribution of sites of deposition for 1.7 to 12.2 μm particles (unit density) in silastic lung models were related to published data for the frequency of occurrence of bronchial carcinoma.

Mathematical models are available for estimating the deposition rates as a function of particle size for the major regions

of the human respiratory system including the nasopharynx, tracheobronchial tree and pulmonary regions (Findeisen, 1935; Landahl, 1950a,b,1963; Beeckmans, 1965; Task Group on Lung Dynamics, 1966). However, existing models are not intended to characterize the local nonuniformities which, as noted above, may be important in the development of certain respiratory diseases, in the establishment of air quality standards according to particle size, and in the use of aerosols for diagnosis and therapy of respiratory diseases.

The goals of this study were:

1. to collect and analyze experimental data of local patterns of deposition in idealized models of a single lung bifurcation;

2. to develop a theoretical model adequate to explain the measured deposition patterns at bifurcations in lung models.

1.2 Background to Lung Modeling

1.2.1 Initial Considerations

Three major factors which should be considered when modeling the deposition of particles in the human lungs are the morphology of the respiratory tract, the physiology of respiration and the dynamics of the particles. The morphology and physiology interact to define the local air temperature, pressure and velocity profiles. The particle dynamics determine whether they will follow

the air streamlines or deposit on the boundaries of the tract.

1.2.2 Structure and Behavior of the Conducting Airways

The conducting airways of the human lungs have a complex anatomical structure and an equally complex dynamical behavior. The irregular dichotomy pattern of branching (Weibel, 1963: 111-114) and the irregular dimensions of the airways are shown in Figure 1.1 by the sketch of the trachea and of the first four generations of the bronchi. The airway cross sections are seldom shaped like circular cylinders. U or horseshoe-shaped sections of cartilage which partially encircle the walls of the trachea and the extrapulmonary parts of the primary bronchi (Ham, 1968) cause the inside wall of the trachea and primary bronchi to be macroscopically corrugated to a maximum depth of 10 to 15% of the airway radius (Hayek, 1960: 60). Lower bronchi are completely encircled by rings of cartilage, but the corrugation pattern is not evident. Smooth muscle tissue joins the ends of the cartilage section on the esophageal side of the trachea and primary bronchi and causes a flattening of the airway cross section.

Saddle-shaped cartilages are present at most bronchial bifurcations to support the two bronchi at the site where they join at an acute angle. Lung tissue covers these saddle-shaped carti-

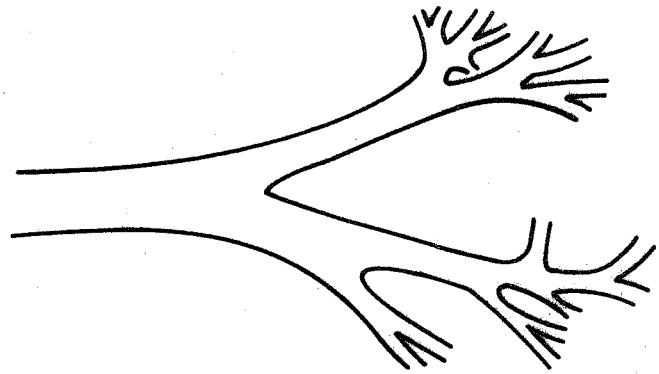

Figure 1.1 Sketch of the Irregular Branching Pattern and Dimensions of Part of the Tracheobronchial Tree of a Human Lung

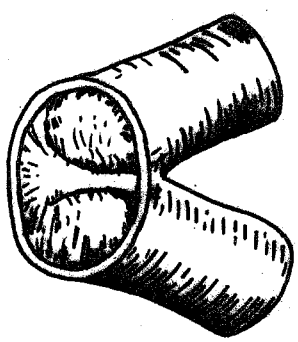

Figure 1.2 Sketch of the Internal Geometry of a Bifurcation Showing the Sharp Ridge at the Junction of the Two Daughter Branches (Hayek, 1960:93)

lages and defines the surface of each junction. The tracheobronchial carina is wedge-shaped in the axial section through the plane of the bifurcation which bisects it. However, it gradually becomes more rounded toward the dorsal and ventral walls of the trachea (Figure 1.2). Other bifurcations in the bronchial tree vary in shape from a sharp ridge to well rounded saddles (Hayek, 1960: 67-68, 147-148).

Horsfield and Cumming (1967) measured the angles of branching in casts of human lungs. The acute angle of branching of a daughter tube from the axis of the parent tube varied between -2° and 112° with a mean of 41°. The more peripheral airways had greater branching angles. The distribution of mean branching angle according to branch diameter was (1) 32° for diameters greater than 4 mm., (2) 30° for diameters of 3 to 4 mm., (3) 36° for 2 to 3 mm., (4) 43° for 1 to 2 mm., (5) 50° for less than 1 mm. Thus the mean angle of bifurcation of two branches in the real lung varies between 60° and 100°.

On a microscale the epithelial cells lining the inside walls are covered with a smooth, thin, slow-moving film of mucus. The mucous membranes of the bronchi are normally folded into longitudinal ridges and channels by contraction of the smooth muscles (Engel, 1962). During normal respiration the trachea distends longitudinally, and the trachea and large bronchi vary in width by

about 5%. The diameters of the lower airways vary about 20% during normal respiration (Hayek, 1960: 65; Marshall and Holden, 1963). The beating heart also causes periodic oscillations in the wall of certain airways (West, 1961).

1.2.3 Airway Models

The details of the complex structure and the dynamical behavior of the conducting airways are difficult to include in a mathematical model of gas and particle transport; age, sex and state of health produce wide variations in these details. Consequently, most mathematical models for particle deposition have been based on circular cylindrical, rigid models of the conducting airways with dimensions representative of the normal adult.

Such airway models have been developed by Findeisen (1935), Landahl (1950a), Davies (1961), Weibel and Gomez (1962), Weibel (1963), and Horsfield and Cumming (1968). Figure 1.3 demonstrates the regular dichotomous branching pattern of Weibel's Model "A" (Weibel, 1963: 136-140) which is widely used in mathematical deposition models. The complete model has 16 generations of conducting airways in the tracheobronchial tree and seven partially or completely alveolated generations in the respiratory zone. The number and diameter of the branches in the tracheobronchial tree

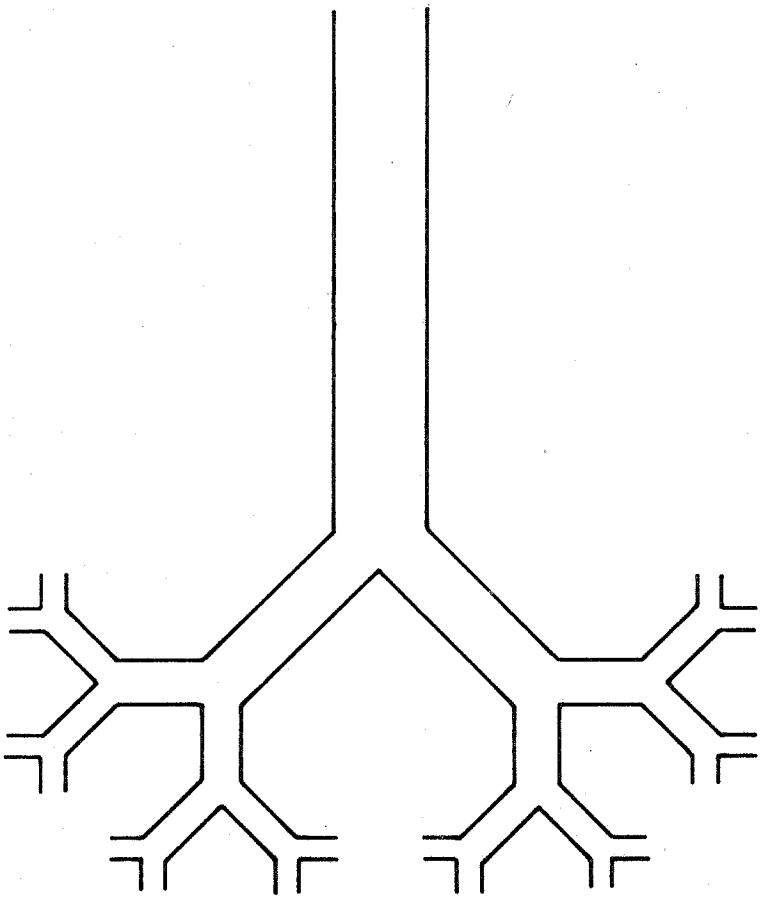

Figure 1.3 A Regular Dichotomy Pattern of Branching as Weibel's Model "A"

are shown in Table 1.1. The dimensions are based on an average adult lung with a volume of 4800 c.c. at 75% of maximal inflation.

1.2.4 Mechanisms of Particle Deposition

The three major mechanisms of particle deposition in the human lung are sedimentation, inertial impaction and Brownian diffusion.

Sedimentation and inertial impaction depend on an aerodynamic parameter called the relaxation time, $\tau = \rho_p d_p^2 C/18\mu$, the ratio of the particle mass to the Stokes resistance coefficient corrected for slip flow; it is also the time required for a particle to decelerate in stagnant air to 36.8% of its initial velocity in the absence of external forces. The terminal settling velocity of a particle in the lungs, $V_s = \tau g$, where g is the acceleration of gravity.

Inertial impaction occurs when a particle trajectory deviates from the air streamlines and intersects the lung wall in regions such as airway bifurcations. A characteristic length for determining the efficiency of inertial impaction is the particle's "stopping distance". It is the distance that a decelerating particle will travel in a direction normal to a boundary before the particle's normal velocity drops to zero (i.e., when a particle, being carried by a stream of air at a velocity, U, reaches a bifurcation of angle α, it will travel a

maximum distance of $h_s = \tau U \sin\alpha$ in a direction normal to the wall.)

Particle deposition by Brownian diffusion depends on the Stokes-Einstein diffusion coefficient: $D = kTC/3\pi\mu d_p$ where k is the Boltzman constant, T the temperature, C the slip flow correction, and the denominator equals the Stokes resistance coefficient for spherical particles. Brownian diffusion deposition occurs for particles less than 0.5μm in the alveoli by radial diffusion and in the conducting airways by convective diffusion.

Another mechanism of deposition, which has been neglected in lung deposition models in the past, is interception. A particle deposits by interception when it travels in a streamline which lies within a distance equivalent to the particle's radius from the lung wall. Interception is most significant for particles larger than 1μm in regions where inertial impaction is predominant.

1.2.5 Review of Particle Deposition Models

Findeisen (1935) and Landahl (1950a, 1963) derived theoretical and semi-empirical estimates for each mechanism of deposition for steady flow through cylindrical tubes. Cases considered included parabolic, plug and fully developed turbulent flows. Their calculated results of the total deposition for a few particle sizes were in fair agreement with experimental data.

The Task Group on Lung Dynamics (1966) developed a general model for particle deposition and retention in the human respiratory tract. Their particle deposition model employed the deposition probability relations and the lung model of Findeisen; however, they used the Gormley and Kennedy (1949) equation for diffusion during the inspiratory and expiratory phases of flow. Figure 1.4 shows the dependence of regional and total lung deposition on particle size as predicted from the Task Group on Lung Dynamics model for a 1450 c.c. tidal volume at 15 breaths per minute. The total deposition curve has the characteristic shape of those of efficiency versus particle size for aerosol filtration by fibrous filters (Thomas and Yoder, 1956). The minimum efficiency is predicted for 0.5μm particles. Particles larger than 0.5μm are removed by sedimentation and inertial impaction, while particles smaller than 0.5μm are removed by Brownian diffusion.

Particles larger than 10μm are predicted to be entirely removed by inertial impaction and sedimentation in the nasal-pharyngeal region. Sedimentation controls the deposition of 0.5 to 10μm diameter particle in the pulmonary region (respiratory bronchioles, alveolar ducts and alveoli). However, sedimentation and inertial impaction cause deposition of these particles in the tracheobronchial tree and nasal-pharyngeal region. The increase in

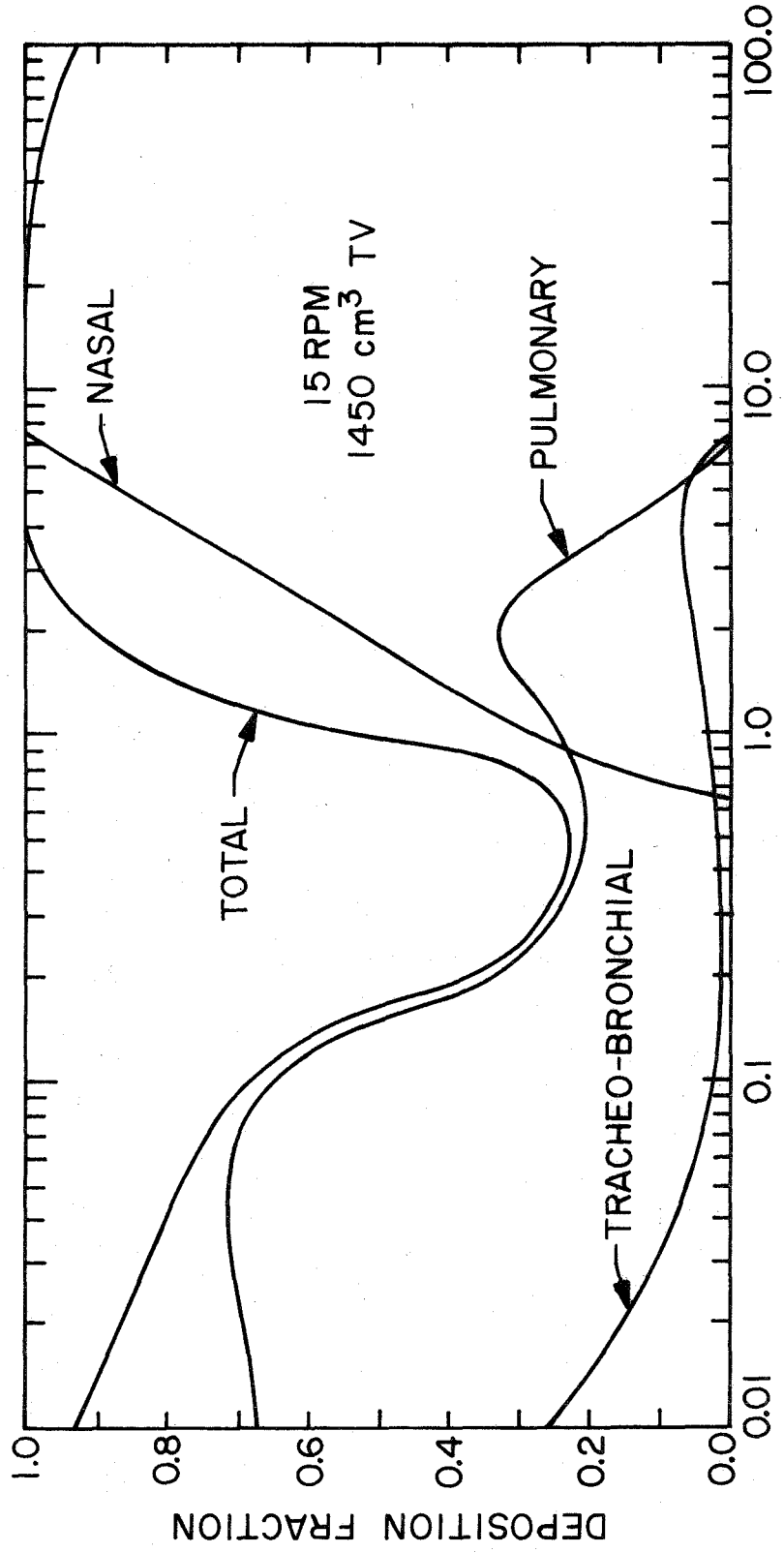

Figure 1.4 Deposition of Monodisperse Aerosols of Various Aerodynamic Diameters in the Respiratory Tract of Man Assuming a Respiratory Rate of 15 RPM and a Tidal Volume of 1450 cm^3 (Task Group on Lung Dynamics of the ICRP, 1966)

deposition in the tracheobronchial tree with decreasing particle size below 0.1μm is caused by the increased probability of diffusion deposition. This also explains the leveling and the decrease of pulmonary deposition below 0.1μm.

Beeckmans (1965) computerized and refined the models of Landahl and included the effects of intrapulmonary gas mixing and recycling of undeposited aerosol. His calculations for the total and regional deposition of 0.05 to 6μm aerosols were not significantly different from Landahl's predictions. These calculations also agreed satisfactorily with the experimental data of Landahl, Tracewell and Lassen (1951, 1952).

Regional deposition has also been measured in vivo and compared with the above models. Lippmann and Albert (1969) collected extensive experimental data for the deposition of radioactively tagged particles in the tracheobronchial tree of human subjects. Their averaged experimental data agreed fairly well with calculations based on Landahl's equation for inertial and sedimentation deposition in Weibel's Model "A". Although the dependence of the deposition efficiency data on particle size for all experimental subjects agreed with the calculations, the magnitude of deposition varied widely from person to person. The varying airway dimensions of the subjects compared to Weibel's Model were the major cause of

this discrepancy.

In spite of their high degree of simplification, the deposition models are useful for obtaining a rough estimate of the regional and total deposition rates in normal human lungs. To improve the estimate for any one person, the exact dimensions of their airways must be employed in place of the idealized airway models. However, none of the deposition models are designed to predict the local nonuniformities of deposition within any generation.

Other mathematical deposition models have been developed by either refining the deposition models discussed above or by following a completely different approach. Gussman and Beeckmans (1971) restructured Beeckmans' (1965) model to account for any atmospheric composition and pressure. Mitchell (1971) modified the rigid wall model by varying the airway diameters sinusoidally during the respiration cycle to simulate the natural patterns of breathing. His predictions of total lung deposition according to particle size generally agree with the predictions of the rigid wall models.

Taking a different approach, Altshuler (1959) proposed a continuous tubular filter bed model in place of the complicated branching model. His model can predict the regional deposition to any depth in the lungs by employing the same deposition equations plus continuous, experimental measurements of the respiratory

flow rate and the inspired and exhaled aerosol concentrations.

From the principles of dimensional analysis, Friedlander (1964) derived an expression for the efficiency of removal of submicron particles by diffusion in the pulmonary region. Because no special structural model of the lung is required, the model is generally applicable for correlating and extrapolating experimental data.

Employing the analogy between heat and mass transfer, Yeh (1972) has suggested using several theoretical and empirical expressions for laminar and turbulent heat transfer in the entrance regions of straight and curved tubes to predict the diffusional deposition of small particles in the conducting airways.

1.2.6 Experimental Particle Deposition Studies in Lung Models

A number of investigators have attempted to check the accuracy of the deposition equations, suggested by Findeisen, Landahl and Beeckmans, for predicting the deposition in each generation of the tracheobronchial tree. Schlesinger and Lippmann (1972) studied the local deposition of radioactively tagged, monodisperse particles of 1.7 - 12.2μm (unit density) in hollow silastic casts of the trachea through the segmental bronchi under steady flow conditions. They compared their experimental data for the deposition

per generation with theoretical values calculated from Landahl's (1950a) expression for inertial impaction with airway dimensions from Weibel's Model "A". Theory and experimental deposition percentages differed by 1.8% to 92% with a mean difference of 39%. Part of this difference was accounted for by dimensional differences between each of the three casts and between the casts and Weibel's Model. However, for this range of particles, the force of gravity cannot be neglected. Sedimentation should contribute to the deposition along an entire generation, and it should be the controlling mechanism downstream from the carina.

For one particle size Schlesinger and Lippmann reported 3.5 times more total deposition in one cast than in another. This wide variation of deposition in casts of nonsmokers indicates again the inaccuracy in assuming an average airway model for theoretical predictions of deposition.

Martin and Jacobi (1972) measured the deposition of submicron radioactive aerosols (0.2 - 0.4μm activity median diameter) in each generation of a hollow plastic model of the trachea through the segmental bronchi. The airways had the dimensions and branching pattern of Weibel's Model "A". For steady inspiratory and expiratory flow (0.1 - 50 liters/min.), their data were in better agreement with Landahl's (1963) equation for diffusion from a well

mixed stream than with the Gormley and Kennedy (1949) relation for diffusion from a stream in Poiseuille flow. However, with increasing depth in the bronchial tree their data gradually approached the Gormley and Kennedy relation; this prompted them to conclude that turbulent diffusion played an important role in the trachea and larger bronchi. Their data are inconsistent with this conclusion because at high flow rates (8 - 50 liters/min.) the deposition in any one generation was generally in better agreement with the Gormley and Kennedy relation than the data at low flow rates (0. 1 - 3 liters/ min.).

1.3 Air Flow in Lung Models and the Real Lung

1.3.1 Flow Analysis in Weibel's Model "A"

An idealized, air flow analysis of Weibel's Model "A" is shown in Table 1. 1. Similar analyses have been made by Schreck and Mockros (1970) and by Pedley et al. (1970). Each branch of each generation is treated as a straight, smooth tube for calculating the time-average velocity, the corresponding Reynolds number and the entrance length. An analysis of the Reynolds numbers and the entrance lengths for a quiet breathing rate of 15 cycles/min. and a tidal volume of 450 c. c. suggests:

1. Plug flow in the trachea through the third generation,

Gen z	Number N_z	Diameter (cm) D_z	Length (cm) L_z	Time-Average Velocity (cm/sec) $\bar{U}_z$	Reynolds Number $Re = \frac{D_z \bar{U}_z}{\nu}$	$\frac{\text{Entrance Length}}{\text{Length of Generation}}$ $\frac{0.057 Re D_z}{L_z}$ *
+ 0	1	1.8	12.0	88.6	960.7	8.21
‡ 1	2	1.22	4.76	96.6	710.0	10.37
§ 2	4	0.83	1.90	105.6	528.0	13.15
‖ 3	8	0.56	0.76	112.5	379.5	15.94
4	16	0.45	1.27	90.7	245.9	4.97
5	32	0.35	1.07	72.3	152.4	2.84
6	64	0.28	0.90	56.8	95.8	1.70
7	128	0.23	0.76	44.1	61.1	1.05
8	256	0.186	0.64	32.4	36.3	0.60
9	512	0.154	0.54	23.5	21.8	0.35
10	1024	0.130	0.46	16.8	13.2	0.21
11	2048	0.109	0.39	11.5	7.55	0.12
12	4096	0.095	0.33	7.81	4.47	0.073
13	8192	0.082	0.27	5.06	2.50	0.043
14	16384	0.074	0.23	3.24	1.44	0.026
15	32768	0.066	0.20	1.99	0.79	0.015
16	65536	0.060	0.165	1.25	0.45	0.009

* Langhaar (1942)
+ trachea
‡ primary bronchi
§ lobar bronchi
‖ segmental bronchi

Table 1.1 Air Flow Analysis of Weibel's Model "A" for Normal Resting Breathing Rate =15 cycles/min. and Tidal Volume = 450 cc

2. partially developed laminar flow in the fifth through seventh generation, and

3. developed Poiseuille flow for an increasing fraction of each branch in the eighth through sixteenth generation.

However, during maximal inspiratory and expiratory effort by a normal person, velocities and Reynolds numbers may be 22 to 45 times larger than during quiet breathing; this suggests the presence of turbulent flow in the upper generations. Also, because of variable compliance and resistance, the ventilation is not equally distributed throughout the lung; consequently, branches of the same generation may have different flow rates.

1.3.2 Skewed Profiles and Secondary Flows

The flow analysis in the previous section neglects the complicated flow behavior initiated at the bifurcations and transferred to the daughter branches. Schroter and Sudlow (1969) and Schreck and Mockros (1970) measured the velocity profiles for steady flow in the daughter branches of hollow airway models which were geometrically similar to Weibel's Model. For Poiseuille or plug flow in the parent tube, the flow is symmetrically split by the carina, and the higher axial velocities are centered off the daughter tube axis along the inside wall. The shear rates along the inside wall are about four

times larger than along the outside wall, and the peak axial velocity is twice the average bulk flow velocity. The flow is also skewed as a result of the lateral convection or secondary flows generated at the bifurcation (Figure 3.2).

Although secondary flows and the radial molecular momentum transport increase the uniformity of the flow distribution distally along the branch, only the slower flow regions redistribute significantly. Even though the flow profiles in the daughter branches become more complicated when this asymmetric flow distribution reaches a second bifurcation, they follow the same general trends discussed above.

Sudlow and Shroter observed secondary flows, during inspiration and expiration, at all flow rates (Re = 50 - 4500) and regardless of the shape of the entry profile. On inspiration a pair of symmetric vortices occur in each daughter branch (Figure 3.2); they are strong enough to complete one helical cycle within three branch diameters downstream. On expiration a set of four vortices are generated in the parent tube at the bifurcation.

These results suggest that simple parabolic flow is only applicable in the conductive airways where $Re \leq 1.0$. There the fluid inertia is negligible and the convective fluid transport is equal to or less than the molecular transport.

1.3.3. Turbulence

A simplified flow analysis of Weibel's Model indicates undeveloped flow with a flat profile in the trachea for Re up to approximately 2000(Schlichting, 1968: 433). However, this fails to account for disturbances produced by the rough walls, the noncircular cross section and the larynx.

In hollow casts of the trachea and the first bifurcation, Dekker (1961) observed $Re_{crit} = 1800$ for steady inspiratory flow. For casts containing a larynx with the glottis in a natural, open position, Re_{crit} was 450 for steady inspiratory flow. West (1961) observed turbulence in the trachea of lung casts during exhalation at Re of 800, although his hollow casts did not include a larynx. As the position of the vocal cords change in the real lung (Zamel et al., 1970; Ham, 1968), the glottis of the larynx functions like a variable orifice. Consequently, during inspiration a jet of turbulent air enters the trachea at Re well below 2000. Because the trachea is not perfectly vertical, the jet of turbulent air is directed against the ventral wall of the trachea. Although the length of the trachea would be insufficient for the complete development of turbulent flow, the additional turbulence created by the jet and the corrugated walls may cause the intensity of turbulence to approach a fully developed state by the end of the trachea for $Re > 3000$.

A model for the decay of turbulence (Owen, 1969) indicates that turbulence will gradually decay in any branch in which $Re < 3000$. Assuming a peak of Re of 1865 in the trachea corresponding to 1.9 second, 450 c.c. inhalation, Owen's model predicts a 10% decay in the trachea and in each of the first two orders of bronchi. Using Batchelor's (1953) theory for the change in turbulent energy occurring at regions of rapid flow contraction, like the first three generations of bifurcations in Weibel's Model "A", 15%, 16% and 10% decay occur respectively in these first three orders of bifurcations. Therefore, turbulence generated in the trachea at Re of 1865 will have approximately 50% of its initial intensity when it enters the third order of bronchi. At inspiratory flow rates with $Re > 3000$, decay would be even slower.

These decay calculations neglect the possible effects of the strong secondary flows generated at the bifurcation. The regions of very high and very low shear rate caused by the secondary flows could also be regions of high and low turbulent intensity and dissipation. However, Pedley, Schroter and Sudlow (1971) argue that the boundary layer remains laminar in the daughter tube for $Re < 15000$, and they have experimental evidence to verify this assumption for the parent tube Re up to 10000. Thus, the turbulent eddies are localized in the core, and the arguments given above are sufficient for

predicting their rate of decay.

1.3.4 Wall and Flow Oscillations

Another complication to the idealized flow behavior in the lungs is the effect of the heart beat on the flow in the conducting airways. West (1961) measured these flow oscillations in the segmental bronchi of people with normal bronchial trees and found that they were only detectable during pauses or breath holding periods between inspiration and expiration. The peak oscillatory flow rates observed were 0.5 liters/min. which is approximately 20% of the peak flow rate in the segmental bronchi during quiet breathing. These oscillations will improve the gas mixing in the airways and the alveoli.

The minor variation in airway dimensions occurring with the expansion and the contraction of the lungs during breathing can generate radial velocities which would only be significant in comparison to the axial velocities in the smallest airways.

Calculations also indicate that surface waves would probably only be generated in the slowly moving, viscous mucous film in the trachea and only at air velocities in the turbulent regime (Levich, 1962: 659).

Schroter and Sudlow (1969) have estimated that the macroscopic

corrugations in the airways are below the critical protuberance height at which laminar flow can be disturbed.

1.3.5 The Range of Validity of the Quasi-Steady Flow Hypothesis

The mathematical deposition models reviewed above have assumed, for ease of calculation, that steady flow conditions prevail in the lung models. However, in the real lung the inspiratory and expiratory flow is unsteady with the flow rate varying approximately sinusoidally over time, and the breathing frequency can vary from an average of eight breaths per minute for sedentary conditions to 50 breaths per minute during sustained work and exercise.

A more accurate flow simulation than steady flow is quasi-steady flow. This means that the pulsatile flow in the lungs can be simulated by a continuous sequence of steady flow profiles. However, different and sometimes conflicting criteria for quasi-steady flow in the airways have been suggested by various writers.

Wormersley (1955) analytically determined that quasi-steady flow can be assumed in oscillating, established, parabolic pipe flow only when the dimensionless frequency parameter, $(\text{Freq} = R(\omega/\nu)^{\frac{1}{2}})$, is less than 1.0. Table 1.2 lists values of this parameter for 12, 15 and 30 breathing cycles per minute in Weibel's

		$R(\omega/\nu)^{\frac{1}{2}}$			
Gen	Radius	12 BPM[+]	15 BPM	16.7 BPM	30 BPM
*0	0.950	2.61	2.92	3.08	4.14
1	0.610	1.68	1.88	1.98	2.66
2	0.415	1.14	1.28	1.348	1.80
3	0.280	0.77	0.861	0.91	1.22
4	0.225	0.62	0.692	0.733	0.979
5	0.175	0.4815	0.538	0.57	0.763
6	0.140	0.386	0.431	0.50	0.61
7	0.115	0.316	0.354	0.374	0.501
8	0.093	0.256	0.286	0.302	0.404
9	0.077	0.212	0.237	0.250	0.335
10	0.065	0.179	0.200	0.21	0.282
11	0.0545	0.15	0.168	0.177	0.237
12	0.0475	0.13	0.146	0.154	0.206
13	0.0410	0.113	0.126	0.133	0.1785
14	0.0370	0.102	0.114	0.120	0.161
15	0.0330	0.0907	0.102	0.107	0.1435
16	0.0300	0.0825	0.092	0.0974	0.131

* trachea

[+]12 BPM = 2.5 sec. inhalation, f = .2/sec.
15 BPM = 2.0 sec. inhalation, f = .25/sec.
16.7 BPM = 1.8 sec. inhalation, f = .278/sec.
30 BPM = 1.0 sec. inhalation, f = .5/sec.

Table 1.2 Variation of the Dimensionless Frequency Parameter, $R\sqrt{\omega/\nu}$, for Various Breathing Rates in the Upper Respiratory Tract. R = generations radius, cm., $\omega = 2\pi f$, f = breathing rate, sec.$^{-1}$, ν = kinematic viscosity of air = 1.66×10^{-1} cm.^{2}/sec. at 98.6°F.

Model "A". The results indicate that the quasi-steady flow assumption is only valid in airways distal to the fourth generation for 12 and 15 breaths/min. and distal to the sixth generation for 30 breaths/min.

Schroter and Sudlow (1969) interpreted the frequency parameter as indicating the relative magnitude of the oscillatory disturbances created in the boundary layer to the magnitude of the boundary layer for steady flow. To account for the effect of flow oscillations in regions of partially developed flow, they redefined the parameter as $Freq' = \delta(\omega/\nu)^{\frac{1}{2}}$, where δ represents the boundary layer thickness. In this case quasi-steady flow can be assumed for $Freq' << 1.0$ and does not hold for $Freq' > 1.0$. In the regions where Freq was greater than 1.0, $Freq'$ is less than 1.0, because the boundary layers are very thin.

Instead of employing the frequency parameter, Jaffrin and Hennessey (1972) evaluated the magnitude of the inertial forces acting on the flow. After calculating the time-averaged ratio of the time-dependent fluid acceleration to the convective acceleration at the bifurcating end of the trachea during inspiration, they concluded that, provided the flow rates are larger than 500 c.c./sec., the quasi-steady hypothesis is justified at the first bifurcation for breathing frequencies below 15 breaths/min. At smaller flow rates, the value of the convective acceleration is decreased because the boundary

layer is more fully developed. Since the concept of the developing boundary layer does not apply during expiration when the four secondary flow vortices are generated at the end of the trachea, their analysis is restricted to inspiratory flow.

In conclusion, the quasi-steady flow approximation is probably valid throughout the lung during time-averaged inspirations at quiet breathing frequencies, provided the time-averaged flow rate is larger than 500 c.c./sec. in the trachea. Therefore, experimental velocity profiles and pressure drop measurements obtained during steady flow conditions are applicable for predicting the behavior in the real lung during quiet breathing. As indicated in Chapter 5, Section 5.2.4, the same conclusions cannot be generally applied to experimental particle deposition measurements.

1.3.6 Time to Reach the Steady Boundary Layer Thickness

As a model for the flow along the carina, consider a flat plate, initially at rest, which is impulsively set into motion. Under these conditions Stuart (1963) argues that the criterion, $Ut/x = t' > 2.65$, can be employed to estimate the time needed for steady boundary layer flow to develop at a distance, x, along the plate. For a 450 c.c. inhalation over 1.6 seconds, the time-averaged velocity in the trachea is 100 cm./sec., which is set equal to U.

Using $t' = 3.0$ and $x = 1.0$ cm., t equals 0.03 seconds. Therefore, a time-averaged, steady boundary layer thickness is valid for 98% of the inspiration time at $x = 1.0$ cm. and 95% of the inspiration time at $x = 2.54$ cm.

Chapter 2

THEORETICAL ANALYSIS OF PARTICLE DEPOSITION IN THE TWO-DIMENSIONAL MODEL OF A LUNG BIFURCATION

2.1 Selection of the Airway Model and Flow Regimes

A rigid, two-dimensional ("2-D") model of a lung bifurcation with its associated parent and daughter branches was chosen for the initial analysis. As shown in Figure 2.1, the model is an axial section through the plane of a lung bifurcation having the dimensions of the trachea and primary bronchi in Weibel's Model "A". By adjusting the bifurcation angle and the length to diameter ratio of the branches, the model can be made geometrically similar to any branching section in the tracheobronchial tree. Analytical expressions for the local velocity profiles can be derived more easily for this model than for three-dimensional models. However, the complex secondary flows, which may have significant effects on deposition in the real geometry, are neglected in this initial analysis.

The sharp 90° wedge was selected to approximate the inter-bronchial angle for ease of analysis of the aerodynamics and to simplify the construction of an experimental model. In the real lung the first bifurcation is actually asymmetric with the right bronchus deviating less from the axis of the trachea than the left bronchus.

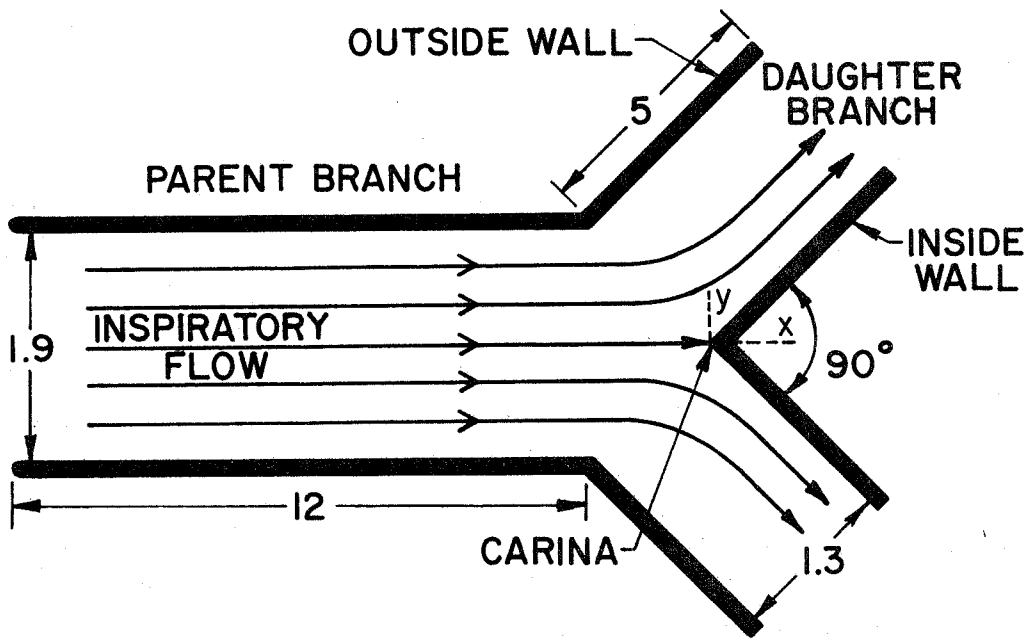

Figure 2.1 Two-Dimensional Model of a Lung Bifurcation with Dimensions (cm.) of the Trachea and Primary Bronchi in Weibel's Model "A". Branch Lengths Not to Scale.

The lumen of the right bronchus is also approximately 3 m. m. larger than the left, and the axis of each bronchi is slightly curved over its length. During respiration the carina and the bronchial wall to a distance of 1 cm. downstream are rigid; however, the bronchial wall beyond this region varies slightly in its degree of curvature (Hayek, 1960: 66-69). Although the tracheal bifurcation angle is fixed for each person, it can vary between 45° and 100° for different people (Alavi, et al., 1970; Hayek, 1960:65). The reported mean interbronchial angle for the entire lung is 75° (Horsfield and Cumming, 1967). The real trachea makes a smooth transition with the outside wall of the primary bonchi, while the model has sharp 135° angles.

Most of the particle deposition near the bifurcations occurs during inspiratory flow at the carina and downstream along the walls of the daughter branches. The basic flow model with which experimental results have been compared in this paper is the steady, two-dimensional potential flow over a wedge with a laminar boundary layer. Steady potential flow approximates the undeveloped flow in the core of the parent branch, and classical boundary layer theory approximates the flow profiles along the daughter branches of bifurcations in the upper-respiratory tract during normal breathing conditions.

2.2 Air Flow Analysis

2.2.1 Potential Flow Solution

The initial objective was to obtain a potential flow solution for the entire "2-D" model. Milne-Thomson (1968: 289-292) gives a solution procedure for the general problem of a canal with a side branch. Because the "2-D" model is symmetric, the streamlines can be derived for either the top or bottom half of the model--the dividing line is the stagnation streamline. Following Milne-Thomson's general procedure, a solution was derived for the complex potential, W, in a symmetric "2-D" model with bifurcation angle of 2α:

$$W = \frac{Uh}{\pi} \log\left[\frac{\zeta/d - 1}{\zeta + 1}\right]. \qquad (2.1)$$

The complete derivation and a description of the variables is given in Section 1 of Appendix A.

The fluid velocity components (u_f, v_f), corresponding to the position co-ordinate (x, y), are defined in terms of the implicit variable ζ:

$$u_f - iv_f = U \exp(-i\alpha)\zeta^{\alpha/\pi}. \qquad (2.2)$$

The position coordinates (x, y) in the top half of the 90° model are also determined in terms of ζ:

$$x + iy = \frac{\sqrt{2}h}{\pi} \exp(i\pi/4)\left\{1/2 \log\left|\frac{\zeta^{1/2} - \sqrt{2}\zeta^{1/4} + 1}{\zeta^{1/2} + \sqrt{2}\zeta^{1/4} + 1}\right| + \tan^{-1}\left[\frac{\sqrt{2}\zeta^{1/4}}{1 - \zeta^{1/2}}\right]\right\}$$

$$- \frac{h_2}{\pi} \exp(i\pi/4)\left\{\log\left|\frac{\zeta^{1/4} - h/h_2}{\zeta^{1/4} + h/h_2}\right| + 2\tan^{-1}\left[\zeta^{1/4}\, h_2/h\right]\right\} \qquad (2.3)$$

Because Equation 2.3 cannot be analytically inverted, the components of the potential velocity cannot be explicitly evaluated in terms of coordinates (x, y). The velocity components for any coordinate position (x, y) can be numerically evaluated by trial and error on a computer from Equations 2.2 and 2.3. However, such a procedure would be too inefficient and inaccurate for use in calculating particle trajectories in the lung model.

2.2.2 Approximate Solution for Potential Flow Around the Model Wedge

Particles 20 μm in diameter are approximately the largest capable of penetrating the nasal and pharyngeal regions. The stopping distance for 20 μm particles of unit density, traveling at 100 cm./sec., is 0.087 cm. Hence, particles which deposit along the wedge of the bifurcation during inhalation are carried in the parent branch by the flow near the stagnation streamline. Smaller particles must travel on streamlines passing even closer to the wedge to deposit by inertial impaction and sedimentation. Therefore,

an analytical expression for the streamlines passing near to the carina should be adequate for modeling the deposition.

An approximate solution for the complex potential function for flow along a sharp wedge of angle 2α in a bifurcating channel is

$$W = \frac{-A}{m+1} U \exp(-m\pi) z^{m+1} + iUh, \qquad (2.4)$$

where $m = \alpha/(\pi-\alpha)$. Equation 2.4 was obtained by expanding the complex potential function (Equation 2.1) in an infinite series about the carina, and then neglecting the second- and higher-order terms of ζ. The expansion is only valid for the region in which $|\zeta| < 1$ or $<d$, whichever is smaller. The complete derivation of Equation 2.4 and a discussion of its region of applicability is given in Section 2 of Appendix A.

The negative of the first term on the right of Equation 2.4 is the classical result for inviscid flow about sharp wedges (Milne-Thomson, 1968: 155). The negative sign and the extra term occur because the boundary condition, $\psi = Uh$, was chosen for the wedge surface in the model rather than $\psi = 0$.

The derivation of Equation 2.4 was necessary to determine the constant, A, for the unique geometry of a bifurcating channel:

$$A = \left\{ \frac{h}{\pi - \alpha} \left[\left(\frac{h_2}{h} \right)^{\pi/\alpha} + 1 \right] \right\}^{-m} . \qquad (2.5)$$

The stream function and the velocity components for any bifurcating channel are given below with the origin of the polar coordinate system taken at the carina and $\theta = \pi$ along the stagnation streamline:

$$\psi = \frac{A}{m+1} Ur^{(m+1)} \sin[m\pi - (m+1)\theta] + Uh, \tag{2.6}$$

$$u_f = A\,Ur^{m} \cos m(\pi - \theta), \tag{2.7}$$

and

$$v_f = A\,Ur^{m} \sin m(\pi - \theta). \tag{2.8}$$

For the "2-D" model with the 90° wedge (Figure 2.1), $m = 1/3$ and $A = 0.82$ cm.$^{-1/3}$. AU represents the fluid velocity in the channel at a distance of one centimeter from the carina. Equation 2.7 also indicates that the velocity component, u_f, decreases toward the carina and increases along the wedge for all m. v_f in Equation 2.8 continually increases over this same region for $m > 0$.

Figure 2.2 is a computer plot of the streamlines given by Equation 2.6 for the top half of the "2-D" model. The free stream velocity, U, equals 100 cm./sec. which corresponds to the time-average flow for a 2 second, 600 c.c. inhalation through the bifurcation model. On the stagnation streamline or negative x-axis, $\psi = 95$ cm.^{2}/sec., while $\psi = 93, 91, \ldots\ldots 75$ cm.^{2}/sec. are the values of the stream functions on the successive streamlines above the negative x-axis.

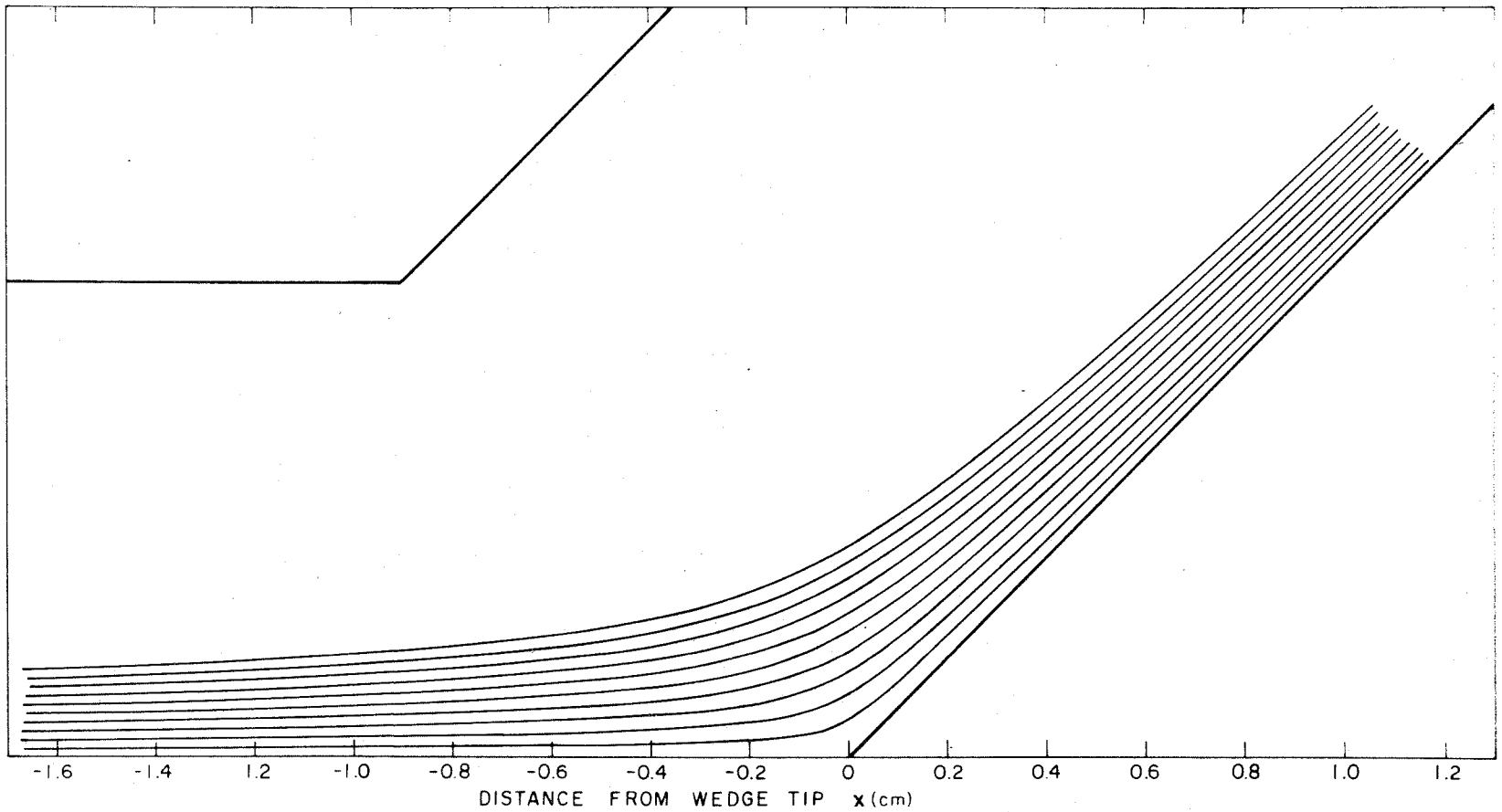

Figure 2.2 Streamlines of the Potential Flow in the Top Half of the Symmetric Two-Dimensional Model with the 90° Wedge (U = 100 cm/sec)

The infinite series expansion, from which Equations 2.4 through 2.8 were derived, is only valid for $r < 0.7$ cm. in the 90° model. Using Equation 2.6, the stream function on the outside wall of the daughter branch, evaluated at $r = 1.3$ cm., $\theta = 3\pi/4$, is 19.4 cm.^{2}/sec. A general solution for the entire channel would give $\psi = 0$ on the outside wall. Thus the approximate solution underestimates the total flow through the channel by 20%--probably because it does not account for the infinite velocities around the sharp 135° angle on the outside wall. Therefore, the general solution would most likely give the same streamline spacing and local fluid velocities in the narrow region along the wedge from which particle deposition occurs. Even in the worst case, a 20% underestimate of the local fluid velocities would only underestimate the local deposition rate by roughly 20%.

2.2.3 Steady Laminar Boundary Layer Flow

Under normal breathing conditions the boundary layers along the daughter branches of the bifurcation regions should be laminar. The boundary layer set up along the wedge of the bifurcation model was of primary interest for studying the local particle deposition by inertial impaction and convective diffusion.

Laminar boundary layers along wedges are discussed by

Schlichting (1968: 150-151). The velocity components in the boundary layer (u_{f1}, v_{f1}) correspond to the coordinates (x_1, y_1) respectively parallel and perpendicular to the wedge with the origin at the carina. u_{f1} and v_{f1} were evaluated for the 90° wedge from the classical Falkner and Skan (1931) solution but in terms of the similarity variable, η, defined by Schlichting.

For the 90° wedge, where $m = 1/3$, η is defined as

$$\eta = y_1 \sqrt{\frac{2AU}{3\nu}}\, x_1^{-1/3} . \tag{2.9}$$

A is the constant given by Equation 2.5. U is the velocity of the free stream potential flow in the parent branch and ν is the kinematic viscosity. The velocity components are as follows:

$$u_{f1} \simeq AUx^{1/3}\left[0.98\eta - 0.2496\eta^2 + 0.00408\eta^5 \ldots\ldots\right];$$

$$v_{f1} \simeq -\sqrt{\left(\frac{2\nu AU}{3}\right)}x^{-2/3}\left[0.0416\eta^3 - 0.00136\eta^6 + \ldots\ldots\right]. \tag{2.10}$$

The thickness of the boundary layer along a wedge, when u_{f1} is 99% of the velocity of the potential flow along the wedge, is determined from the following:

$$\zeta(x_1) = \left\{\eta \left| \frac{u_{f1}}{U(x_1)} = 0.99 \right.\right\} \sqrt{\left(\frac{2}{m+1}\right)\frac{\nu}{AU}}\; x_1^{\left(\frac{1-m}{2}\right)} . \tag{2.11a}$$

For the specific case of the 90° wedge:

$$\delta(x_1) = 3.38\sqrt{\frac{\nu}{AU}}\, x_1^{1/3} \tag{2.11b}$$

The displacement thickness, as defined by Schlichting (1968: 28), is evaluated for the 90° wedge with $y_1 = \Delta(x_1)$ from Equation 2.11b as the upper limit of integration:

$$\delta_1 x_1 = \delta(x_1) - 0.49A\left(\frac{2AU}{3\nu}\right)^{1/2} \delta^2(x_1)$$

$$+ 0.0832A\left(\frac{2AU}{3\nu}\right) x_1^{-1/3} \delta^3(x_1) - 0.00068\left(\frac{2AU}{3\nu}\right)^{-5/2} x_1^{-5/3} \delta(x_1)^6 \tag{2.12}$$

When evaluated at any x_1, $\delta_1(x_1) \cong 1/3\,\delta(x_1)$.

2.3 Theories of Deposition by Inertial Impaction, Sedimentation, and Interception

2.3.1 General Equation of Particle Motion

The general equation for the nonuniform rectilinear motion of a rigid sphere moving at low Reynolds numbers through a fluid is (Fuchs, 1964: 70-76):

$$4/3\,\pi r_p^3 \rho_p \frac{du}{dt} = 6\pi\mu r_p (u_f - u)$$

$$+ 4/3\,\pi r_p^3 \rho_g \frac{du_f}{dt} + 2/3\,\pi r_p^3 \rho_g \left(\frac{du_f}{dt} - \frac{du}{dt}\right)$$

$$+ 6r_p^2 \sqrt{\pi \rho_g \mu} \int_{to}^{t} \frac{\left[\frac{du_f}{dt'} - \frac{du}{dt'}\right] dt'}{\sqrt{t - t'}} + 4/3\,\pi r_p^3 g(\rho_p - \rho_g). \tag{2.13}$$

Equation 2.13 is derived by first solving the Navier-Stokes equations with the inertial terms neglected. Using this solution, the drag force on the particle is then calculated by integrating the local pressure and viscous forces over the surface of the sphere (Landau and Lifshitz, 1959; Basset, 1888).

The term on the left-hand side of Equation 2.13 is the resultant force acting on the particle. The first term on the right has the form of the Stokes frictional drag. The second is due to the pressure gradient in the air surrounding the particle, caused by the acceleration or deceleration of the air. It can also be interpreted as the force the particle would experience if it were completely entrained ($u_f = u$) in the accelerating or decelerating air. The third term is the force required to accelerate the apparent mass of the particle relative to the air. The fourth term, "the Basset term", accounts for the increased instantaneous flow resistance associated with the deviation of the air flow pattern from steady state. The fifth term is the force on the particle caused by the acceleration of gravity.

For particles traveling in air in the real lung or the model, the second, third and fourth terms are negligible, because $\rho_g \ll \rho_p$ and the magnitude of the instantaneous and relative accelerations and decelerations of the particles and fluid are small. "The Basset term", which has been analyzed and evaluated by Basset (1888) and Fuchs

(1964: 72-74), is only significant for $\rho_g \geq \rho_p$ or when a strong external force accelerates the particle at a high rate. Neglecting these terms and including the slip flow correction, Equation 2.13 becomes

$$\frac{du}{dt} = -(u - u_f - V_s)/\tau , \tag{2.14}$$

where τ and V_s are respectively the particle's relaxation time and terminal settling velocity discussed in Section 1.2.4.

The Cunningham slip correction (Davies, 1945) is given by

$$C = 1 + \frac{\lambda}{r_p}\left[1.257 + 0.4\exp(-1.10\, r_p/\lambda)\right], \tag{2.15}$$

where λ is the mean free path of the gas. It must be used for particles less than 10μm in diameter in the lung.

Particle motion in the real lung and the model is actually curvilinear rather than rectilinear. Since the resistance of the fluid for a curved trajectory is assumed to follow the form of the Stokes drag, the vector form of Equation 2.14 describes the curvilinear motion. The component of the particle motion along any axis obeys Equation 2.14 because the motions resolved along different axes are independent of one another (Fuchs, 1964: 107).

Equation 2.14 is valid for $Re_p < 0.1$, where $Re_p = 2r_p|\vec{u} - \vec{u}_f|/\nu$. The maximum value of Re_p determined during the trajectory calculations (Section 2.3.6) of a 10μm particle in 100 cm./sec. potential

flow in the "2-D" model, neglecting gravity, was 0.0445. For a 5.7μm particle depositing by simultaneous inertial impaction and sedimentation in 200 cm./sec. potential flow on a 70° wedge, the maximum $Re_p = 0.0595$. Therefore, Equation 2.14 is probably an adequate approximation for particles in the respirable range (< 10μm) at the flow conditions assumed in the model.

Equation 2.14 is not valid for particles within five diameters of the wedge wall; however, the increased resistance can generally be neglected because the rapidly moving particles spend little time close to the wall before contacting it by sedimentation or inertial impaction. Particle-particle interaction phenomena, like hindered settling, can also be neglected because the concentration of inhaled aerosols > 0.5μm in diameter is normally to small.

The following assumptions concern the nature of interactions between particles and the model boundaries:

1. All collisions are effective with no rebound,
2. there is no particle re-entrainment caused by air shear,
3. a particle deposits when it arrives at a distance of one radius from the model wall.

The assumptions hold well for the real lung whose walls are moist and almost completely covered by sticky mucus; however, care must be taken to maintain them in experimental lung models.

A similitude analysis of particle deposition by inertial impaction, sedimentation and interception at bifurcations in the conducting airways is given in Section 3, Appendix A. The results show the limited extent to which deposition data obtained in one bifurcation model of one lung generation can be rigorously applied to predict the deposition in other generations.

2.3.2 Sedimentation

Sedimentation in the "2-D" model is analyzed for a vertical parent branch, like the trachea in an erect person. Because the quasi-steady flow approximation is assumed to hold, the particles settle at their terminal velocity. When the flow is steady and inertial effects are neglected the particle velocity, determined from Equation 2.14 is $\vec{u} = \vec{u}_f + \vec{V}_s$.

The deposition efficiency, ϵ, and the local particle transfer coefficients for sedimentation (neglecting inertial impaction and interception) are independent of the velocity distribution, provided the flow is fully developed and nonturbulent. For laminar flow having an average velocity U in a horizontal channel of length L and width h, Fuchs (1964: 110) determined

$$\epsilon = V_s L/Uh .$$

Similarly, for the "2-D" model with the inside walls of the daughter

branch slanted at an angle of α from the vertical and with steady potential flow,

$$\epsilon = \frac{V_s \sin\alpha\, L}{U_2 h_2} = \frac{V_s \sin\alpha\, L}{Uh} \quad . \tag{2.16}$$

Since gravity acts uniformly, the local particle transfer coefficient is independent of x_1; therefore,

$$k_{loc} = k_{av} = \frac{\epsilon Uh}{L} = V_s \sin\alpha \; . \tag{2.17a}$$

The results are consistent with the parameter dependence predicted by Equations A.24, A.25 and A.26. In dimensionless form

$$k_{loc} = k_{av} = U(Stk/Fr) \sin\alpha . \tag{2.17b}$$

All theoretical curves for sedimentation in Chapter 6 are calculated from Equation 2.17a.

If steady laminar boundary layers exist along the wedge, the fluid velocity components (u_{f1}, v_{f1}) depend on x_1 and y_1; therefore, k_{loc} and ϵ for sedimentation depend on the local velocity distribution. In theory, local deposition by sedimentation could be significantly lower than predicted by Equation 2.17b in regions in which $v_{f1} + V_s \sin\alpha \geq 0$ (Friedlander, 1959). Instead of deriving complex relations for k_{loc} and ϵ for pure sedimentation in the "2-D" model with laminar boundary layers, the computer program, described in Section 2.3.7 and 2.3.4, can be modified to calculate k_{loc} for

simultaneous inertial impaction and sedimentation in steady laminar boundary layer flow.

2.3.3. Interception

Interception of particles on simple objects is a significant factor in the overall collection efficiency only when the particle's diameter is the same order of magnitude as the collecting object. Nevertheless, even when the particle is small compared to the object, interception may be the only significant mechanism of collection if Brownian motion, inertial forces and sedimentation are negligible. This may be the situation in parts of the real lung and in the bifurcation model at a horizontal orientation for particles between 0.5 and 2.0μm.

For deposition by pure interception, the Stokes and Froude numbers are neglected in the similitude relations of Equations A.20 through A.26. In the case of potential flow in the bifurcation model, Equation 2.6 predicts and Figure 2.2 demonstrates that the streamlines are symmetric about a line drawn perpendicular to the wedge at the carina. Therefore, the deposition efficiency and the average particle transfer coefficient by pure interception are simply

$$\epsilon = r_p/h, \quad \text{and} \quad k_{av} = r_p U/L. \tag{2.18}$$

The interception efficiency is greater for pure potential flow than for potential flow with a laminar boundary layer along the wedge because the boundary layer displaces the potential streamlines by a distance of $\delta_1(x_1)$ (Equation 2.12). Consequently, less interception is expected at lower Reynolds Numbers. Also, a particle with a radius less than the local displacement thickness cannot deposit by pure interception because the boundary layer velocity component, v_{fl}, is positive everywhere along the wedge. Hence, ϵ and k_{av} for a steady laminar boundary layer along the wedge of length L are given by

$$\epsilon \leq \frac{[r_p - \delta_1(L)]}{h} \quad \text{and} \quad k_{av} \leq \frac{[r_p - \delta_1(L)]U}{L}. \qquad (2.19)$$

The local transfer coefficient for interception from potential flow can be determined with the aid of the stream function in Equation 2.6. Particles are assumed to be deposited at fixed positions along the wedge by the streamlines that intersect their centers at the deposition locations. Using the analytic expression for ψ, in terms of x and y, and the x = -1 cm. starting coordinate, the starting y coordinate can be calucated by interation. From the series of deposition locations and starting positions, the local particle transfer coefficient can be calculated as described in Section A.3 or 2.3.6. A computer program (Appendix E.2) was written and used to make

these calculations for particle sizes run in the "2-D" experimental model. Plots of the local transfer coefficient versus distance along the wedge for each of the particle sizes are shown in Figures 5.2 through 5.7. These plots indicate that interception is the dominant mechanism in the deposition of respirable aerosols by simultaneous inertial impaction and interception in a potential flow regime downstream from the carina.

2.3.4 Deposition by Inertial Impaction and Sedimentation of Particles of Finite Diameter

Because an analytical solution to Equation 2.14 was not possible, a numerical solution was obtained for a steady potential flow in the bifurcation model in a vertical orientation. The time is divided into equal small intervals and the particle trajectory into corresponding segments (Fuchs, 1964: 135-137). The x and y components of the equation of motion are

$$\frac{du}{dt} = \left[u_{fi} + V_s - u \right] / \tau \qquad (2.20)$$

and

$$\frac{dv}{dt} = \left[v_{fi} - v \right] / \tau \qquad (2.21)$$

where u_{fi} and v_{fi} are the potential velocity components at the beginning of the interval. Integrating and assuming that $u = u_i$ at $t = 0$, the particle velocity components at the end of the interval at time t are

$$u = u_i + [u_{fi} + V_s - u_i][1.0 - \exp(-t/\tau)] \tag{2.22}$$

and

$$v = v_i + [v_{fi} - v_i][1.0 - \exp(-t/\tau)]. \tag{2.23}$$

Integrating again gives the x and y coordinates of the particle's trajectory at the end of the time interval:

$$x = x_i + (u_{fi} + V_s)t + \tau[u_i - (u_{fi} + V_s)][1.0 - \exp(-t/\tau)] \tag{2.24}$$

and

$$y = y_i + v_{fi}t + \tau[v_i - v_{fi}][1.0 - \exp(-t/\tau)]. \tag{2.25}$$

Calculation of a particle trajectory in the model begins at one centimeter before the wedge. This starting point is at a sufficient distance upstream from the curvilinear flow region such that the potential flow is rectilinear and nearly constant. Hence, the particle's initial velocity is equivalent to the potential flow velocity plus the terminal settling velocity: $u_i = u_{fi} + V_s$; $v_i = v_{fi}$.

Equations 2.7 and 2.8 are used for u_{fi} and v_{fi} in Equations 2.22 through 2.25 to calculate the particle's trajectory step by step. The trajectory terminates either for deposition on the wedge wall defined by $u = v = 0$ for $y_1 = r_p$ and $x_1 \geq 0$ or when the particle exits the daughter branch.

The local deposition flux is obtained numerically from $F_s = F_o \Delta y / \Delta x_1$, derived in Section 3 of Appendix A. $\Delta y = y_2 - y_1$, where y_2 and y_1 are the vertical starting coordinates for two particle

trajectories at x = -1 cm. $\Delta x_1 = x_{12} - x_{11}$ is the separation distance of the two impaction sites. The local transfer coefficient at the average deposition location, $(x_{11} + x_{12})/2$, is $k_{loc} = F_o \Delta y / c_\infty \Delta x_1 = G \cos \phi \Delta y / \Delta x_1$. G is the average speed of the two particles at their starting positions and ϕ is the angle between the average velocity vector and the stagnation streamline. The accuracy of this technique is improved when all particles are started within the same small distance, Δy, of each other.

Incorporating the equations discussed in this section, a computer program was written in Fortran IV (Appendix E. 1) to determine the local particle transfer coefficients along the wedge of the bifurcation model. The variable inputs are the wedge angle, the parent and daughter branch dimensions, the free stream velocity (U), the particle radius and the relaxation time, the Δy increment between starting positions, a time interval for the trajectory steps, and an arbitrary limit on the distance of travel of a particle along the wedge. A time interval of 0. 00001 seconds was used in all theoretical results presented in this thesis. By trial and error it was determined to be the largest time interval allowable to accurately predict the trajectories for all particle diameters studied. Results, obtained by this program for deposition by inertial impaction and sedimentation of particles of finite diameter when potential flow is assumed, are presented in

Plots 1 through 8 and discussed in Section 6.3.

The average transfer coefficient along the wedge can be determined by averaging the results for the local transfer coefficient over the length of the wedge. However, it is easier to use the following relations:

$$\epsilon = y_{max}/h \quad ; \quad k_{av} = \epsilon Uh/L. \tag{2.26}$$

y_{max} is the maximum starting position that a particle or desired size can have to deposit on the surface of the wedge. It is determined by trial and error from the computer program in Appendix E.1.

The following is an alternative method of estimating the local transfer coefficients for simultaneous deposition by inertial impaction and sedimentation of particles of finite diameter. The local transfer coefficient for inertial impaction including interception is first determined by setting $V_s = 0$ in the computer program described in this section. The transfer coefficient for sedimentation from Equation 2.17a is then added to this solution at every location, and the sum is used to estimate the transfer coefficient for the two mechanisms occurring simultaneously. This approach of summing the separate transfer coefficients for each mechanism is traditionally used in the design of particle collection equipment.

Figure 2.3 shows the error involved in using this alternate

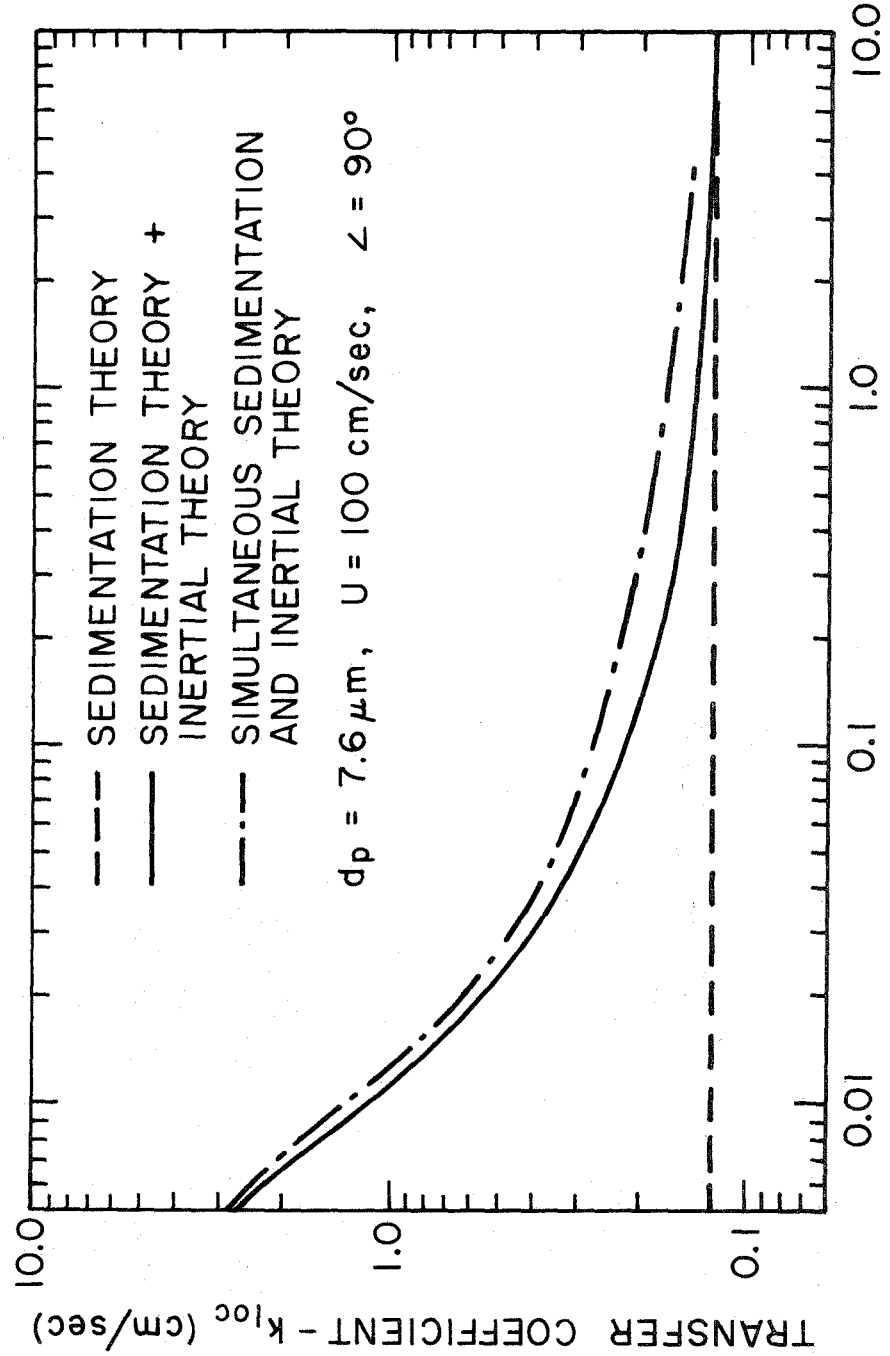

Figure 2.3 Comparison of Two Methods of Estimating the Transfer Coefficients When Deposition is Caused Simultaneously by Inertial Impaction (Including Interception) and Sedimentation. Calculations for 7.6 μm Diameter Particles (Unit Density) Depositing on a Vertically Oriented 90° Wedge in Potential Flow with U = 100 cm/sec.

method to estimate the transfer coefficient of 7.6μm particles on a 90° wedge for U = 100 cm./sec. The wedge is oriented with its two walls at 45° angles from the vertical. The alternative method (sedimentation theory + inertial theory) underestimates the simultaneous sedimentation and inertial theory along the entire wedge, and by a maximum degree of 23% at x_1 = 0.4 cm. These results demonstrate that the difference between the transfer coefficients predicted by the two methods can be non-negligible. Therefore, the simultaneous method of calculation was used for all comparisons of theory with experimental data.

2.3.5 Inertial Impaction of Particles of Finite Diameter: Steady Potential Flow

When the "2-D" model is oriented with the acceleration of gravity perpendicular to the plane of the bifurcation, no sedimentation can occur on the wedge. Consequently, V_s is set equal to zero in the computer program discussed in Section 2.3.4.

A typical example of the calculated particle trajectories is shown in Figure 2.4 for 20 micron particles (dashed lines) in potential flow with U = 100 cm./sec. The particles were started at x = -1.0 cm. and were separated vertically by 40 microns. A time interval of 0.0001 seconds and a relaxation time of 0.00123 seconds were used.

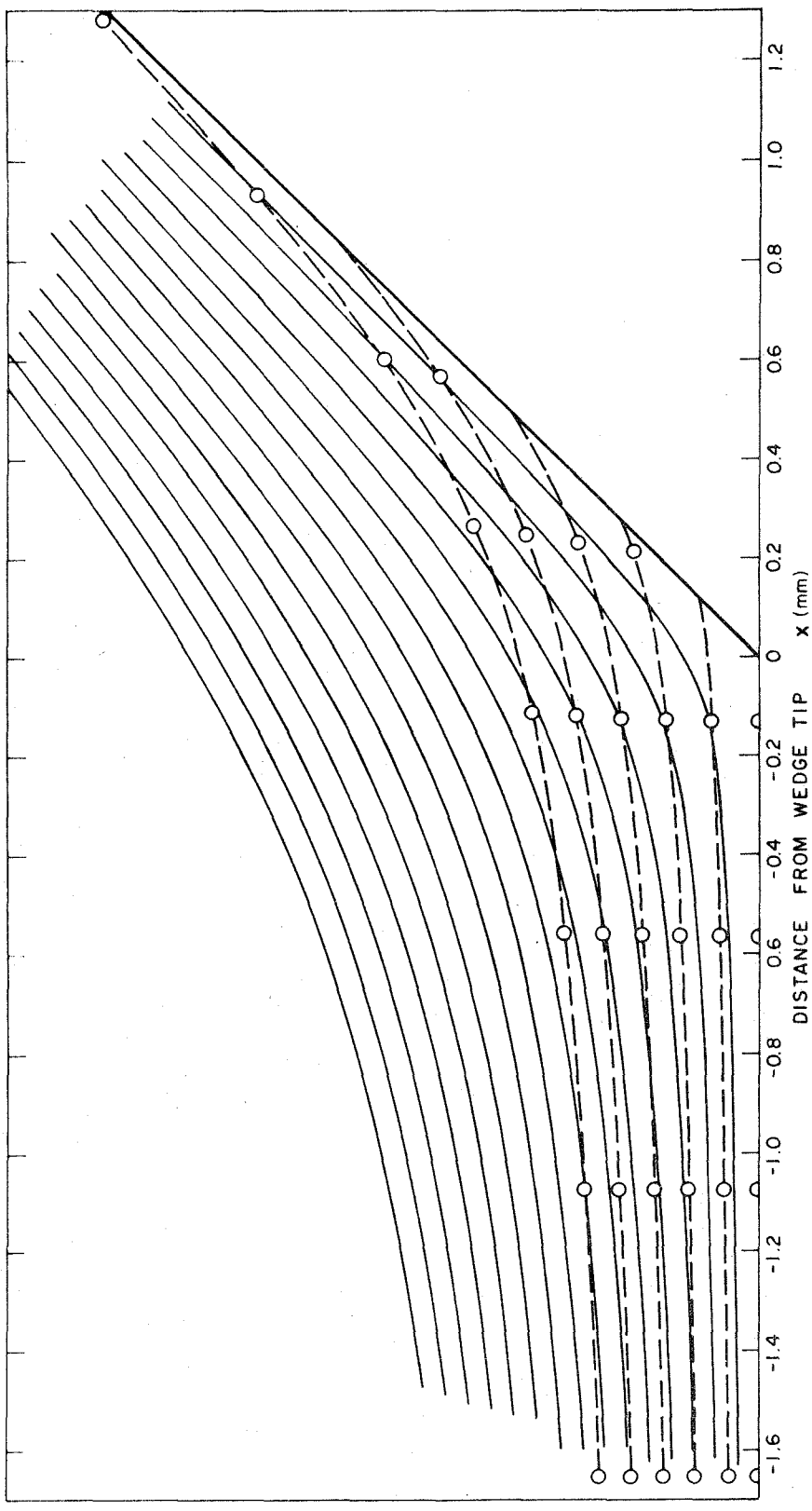

Figure 2.4 Trajectories (---) for 20 μm Diameter Particles with Potential Flow Streamlines (——) in the Top Half of the Two-Dimensional Model at the Carina (U = 100 cm/sec)

The observed deposition locations are closer together near the carina than downstream; therefore, the local transfer coefficients are greater at the carina than downstream.

With a time interval of 0.00001 seconds and the same initial spacing and relaxation time, the most distant impaction site of the 20μm particles was at 1.5 cm. downstream. The vertical starting position corresponding to this deposition site was y = 0.024 cm., which is slightly more than one-fourth the stopping distance of the 20μm particle in U = 100 cm./sec. Hence, only particles which travel within a few particle diameters of the stagnation streamline in the trachea will deposit by inertial impaction and interception on the wedge. Besides demonstrating the low deposition efficiency, these results indicate the strong local effect of interception. This conclusion is reinforced by the critical Stokes number analysis (Section A.4); neglecting interception, a free stream velocity of at least 369 cm./sec. is required for any inertial deposition of 20μm particles on the carina.

Figure 2.5 presents the numerical solutions for the inertial deposition of 1, 2, 3, 4, 5, 10 and 20μm diameter particles (unit density) on the 90° wedge of the "2-D" model. The interception effect is included in the solution and the free stream potential velocity in the parent branch is 100 cm./sec. The points for each particle size

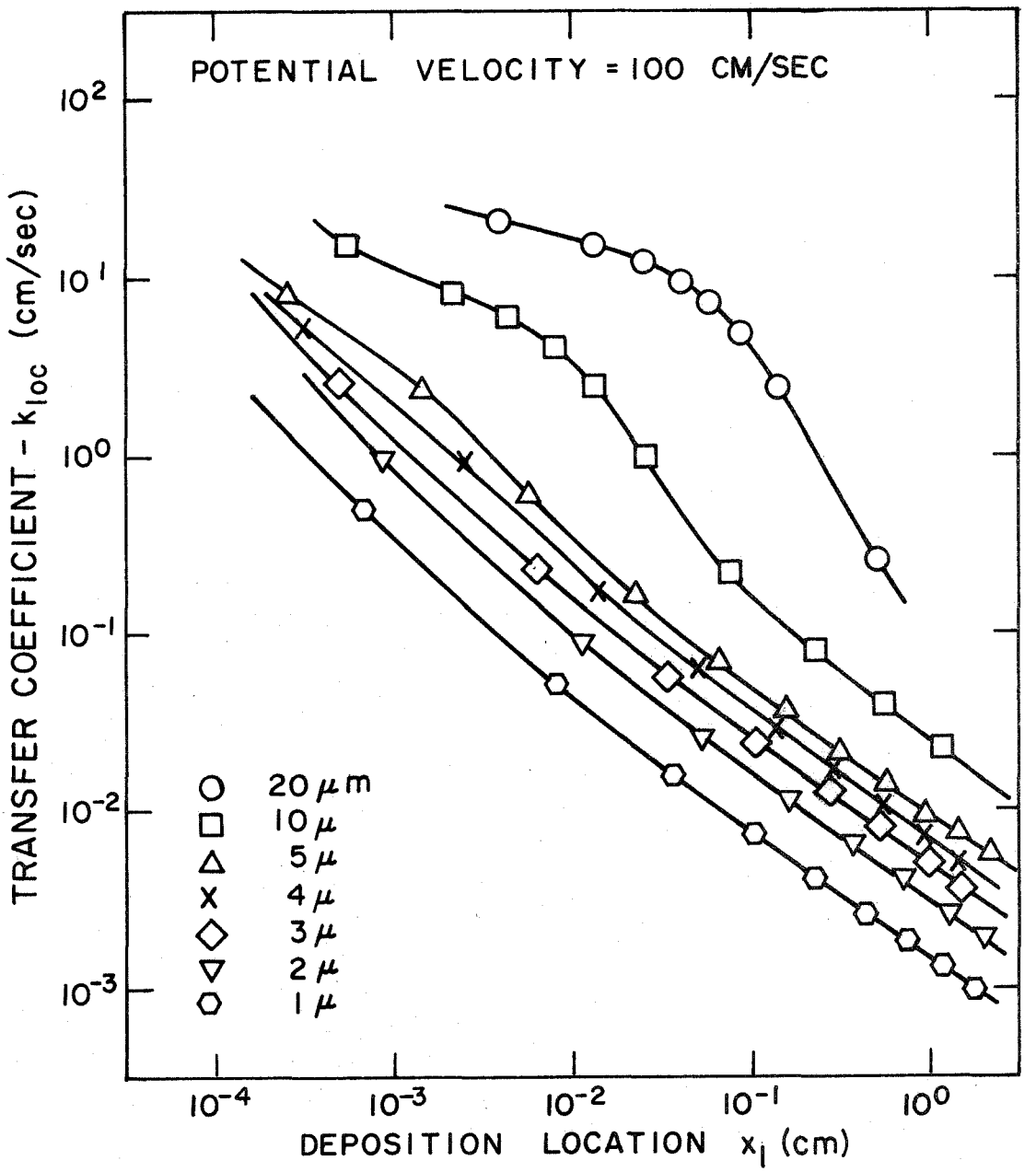

Figure 2.5 **Theoretical** Inertial Impaction with Interception for Various Particle Diameters Along the 90° Wedge of the "2-D" Model in Steady Potential Flow. Points **Represent** Theoretical Calculations.

were calculated from the computer program discussed in Section 2.3.4 and a solid line was drawn through them. Table C.1 (Appendix C) lists the relaxation time, stopping distance perpendicular to the 90° wedge, and the Δy starting intervals for all particles discussed in Figure 2.5.

For each particle diameter, the local transfer coefficient depends on the distance along the wedge, x_1, raised to a negative power which also depends on x_1. Accordingly, the deposition at the carina is predicted to be two to three orders of magnitude larger than at the end of the daughter branch. The variation in magnitude of the transfer coefficient from one particle diameter to another at a fixed deposition location depends on some function of the Stokes and Interception numbers (Equation A.22). The regions of small, negative slope, close to the carina for 10 and 20μm particles, are similar to the region of uniform inertial impaction predicted for stagnation flow onto a perpendicular wall. Pure inertial impaction is dominant in this region close to the carina as demonstrated by the pure inertial deposition (neglecting interception) curve for 7.6μm particles in Figure 5.2.

The variation in the spacing of the calculated deposition points in Figure 2.5 and the enhanced inertial deposition for larger particles is expected from the form of the trajectories in Figure 2.4. The

particles of largest diameter are least affected by the deceleration of the air toward the carina and the subsequent bending and acceleration beyond the carina, because their momentum carries them in fairly straight trajectories into the tip of the wedge. However, large particles deposit mainly by interception downstream from the carina in the region where their trajectories follow the streamlines more precisely.

Because particles with small relaxation times follow the streamlines very closely throughout their trajectories, inertial impaction is negligible and interception is the dominant mechanism of their deposition. The increasing dominance of interception over inertial impaction for smaller particles is clearly observed in Figures 5.2 through 5.6; the separation distance between the theory of interception and the theory of inertial impaction (including interception), both in potential flow, decreases with decreasing particle diameter at any location along the wedge.

The magnitude of momentum transferred to the wedge by the impaction of respirable size particles is very small. For example, a 10μm particle is calculated to deposit on the carina at a final velocity of only 15 cm./sec. when carried on the stagnation streamline in potential flow with U = 100 cm./sec. The amount of momentum transferred is only 7.86×10^{-6} dyne-sec.

2.3.6 Quasi-Steady Deposition by Inertial Impaction of Particles of Finite Diameter: Potential Flow

This section evaluates the accuracy of using a steady potential flow, equivalent to the time-average velocity of a pulsatile inhalation, to predict the deposition of particles by inertial impaction with interception in the lung model.

A flow rate versus time curve, having a form typical of normal inhalations, is shown in Figure 4.4 (Silverman and Billings, 1961). Choosing a breathing frequency and a tidal volume for which the quasi-steady flow assumption is valid in the "2-D" model (Section 1.3.5), the pulsatile inhalation can be simulated by a series of different steady flow rates.

Figure 2.6 presents the local transfer coefficients for 1.0μm particles depositing by inertial impaction with interception. They were calculated for seven steady potential velocities which approximate a pulsatile inhalation having a time-average velocity of 100 cm./sec. and a flow rate versus time curve like Figure 4.4. Using the time intervals of the pulsatile inhalation corresponding to the series of steady flow rates, the deposition curves were time-averaged at each of four deposition locations marked by the crosses (+). The time-averaged deposition curve, indicated by the dashed line, corresponds almost exactly with the deposition curve for the

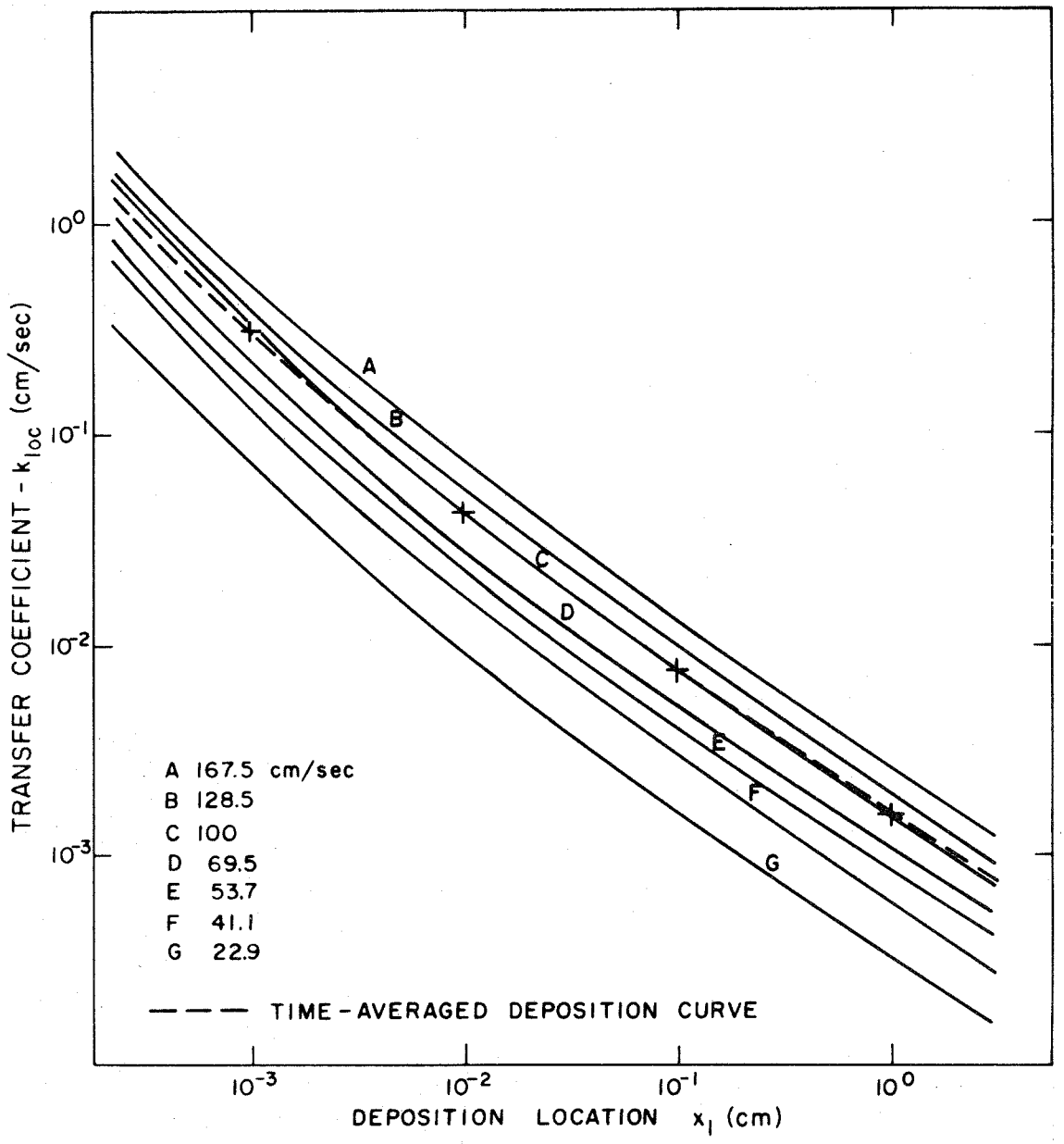

Figure 2.6 Theoretical Inertial Impaction with Interception for 1 μm Particles at Various Potential Velocities and the Time-Averaged Deposition Curve for a 1 sec, 300 cc Inhalation into the "2-D" Model

time-average velocity of 100 cm./sec.

Figure 2.7 for 10μm particles is analogous to Figure 2.6; however, the time-averaged deposition curve corresponds more closely to the 114.5 cm./sec. deposition curve than to the 100 cm./sec. curve. If the deposition curve calculated for potential flow with U = 100 cm./sec. is used to predict the deposition of 10μm particles in the lung model during a pulsatile inhalation (time-average velocity of 100 cm./sec.), the pulsatile deposition will be underestimated. The degree of underestimation at various locations is as follows: 12.9% at 0.001 cm.; 43.8% at 0.01 cm.; 33.9% at 0.1 cm.; 10.9% at 1.0 cm.

All the curves in Figure 2.6 have the same shape, and the distance of separation between any two curves depends mainly on the ratio of the steady potential velocities. There is also a minor increase of interception at the high velocities because the streamlines are displaced closer to the wedge surface. These are the reasons the time-averaged deposition curve corresponds so well with the 100 cm./sec. curve.

The agreement was not as good for the 10μm case, since a disproportionate increase in inertial impaction occurs for the higher velocity runs compared to the lower velocity runs. The increased curvature and decrease in slope of the deposition curve near the

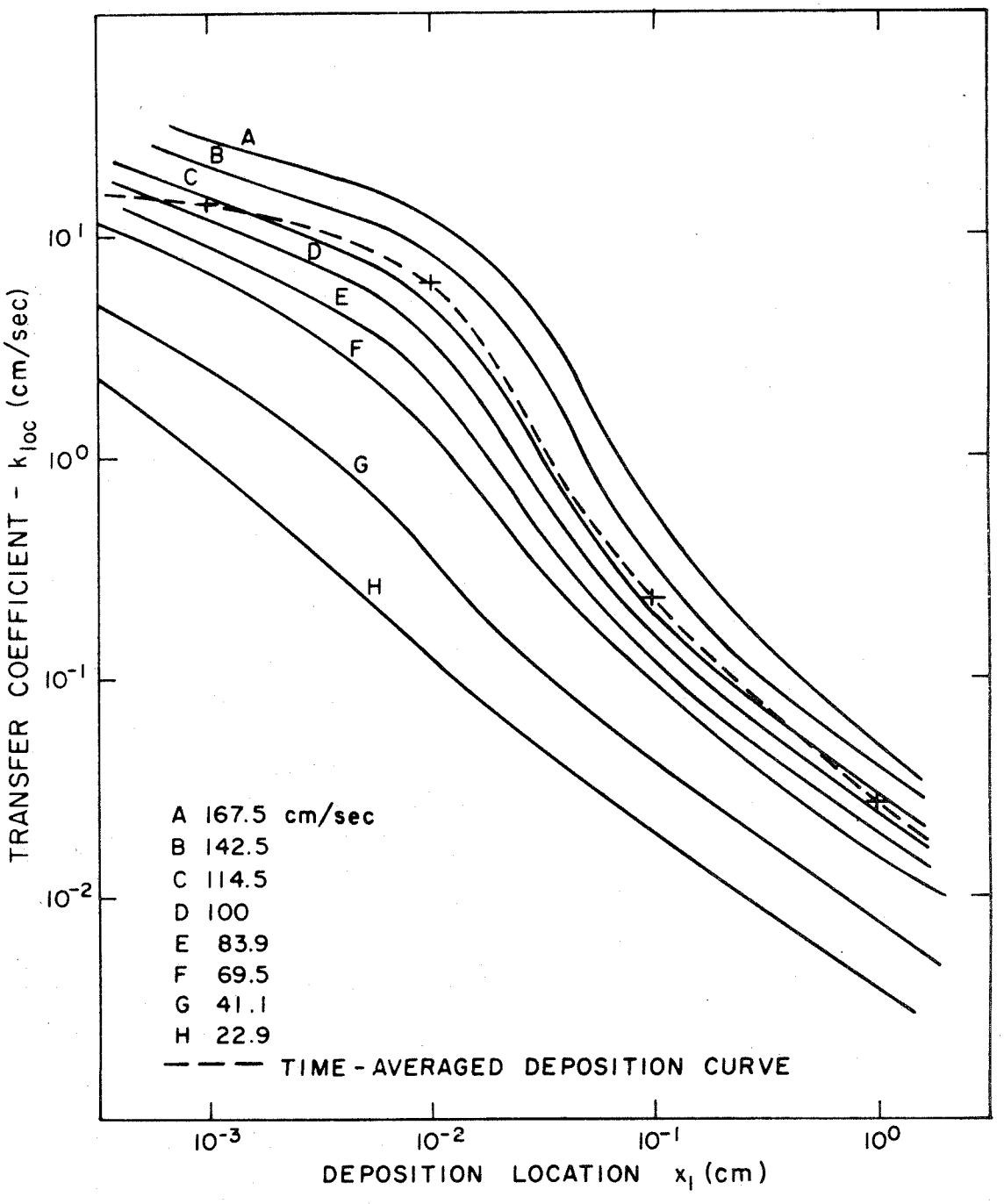

Figure 2.7 Theoretical Inertial Impaction with Interception for 10 μm Particles at Various Potential Velocities and the Time-Averaged Deposition Curve for a 1 sec, 300 cc Inhalation into the "2-D" Model

carina for higher velocity runs is associated with a nonlinear dependence on the Stokes number.

In conclusion, a constant time-average velocity may be used to estimate deposition by inertial impaction with interception during a normal inhalation, but only under limited conditions of flow rate, particle size and breathing frequency.

2.3.7 Inertial Impaction of Particles of Finite Diameter: Steady Laminar Boundary Layer Flow

To determine the local transfer coefficients by inertial impaction with interception for steady laminar boundary layer flow along the wedge, the basic computer program discussed in Section 2.3.4 was used. However, the boundary layer thickness (Equation 2.11b) or the displacement thickness (Equation 2.12) served as a boundary condition for switching the particles from the potential flow regime to the boundary layer flow regime with fluid velocity components defined by Equation 2.10. A time interval of 0.0001 or 0.0002 seconds was used to calculate trajectories in the boundary layer region. The displacement thickness was used to obtain the deposition plots reported below, because the boundary layer thickness in Equation 2.11b gave nearly identical results for all particle diameters.

Figure 2.8 shows the results of the deposition calculations

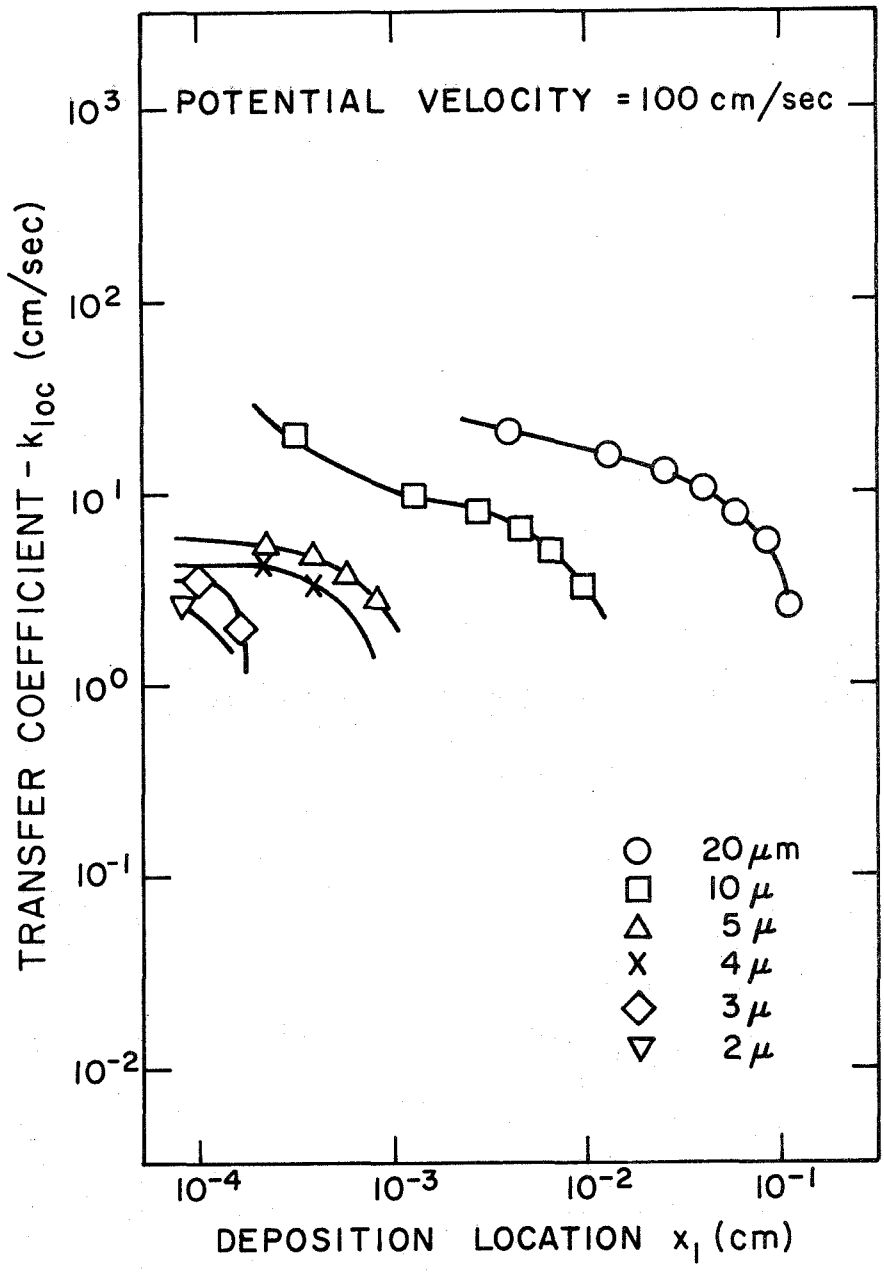

Figure 2.8 Theoretical Inertial Impaction with Interception for Various Particle Diameters Along the 90° Wedge of the "2-D" Model with Steady Laminar Boundary Layer Flow.

for particles in potential flow (U = 100 cm. /sec.) with a steady laminar boundary layer along the wedge. After entering the boundary layer, the particle's velocity rapidly approaches the velocity of the fluid. The 20μm particle is capable of penetrating and depositing at a maximum distance of 0.1 cm. from the carina. The 10μm particle almost reaches 0.01 cm., and the remainder of the particles deposit within distances which are approximately equivalent to their diameters from the carina.

A comparison of Figure 2.8 with the results for steady potential flow in Figure 2.5 shows that the boundary layer results are close to the steady potential flow case near the carina for the 4μm and larger particles. Inertial forces dominate in this region and the deposition pattern is similar to that predicted for stagnation flow on a perpendicular wall because the boundary layer is thin. At the x_1 locations where deposition vanishes in Figure 2.8, interception is controlling in Figure 2.5. At these locations the displacement thickness of the boundary layer is approximately equivalent to a few particle diameters. Also, the fluid velocity component, v_{fl}, normal to the wedge has small positive values. Therefore, deposition should vanish at these locations because particles entering the boundary layer lose their momentum before reaching the surface. Deposition by interception also does not occur because of boundary layer effects

(Section 2.3.3).

Figure 2.9 shows the effect of the velocity of the potential flow on the deposition of 10μm particles with a steady laminar boundary layer. As the velocity increases, the transfer coefficient increases at any distance downstream from the carina. The shape and location of the curves of Figure 2.9 coincide closely with the section of the curves in which inertial impaction is controlling in Figure 2.7. This behavior is expected because, as the stream velocity increases, the boundary layer thickness decreases and the inertial forces acting on the particle increase. Consequently, the particles can penetrate the boundary layer more easily and impact at greater distances along the wedge. The 22.9 cm./sec. curve has an odd shape because the time interval used to calculate the trajectories was too long. However, it would have been expensive and meaningless to recalculate with a smaller time interval.

A plot for 1.0μm particles which was analogous to Figure 2.9 was not included because all the deposition occurred within 0.0001 cm. of the carina.

2.4 Convective Diffusion

2.4.1 Equation of Convective Diffusion and Similitude Analysis

Particle diffusion from a gas can be calculated from the

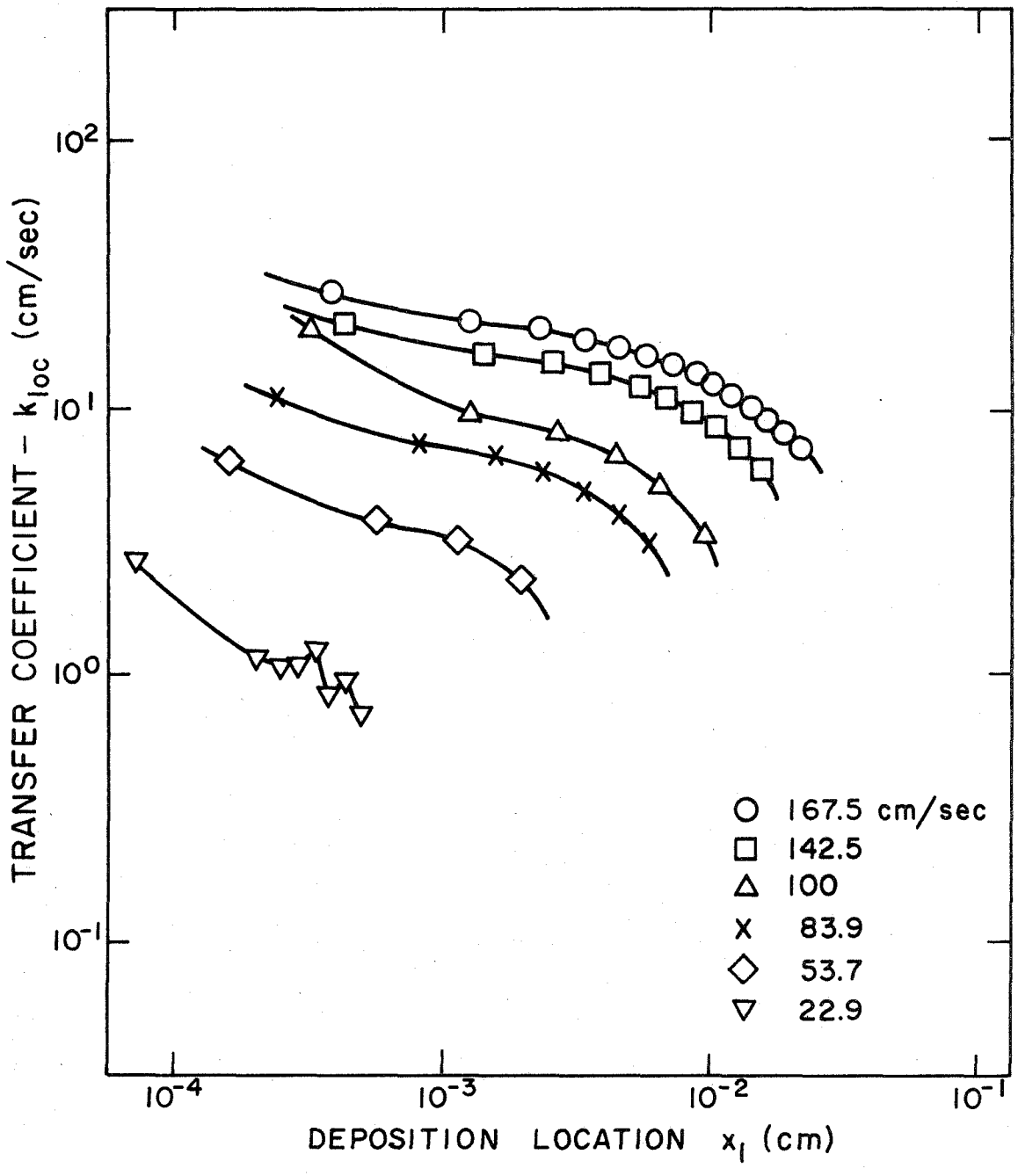

Figure 2.9 Theoretical Inertial Impaction with Interception for 10 μm Particles on the 90° Wedge of the "2-D" Model When Various Potential Velocities Are Used with Steady Laminar Boundary Layer Flow

equation of convective diffusion

$$\frac{\partial n}{\partial t} + \vec{u}_1 \cdot \nabla n = D\nabla^2 n. \tag{2.27}$$

In solving this equation, it is assumed that:

1. The flow is incompressible, isothermal and undisturbed by the presence of the particles.

2. External forces acting on the particles are neglected.

3. Inertial forces on particles are neglected.

4. There is a uniform concentration of particles in the main, undisturbed stream flow far from the surface of the wedge throughout the length of the branch.

Convective diffusion along the wedge of the model is analyzed for the case of a steady laminar momentum boundary layer. For the range of respirable particles the Schmidt Number ($Sc = \nu/D$) is much larger than one and a thin concentration boundary layer will be present under a much thicker, momentum boundary layer.

In the upper tracheobronchial tree, the high rate of convection assures that axial diffusion is negligible compared to radial diffusion. Consequently, the two-dimensional equation for steady convective diffusion along the wedge can be written

$$u_{f1} \frac{\partial n}{\partial x_1} + v_{f1} \frac{\partial n}{\partial y_1} = D \frac{\partial^2 n}{\partial y_1^2} \tag{2.28}$$

with boundary conditions

$$n = 0, \quad y_1 = r_p, \quad x_1 \geq 0;$$

$$n = n_\infty, \quad y_1 = \infty, \quad x_1 \geq 0;$$

$$n = n_\infty, \quad x_1 = 0, \quad y_1 \geq r_p.$$

Since the boundary layer for particle diffusion is thin compared to the momentum boundary layer, it is appropriate to use the first terms in the expansion of the velocity components with respect to distance from the wedge wall (Friedlander, 1967). For any sharp wedge with angle equal to 2α, these take the form (Schlichting, 1968: 150-151):

$$u_{f1} = \beta A U x_1^m \eta$$

and

$$v_{f1} = -\sqrt{\left(\frac{m+1}{2}\right) A U \nu x_1^{(m-1)}} \left\{\frac{\beta}{2}\left(\frac{3m-1}{m+1}\right)\eta^2\right\}. \qquad (2.29)$$

Here $\eta = y_1\sqrt{\left(\frac{m+1}{2}\right)\frac{AU}{\nu}}x_1^{\left(\frac{m-1}{2}\right)}$ and $m = \alpha/(\pi-\alpha)$. β is a constant from the series expansion in η and is tabulated for each value of m. A is the dimensional constant defined by Equation 2.5. For the specific case of the 90° wedge

$$u_{f1} = 0.8(AU)^{3/2}\nu^{-1/2}y_1$$

and

$$v_{f1} = 0. \qquad (2.30)$$

Introducing the dimensionless variables $n^* = n/n_\infty$, $x_1^* = x_1/R_2$ and $y_1^* = y_1/r_p$, and using Equation 2.29, Equation 2.28 becomes

$$x_1^{*3(m-1)/2} y_1^* \frac{\partial n^*}{\partial x_1^*} + \left(\frac{3m-1}{4}\right) x_1^{*3(m-1)/2} y_1^{*2} \frac{\partial n^*}{\partial y_1^*}$$

$$= \left[Pe\, Re^{1/2} I^3 E \right]^{-1} \frac{\partial^2 n^*}{\partial y_1^{*2}} \qquad (2.31)$$

with boundary conditions:

$$n^* = 0, \quad y_1^* = 1, \quad x_1^* \geq 0;$$

$$n^* = 1, \quad y_1^* = \infty, \quad x_1^* \geq 0;$$

$$n^* = 1, \quad x_1^* = 0, \quad y_1^* \geq 1.$$

Here E is a dimensionless constant:

$$E = \beta \left(\frac{m+1}{2}\right)^{1/2} \left(\frac{R_2}{h}\right)^{3/2} \left[A R_2^m \right]^{3/2}$$

Re and I are respectively the Reynolds number and Interception number defined for the daughter branch in Section 3 of Appendix A. Pe is the Peclét number, $2R_2U_2/D = ReSc$.

Inspection of Equation 2.31 and the associated boundary conditions shows that:

$$n^* = H_3(x_1^*, y_1^*, Pe\, Re^{1/2} I^3 E). \qquad (2.32)$$

The local transfer coefficient has the form

$$k_{loc} = -D/r_p \left.\frac{\partial n^*}{\partial y_1^*}\right|_{y_1^*=1}$$

$$= U\,Pe^{-1}\,I^{-1}\,\frac{h}{h_2}\,H_4(x_1^*,\ Pe\,Re^{1/2}\,I^3\,E). \qquad (2.33)$$

Likewise, the overall efficiency has the form

$$\varepsilon = k_{av}L/Uh = Pe^{-1}\,I^{-1}\,H_5\,(L/h_2,\ Pe\,Re^{1/2}\,I^3\,E),$$

or on rearranging

$$\varepsilon\,Pe\,I = H_5(L/h_2,\ I\,Pe^{1/3}\,Re^{1/6}\,E^{1/3}). \qquad (2.34)$$

Equations 2.33 and 2.34 indicate the dimensionless parameter dependence for modeling the deposition by convective diffusion of particles of finite diameter on the wedge of bifurcation models. For fixed values of Re, L/h_2, h_2/h, and α, $\varepsilon\,Pe\,I$ is a single valued function of $I\,Pe^{1/3}$ over the range where $Pe \gg 1$, $Re < 2000$, and $I \ll 1$.

For the case of point particles, $I \to 0$; hence

$$\varepsilon = H_6(L/h_2,\ Pe^{-2/3}\,Re^{1/6}\,E^{1/3}). \qquad (2.35)$$

This is the only case in which similarity in particle deposition from inhaled air can be maintained between bifurcation models of a different scale which are geometrically similar.

2.4.2 Deposition of Point Particles by Convective Diffusion

Equation 2.31 must be solved numerically to determine the transfer coefficient of diffusion range particles of finite diameter. However, Equation 2.28 can be solved analytically if the particle diameter is neglected in the boundary condition. This should be a fairly accurate assumption for the small particles in the diffusion range ($d_p < 0.5\mu m$).

Substituting Equation 2.29, Equation 2.28 is rearranged in terms of the similarity variable η and the function $g(\eta) = n^*$ as follows:

$$-\beta\eta^2 \frac{dg}{d\eta} = \frac{D}{\nu} \frac{d^2g}{d\eta^2} \tag{2.36}$$

with the boundary conditions $g = 0$, $\eta = 0$ and $g = 1$, $\eta = \infty$.

This equation was solved by standard techniques. The local transfer coefficient and deposition efficiency by convective diffusion along the wedge in any bifurcation model for steady laminar boundary layer flow are either

$$k_{loc} = 0.435(m+1)^{1/2}\beta^{1/3}(AU)^{1/2}D^{2/3}\nu^{-1/6}x_1^{(m-1)/2} \tag{2.37}$$

and

$$\varepsilon = 0.87(m+1)^{-1/2}\beta^{1/3}(A/U)^{1/2}D^{2/3}\nu^{-1/6}h^{-1}L^{(m+1)/2} \tag{2.38}$$

or in terms of the Reynolds and Peclét numbers in the daughter branch

$$k_{loc} = 0.629\,U_2(m+1)^{1/2}\beta^{1/3}(h_2/h)^{1/2}A_1^{1/2}\,Pe^{-2/3}\,Re^{1/6}x_1^{(m-1)/2} \tag{2.39}$$

and

$$\epsilon = 0.629(m+1)^{-1/2}\beta^{1/3}(h_2/h)^{1/2}A_1^{1/2}Pe^{-2/3}Re^{1/6}(L/R_2)^{(m+1)/2}. \quad (2.40)$$

$A_1 = AR_2^m$ and Equation 2.40 agrees with the similitude prediction in Equation 2.35.

The thickness of the concentration boundary layer, $\delta_c(x_1)$, is calculated from D/k_{loc}, using Equation 2.37 or 2.39. The ratio of the thickness of the concentration boundary layer to the momentum boundary layer in Equation 2.11a, is given by

$$\frac{\delta_c(x_1)}{\delta(x_1)} = 0.6Sc^{-1/3} \quad (2.41)$$

for any wedge. Equation 2.41 and Equations 2.37 through 2.40 are rigorously applicable in the region of the daughter branches in which the inspiratory flow is undeveloped or for $x_1 \leq 0.1\ R_2Re$.

Kays (1966) gives an expression for the local heat transfer coefficients along wedges of constant temperature which must be evaluated by numerical integration for each combination of Prandtl number, Pr, and m. The value of k_{loc} in Equations 2.37 and 2.39 can be evaluated directly for any particle diameter when the numerical value of β is supplied from tables. In the case of a 90° wedge when Pr = Sc = 10, k_{loc} from Equation 2.39 agrees with Kays'

relation. Values of k_{loc} from Equation 2.39 for Sc = 1.0 are only a few percent higher than those from Kays' relation. Therefore, Equations 2.37 and 2.39 can be used to predict k_{loc} for gases as well as particles in the lungs.

For a 90° wedge (m = 1/3) Equation 2.47 has the form

$$k_{loc} = 0.49\,(AU)^{1/2}\,\nu^{-1/6}\,D^{2/3}\,x_1^{-1/3}. \qquad (2.42)$$

Thus the local transfer coefficient for gases and for all particles in the diffusion range have the same -1/3 power dependence on distance along the 90° wedge, and 10 times more deposition is predicted at $x_1 = 0.001$ cm. than at $x_1 = 1.0$ cm. The deposition models used by Landahl, Beeckmans and others predict a uniform deposition pattern because they fail to account for the entrance flow condition in the daughter branch.

2.4.3 Deposition of Point Particles by Convective Diffusion in Quasi-Steady Laminar Boundary Layer Flow

The deposition by convective diffusion during a normal, pulsatile inspiration can be analytically predicted if the quasi-steady flow assumption is valid. Equation 2.37 is time-averaged over the inhalation period as in Equation A.24 . The potential velocity is the only time dependent variable in Equation 2.37; therefore, the general transfer coefficient for quasi-steady convective diffusion is

$$k_{loc} = 0.435(m+1)^{1/2} \beta^{1/3} A^{1/2} \overline{\sqrt{U}}\, D^{2/3} \nu^{-1/6} x_1^{(m-1)/2} \qquad (2.43)$$

where $\overline{\sqrt{U}}$ is the time-averaged value of $U^{1/2}$. For an inhalation curve of the form shown in Figure 4.4, $\overline{\sqrt{U}} = 9.62$ when the time-average velocity, $\overline{U} = 100$ cm./sec. Therefore, less deposition by convective diffusion is expected for pulsatile inhalations than by steady inhalations having the same time-averaged flow rate.

Chapter 3

THEORETICAL ANALYSIS OF PARTICLE DEPOSITION IN THE THREE-DIMENSIONAL MODEL OF A LUNG BIFURCATION

3.1 Selection of the Airway Model and Flow Regimes

The two-dimensional bifurcation model (Chapter 2) is useful for deriving simple theoretical relations for the local rates of particle deposition. The air flow pattern becomes considerably more complex in the case of flow through branched tubes. Figure 3.1 shows an axial section in the plane of the bifurcation of the branched tube model used in this study. The model is symmetric with dimensions approximately equivalent to the first bifurcation in Weibel's Model "A". The 70° bifurcation angle is close to the mean interbronchial angle of 75° reported by Horsfield and Cumming (1967). The sharp 135° angle in the "2-D" model is replaced by a gradual transition having a radius of curvature equivalent to the radius of the trachea.

The model is also geometrically similar to the tubular model which Schroter and Sudlow (1969) used to measure detailed velocity profiles. Therefore, if the same Reynolds numbers are maintained for steady inspiratory flow, similar velocity profiles should occur in the daughter branches. The velocity profiles in the plane and normal

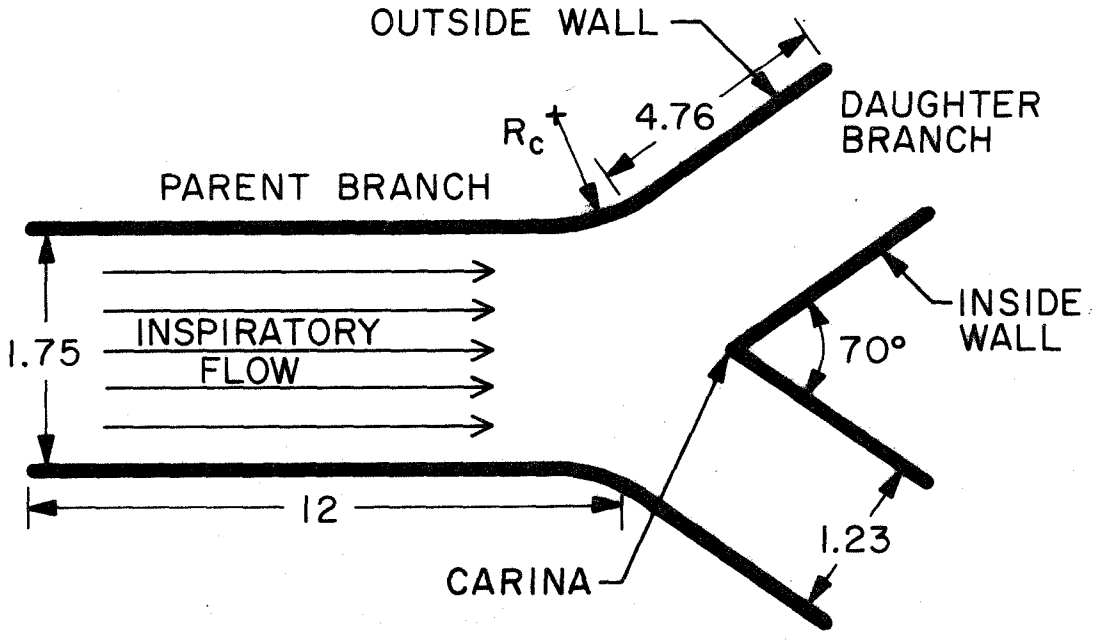

Figure 3.1 Axial Section in the Plane of the Bifurcation of the "3-D" Model, Showing the Diameters and Lengths of Branches in Centimeters. The Radius of Curvature R_c of the Junction Between the Parent Branch and the Outside Wall of the Daughter Branch = 0.875 cm. Branch Lengths not Drawn to Scale.

to the plane of the bifurcation, as shown in Figure 3.2, are qualitatively similar to the profile measured by Schroter and Sudlow for a flat inspiratory profile in the parent branch (Section 1.3.2). The secondary flows observed by Schroter and Sudlow during inspiratory flow are also shown in Figure 3.2 along with the position of the steady laminar boundary layer along the inside wall of the daughter branch.

The air flow analysis in the three-dimensional ("3-D") model is restricted to two cases:

1. An analysis of the application to the "3-D" model of the flow regimes determined for the "2-D" model, and

2. An analysis of the secondary flows and other complications.

3.2 Air Flow Analysis in the Three-Dimensional Model

3.2.1 Application of Two-Dimensional Flow to the Three-Dimensional Model

The "3-D" model can be sliced into axial sections oriented in the plane of the bifurcation. This is demonstrated in Figure 3.3 which depicts the division of the cross-section of the daughter branch into rectangular sections that approximate the cross-sectional area of the branch. When the secondary flows are neglected, the "2-D" potential flow solution (Section 2.2.2) can be applied as an approx-

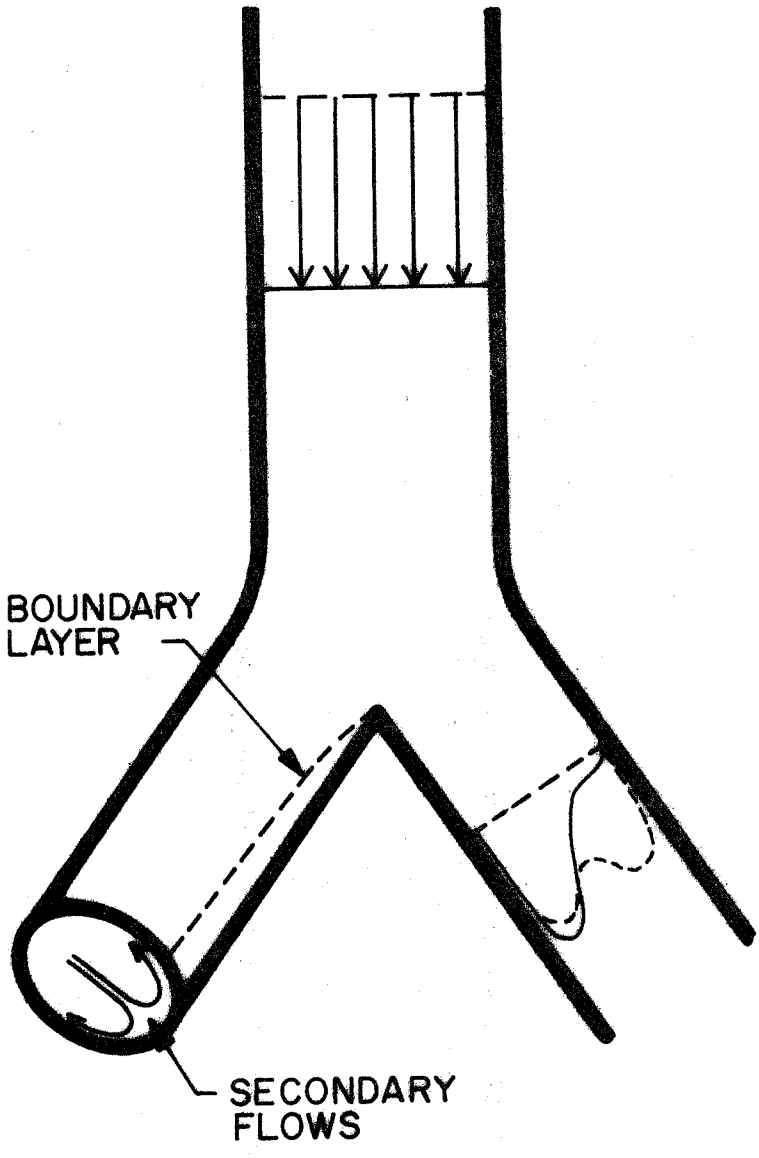

Figure 3.2 Qualitative Representation of the Flow in the Daughter Branches of the Three-Dimensional Model for Steady, Inspiratory Flow with a Flat Profile in the Parent Branch. The Velocity Profiles in the Plane of the Bifurcation (——) and in the Normal Plane (----) Are Indicated in Right Branch. The Orientation of the Secondary Flows and the Position of the Laminar Boundary Layer Are Shown in the Left Branch.

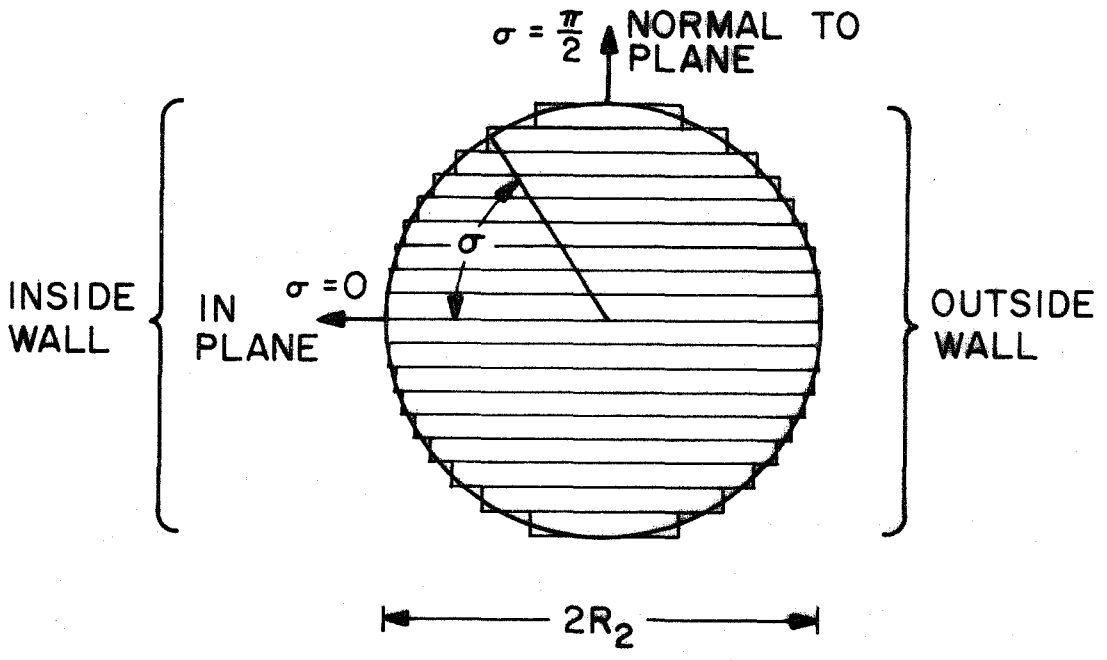

Figure 3.3 Method of Approximating the Cross Section of a Daughter Branch of the "3-D" Model by a Series of Rectangular Sections. $\sigma = 0$ at the Carina in Figure 3.1.

imation to the flow through each rectangular section along the inside wall of the branch. Hacker, Brun and Boyd (1953) used the same approach to describe the potential flow in 90° elbows of various cross sections. Likewise, the boundary layer along a 70° wedge (Section 2.2.3) can be approximately applied to each rectangular section.

Figures 1.2 and 4.12 show that the cross section in the junction on the upstream side can be elliptical with an area less than the cross-sectional area of the parent branch and also less than the combined areas of the daughter branches. To take into account the area change in estimating the local fluid velocity in the rectangular sections (Figure 3.3), A and U in Equations 2.5, 2.7 and 2.8 can be approximated as follows:

$$A_3 = \left\{ \frac{h_3}{\pi-\alpha} \left[\left(\frac{h_2}{h_3} \right)^{\pi/\alpha} + 1 \right] \right\}^{-m} , \tag{3.1}$$

$$u_f = A_3 \frac{S_1}{S_3} U r^m \cos m(\pi - \theta) , \tag{3.2}$$

and

$$v_f = A_3 \frac{S_1}{S_3} U r^m \sin m(\pi - \theta) . \tag{3.3}$$

In Equations 3.2 and 3.3 U is multiplied by the ratio of the cross-sectional area of the parent branch to the area of the smallest cross section before the wedge; in other words, U in Equations 2.7 and 2.8 is replaced by the average velocity in the smallest cross section.

In Equation 3.1, h_3 is the half width of the desired axial section at the location of the smallest cross section. To reevaluate A as in A_3, h_3 replaces h in Equation 2.5.

3.2.2 Analysis of Secondary Flows and Other Complications

Scherer (1972) developed a model for high Reynolds number flow in a human bronchial bifurcation which predicted that the maximum magnitude of the velocity of the secondary flow in Figure 3.2 is approximately 25% of the average axial velocity in the parent tube. Secondary flows of this intensity can complete approximately one cycle within three diameters downstream in his model. This agrees with the experimental observations of Sudlow and Schroter (Section 1.3.2) and with observations in the "3-D" model (Section 4.3).

A cruder estimate of the intensity of the secondary flow can be made by assuming that the motion is similar to a circular helix having a diameter equivalent to the daughter branch radius. In this case, if the secondary flow completes one helical cycle within three diameters downstream, the maximum intensity is 50% of the average axial velocity in the daughter branch. The secondary flows were observed experimentally during inspiration (Schreck and Mockros, 1970) to be fully developed at the point where the daughter branches become circular in cross section.

In their model which was geometrically similar to Figure 3.1, Schroter and Sudlow (1969) also studied the flow on the outside wall, opposite the carina. For a steady, flat profile in the parent branch and for Re from 100 to 4500, they reported the following:

> ....flow separation with reverse flow occurs, just downstream of the junction. The smoke tracer behaves more irregularly and smoke can be seen to move upstream from several entry points. A separation "bubble" is formed of sluggish and reversed flow. This extends at least 1/3 of a diameter across the tube, and at lower Re, was seen to persist at least 1.5 diameters downstream. The mean residence time of particles of fluid within this region is very high.

When pulsatile flow occurs in the model, quasi-steady flow can be assumed only for the conditions suggested in the conclusion of Section 1.3.5. Another complication, occuring only for single breath inspirations, is the replacement of the relatively particle-free air in the model with the particle-laden, inhaled air. The local variation in the replacement rates cause variations in the exposure time of different sections of the model to the inhaled concentration of particles.

The effects of free stream turbulence in flow through real lung airways is discussed in Chapter 7, Section 7.1.3.

3.3 Deposition by Inertial Impaction, Sedimentation, and Interception

When the "3-D" model is oriented vertically, the two-dimensional solution for simultaneous inertial impaction, sedimentation and interception (Section 2.3.4) approximates the deposition along the inside wall of the two rectangles bisecting the branch cross section in Figure 3.3. If the effects of the secondary flows can be neglected, the solution will also approximate the local transfer coefficient at the end of each of the other rectangles next to the inside wall. Multiplying each of these coefficients by the ratio of the width of the rectangle to the arc length to which it corresponds gives the local transfer coefficient along the branch wall in that arc length. In the limit as the width of the rectangular sections become vanishingly small, the multiplying factor equals $\cos\sigma$. As shown in Figure 3.3, σ is the acute angle between a normal to the wall at the deposition location and a normal to the wall in the plane of the bifurcation.

The average transfer coefficient along the branch of the "2-D" model, k_{av}, determined as discussed in Section 2.3.4, is used to calculate the overall deposition efficiency in the "3-D" model as follows:

$$\epsilon = \frac{2k_{av}L}{\pi R_2 U_2} = \frac{4k_{av}R_2 L}{\pi R_1^2 U} \quad . \tag{3.4}$$

Theoretical studies are lacking on the effects of secondary flows on inertial impaction, sedimentation or interception in a branched tube. The secondary flows might enhance the deposition estimated in Equation 3.4 by increasing the effectiveness of interception. Neglecting viscous boundary layers, choosing particles of a size which are entrained by the fluid, and assuming steady inspiratory flow, particles will travel in helical paths along the daughter branch. Assuming one helical cycle per three diameters downstream (Sections 1.3.2 and 4.3), the helical path is 12% longer than an axial path when the flow can be approximated by a circular helix with a diameter of R_2. In another case, if the secondary motion follows the curvature of the branch from the inside to the outside and returns to the inside along the diameter and if one cycle is completed within three diameters, the helical path length is 30% longer than an axial path. Thus, 12 to 30% more particles may flow past any wall location as a result of the secondary flows, leading to an increase in deposition.

Inertial impaction might be enhanced by the centrifugal forces imposed on the particles by the secondary flows. If the secondary flow has a maximum velocity of 25% of the bulk velocity in the parent branch and if the resultant flow has a uniform, circular helical motion with diameter R_2, the ratio of the instantaneous centrifugal force to

the gravitational force in a direction normal to the branch wall is given by

$$\frac{U^2}{8 R_2 \bar{g} \sin\alpha \cos\sigma} \quad . \tag{3.5}$$

Here α is the angle of inclination of the daughter branch from the vertical and σ is defined in Figure 3.3. The ratio equals 3.6 for $\sigma = 0$ and U = 100 cm./sec. in the "3-D" model with vertical orientation. Therefore, the local deposition velocity of a particle in potential flow will be enhanced by 360% if secondary motions of this intensity occur along the wall of the daughter branch.

The above analysis applies under potential flow conditions; that is, when the secondary motions occur up to the wall of the branch. However, in reality the secondary motions are contained in the inviscid core outside the laminar boundary layer (Pedley et al., 1971). Hence, the secondary flow with a maximum velocity of 25% of the parent branch can project a particle into the boundary layer in the direction normal to the wall with an initial velocity of $\tau U^2/8R_2$. The particle can deposit only if its stopping distance

$$h_s = \tau^2 U^2/8R_2 \tag{3.6}$$

is greater than the thickness of the boundary layer. The steady, boundary layer thickness along a 70° wedge

$$\delta(x_1) = 3.65\sqrt{\nu/AU}\, x_1^{11/29} \qquad (3.7)$$

is thicker than the stopping distance calculated from Equation 3.6 for 10 and 20μm particles at U = 100 cm./sec. for $x_1 \geq 10^{-4}$ cm. For U = 200 cm./sec. the stopping distance for 10μm is less than the boundary layer thickness throughout, while the stopping distance for 20μm is greater than the boundary layer thickness only for $x_1 < 0.003$ cm. The boundary layer thickness is also greater than the radius of all respirable particles for $x_1 > 10^{-4}$ cm.

Therefore, a steady, laminar boundary layer should prevent the secondary flows from enhancing the deposition by interception and by centrifugal inertial impaction for the same reasons that the boundary layer inhibited the deposition from potential flow in Section 2.3.7. For pulsatile inhalations with unsteady boundary layers, Section 1.3.6 suggests that enhancement could occur during the few fractions of a second in which the boundary layer is undeveloped.

3.4 Deposition by Convective Diffusion

The regions of high and low shear rate (Figure 3.2) should correspond to regions of high and low particle transfer by convective diffusion. The secondary motions could also increase the local shear rates around the circumference of the branches.

The local transfer coefficient for convective diffusion of point

particles along the 70° wedge in Figure 3.1 for quasi-steady laminar boundary layer flow is determined from Equation 2.43:

$$k_{loc} = 0.413\sqrt{\overline{U}}\, D^{2/3} \nu^{-1/6} x_1^{-11/29}. \qquad (3.8)$$

However, if the modification described in Section 3.2.1 is used, A in Equation 2.43 is replaced by $A_3 S_1 / S_3$. For the specific case of the "3-D" experimental model (Section 4.3), $A_3 S_1 / S_3 = 1.14$ cm.$^{-7/29}$. Consequently, the local transfer coefficient for convective diffusion of point particles along the line $\sigma = 0$ is

$$k_{loc} = 0.489\sqrt{\overline{U}}\, D^{2/3} \nu^{-1/6} x_1^{-11/29}. \qquad (3.9)$$

Because the deposition flux by convective diffusion occurs normal to the branch wall in the "3-D" model, Equations 3.8 and 3.9 can be rigorously applied to only the inside wall of the rectangular section which bisects the cross section in Figure 3.3. Particle transfer rates also depend on the local thickness of the concentration boundary layer which has a variable and unknown functional dependence on position around the circumference of the branch. Therefore, expressions for k_{av} and ϵ as a function of the various dimensional groups of Equations 3.8 or 3.9 must be evaluated from empirical data.

Estimates of k_{av} and ϵ in the "3-D" model for pulsatile flow can be made from the theory of convective diffusion to a flat plate

(Levich, 1962: 87-91) or from Levich's (1962: 112-115) solution for convective diffusion to a tube in Poiseuille flow. Both theories, when converted to quasi-steady form, are expected to underestimate the deposition in the region in which Equation 3.8 is applicable. They also should overestimate the deposition on the outside wall, but to a lesser extent than Equation 3.8.

Other factors affecting the local deposition in the daughter branch, which are not accounted for in Equation 3.8, include the following. During pulsatile flow, a finite time period is required to fill the initially particle-free concentration boundary layer with particles. This time period is greater for larger x_1 and for larger particles in the diffusion subrange. For high breathing rates the time period can be a significant fraction of the inhalation time. However, the secondary motions probably speed the replacement of partially clean air along the outside wall with particle-laden air.

The shape of the concentration profile entering the daughter tubes can also influence the local deposition in the branch. Uniform velocity and concentration profiles with thin boundary layers are assumed for the range of Reynolds numbers considered in the three-dimensional model.

Chapter 4

EXPERIMENTAL APPARATUS AND PROCEDURE

4.1 General Description of the Apparatus and Procedure

A diagram of the complete experimental apparatus is shown in Figure 4.1. The experimental procedure was as follows: Monodisperse, latex hydrosols ranging in diameter from 0.088μm to 7.6μm were nebulized, dried and deionized to produce a neutralized, monodisperse aerosol. The concentration of particles in the model holding chamber was determined by light scattering photometry or by gravimetry. Before each breath, the flow of particles through the holding chamber was stopped. The gate was then opened, and the aerosol in the holding chamber was flushed through the bifurcation model at a rate which simulated a normal inhalation. Room air was sucked back through the model during the exhalation stroke which immediately followed the inhalation stroke. A pause between each breath allowed the particle concentration in the holding chamber to build up to a large and fairly steady value. After a sufficient number of inhalations the collection surfaces in one daughter branch were removed and the number of particles deposited in discrete areas were manually counted under an optical or electron microscope. From the count data, the average particle concentration during the run, and other experimental parameters, the local particle transfer coefficients were calculated.

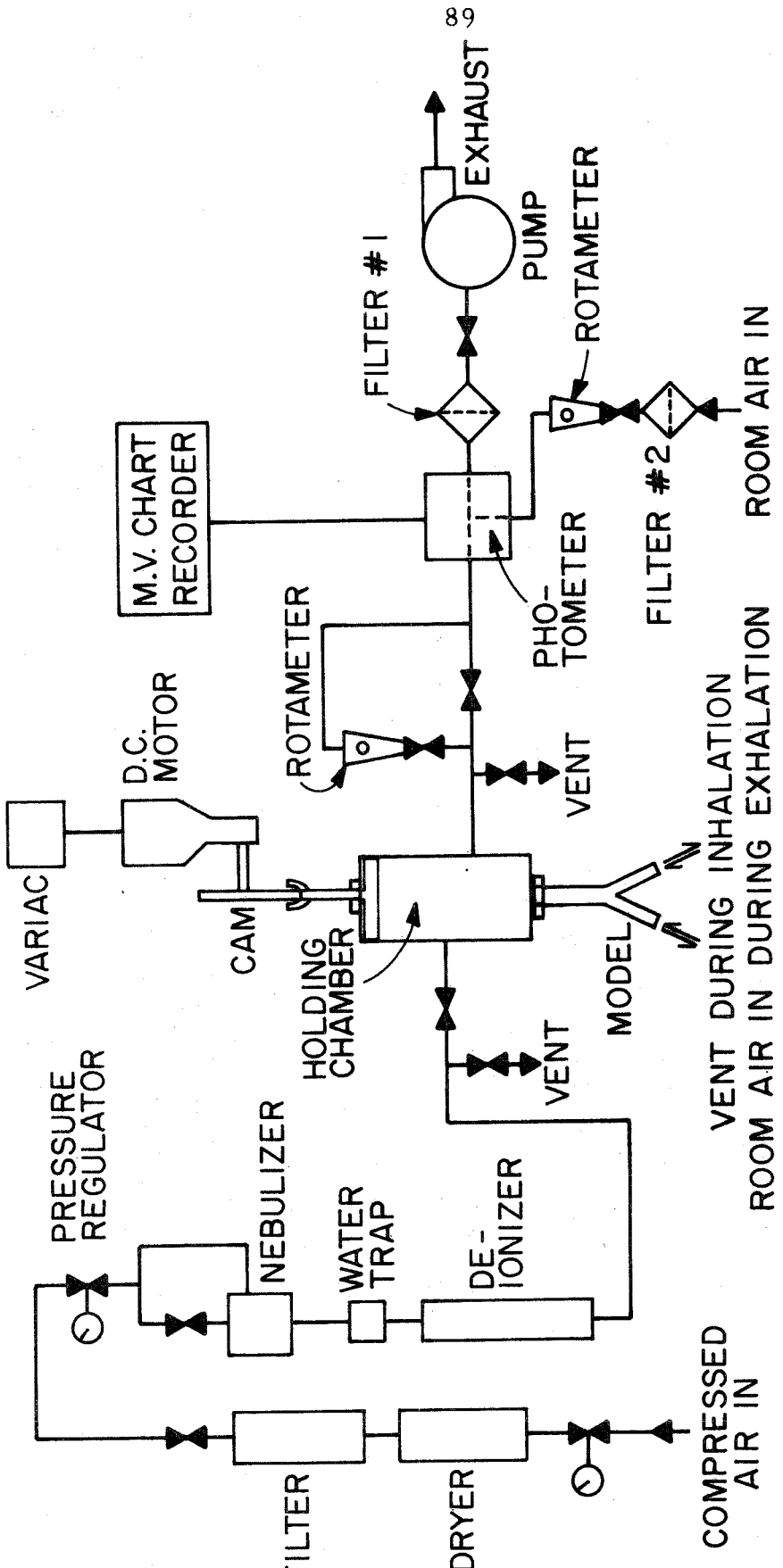

Figure 4.1 Diagram of the Experimental Apparatus. Aerosol Exiting the Model During the Inhalation Stroke and Escaping Through the Vent Valves Is Carried Away by the Steady Air Flow in the Exhaust Hood in Which the Model Apparatus Is Situated.

4.2 Two-Dimensional Apparatus and Experimental Flow Conditions

The "2-D" apparatus[1] (Figure 4.2) has three sections including the "2-D" model, aerosol holding chamber and motor-cam-piston assembly. Figure 4.3 shows a horizontal axial section of the "2-D" model and part of the aerosol holding chamber. The plane of the bifurcation was horizontally oriented in the experimental apparatus to eliminate deposition by sedimentation. Transparent glass plates formed the walls of the one daughter branch and served as removable collecting surfaces. The model had a vertical dimension shown in Figure 4.2 of 18.1 cm. to assure that the air flow was two-dimensional in axial sections between 7.5 and 10.5 cm. from the base of the model.

In Figures 4.2 and 4.3 the aluminum gate forms an air-tight seal between the parent branch and the aerosol holding chamber. The total volume of the holding chamber during the pause between breathing cycles was about 13.5 liters. After the inhalation stroke of the piston (diameter = 7.5 in.), the volume was 5.6 liters less. After each breathing cycle the air with a low particle concentration in the holding chamber was mixed with air of high particle concentration which flowed into the holding chamber. Thorough mixing was accomplished by positioning the inflow tube at the top of the chamber (Figure 4.2) and

---

[1] The "2-D" apparatus was originally designed in 1969 by Richard Vincent, an undergraduate student in Chemical Engineering, who used the model for a preliminary analysis of the deposition of 1.099μm particles.

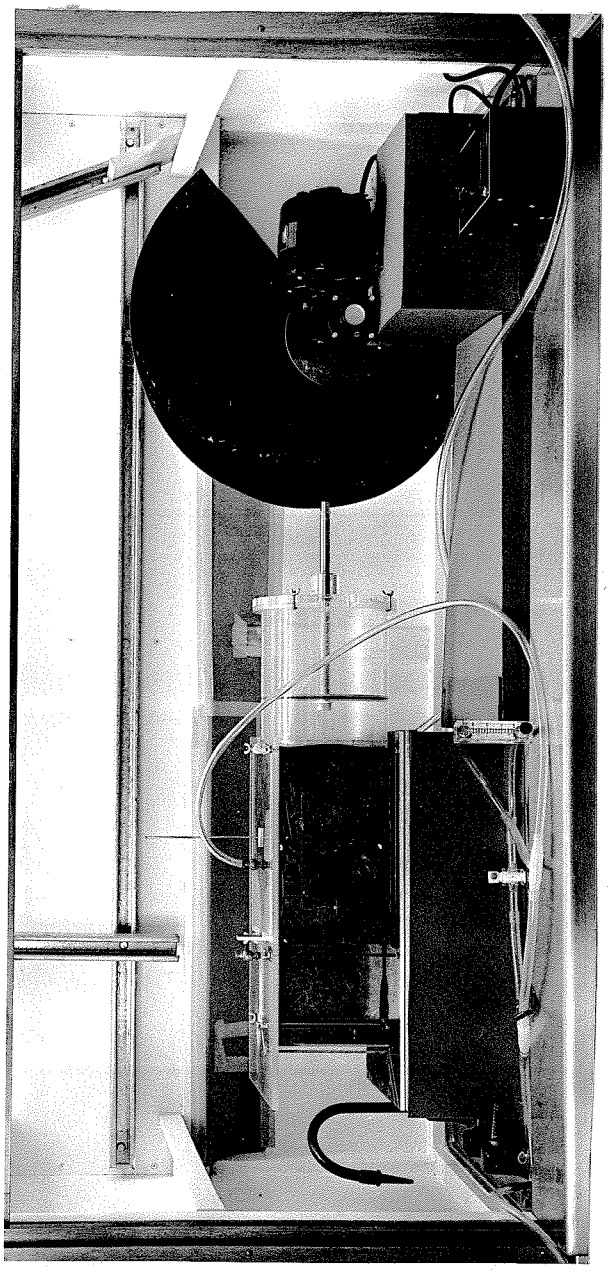

Figure 4.2 Two-Dimensional Apparatus: From Left to Right are the "2-D" Model, Aerosol Holding Chamber, Piston, Inhalation Cam and Motor with Speed Control

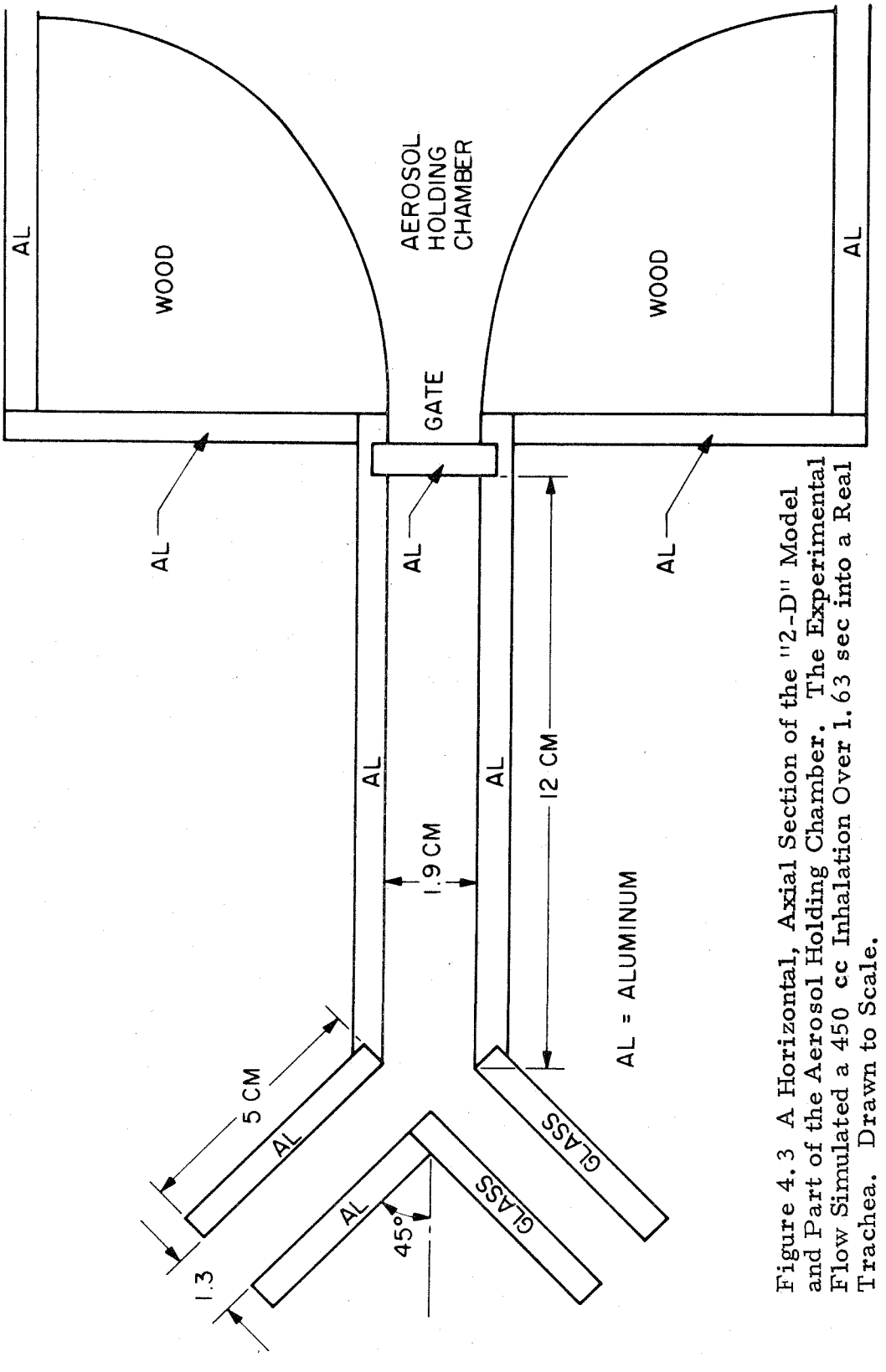

Figure 4.3 A Horizontal, Axial Section of the "2-D" Model and Part of the Aerosol Holding Chamber. The Experimental Flow Simulated a 450 cc Inhalation Over 1.63 sec into a Real Trachea. Drawn to Scale.

the outflow at the side and by slowly turning a vertically oriented baffle (18 cm. x 8.25 cm. x .32 cm.) in the center of the chamber.

The 5.6 liters of air, flushed through the bifurcation model by the motor-cam-piston assembly, corresponded to a 450 c.c. inhalation into a human trachea with a diameter of 1.9 cm. Figure 4.4 shows the flow rate vs. time curve for a 450 c.c. inhalation of one second during sedentary conditions (Silverman and Billings, 1961). The flow rate vs. time curve produced by the cam in Figure 4.2 had the same shape as Figure 4.4.

The cam was driven by a Bodine Speed Reducer Motor[1] with a Minarik Speed Control[2]. For all experimental runs in the "2-D" model the inhalation time was 1.63 seconds.

The velocities and the Reynolds numbers[3] in the model during 5.6 liter, 1.63 second inhalations, assuming flat velocity profiles, were as follows:

1. Parent Branch:

   Time-average velocity = 100 cm./sec., $Re_c = 2250$

   Peak velocity = 163 cm./sec., $Re_c = 3670$

---

[1] Model NSH-54R1, Bodine Electric Company

[2] Model SH-52, Minarik Electric Company

[3] For the rectrangular channels, $Re_c = 4R_H U/\nu$, where R_H is the hydraulic radius.

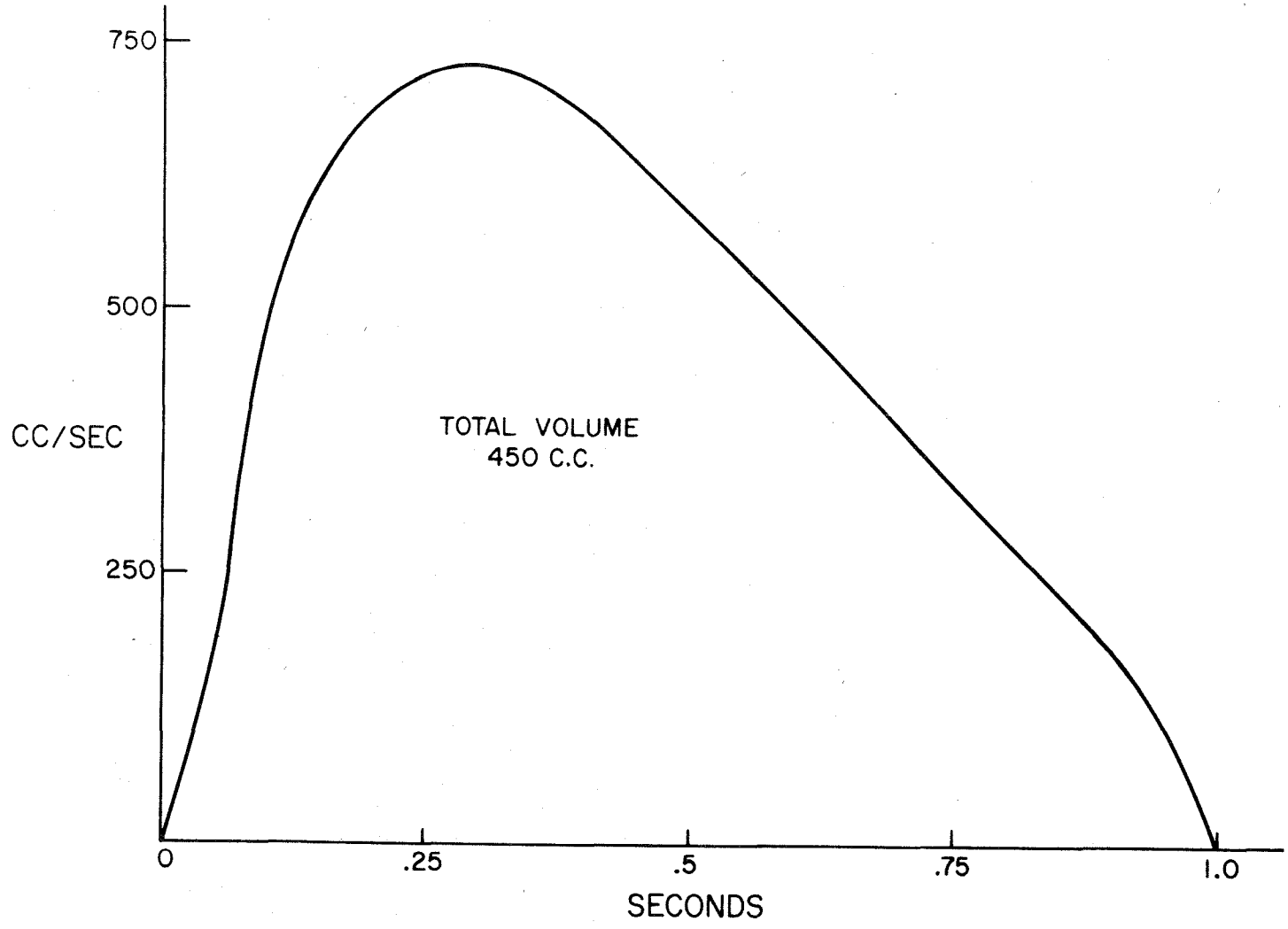

Figure 4.4 Flowrate vs. Time Curve for a Normal 450 CC Inhalation Which Was Used to Design the Cams for the "2-D" and "3-D" Models.

2. Daughter Branch:

Time-average velocity = 73 cm./sec., Re_c = 1160

Peak velocity = 119 cm./sec., Re_c = 1890

The well-faired entrance to the parent branch maintained non-turbulent flow in the model for the experimental flow conditions. No attempt was made to simulate the glottis of the larynx at the entrance of the parent branch.

Experimental checks were made on the velocity profiles in the model using total and static pressure tubes and a high speed blower. At steady, inspiratory velocities between 400 and 600 cm./sec. in the parent branch, the velocity profiles at the bifurcation end of the branch were flat over approximately 70% of the branch width.

The velocity, U, which was measured at x = -2.6 cm. along the stagnation streamline in the center of the model, had values of 476, 574 and 610 cm./sec. for three, steady inspiratory flows. At these three values of U the velocity, u_f, was measured at x = -1 cm. along the stagnation streamline at the center of the model. The average value of A calculated from Equation 2.7 for these three measurements was 0.92 cm.$^{-1/3}$. This compares to A = 0.82 cm.$^{-1/3}$ calculated theoretically from Equation 2.5 . If these results are applied to the pulsatile experimental runs, the local fluid velocity around the wedge was 12% higher than theoretically predicted.

At peak velocities of 163 cm./sec. and 119 cm./sec. in the parent and daughter branches, $Re_x << Re_{x\,crit} = 3.2 \times 10^5$ (Schlichting, 1968: 39). Flow visualization with smoke also indicated that during steady inhalations laminar flow was maintained along the wedge walls between 7.5 and 10.5 cm. from the base of the model.

4.3 Three-Dimensional Apparatus and Experimental Flow Conditions

The "3-D" apparatus (Figure 4.5) has the same functional sections as the "2-D" system. However, the apparatus was oriented vertically to simulate the inhalation process for people who are standing or sitting. Consequently, sedimentation occurred simultaneously with inertial impaction, interception and convective diffusion.

Figure 3.1 shows the airway dimensions of the "3-D" model and the shape of the junction in the plane of the bifurcation that also bisects the carina. The radius of curvature of the junction between the parent branch and the outside wall of the daughter branch is equivalent to the radius of the parent branch. The parent branch was machined from a brass tube, while the bifurcation and the daughter branches were machined from an aluminum block. Use of metal allowed more precise construction of the bifurcation than would have been possible with glass and avoided the static charge problems inherent in plastic models.

For easy access to the daughter branch walls, the aluminum

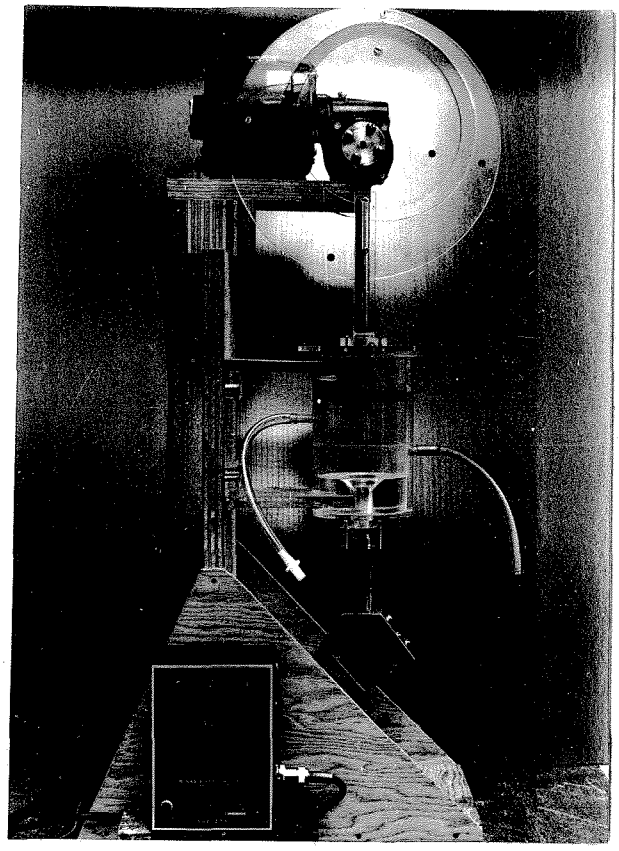

Figure 4.5 Three-Dimensional Apparatus: From Top to Bottom are the Motor-Cam-Piston Assembly, Aerosol Holding Chamber, Gate, "3-D" Model, and Speed Control

block was cut into two sections (Figure 4.6). One daughter branch was cut along the dotted line normal to the bifurcation plane in Figure 4.7, and the section of the block which joins the parent branch was also bisected normal to the bifurcation plane. Particles in the optical size range were collected on transparent, plastic tapes which coated the inside and outside wall of the daughter branch.

The brass tube fits snugly into the aluminum block and makes a smooth junction as shown in Figure 4.8. The two aluminum sections are held together by screws, and the joint is sealed by a rubber washer around the end of the brass tube. Figures 4.6 and 4.8 also show that the transition from the parent branch to the daughter branches in the plane normal to the bifurcation occurs smoothly over a distance of about 1.2 cm. from the end of the brass tube to the junction. The exact shape of this transition at bifurcations in vivo is not known. In this model the shape was based on the observation of excised lungs and lung casts. If the entrance to the daughter branch is enlarged compared to the downstream diameter, the transition occurs more gradually and closer to the carina than in this model.

The carina in Figure 4.9 has the shape of a sharp ridge formed by the interception of the two daughter branches machined from the aluminum block. The ridge is shaped like a sharp wedge in all axial sections in the plane of the bifurcation from the dorsal to the ventral walls of the junction. As discussed in Section 1.2.2 and Figure 1.2,

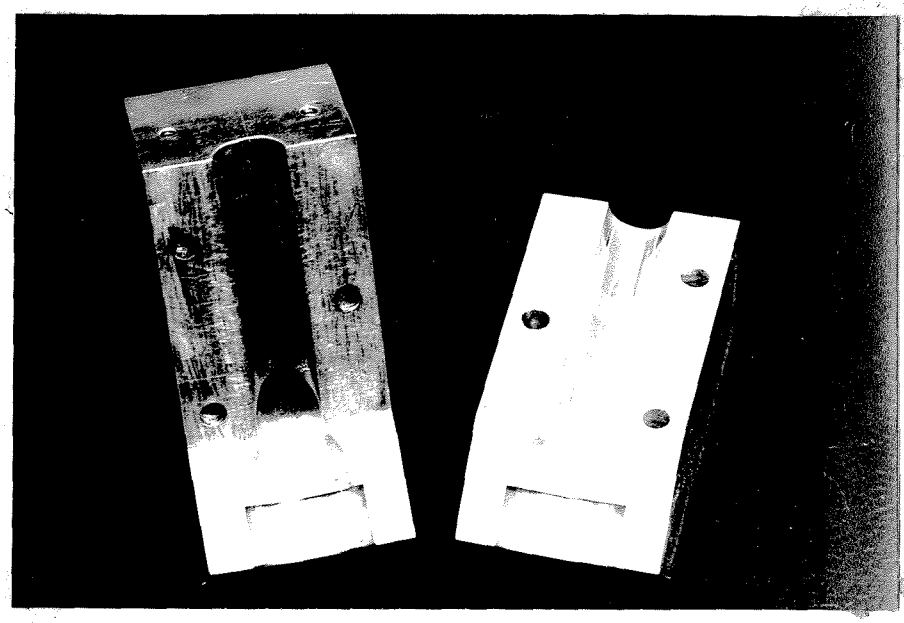

Figure 4.6 Two Aluminum Sections which Join to Form the Daughter Branch in which the Deposition was Measured. The Inside Wall of the Daughter Branch is Shown on the Left Section and the Outside Wall on the Right Section.

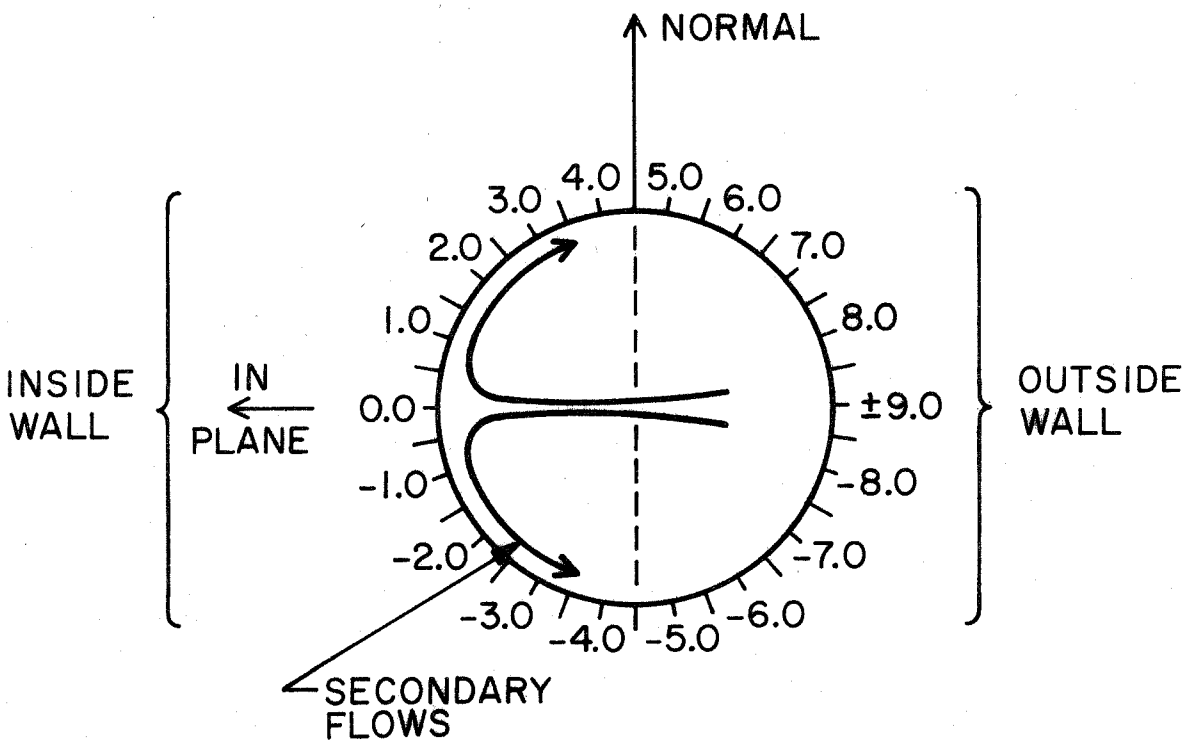

Figure 4.7 Cross-Sectional View of a Daughter Branch of the "3-D" Model Demonstrating the Position of the Secondary Flows. The Numbered Segments Around the Circumference Indicate the Y Locations of the 18 Equally Spaced Strips Over Which the Counts Were Made. Each Y Segment Corresponds to a Distance of π (Diameter)/18 or 0.215 cm.

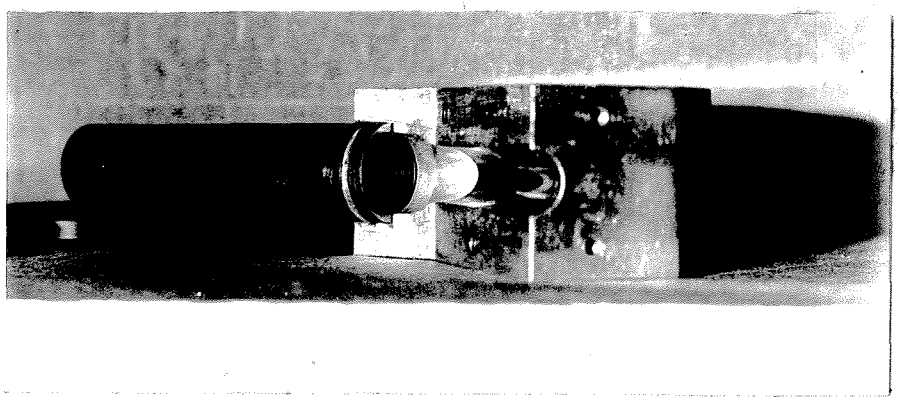

Figure 4.8 View of the Smooth Junction which the Brass Parent Branch Makes with the Machined Aluminum Block

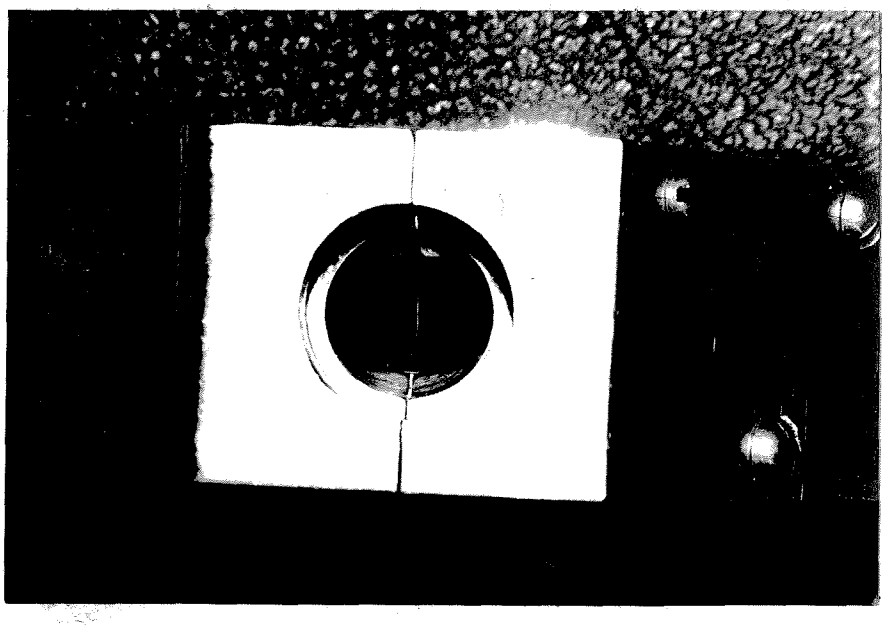

Figure 4.9 View of the Bifurcation in the Aluminum Block from the Position of the Parent Branch. Note the Sharp Ridge-Like Shape of the Carina

the shape corresponds fairly well to some of the bifurcations in the lung and only differs slightly from the tracheobronchial carina which is more rounded toward the dorsal and ventral walls.

Parts of the apparatus connected to the bifurcation model (Figure 4.5) are designed to pass a breath of aerosol through the model. A manually-operated gate separates the brass tube from the lucite holding chamber, and the chamber has a volume of 720 c.c. with the piston (4" diameter) in its preinspiratory position. To mix the aerosol, the inlet and outlet ports were positioned on opposite sides of the chamber with one above the other.

The lucite cam was designed to flush 450 c.c. of air through the model during the inspiratory and expiratory phases, as in Figure 4.4 (Silverman and Billings (1961: Figure 3) show that the flow rate vs. time patterns for inhalation and exhalation are nearly identical). Inhalation of particle-laden air took place during the first 180° of the cam rotation, and exhalation of room air into the holding chamber occurred during the next 153° of rotation (Silverman and Billings (1961: Figure 2) show that the expiration time is 85% of the inspiration time). When the cam was in the region of the 27° pause, the motor was stopped, the gate closed, and the clamps on the inlet and outlet lines were removed to allow the particle concentration in the chamber to increase before initiating a new breathing cycle.

The same motor and speed control were used as in the "2-D" apparatus; however, the experimental inhalation times were 1.88 and 0.94 seconds. The 450 c.c., 1.88 sec. inhalations corresponded to sedentary breathing for normal adults and inhalations of 450 c.c., 0.94 sec. corresponded to breathing during moderate exertion. The velocities and Reynolds numbers in the model during these two cases, when the velocity profiles were assumed to be flat, were calculated as follows:

1. Parent Branch, 1.88 second inhalations:

   Time-average velocity = 100 cm./sec., Re = 1145

   Peak velocity = 163 cm./sec., Re = 1865

2. Daughter Branch, 1.88 second inhalations:

   Time-average velocity = 100.8 cm./sec., Re = 810

   Peak velocity = 164.2 cm./sec., Re = 1320

3. Parent Branch, 0.94 second inhalations:

   Time-average velocity = 200 cm./sec., Re = 2290

   Peak velocity = 326 cm./sec., Re = 3730

4. Daughter Branch, 0.94 second inhalations:

   Time-average velocity = 201.6 cm./sec., Re = 1620

   Peak velocity = 328.4 cm./sec., Re = 2640

A velocity of 100 cm./sec. in the parent branch was equivalent to a flow rate of 14.4 liters/min. The well-faired entrance to the brass

tube (Figure 4.5) maintained nonturbulent flow in the model.

The velocity profile near the end of the brass tube was measured by static and total pressure tubes with the aluminum section removed. At a steady and average inspiratory velocity of 500 cm./sec., the velocity profile at 1.9 cm. from the end of the brass tube was flat over about 60% of the tube diameter. The velocity was also measured at $x = -1$ cm. along the stagnation streamline which is axially centered in the parent branch. When $U = 581$ cm./sec. at $x = -4.2$ cm., $u_f = 665$ cm./sec. at $x = -1$ cm. Therefore, $A = 1.14$ cm.$^{-7/29}$ from Equation 2.7 for the 70° wedge. Equation 2.5 gives $A = 0.813$ cm.$^{-7/29}$.

This discrepancy between experiment and theory arose because the "2-D" theory does not account for the narrowing of the cross section in the "3-D" model between $x = -1$ cm. and $x = -1.3$ cm. Here the cross section is elliptical (Figure 4.9) with semiaxes of 0.875 cm. and 0.615 cm. and an area of 1.7 cm^2. Consequently, 1.4U is the average velocity in this cross section and $A = 1.14$ cm.$^{-7/29}$ in Equation 2.7. Equations 3.1 and 3.2 in Section 3.2.1 give $A_3 = 0.813$ cm.$^{-7/29}$ and $u_f = 665$ cm./sec. for $U = 581$ cm./sec. Therefore, Equations 3.1 through 3.3 account for the 40% increase in fluid velocity.

Turbulent flow was not expected along the inside wall of the daughter branch, because $Re_x \ll Re_{xcrit}$ for all the experimental flow conditions. Flow visualization was done in the daughter branch, which was used for particle collection, by blowing smoke from the total pressure

tube (1/16" O.D.). It was inserted into the other daughter branch with its tip near the stagnation streamline. For steady inspiratory flow at $U = 100$, 163 and 200 cm./sec. and for a pulsatile inhalation with $\overline{U} = 100$ cm./sec., the flow was laminar along the inside wall between $Y = \pm 2$ (Figure 4.7).

When the smoke was injected at the entrance of the daughter branch near the wall between $Y = +2$ and $Y = +9$ or between $Y = -2$ and $Y = -9$, secondary flows were also observed, as shown in Figure 3.2. The secondary motions were initiated very close to $X = 0$ in the region around $Y = \pm 2$. For $U = 100$ cm./sec. the secondary flow completed between one-half to one revolution over the length of the daughter branch. At $U = 163$ cm./sec. about one revolution was completed, and for $U = 200$ cm./sec. between one and two revolutions were completed. During the pulsatile inhalation with $\overline{U} = 100$ cm./sec., the secondary motion completed about one revolution over the length of the branch.

The results of the flow visualization study generally agreed with those of Sudlow and Schroter (1969) in a geometrically similar model. This added support to the assumption that their velocity profiles are applicable to the flow conditions in the "3-D" model.

4.4 Aerosol Generation Equipment and Procedure

Monodisperse, spherical, latex hydrosols[1] ranging in diameter from

[1] Diagnostic Products, Dow Chemical Company, Midland, Michigan.

0.088 μm to 7.6 μm were nebulized, dried and deionized to produce neutralized, monodisperse aerosols. They were composed of Polystyrene latex (PSL), Polyvinyl toluene latex (PVTL) or Styrene divinyl benzene latex (SDVBL). Table B.1 (Appendix B) lists the average diameters, standard deviations, concentrations, polymer type and densities of the hydrosols used in the experiments.

The aerosol was generated with a Bird 500 c.c. Micronebulizer[1] from a stock solution of hydrosol, freshly diluted before each run with double distilled water in the ratios listed in Table B.1. The nebulizer was operated at a jet pressure between 8 and 13 psig. with an aerosol output of 7.3 liters/min. @ 25° C and 74 cm. Hg. for all particles except 0.088μm. These operating conditions were the optimum for delivering a concentrated, dry aerosol with a minimum number of aggregates to the model holding chamber in the flow system shown in Figure 4.1. For the 0.088μm runs the jet pressure was 13 psig. with an aerosol output of 3.6 liters/min. @ 25° C. and 74 cm. Hg. Because of the formation of aggregates this aerosol was highly polydisperse; this was required to obtain sufficient mass for concentration measurements during the runs.

The nebulized particles were initially highly charged because of the formation of charged droplets. The deposition of these particles in the lung models could have been significantly influenced by electrostatic

---

[1] Bird Space Technology, Inc., Palm Springs, California, U.S. Patent 3,353,536.

forces of interaction between the particles and between the particles and the collection surfaces. Therefore, the initial charge distribution on the aerosol was lowered to its equilibrium Boltzmann distribution by mixing with the bipolar ions generated in the air (Whitby and Liu, 1968) inside a deionizer[1] (Figure 4.1). It consisted of a steel, cylindrical holding chamber (17.5"x3") surrounding a sealed source of Kr-85 gas. Besides neutralization, drying also occurred during the 15 second residence time in the deionizer. Appendix B describes measurements which verified the efficiency of the deionizer.

4.5 Aerosol Concentration Measurements

During the pause between breaths, the aerosol concentration in the holding chambers increased at rates approximating the behavior of ideal constant flow stirred tanks. The theoretical average residence time was 111 seconds for the "2-D" model and 6 seconds for the "3-D" model. As shown in Figure 4.1 the outflow of the chamber was drawn through a Sinclair-Phoenix Aerosol Smoke and Dust Photometer[2] and was captured on filter #1. In the photometer the particle concentration was measured by forward light scattering, which is proportional to the

---

[1] 3M Company, Model 3B4G, 3 millicuries, 12" active length.

[2] Model JM3000-AL. The sample air from the holding chamber is diluted in the photometer by clean air which was drawn from the room through filter #2. The ratio of the clean air to the sample air was 0.65 l./min./3.6 l./min. for 0.088μm runs and 1.4 l./min./7.3 l./min. for the other runs.

number of particles and their cross-sectional area. After two or two and one-half residence times the concentration was fairly stable; the chamber was then isolated and the breath initiated.

The photometer was utilized for all particle sizes except 0.088μm, 5.7μm and 7.6μm diameter. The intensity of the scattering from the 0.088μm particles was too low to detect when the distribution was monodisperse. Although the polydisperse distributions of 0.088μm particles from the experimental runs scattered much light, the concentration of singlets could not be determined from the photometer. The photometer could detect the 5.7μm and 7.6μm particles, but their concentrations were too low to measure accurately.

The photometer was calibrated separately as follows: The mass of particles captured on the filter[1] over 3 to 6 hours was converted to a monodisperse particle concentration, and the photometer readings recorded during the passage of the aerosol were time-averaged. This was repeated for various hydrosol concentrations. Because the calibration curves of photometer reading versus concentration were linear over the range of interest in the experiments, the concentration of aggregates was a small fraction of the singlet concentration during the experimental runs. The number of aggregates observed at the collection sites in the models was also a small fraction of the total number of singlets counted.

---

[1] Millipore 0.45μm HAWG 047 00

For the 0.088μm, 5.7μm and 7.6μm runs, the mass concentration of particles in the chamber at the time of inhalation was determined as follows: First, the mass of particles collected on filter[1] #1 was converted to an average mass concentration for the air exiting the chamber during the pause between breaths. Second, concentration vs. time curves obtained for each model chamber at the sample flow rates during the pause periods could all be fit by the relation $n = n_o(1-\exp(-t/t_1))$, where n_o is the concentration of aerosol entering the chamber and t_1 is the characteristic time of the chamber. Since the time-average concentration, predicted from this expression during the pause of length t, was equivalent to the average mass concentration measured above, the concentration at the beginning of the inspiration was easily calculated.

Third, in the 5.7 and 7.6μm runs, the number concentration was determined by assuming the same size distribution in the model and at the filter, as in the hydrosol. However, for the 0.088μm runs the distribution of singlets, doublets, triplets, etc. was determined during each run from particles deposited on the electron microscope grids in the "3-D" model. The distributions on the grids were corrected to the distribution in the air in the model by weighting the number of each type of aggregate by its local transfer coefficient. The transfer coefficient for

---

[1] 5.7μm and 7.6μm collected on Millipore 0.45μm HAWG 047 00, 0.088μm collected on Millipore 100 mμ VCWP 047 00.

each size of aggregate was estimated for an aerodynamically equivalent sphere and by using the theoretical equations discussed in Chapter 3.

Tube losses between the holding chamber and the photometer or between the holding chamber and the filter were negligible for all particles, except 5.7μm and 7.6μm diameter. The fraction lost by sedimentation in the horizontal section of tubing was calculated (Fuchs, 1964: Eqn.26:14). The fraction lost in the 90° bends by inertial impaction was estimated by first approximating the circular cross section by rectangles (Figure 3.3). The predictions by Hacker, Brun and Boyd (1953: Fig. 9) for the deposition efficiency of droplets in 90° elbows in potential flow were then applied to each rectangular section. Total calculated losses were 13.6% for 5.7μm and 20% for 7.6μm particles.

Errors in the measurement of concentration caused by free stabilizing agent and inorganic impurities in the hydrosol solution were insignificant (Appendix B).

4.6 Measurements with the Two-Dimensional Model

Particles were collected on the glass plates which formed the inside and outside walls of the "2-D" model. Calculations suggested and experiments verified that adhesives were needed to prevent losses for only the 7.6μm particles (Appendix B). Consequently, the surface of the plates was used to collect the 2.68μm, 2.02μm and 0.365μm particles. The plates were cleaned before each run in an ultrasonic bath

of distilled water and detergent, followed by rinsing with double distilled water and with toluene or chloroform. Before the plates were placed in the model, they were decharged by exposure to a Staticmaster[1] for at least one hour.

In the 0.79μm runs and runs #24 and #25 for 1.1μm, the collecting surface of the clean glass plates was coated by an opaque layer of carbon black before decharging. The carbon black was applied evenly from a burning candle.

For the 7.6μm runs and run #36 of the 1.1μm particles, three strips of 1/2" wide, "Scotch" Brand Double Stick Tape were placed evenly on the clean glass plates. Next they were decharged with the Staticmaster for at least one hour.

The collecting plates were exposed to between 30 and 60 breaths to allow sufficient deposition for statistically meaningful counts. All singlet particles were manually counted by placing the plates on the stage of an optical microscope[2] at 645X magnification. The clean glass and cellophane tape runs were counted by substage illumination, and the carbon coated runs were counted by side illumination.

The particles were counted in strips (2.54 cm. x 0.01375 cm.)

---

[1] Staticmaster Ionizing Unit, Model N. 2U500, Po-210 Nuclear Products Company, El Monte, California.

[2] American Optical Spencer Microstar binocular microscope, 43X objective, 15X eyepieces.

along the center line of the plates at distances of 0.0069, 0.0275, 0.11, 0.22, 0.3175, 0.635, 1.27 and 2.54 cm. from the leading edge (Figure 4.10). The raw count data are shown in Appendix C with the number of breaths, the average particle concentration, and the counting area. The particles on the outside slides were counted only for the first few runs to determine the magnitude and trend in comparison to the inside slide.

It was desirable to count at least 100 particles in each area to minimize the statistical error; however, constraints of time and particle concentration prohibited this for most runs. This is clearly demonstrated in Appendix C where the number of counts at 2.54 cm. from the leading edge are 10-50 times lower than at the tip.

Most of the aggregates were observed in the locations near the leading edge. However, the ratio of the number of aggregates to the number of singlets at any location was negligible for the 7.6, 2.68 and 2.02 μm particles. The maximum ratio was between 10 and 20% near the leading edge for the 1.099, 0.79 and 0.365 μm particles, but some of these aggregates may have been formed by singlets colliding with previously deposited singlets, doublets, etc.

4.7 Measurements with the Three-Dimensional Model

4.7.1 Optical Microscopy

All particles, except for those of 0.088 μm and 0.365 μm diameter,

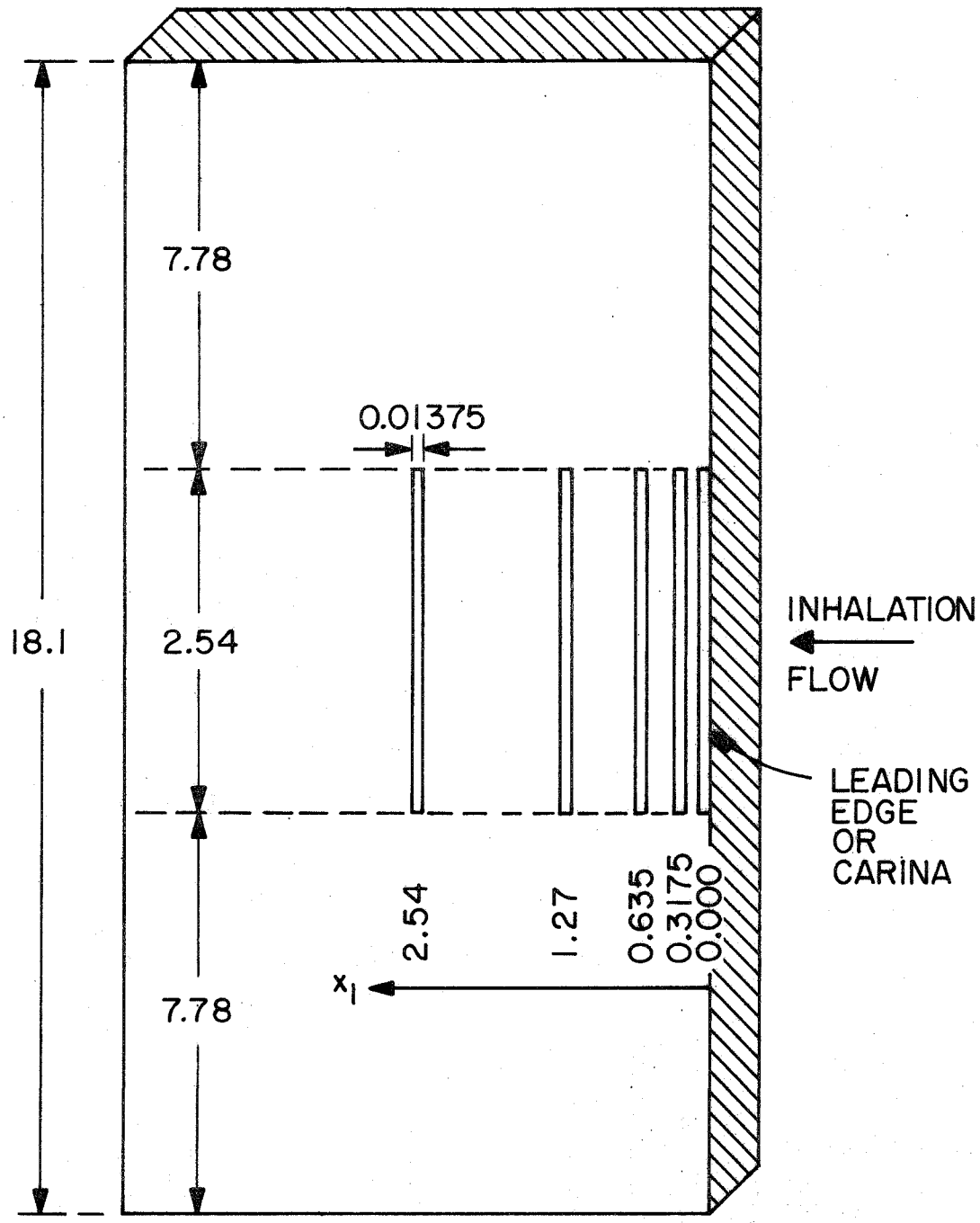

Figure 4.10 Sketch of Wall of Daughter Branch of "2-D" Model Showing the Relative Locations of the 2.54 cm x 0.01375 cm Strips in which Particles were Counted. All Dimensions in cm.

were counted by optical microscopy. Because it was not feasible to count the particles deposited directly on the aluminum walls of the daughter branch, the walls of each section in Figure 4.6 were covered with a single, precut strip of "Scotch" Brand Tape[1] with the smooth, nonadhesive side exposed to the aerosol. The excess width of tape was folded along the flat edges having screw holes. Final cutting of the tape to conform to the concave shape of the carina was done with a scalpel, following the contour of the carina. The tape caused a 0.5% reduction in the branch cross-sectional area. Next, and before decharging, some of the tapes were coated with adhesive.

All tapes were decharged by exposure for at least an hour to the Staticmaster. No static charge could accumulate during the run because the deposited particles were maintained at their Boltzmann charge distribution by the bipolar ions. After the inhalations were completed, the two tapes were carefully removed from the models without touching the collecting surfaces. The sticky side of each tape was placed flat on top of two strips of 1/2" wide "Scotch" Brand Double Stick Tape which had been previously adhered to a clean, glass microscope slide. The exposed surface of each tape had the shape and dimensions shown in Figure 4.11.

Calculations suggested and experiments verified that adhesives

---

[1] No. 600, 1" wide, 60 μm thick, transparent, plastic; manufactured by Minnesota Mining & Manufacturing Company.

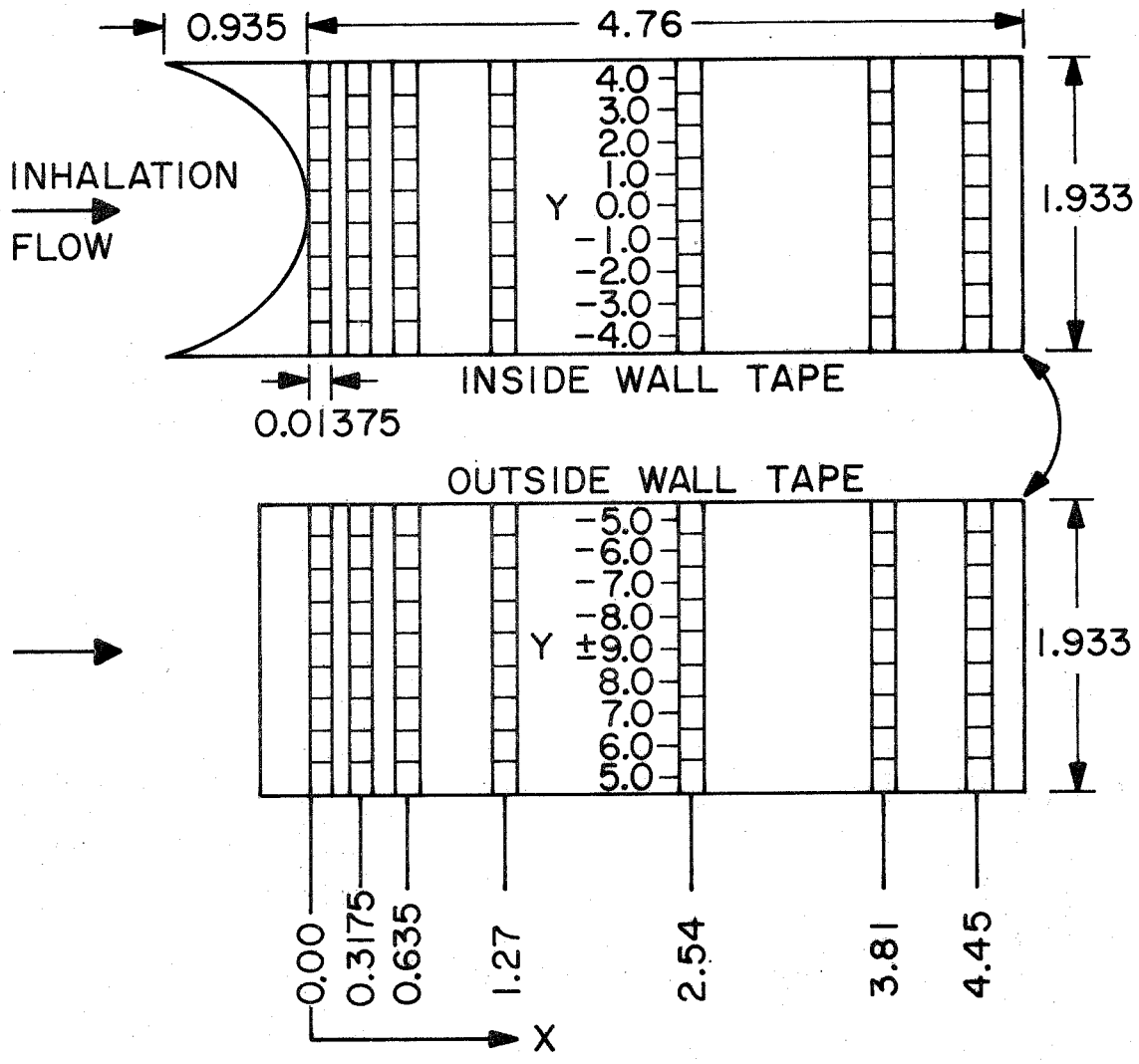

Figure 4.11 Sketch of the Exposed Surface of Tapes which Covered the Inside and Outside Walls of Daughter Branch in "3-D" Model and the Relative Locations of the Areas in which the Particles were Optically Counted. All Dimensions in Centimeters Except for Y Labels.

were needed to prevent losses for 5.7μm particles at the low flow rate and for 5.7μm and 2.02μm at the high flow rate (Appendix B). Consequently, in the 0.79, 0.81 and 1.1μm runs and in runs #4 and #12 of 2.02μm, particles were collected directly on the clean, nonadhesive surface of the tape. For the remaining 2.02μm runs and the 5.7μm runs, two different adhesives were applied to the top of the tape. 2.02μm run #14 used a thin coating of clear silicone liquid[1], while runs #17, #19 and #24 for 2.02μm and all of the 5.7μm runs used a thin, smooth coating of vaseline[2]. Since the patterns and magnitude of deposition in runs #14, #17 and #19 agreed with run #12, the adhesive made no significant different for the 2.02μm particles at 100 cm./sec.

During a run the model was exposed to between 300 and 600 breaths to allow sufficient deposition for statistically meaningful counts. Tapes on the glass microscope slides were manually counted with the microscope used for the "2-D" model and by substage illumination.

Singlets in all runs were counted in discrete areas shown in

---

[1] Dow Corning 200 Fluid: A dimethylpolysiloxane with viscosity of 30,000 c.s. @ 25°C. It was mixed 1:50 with benzene and applied with an eyedropper to the tape surface. The section was canted a few degrees from horizontal to allow slow flow from the end of the branch to form a thin (~1μm) coating.

[2] Jar of vaseline, paint brush and aluminum sections with tape coating were placed in an oven at 55°C until the vaseline melted. Materials were removed from the oven and vaseline was applied to the tape by brushing in an axial direction until the vaseline began to harden. Under the microscope the coating appeared smooth and thin (~1μm). In run #17 the model was not preheated before the hot vaseline was applied.

Figure 4.11, which included 18 contiguous areas around the circumference of the daughter branch (Figure 4.7) at each of 9 or 10 locations downstream. For all runs, except 5.7μm, the magnification was 645X, the counting area was 0.002949 $cm.^2$ (0.01375 x 0.2147), and the axial locations were at 0.0069, 0.0275, 0.11, 0.22, 0.3175, 0.635, 1.27, 2.54, 3.81 and 4.45 cm. downstream from the base of the concave section of the carina. For the 5.7μm runs the magnification was 150X, the counting area was 0.01204 $cm.^2$ (0.056 x 0.2147), and the axial locations were at 0.028, 0.112, 0.224, 0.392, 0.672, 1.27, 2.54, 3.81 and 4.45 cm.

The raw count data matrices are shown in Appendix C. The row numbers of each matrix, 1, 2, 3, ..., 19, correspond respectively to Y = +9, +8, +7, ..., 0, -1, -2, ..., -9 in Figures 4.7 and 4.11. Fractional counts resulted when counting was done in an area twice as large as usual.

Like the "2-D" runs, most of the aggregates were doublets and triplets and were observed near the carina. The ratio of the aggregate count to singlet count at any location was negligible for the 5.7μm and 2.02μm particles. The maximum ratio was between 10 and 20% near the leading edge for the 1.1μm and 0.79μm runs.

4.7.2 Electron Microscopy

The 0.088μm and 0.365μm particles were counted by electron microscopy. Although the 0.365μm particles were counted on the glass plates in the "2-D" model by optical microscopy, they could not be distinguished clearly on the tapes of the "3-D" model with the optical microscope.

The branch walls of the "3-D" model were covered by four strips of tape[1], having adhesive on both sides in such a manner that no excess tape was folded along the flat walls of the aluminum sections. The tape caused a 2.2% decrease in the cross-sectional area of the branch. Circular holes of 0.198 cm. diameter were precut in the tapes, and 42 electron microscope grids[2] of 3.1 mm outside diameter were carefully centered over the holes in the tape in the model so that their edges were held by the adhesive. The thin, copper grids were easily bent to conform to the contour of the walls. The holes under the mesh portion of the grids prevented the tape adhesive from tearing the thin, Formvar films covering the exposed surface of the grids. Grids were centered at Y = ±9.0, +6.0, +3.0, 0.0, -3.0, -6.0 at X = 0.155, 0.465, 0.775, 1.08, 2.0, 3.0

[1] "Scotch" Brand Double Stick Tape, 1/2" wide and 80μm thick manufac- by Minnesota Mining and Manufacturing Company.

[2] Cohen-Pelco Handle Grids, 500 mesh, copper, 15μm thick, 3.1 mm O.D. Catalog #3HGC500, Ted Pella Company, Tustin, California. Grids were coated with Formvar prepared from a solution of 0.5 - 1% w/v Polyvinyl Formal 15/95 Powder in Ethylene Dichloride. Carbon was evaporated onto the Formvar coating to improve its heat conductivity.

and 4.0 cm. from the carina as shown in Figure 4.12. The collecting surface of the grids protruded approximately 15 μm above the surface of the tape. They should not have disturbed the streamline flow or interfered with the downstream deposition on other grids, because they lay well within the boundary layer and because deposition of 0.365 and 0.088μm particles is controlled by diffusion. After the grids were in position, the collecting surface of the model sections were decharged by the Staticmaster for at least one hour.

During a run, the model was exposed to between 500 and 2000 breaths to allow a statistically significant number of particles to be deposited. The particles were manually counted with the aid of a transmission electron microscope[1] at 6000X and 18000X magnification, respectively, for the 0.365μm and 0.088μm runs.

The particles were counted in 10 contiguous columns, with approximately 30 mesh windows per column, located in the center of each grid. The fluctuation in counts in this region of the grids appeared to be random. The number of windows counted per grid, the average area of the windows on each grid, and the average number of singlets counted per window on each grid are tabulated in matrix form in Appendix C. The labels on the rows of the matrices, 1, 2, 3, 4, 5, 6, 7 correspond to the Y locations +9, +6, +3, 0, -3, -6, -9. Although the areas of the windows

[1] Carl Zeiss Electron Microscope, EM 9A.

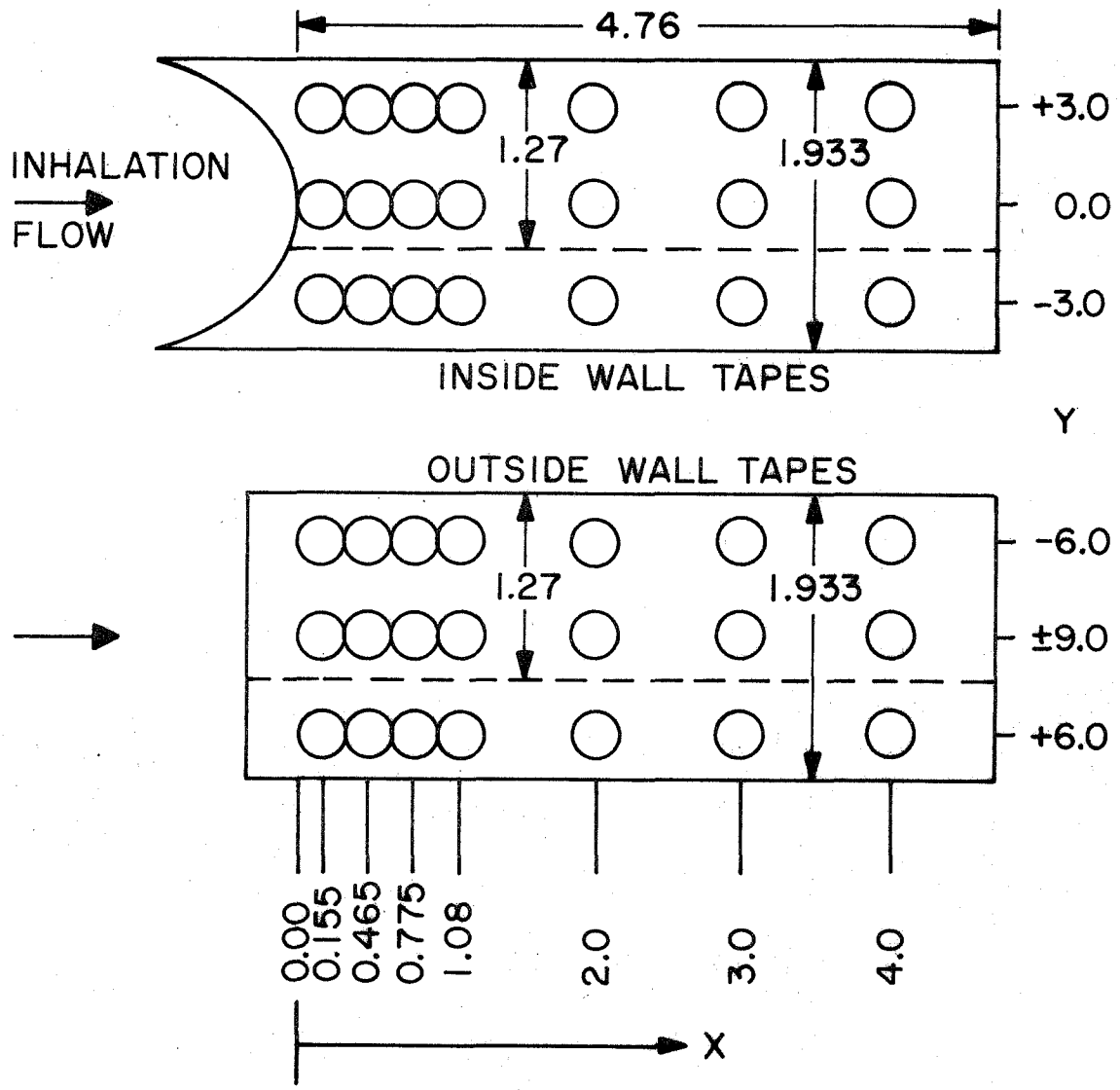

Figure 4.12 Sketch of the Exposed Surface of Tapes which Covered the Inside and Outside Walls of the Daughter Branch in the "3-D" Model During the 0.088 μm and 0.365 μm Runs. The Dashed Line Marks the Border Between the Two Strips of Tape on Each Wall. The Circles Mark the Locations of the 42 Electron Microscope Grids. All Dimensions in Centimeters Except for Y Labels.

were uniform within one grid, the average area per window varied between grids[1]. The average area was determined for each grid by random sampling of windows and measuring their areas with a micrometer eyepiece[2] on the optical microscope used in Section 4.7.1.

All of the grids were counted in 0.365μm run #28. Since the deposition pattern was essentially symmetrical about Y = 0, only the grids at Y = ±9, +6, +3 and 0 were counted in 0.365μm run #32 and in the two 0.088μm runs. This allowed a significant shortening of the overall counting time.

The number distribution of aggregates were much more polydisperse for the 0.088μm runs than for the 0.365μm runs. The number percent and mass percent of singlets in the air in the model were, respectively, 44% and 10% in run #31 and 25% and 0.8% in run #33. From the mass percentages and the mass collected on filter #1, the singlet concentration in the inhaled air was estimated as described in Section 4.5.

4.8 Calculation of the Local Transfer Coefficient from Data

The local transfer coefficient at any point in the models was calculated as follows:

---

[1] The grids were all 500 mesh; however, the width of the copper mesh separating the windows varied between grids.

[2] Filar Micrometer Eyepiece, American Optical Catalog #426C. A 10X eyepiece with the 43X objective of the microscope was used to measure the window dimensions.

$$k_{loc} = \frac{(\#\ counts)}{(area)(\#\ breaths)(time)(correction\ factor)(concentration)} . \quad (4.1)$$

The "concentration" is an arithmetic average of the particle concentrations which were measured for each inhalation.

The "correction factor" corrects the inhalation "time" to the approximate time period during which the given location was exposed to the particle-laden air. The exposure time is shorter than the inhalation "time" because the volume of clean air, which is initially present between the gate and the count location in the daughter branch, must be displaced by dirty air before deposition can occur. The "correction factor" assumes the flow profile in the parent branch and the daughter branches is flat with a magnitude equivalent to the time-average experimental flow rate. Table B2 lists the correction factors which were used for each count location in the "2-D" model. In the "3-D" model a constant correction factor of 0.937 was used for all the locations; it corrects for the time of passage of the volume of clean air in the parent branch and the bifurcation region before the carina.

The local transfer coefficients for all experimental runs in both models are listed in Appendix C. The phrase "raw mass transfer coefficient" is used in place of local transfer coefficient in the heading to the matrices of data from the "3-D" model.

In the "3-D" contour maps described in Chapter 6, weighted average local transfer coefficients were used to generate the contours

which represent the data from more than one run. Each was calculated from the following formula:

$$\text{Weighted Average } k_{loc} = \frac{\sum_{i=1}^{N} k_{loc_i} (\#\ \text{breaths}_i)(\text{concentration}_i)}{\sum_{i=1}^{N} (\#\ \text{breaths}_i)(\text{concentration}_i)}, \quad (4.2)$$

N equals the number of runs to be averaged. This formula was derived by assuming that the statistical error in the "# counts" was the predominant source of the variance in each k_{loc_i} and by assuming that all k_{loc_i} had similar magnitudes. Both assumptions were valid for the data used to calculate the contours.

Chapter 5

EXPERIMENTAL RESULTS AND ANALYSIS: TWO-DIMENSIONAL MODEL

5.1 General Data Analysis

Runs were made with 0.365, 0.79, 1.099, 2.02, 2.68 and 7.6μm diameter particles in the "2-D" model with 5.6 liter inhalations in 1.63 seconds. The flow pattern simulated a 450 c.c., 1.63 sec. inhalation of particle-laden air into a human trachea with a diameter of 1.9 cm. Measured local transfer coefficients for the "2-D" model are tabulated in Appendix C, and the transfer coefficients along the inside wall are compared with theory in Figures 5.1 through 5.7.

In Figure 5.1 the "V" shape of the curve representing the data at any one of the three deposition locations is characteristic of plots of efficiency versus particle size reported by Thomas and Yoder (1956) for aerosol filtration by fibrous filters. This is to be expected since the basic mechanisms--diffusion in the small particle size range and impaction and sedimentation in the large size range--are the same for filtration and lung deposition. The minimum deposition efficiency occurs within the transition range between the two mechanisms at a diameter between 0.5μm and 1.0μm, as in filtration. The "V" shape is similar to plots of the deposition fraction versus particle size predicted (Figure 1.4) and measured (Landahl, Tracewell and Lassen, 1951, 1952) for the

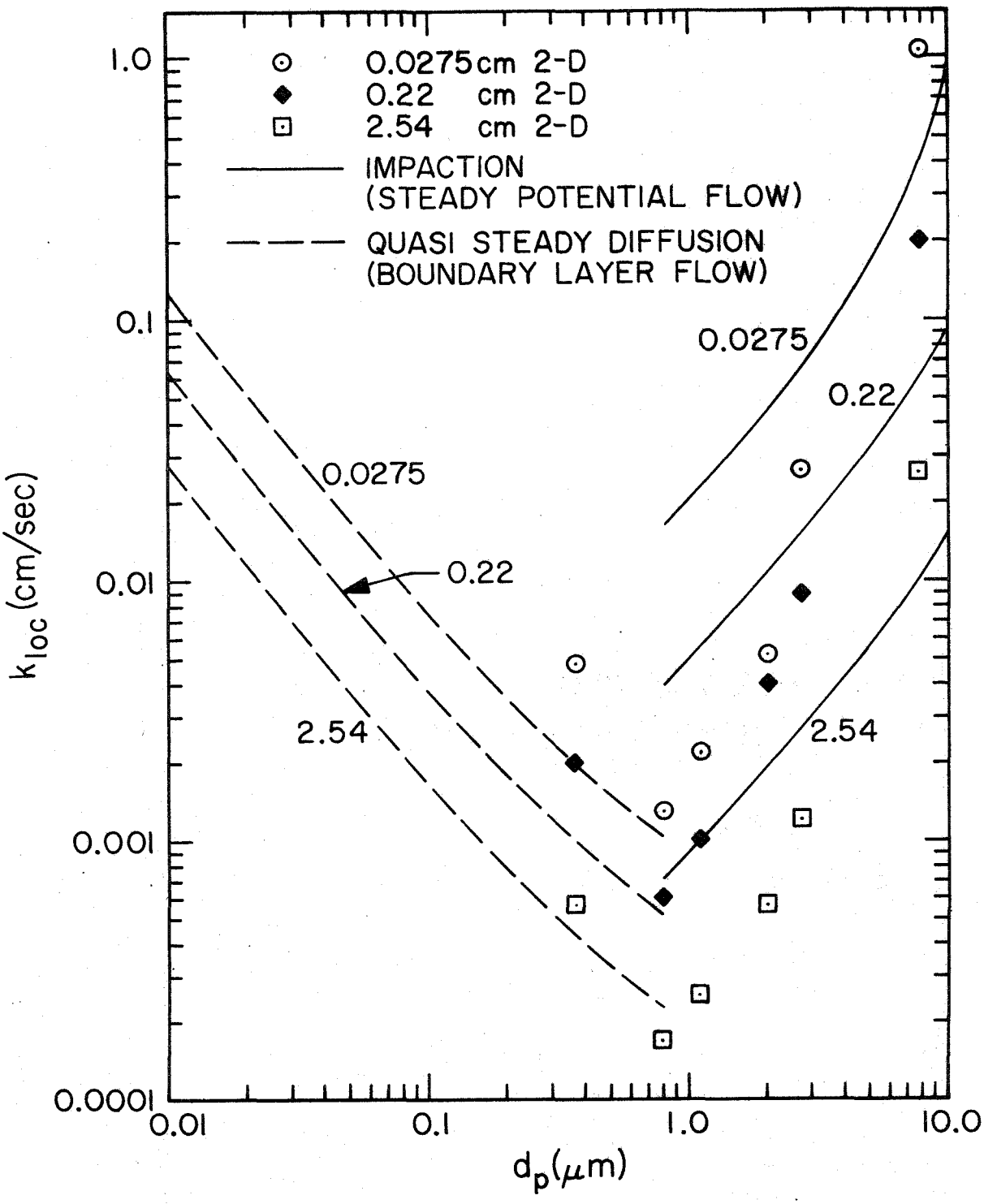

Figure 5.1 Comparison of Theories with Local Transfer Coefficients Measured at 0.0275, 0.22 and 2.54 cm Downstream from the Carina in the 2-D Model for Simulated 450 cc, 1.63 sec Inhalations. d_p refers to Spheres of Unit Density. U=100 cm/sec for Impaction(w/ Interception), $\overline{U}$=100 cm/sec for Diffusion(Point Particles) and A=0.92.

entire respiratory tract. This is expected since deposition by the same mechanisms occur in each generation of the lung.

The highest local dosage occurs near the carina and is an order of magnitude or more greater than the deposition at the end of the branch, depending on particle size. Larger particles (impaction subrange) produce higher local dosages near the carina, relative to the average deposition, than smaller particles (diffusion subrange).

In Figure 5.1 deposition data are compared with the theory of impaction including interception in potential flow, and quasi-steady diffusion theory for point particles in laminar boundary layer flow (Sections 2.3.5 and 2.4.3). The impaction calculations were made for U = 100 cm./sec., which corresponded to the time-average velocity in the trachea during the run, and at $A = 0.92$ cm.$^{-1/3}$ (Section 4.2). The diffusion calculations were based on Equation 2.4.3 with a velocity distribution from Figure 4.4. The time-average velocity $\overline{U}$ was 100 cm./sec. and A was 0.92 cm.$^{-1/3}$

The 2.68μm and 7.6μm data agree fairly well with the theory of impaction including interception, and the data for the 0.365μm and 0.79 μm particles are in fair agreement with diffusion theory. Data for the 1.099μm and 2.02μm particles fall in a region between the two theories.

Agreement between impaction theory for potential flow and experimental data has been reported for the collection of particles on cylinders and spheres (Fuchs, 1964:162; Walton and Woolcock, 1960).

One explanation for the deviation of theory from experiment in the 0.8 to 4μm range is the effect of unsteady aerodynamic boundary layers which were not taken into account in the impaction calculation.

Separate impaction calculations which accounted for a steady boundary layer along the wedge are discussed in Section 2.3.7. Results of those calculations (Figure 2.8), made for U = 100 cm./sec. and $A = 0.82\ cm.^{-1/3}$, predict no deposition beyond $x_1 = 0.01$ cm. for the particles in this study. All the deposition for the 1 to 4μm range is predicted to occur at $x_1 \leq 4\mu m$. However, the results of calculations (Figure 2.9, Section 2.3.7), for steady boundary layer flow at various velocities from Figure 4.4, suggest that 1.0 to 10μm particles deposit more efficiently during the high velocity phases of the unsteady inhalations than during the low velocity phases. Likewise, the distance from the carina at which deposition vanishes is greater during the high velocity phase. Thus, the resulting time-averaged deposition is greater at every location than predicted from steady boundary layer flow with $U = \overline{U}$, but it is still less than deposition calculated for potential flow. The boundary layer affects small particles more than large particles (Section 2.3.7); consequently smaller particles in the 0.8 to 4μm range deviate further from the impaction theory in Figure 5.1.

A further explanation of the increase in deposition during unsteady inhalations as compared to steady boundary layer flow is associated with the time required to reach a quasi-steady boundary layer thickness

during pulsatile flow. As estimated from Section 1.3.6 for $\overline{U} = 100$ cm./sec., the percentage of the inspiration time, during which the momentum boundary layer was thin in comparison to its quasi-steady thickness, was 2% at $x_1 = 1.0$ cm. and 5% at $x_1 = 2.54$ cm. This suggests minor increases in the local deposition. Convective diffusion probably also contributed, but only weakly, to the deposition of particles in the 1 to 4μm range.

The data shown in Figure 5.2 through 5.7 are compared with theories for impaction and interception in a steady potential flow at $U = 100$ cm./sec. and $A = 0.82$ cm.$^{-1/3}$ and with the quasi-steady diffusion theory for point particles in laminar boundary layer flow at $\overline{U} = 100$ cm./sec. and $A = 0.92$ cm.$^{-1/3}$ All theories were evaluated at the same conditions of temperature and pressure--25° C. and 74 cm. Hg.

5.2 7.6μm Particles

In Figure 5.2 the theories for impaction with and without interception and the theory for pure interception are compared with data for 7.6μm particles. The three data points in Figures 5.1 and C.1 were from run #19. The theories show that impaction dominates near the carina, but that interception controls further downstream.

The data agree in trend with impaction theory for particles of $R_p = 3.8\mu$m, but they are two or three times larger in magnitude at most locations. The deviation of theory from data is caused by several factors.

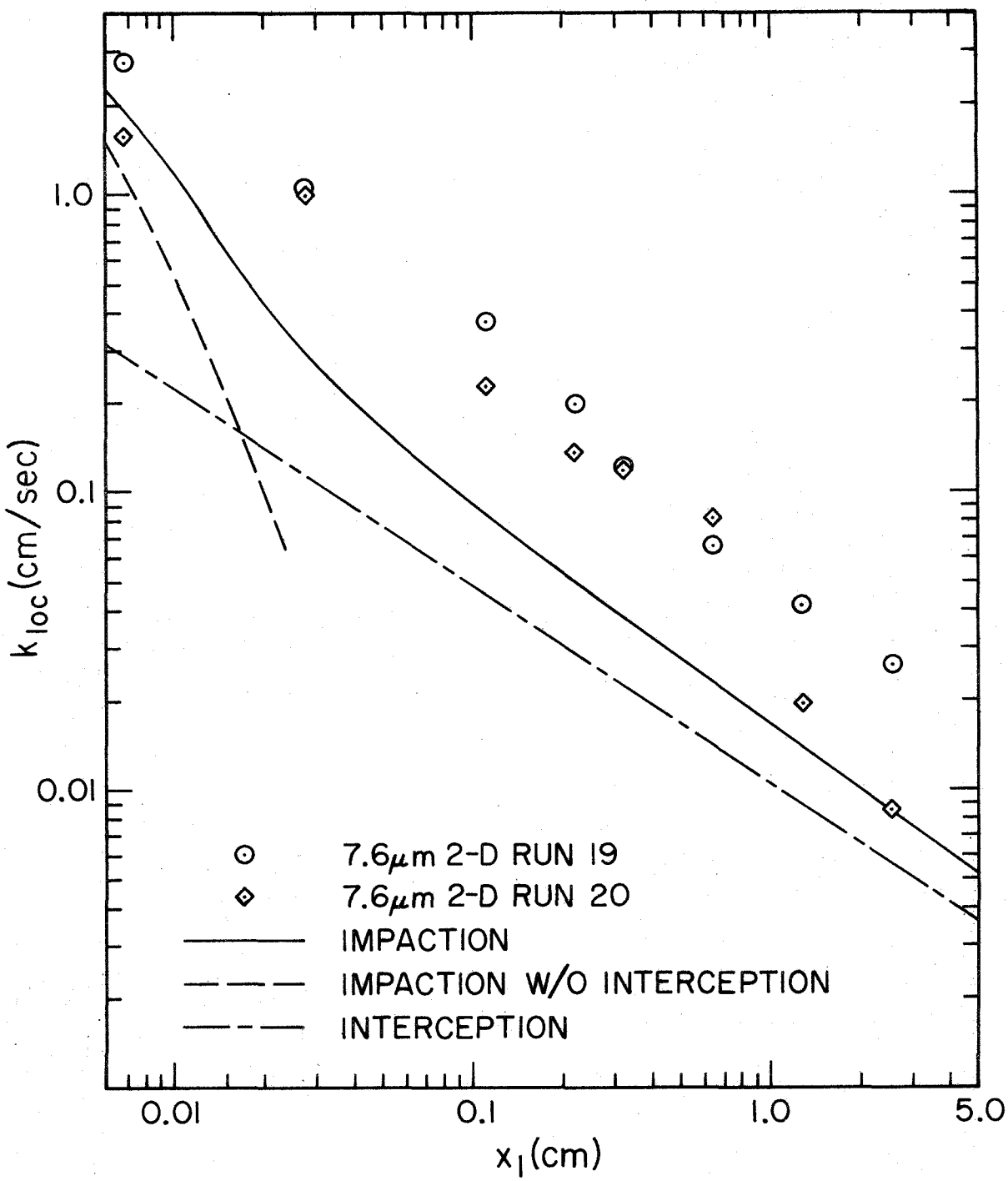

Figure 5.2 Comparison of Theories with Local Transfer Coefficients for 7.6 μm Particles Depositing on a Horizontal 90° Wedge in the 2-D Model for Simulated 450 cc, 1.63 sec Inhalations. Theories Use Steady Potential Flow with U=100 cm/sec and A=0.82.

The calculated transfer coefficients with A = 0.82 are lower than those for A = 0.92 (compare Figures 5.1 and C.1). The 7.6μm (average diameter) particles are distributed with respect to size with $\sqrt{\overline{d_p^2}} = 8.7\mu m$ (Table B.1). Although each deposited particle was not sized, a greater number of particles with $d_p > 7.6\mu m$ was counted than with $d_p < 7.6\mu m$. The local transfer coefficients depend strongly on the Stokes ($\propto d_p^2$) and Interception ($\propto d_p$) numbers. Therefore, calculations based on $d_p = 8.7\mu m$ would more accurately approximate the data than those made for $d_p = 7.6\mu m$.

Finally, the theoretical time-averaged deposition curve for 7.6μm or 8.7μm particles lies above the curve calculated for a steady velocity of 100 cm./sec., the time-average experimental velocity. This is demonstrated most clearly in Figure 2.7 and Section 2.3.6.

5.3 2.68μm Particles

Figure 5.3 compares the theories of impaction (including interception) and of pure interception with data for 2.68μm particles. The three data points in Figures 5.1 and C.1 are an arithmetic average of data from the three runs.

Interception is the dominant contribution to impaction theory along the entire length of the wedge because the magnitude of the pure interception curve is more than 50% of the impaction curve. The data are in fair agreement with either theory when one accounts for statistical errors in the raw count data. However, as plotted, the data generally

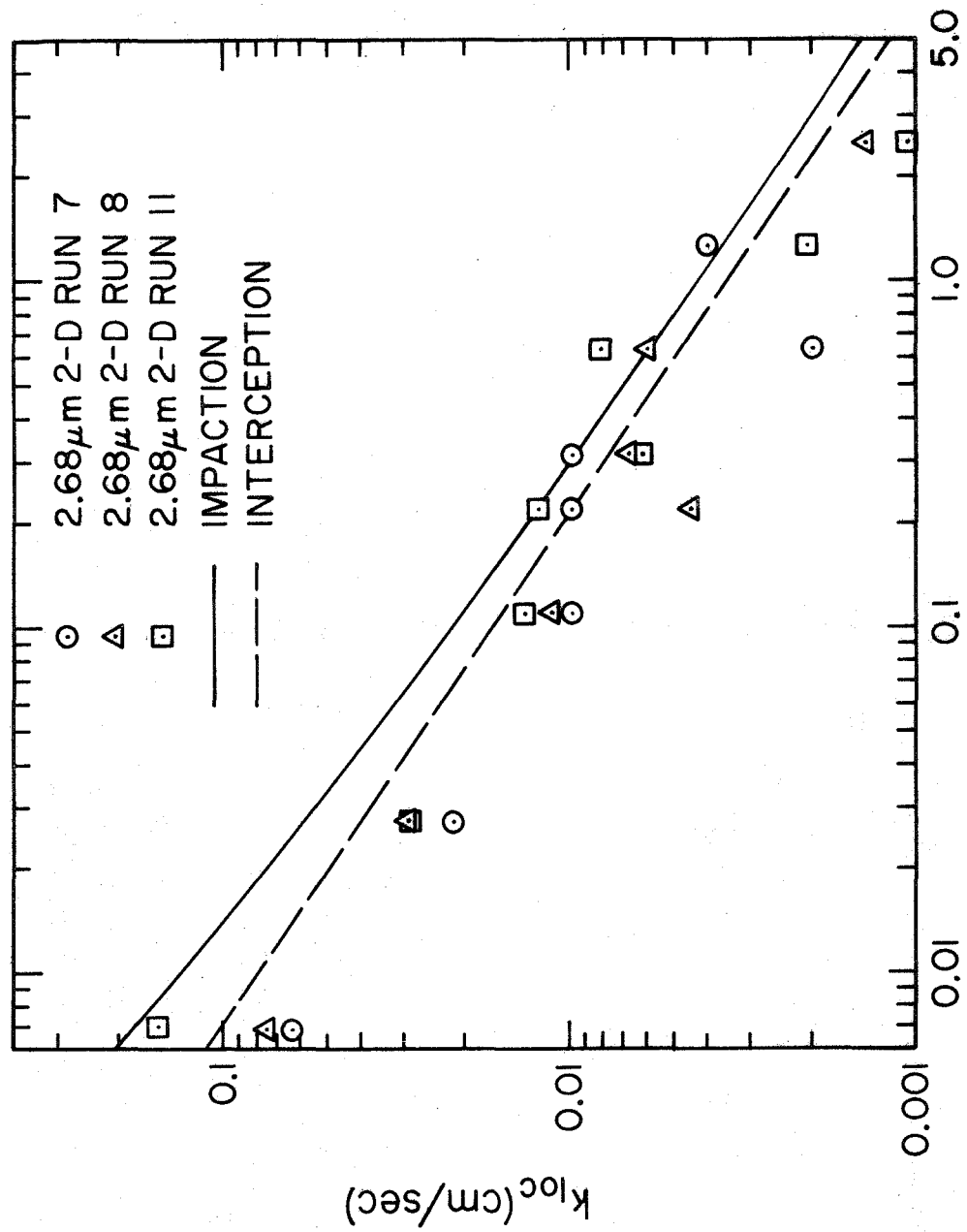

Figure 5.3 Comparison of Theories with Local Transfer Coefficients for 2.68 μm Particles Depositing on a Horizontal 90° Wedge in the 2-D Model for Simulated 450 cc, 1.63 sec Inhalations. Theories Use Steady Potential Flow with U=100 cm/sec and A=0.82 .

agree better with interception theory because the unsteady boundary layers slightly suppress the impaction mechanism. Since the boundary layer is thicker at greater distances from the carina, this suppression is most obvious in data at $x_1 = 2.54$ cm.

5.4 2.02 μm Particles

In Figure 5.4 the theories of impaction, interception and quasi-steady convective diffusion are compared with data for 2.02 μm particles. The three data points in Figures 5.1 and C.1 are from run #41.

The data fall between the theories of interception and quasi-steady diffusion, but they favor the interception theory. As expected, the unsteady boundary layer caused a greater inhibition of deposition for the 2.02 μm particles and a greater deviation of the 2.02 μm data from the impaction theory than for the 2.68 μm particles. The data points at 0.0069 cm. and 0.0275 cm. in Figure 5.4 are lower in magnitude than expected from the trend of the other data which generally agrees with the trend of the impaction and interception theories. This result may have been produced from nonidealities in geometry and flow at the carina in the experimental model (Section C.3).

This analysis suggests that deposition of 2.02 μm particles was controlled by impaction with interception in the unsteady boundary layer along the wedge.

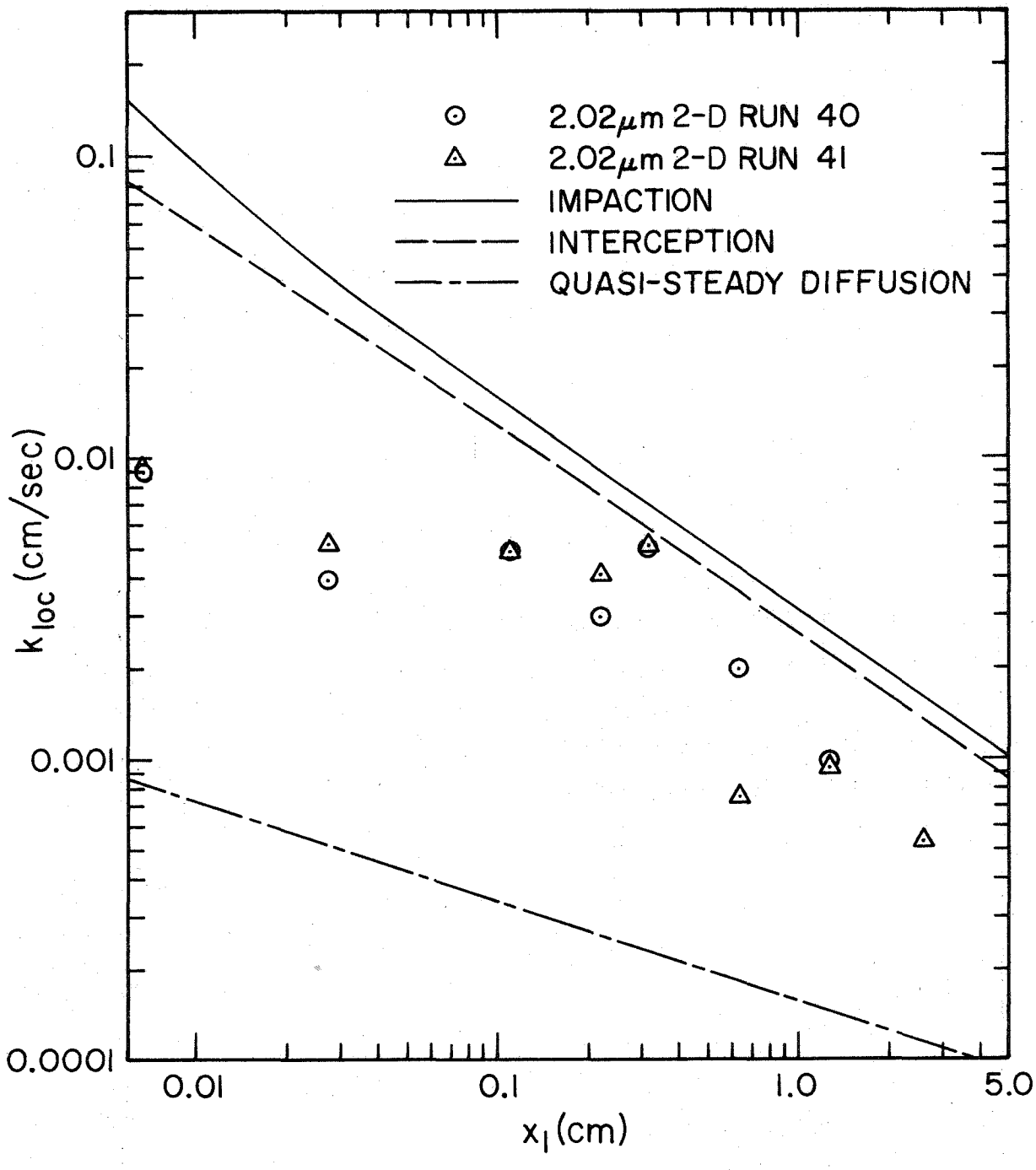

Figure 5.4 Comparison of Theories with Local Transfer Coefficients for 2.02 μm Particles Depositing on a Horizontal 90° Wedge in the 2-D Model for Simulated 450 cc, 1.63 sec Inhalations. Impaction and Interception Use Steady Potential Flow with U=100 cm/sec and A=0.82 . Diffusion(Point Particles) Uses Quasi-steady Boundary Layer Flow with $\overline{U}$= 100 cm/sec and A=0.92.

5.5 1.099μm Particles

Figure 5.5 compares the theories of impaction, interception and quasi-steady diffusion with data for 1.099μm particles. The three data points in Figures 5.1 and C.1 are from run #24.

The data fall between the interception theory and the theory of quasi-steady diffusion, but the magnitudes and the trend of the data generally favor the diffusion theory, and to a greater degree than in the case of the 2.02μm data. Again the unsteady boundary layer is observed to inhibit more effectively the impaction and interception of smaller particles, and especially at 2.54 cm., as shown by the data of runs #24 and #25.

In run #36 particles were collected on double-stick tape instead of carbon black used in runs #24 and #25. The data at 1.27 and 2.54 cm. in run #36 are larger in magnitude than in the other runs because the surface of the strips of tape in these two locations was raised such that the particles were captured more effectively.

In conclusion, the deposition of 1.099μm particles along the wedge was controlled by impaction with interception in the unsteady boundary layer, but convective diffusion with interception probably contributed significantly to the deposition at the more distant locations.

5.6 0.79μm Particles

Figure 5.6 compares the same theories with data for 0.79μm particles. The three data points in Figures 5.1 and C.1 are from run #31.

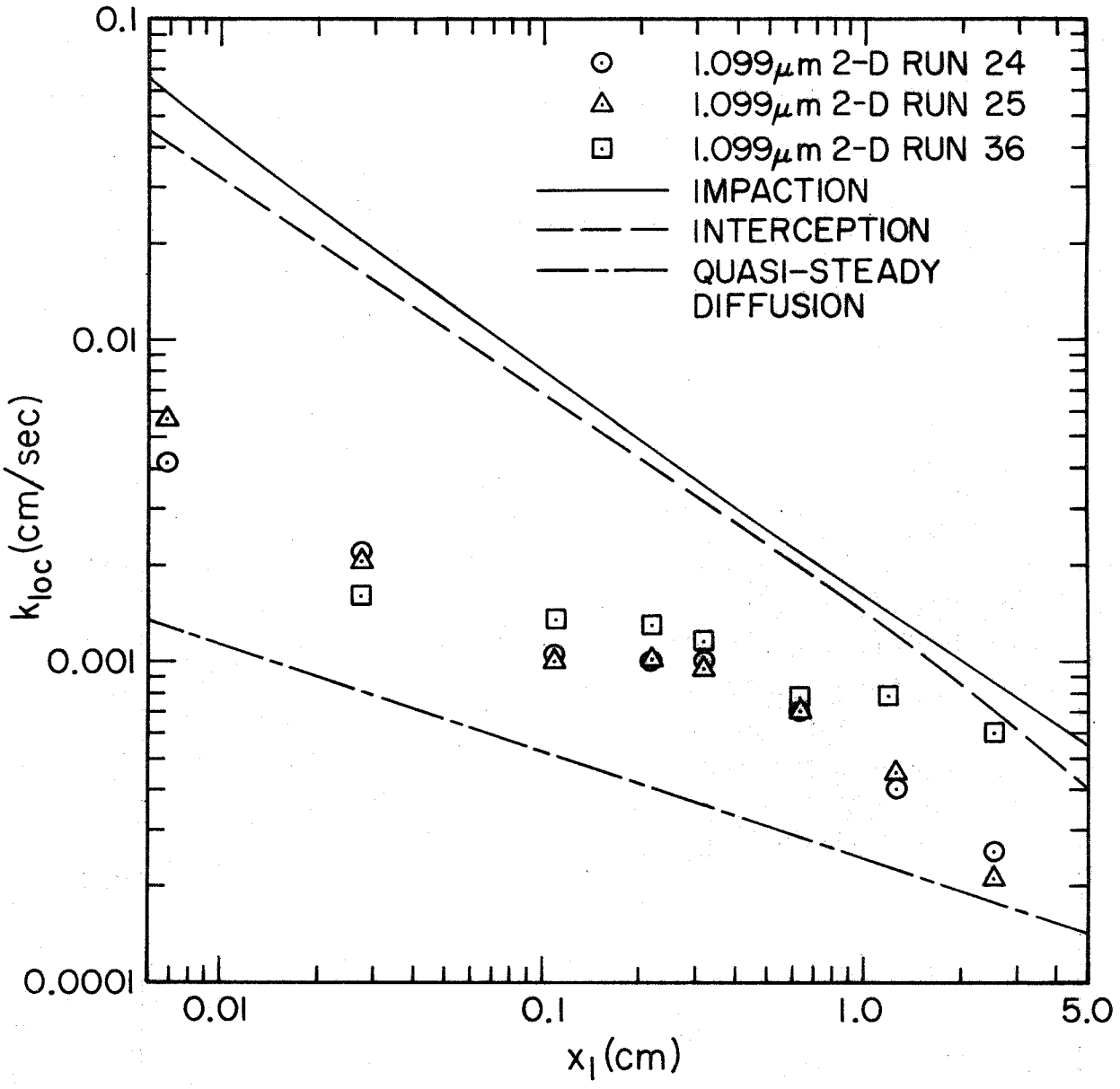

Figure 5.5 Comparison of Theories with Local Transfer Coefficients for 1.099 μm Particles Depositing on a Horizontal 90° Wedge in the 2-D Model for Simulated 450 cc, 1.63 sec Inhalations. Impaction and Interception Use Steady Potential Flow with U=100 cm/sec and A=0.82 . Diffusion(Point Particles) Uses Quasi-Steady Boundary Layer Flow with $\bar{U}$=100 cm/sec and A=0.92 .

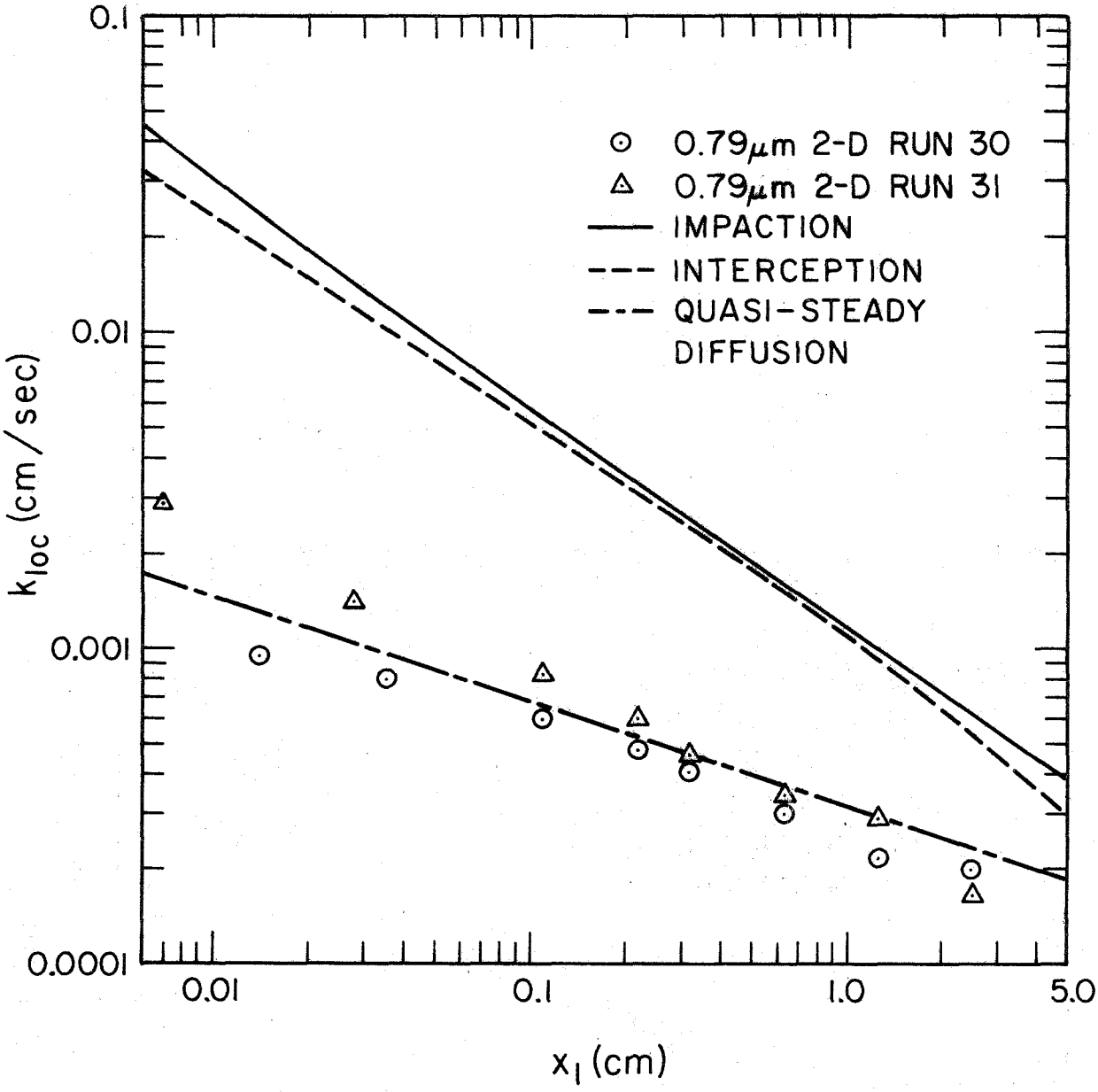

Figure 5.6 Comparison of Theories with Local Transfer Coefficients for 0.79 μm Particles Depositing on a Horizontal 90° Wedge in the 2-D Model for Simulated 450 cc, 1.63 sec Inhalations. Impaction and Interception Use Steady Potential Flow with U=100 cm/sec and A=0.82 . Diffusion(Point Particles) Uses Quasi-Steady Boundary Layer Flow with $\bar{U}$=100 cm/sec and A=0.92 .

Although the data agree well in magnitude and in trend with the theory of quasi-steady diffusion, they deviate further in the negative direction from the diffusion theory at more distant locations than at locations closer to the carina. If the interception effect could be included in the diffusion theory, the data would appear even lower in magnitude relative to the theory than in Figure 5.6. This deviation can be explained as follows: During pulsatile inhalations with the model initially filled with clean air, more time is required to fill the concentration boundary layer with particles in the region far from the carina. Hence the more distant locations should have a relatively lower transfer coefficient in comparison to the quasi-steady diffusion theory than the closer locations.

5.7 0.365μm Particles

Figure 5.7 compares theories of interception in potential flow and diffusion of point particles in quasi-steady boundary layer flow with data for 0.365μm particles. The three data points in Figures 5.1 and C.1 are an arithmetic average of the data from both runs.

The data agree in trend with diffusion theory but are 1.1 to 2.0 times larger at most locations. Improved agreement could probably be obtained by including the finite diameter of the particle in the boundary condition in a numerical solution of the equation of convective diffusion.

To avoid a time-consuming background count, the plates used in run #44 were not cleaned before making run #45. The data for run #45

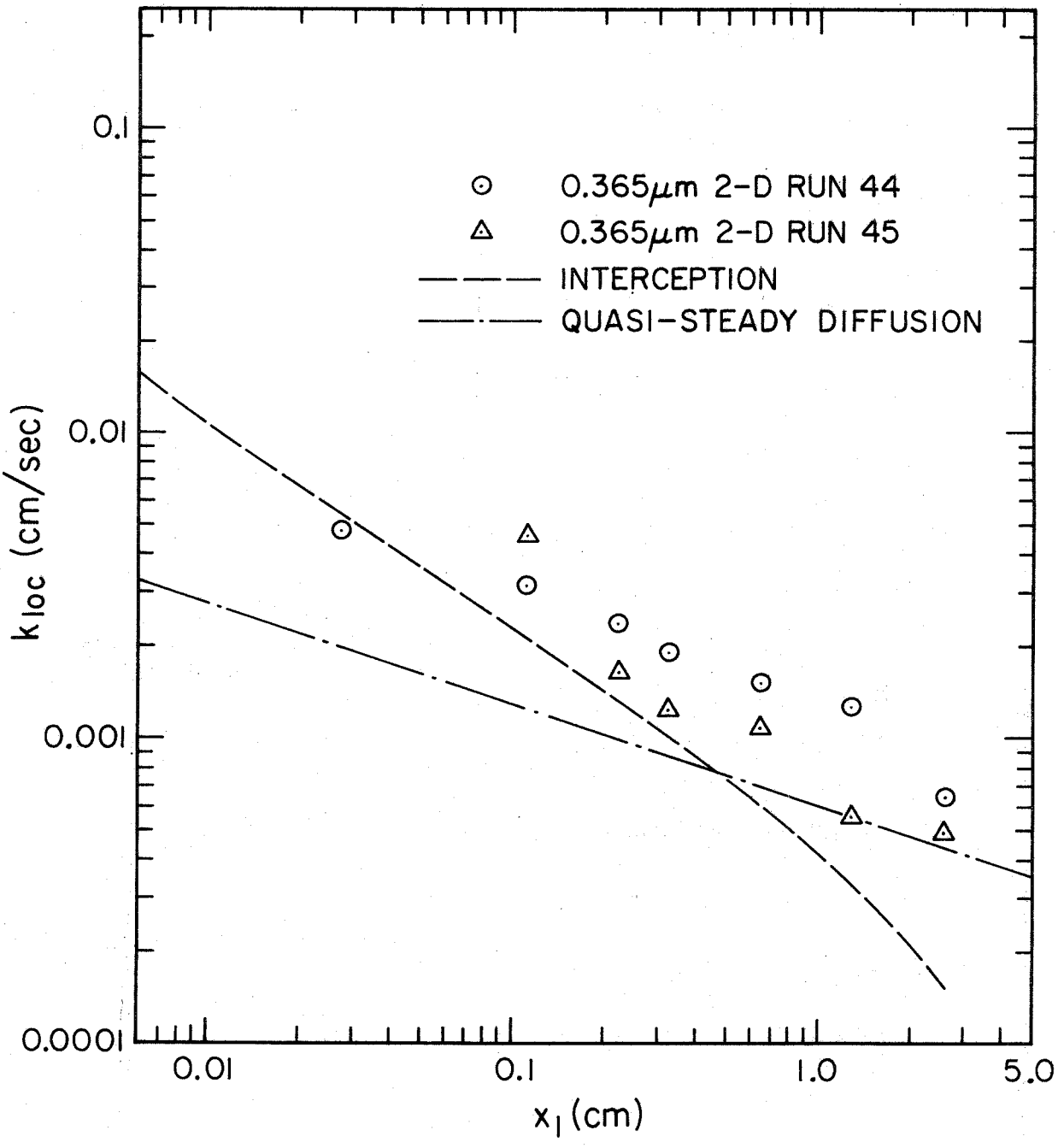

Figure 5.7 Comparison of Theories with Local Transfer Coefficients for 0.365 μm Particles Depositing on a Horizontal 90°Wedge in the 2-D Model for Simulated 450 cc, 1.63 sec Inhalations. Interception Uses Steady Potential Flow with U=100 cm/sec and A=0.82 . Diffusion(Point Particles) Uses Quasi-Steady Boundary Layer Flow with $\overline{U}$=100 cm/sec and A=0.92 .

were generally lower than #44 because some of the singlets depositing in #45 were not counted when they formed agglomerates with particles from run #44. The data at 2.54 cm. were lower compared with diffusion theory than the other data because of the clean boundary layer effect discussed for the 0.79μm data.

5.8 Concluding Analysis

The results of the detailed analysis of each particle diameter agrees with the conclusions of Section 5.1 and suggest additional generalizations. First, interception played a significant role in the deposition of all the particles studied. Deposition by convective diffusion at locations $\geq$ 2.54 cm. from the carina was retarded by the clean air which was present in the model before each inhalation.

Experiments with the "2-D" model supported the validity of the experimental approach and showed acceptable agreement with the approximate theories. Therefore, the next step was an experimental investigation of the deposition in the "3-D" model to evaluate the significance of sedimentation and secondary flows which were absent from the "2-D" model.

Chapter 6

EXPERIMENTAL RESULTS AND ANALYSIS: THREE-DIMENSIONAL MODEL

6.1 Contour Maps and Cumulative Surface Area Distributions of Local Transfer Coefficients

The first set of runs was made for 0.088, 0.365, 0.79, 1.1, 2.02 and 5.7μm particles in the "3-D" model with 450 c.c., 1.88 second inhalations. In the second set 0.088, 0.365, 0.81, 1.1, 2.02 and 5.7μm diameter particles were used with 450 c.c., 0.94 sec. inhalations. Separate runs were also completed for 1.1 and 2.02μm particles with the model in a horizontal or prone orientation (gravity vector perpendicular to the plane of the bifurcation) and for 450 c.c., 1.88 sec. inhalations. Count data and the corresponding local transfer coefficients, k_{loc}, are tabulated in Appendix C.

Deposition patterns for each run were obtained by converting the k_{loc} data into contour Maps 1 - 12. The contours represent locations of constant transfer coefficient similar to topographical maps of the earth's surface. The value of X along the abscissa represents the distance in centimeters downstream from the carina (Figures 4.9 and 4.10), while Y along the ordinate represents locations around the circumference of the branch (Figures 4.8, 4.9 and 4.10). Each Y segment

corresponds to a distance of π (Branch Diameter)/18 = 0.215 cm., and each map represents a surface area of 18.4 cm.^{2} in the daughter branch. The contours were determined by a computer as described in Section C.4.

The surface area between each contour was measured with a planimeter, and a cumulative surface area distribution with respect to values of k_{loc} was plotted for each map. These plots are labeled Graph 1, 2, ..., 12, and each follows its corresponding contour map at the end of this section. The average value of k_{loc} over the surface of the daughter branch, k_{av}, was calculated by dividing the area under the cumulative surface area distribution curve by 100. k_{av} is indicated in each plot along with the percent of the surface area of the daughter branch with $k_{loc} \geq k_{av}$.

A second average transfer coefficient, k_c, was determined only for the surface area in which particle deposition actually occurred. This area was equivalent to the region enclosed by the last contour listed in the legend of each map. Hence, k_c was calculated as follows:

1. The area under the cumulative surface area distribution curve between 0% and the % of the model area enclosed by the last contour listed in the legend was determined by graphical integration.

2. This area was divided by the percentage of the model area enclosed by the last contour listed in the legend.

k_c and the percent of the area with $k_{loc} \geq k_c$ are indicated on each graph.

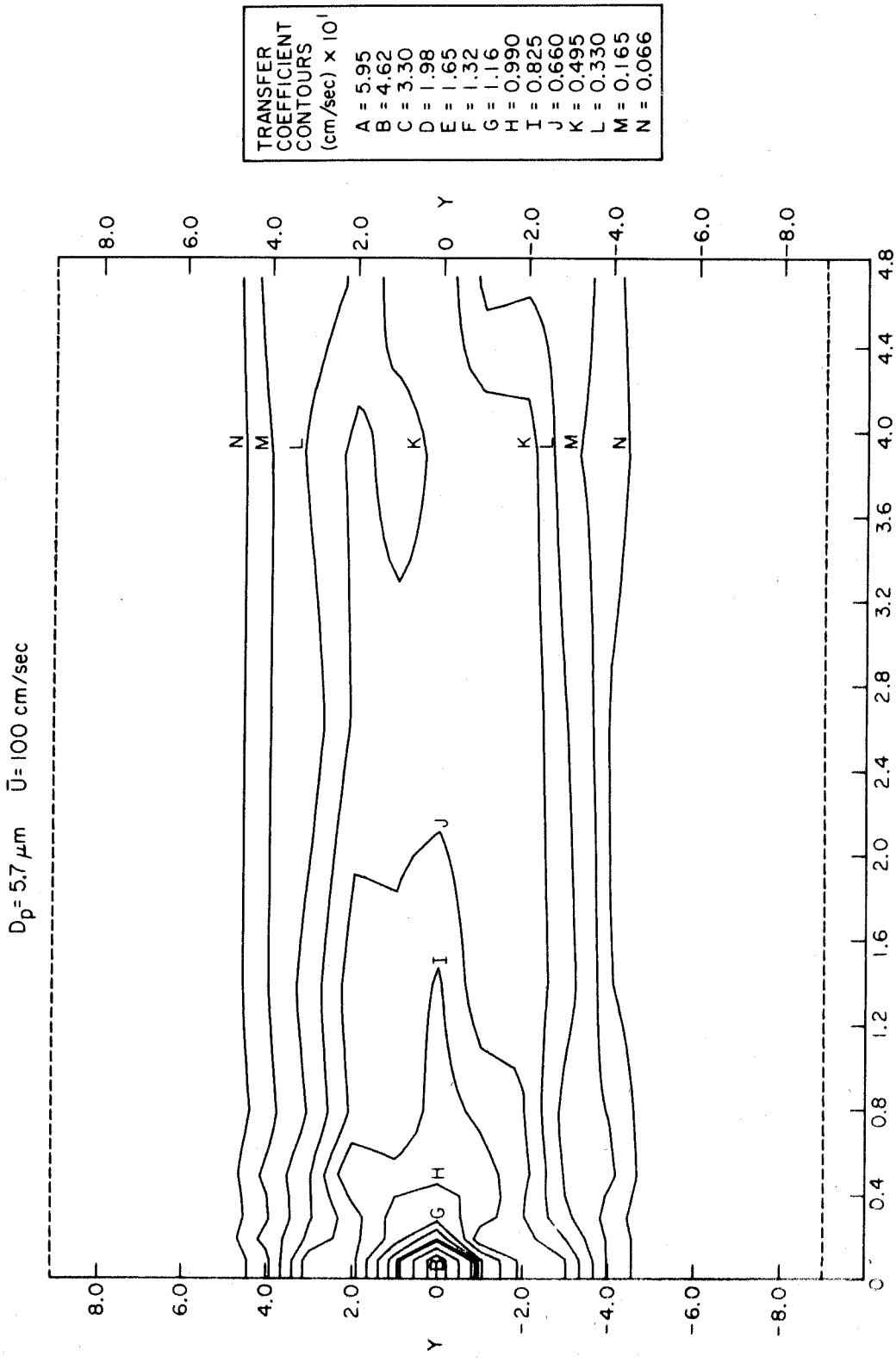

Map 1 Weighted Average of 3-D Runs 21 and 22

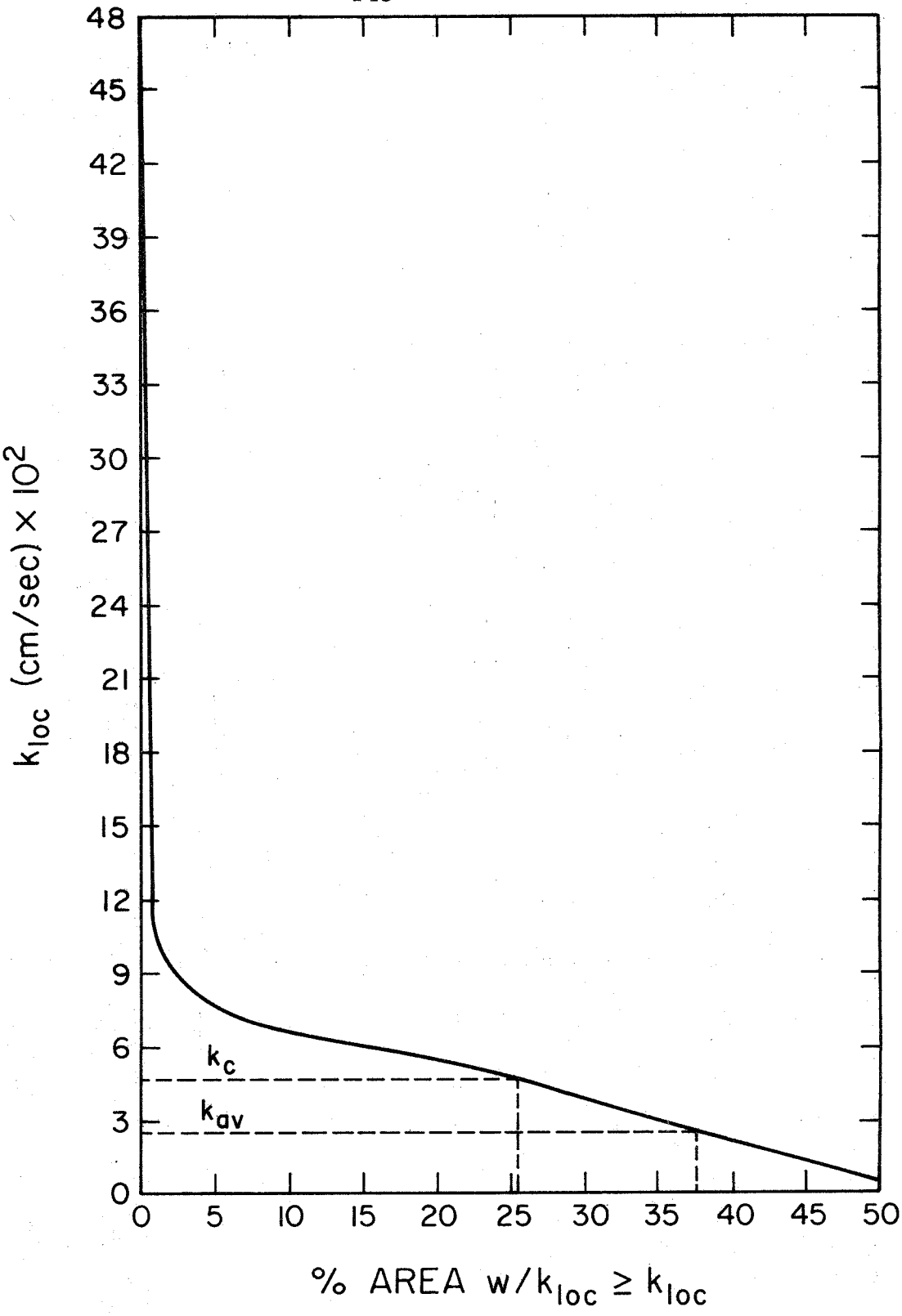

Graph 1 Cumulative Surface Area Distribution for Map 1 Showing the % of the Surface Area of the Daughter Branch with a Local Transfer Coefficient ≥ Stated Value (d_p = 5.7 μm, $\bar{U}$ = 100 cm/sec)

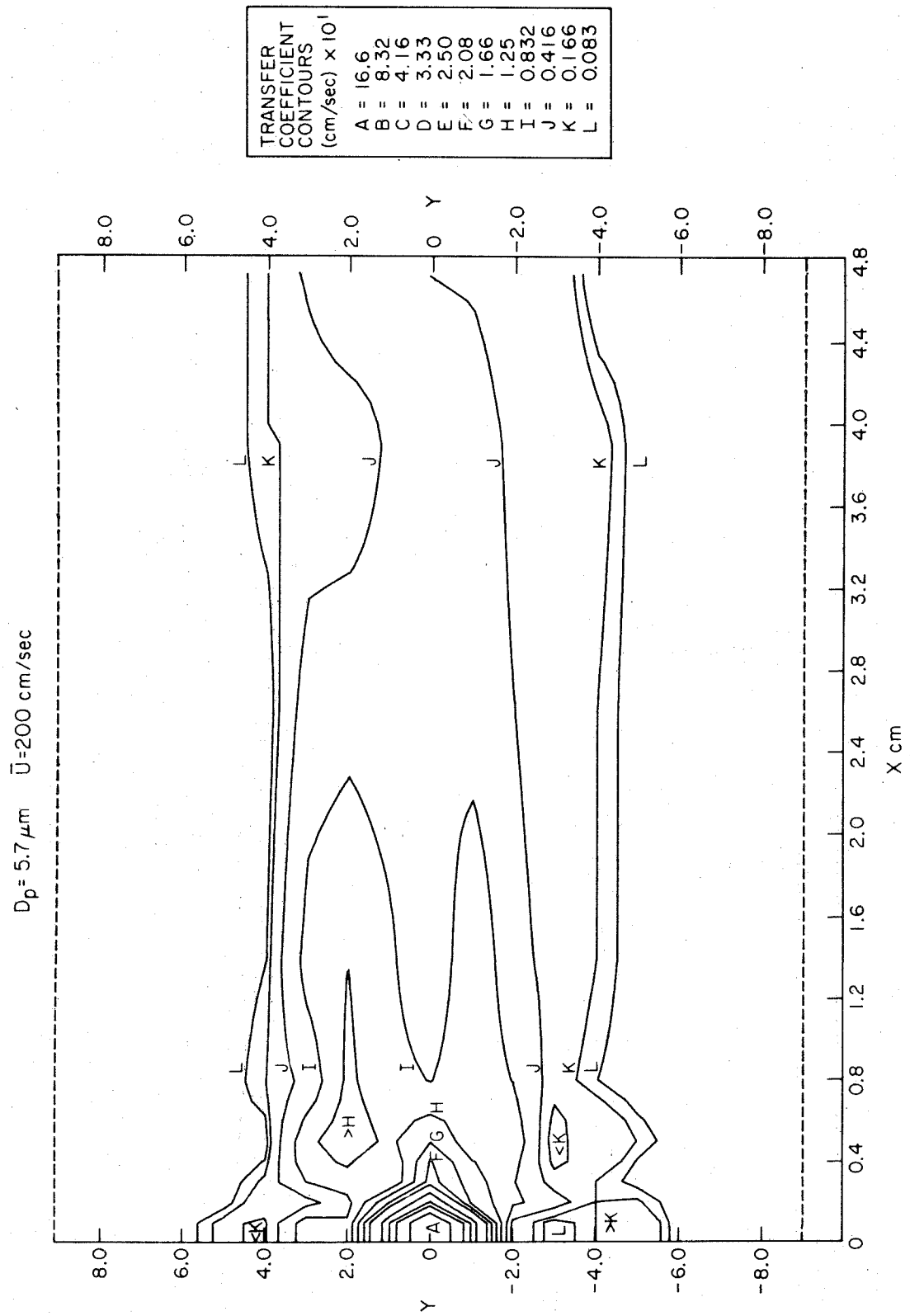

Map 2 3-D Run 27

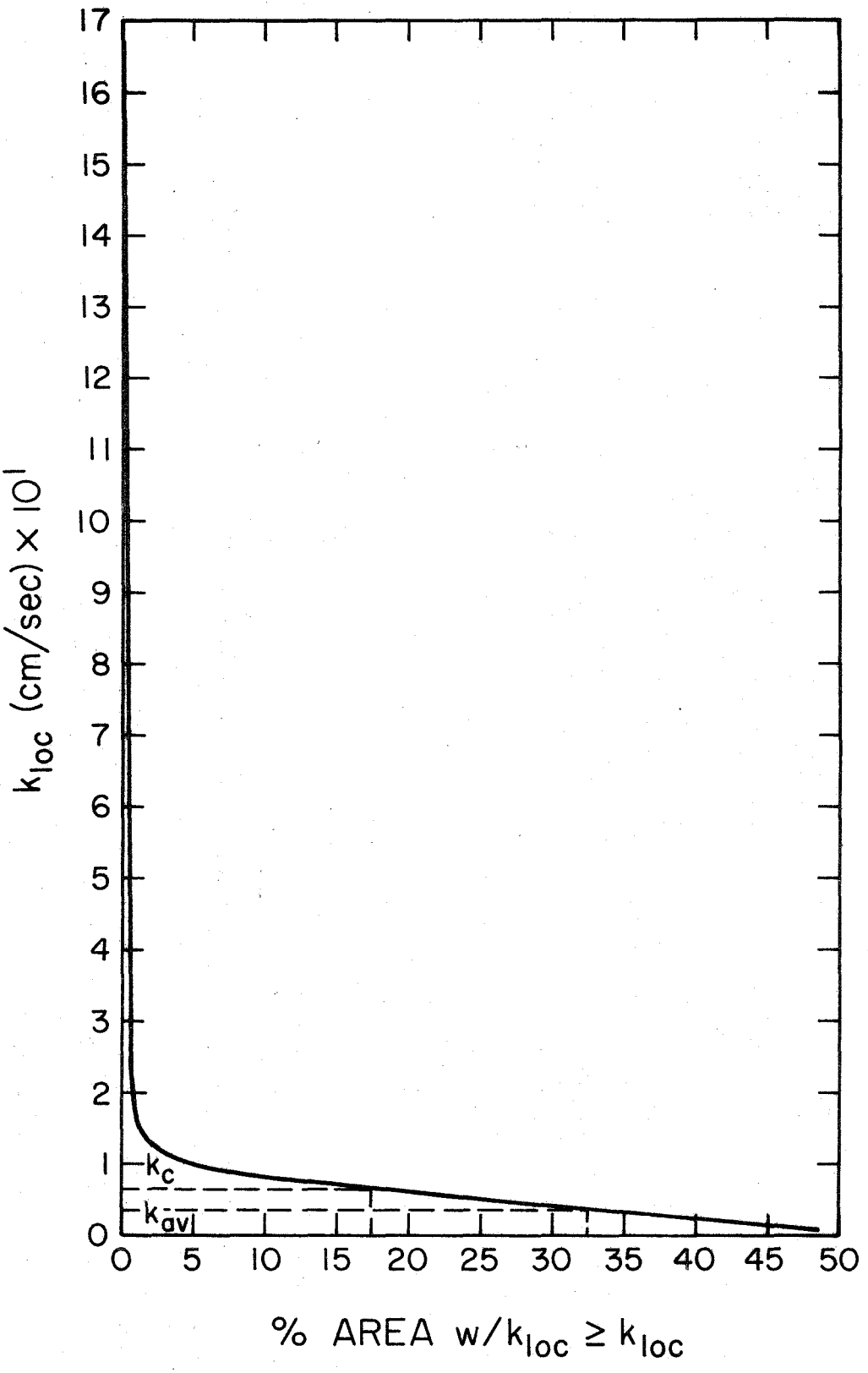

Graph 2 Cumulative Surface Area Distribution for Map 2 Showing the % of the Surface Area of the Daughter Branch with a Local Transfer Coefficient ≥ Stated Value (d_p = 5.7 μm, $\overline{U}$ = 200 cm/sec)

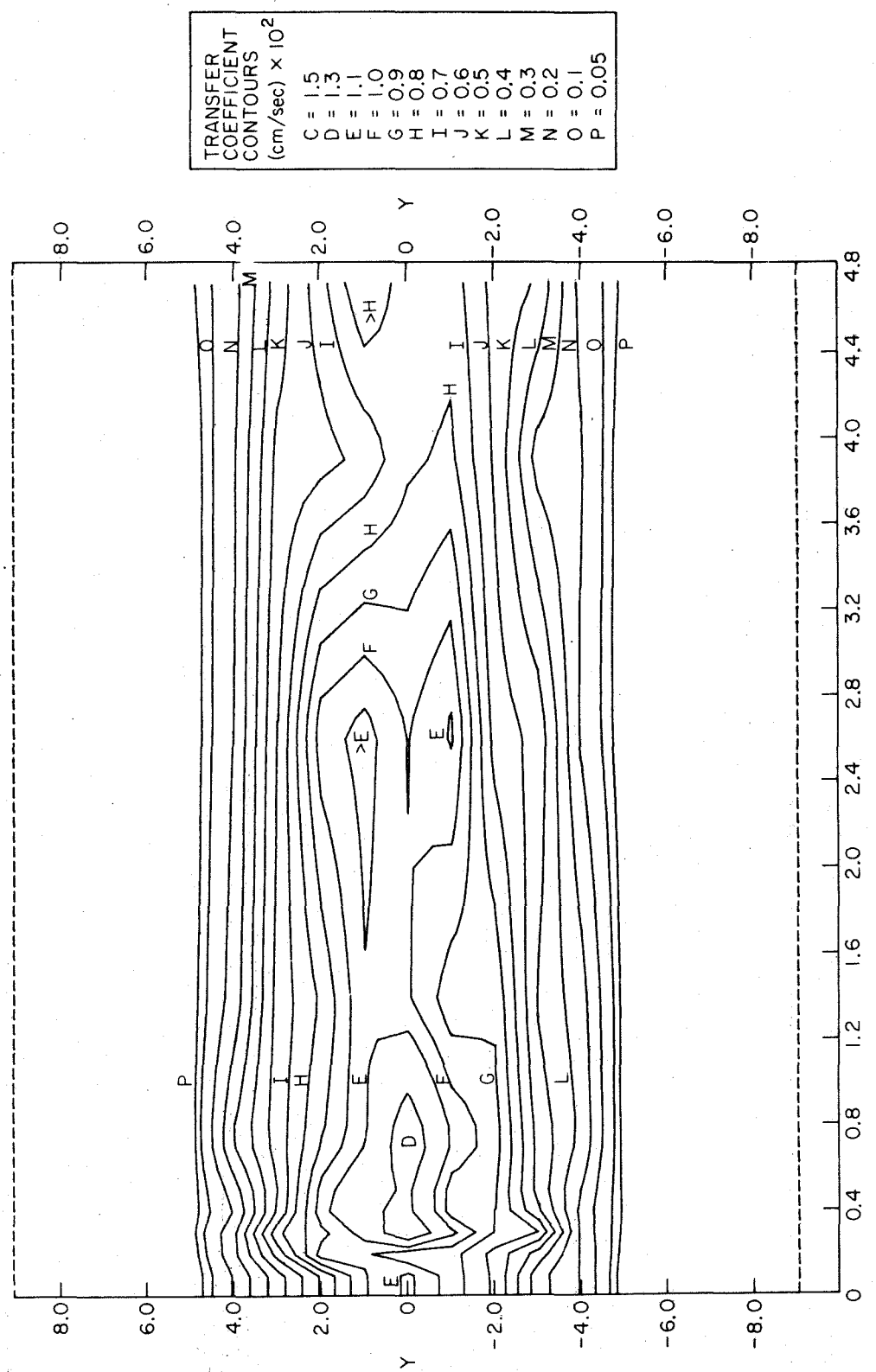

Map 3 Weighted Average of 3-D Runs 12, 14, 17, and 19

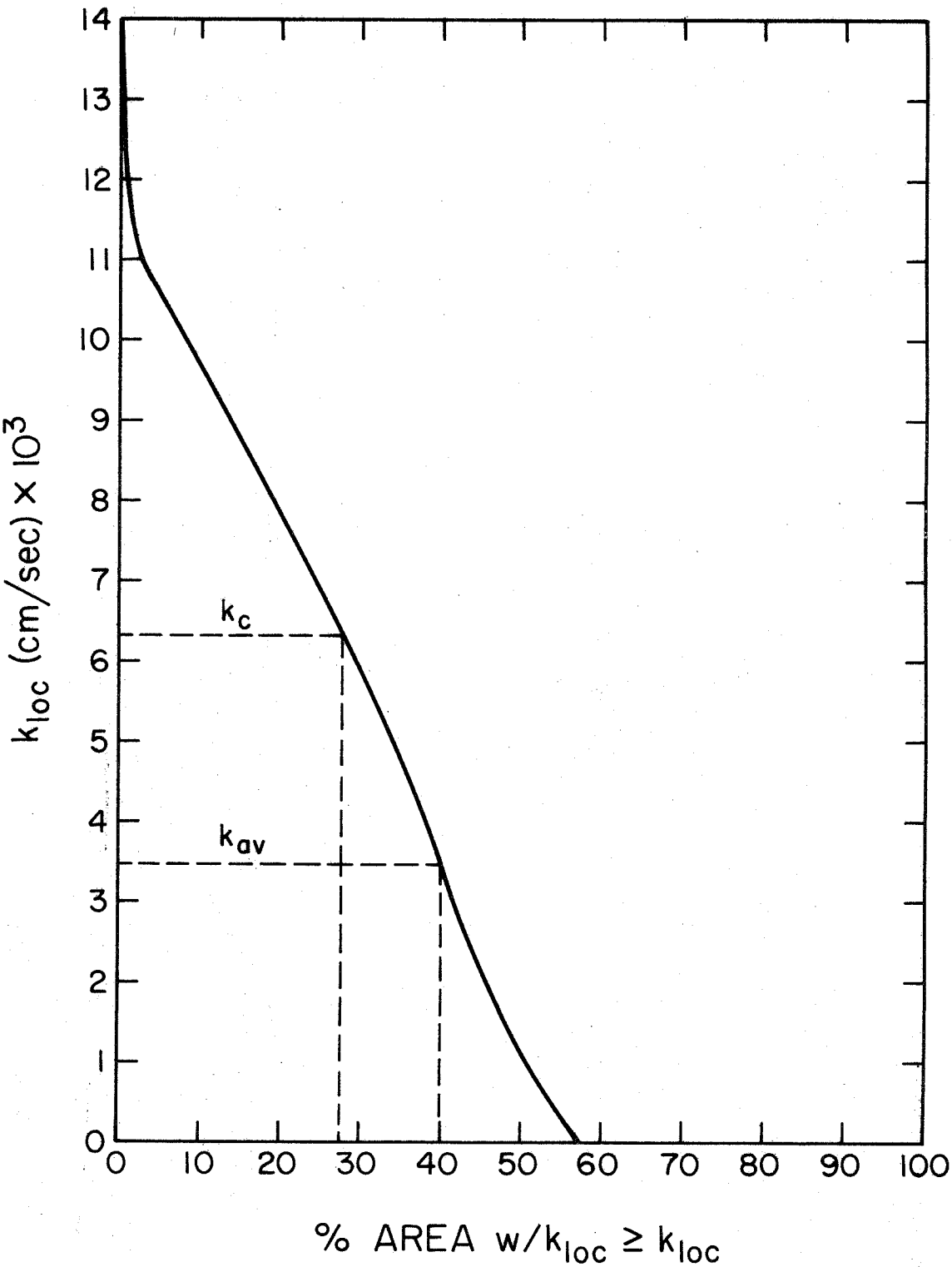

Graph 3 Cumulative Surface Area Distribution for Map 3 Showing the % of the Surface Area of the Daughter Branch with a Local Transfer Coefficient ≥ Stated Value (d_p = 2.02 μm, $\bar{U}$ = 100 cm/sec)

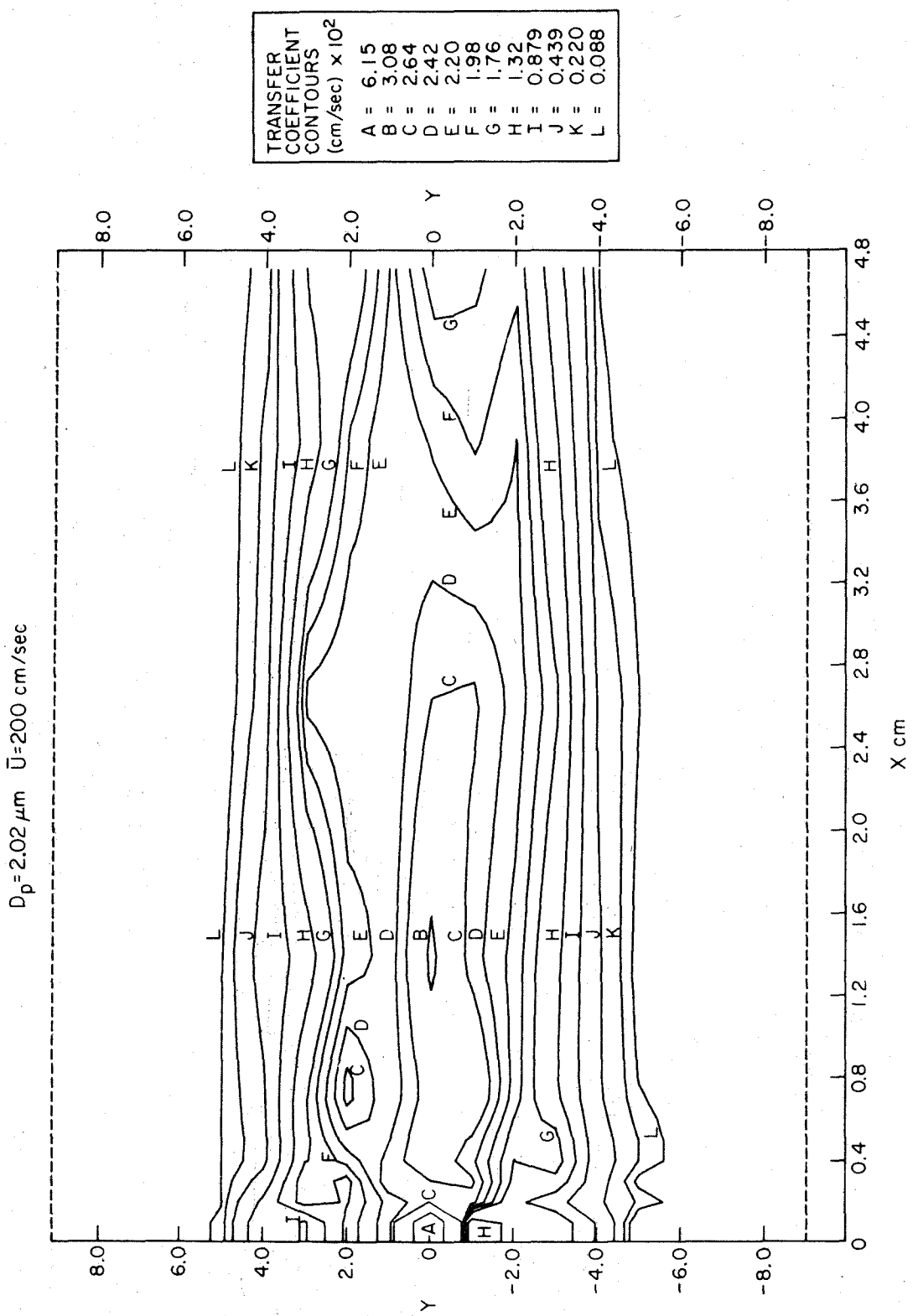

Map 4 3-D Run 24

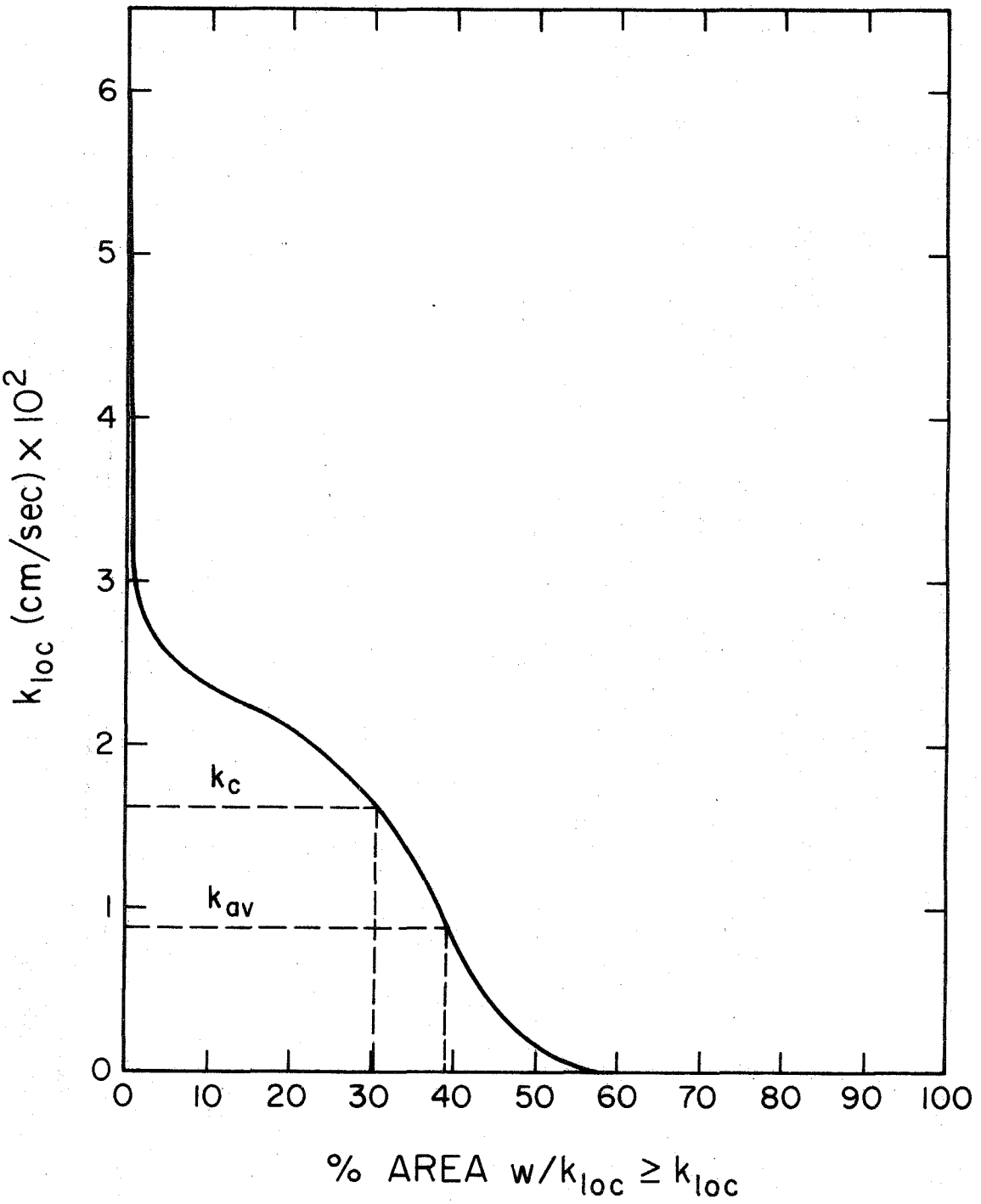

Graph 4 Cumulative Surface Area Distribution for Map 4 Showing the % of the Surface Area of the Daughter Branch with a Local Transfer Coefficient ≥ Stated Value (d_p = 2.02 μm, $\overline{U}$ = 200 cm/sec)

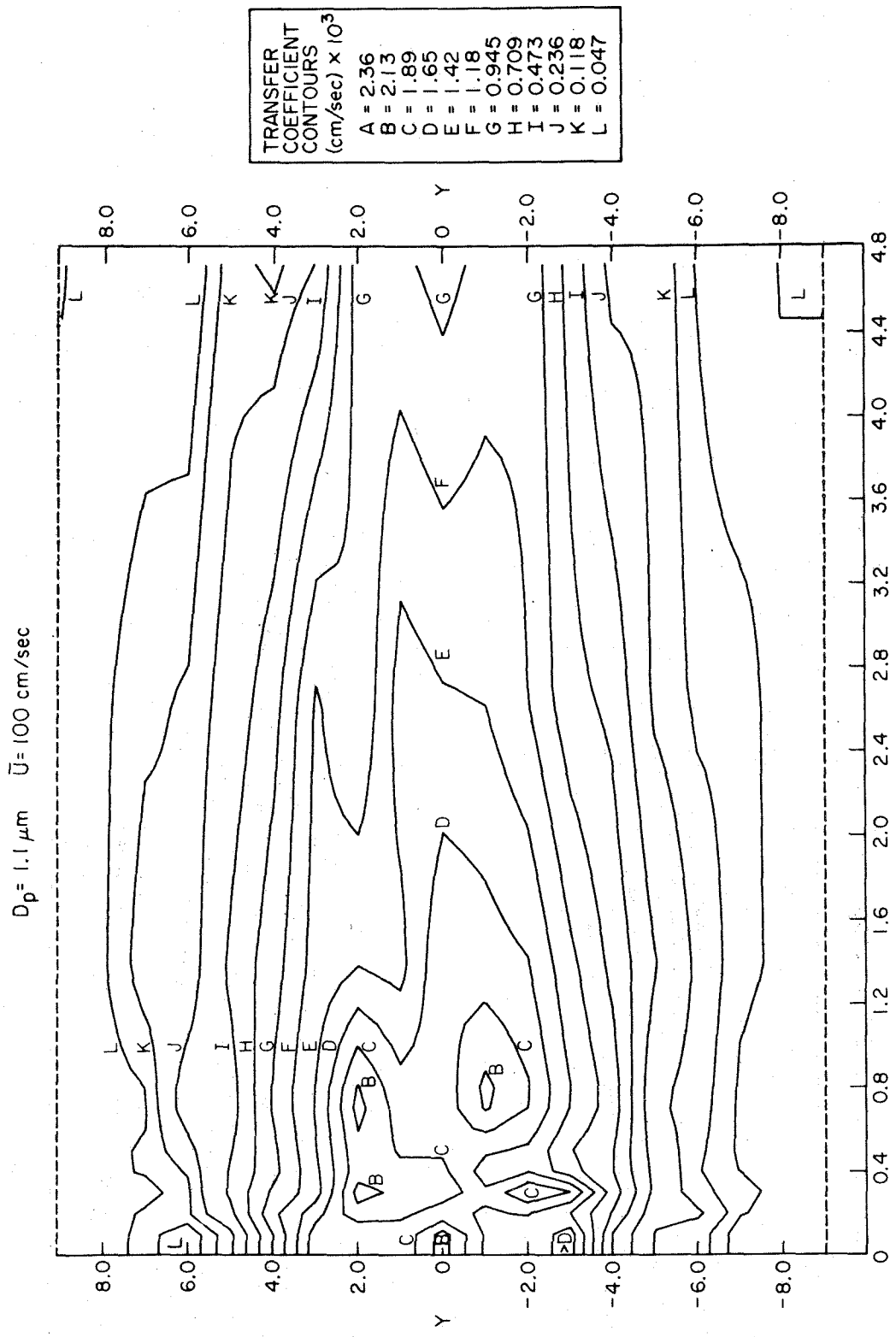

Map 5 Weighted Average of 3-D Runs 10 and 18

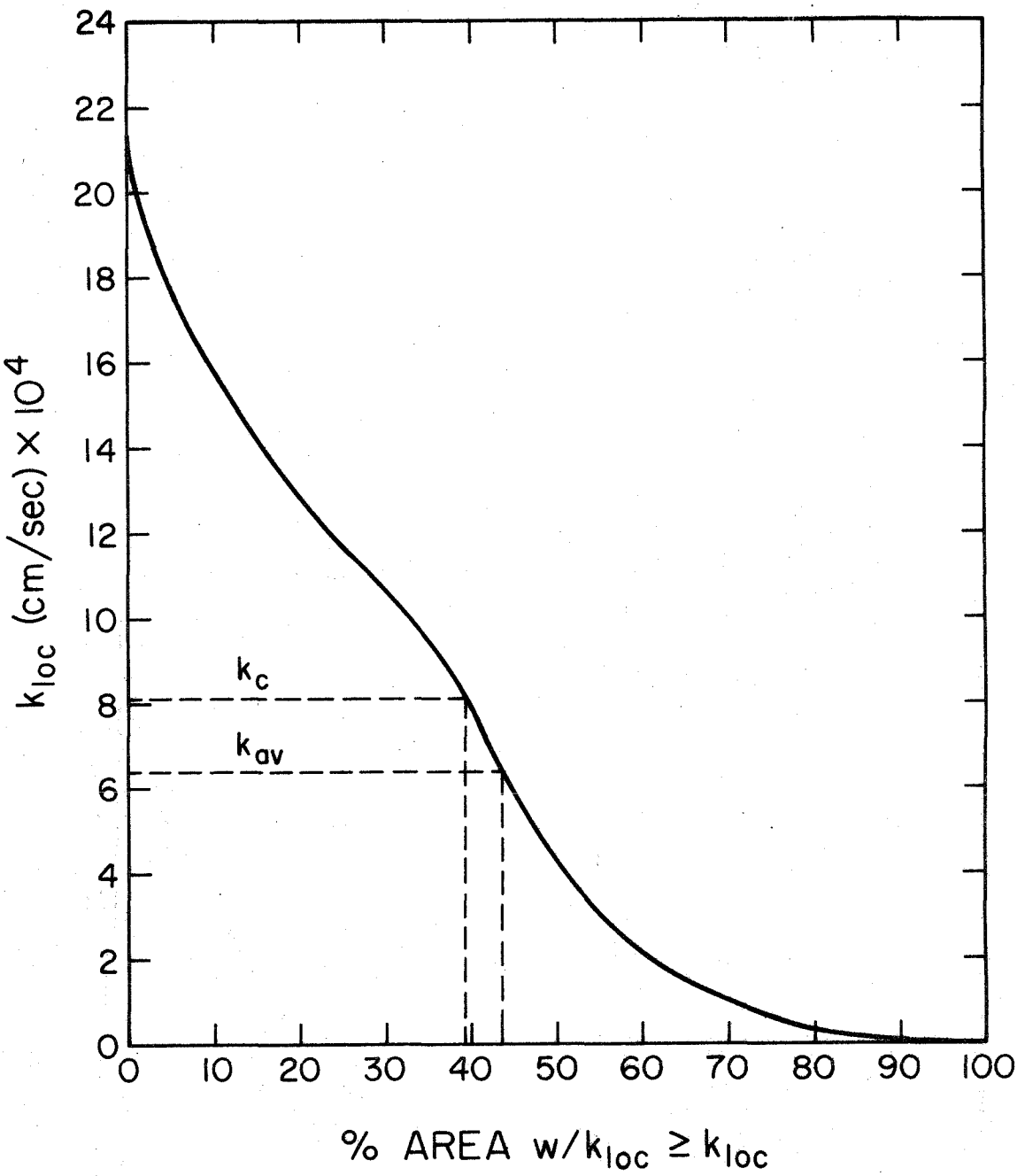

Graph 5 Cumulative Surface Area Distribution for Map 5 Showing the % of the Surface Area of the Daughter Branch with a Local Transfer Coefficient ≥ Stated Value (d_p = 1.1 μm, $\overline{U}$ = 100 cm/sec)

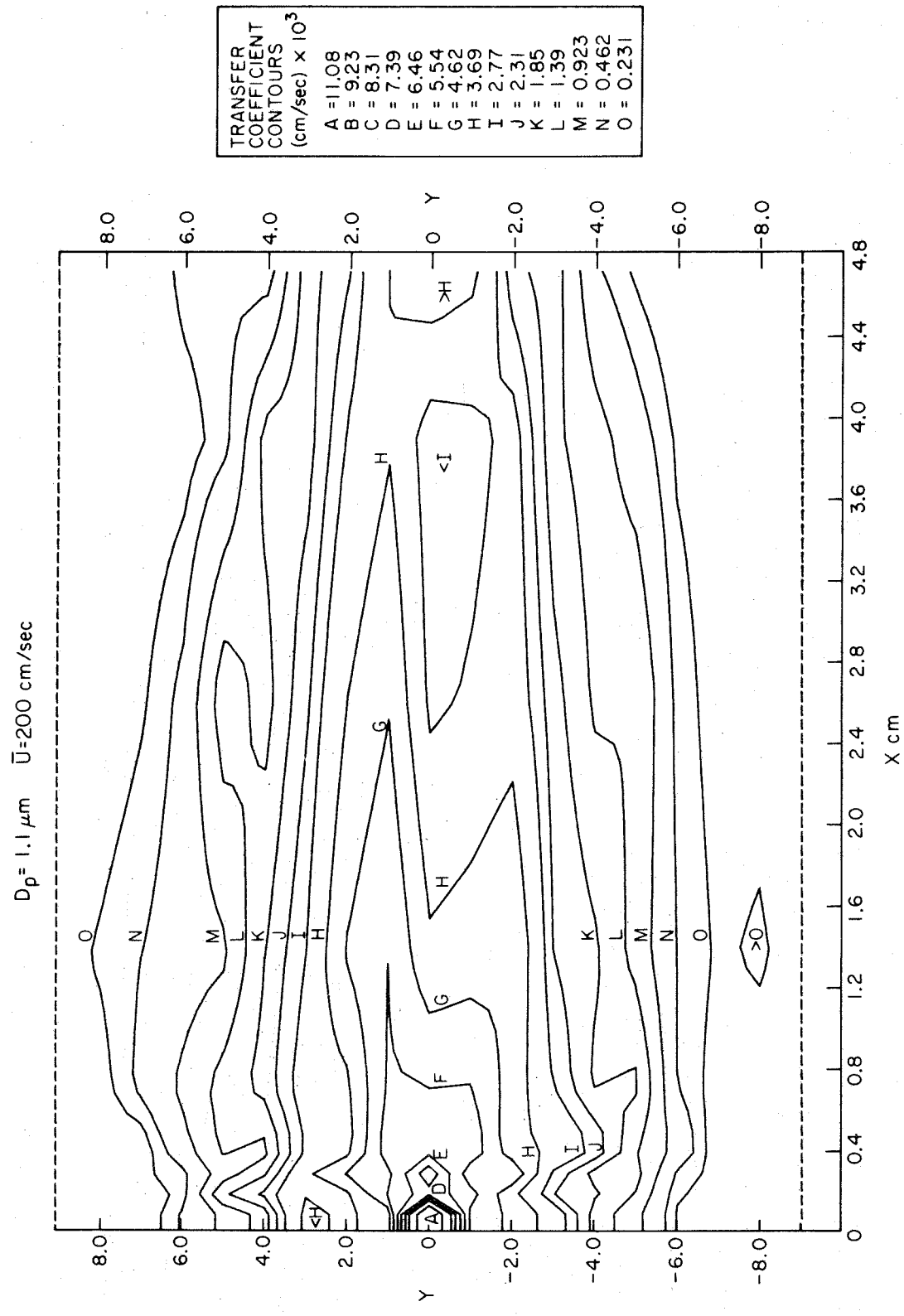

Map 6 3-D Run 25

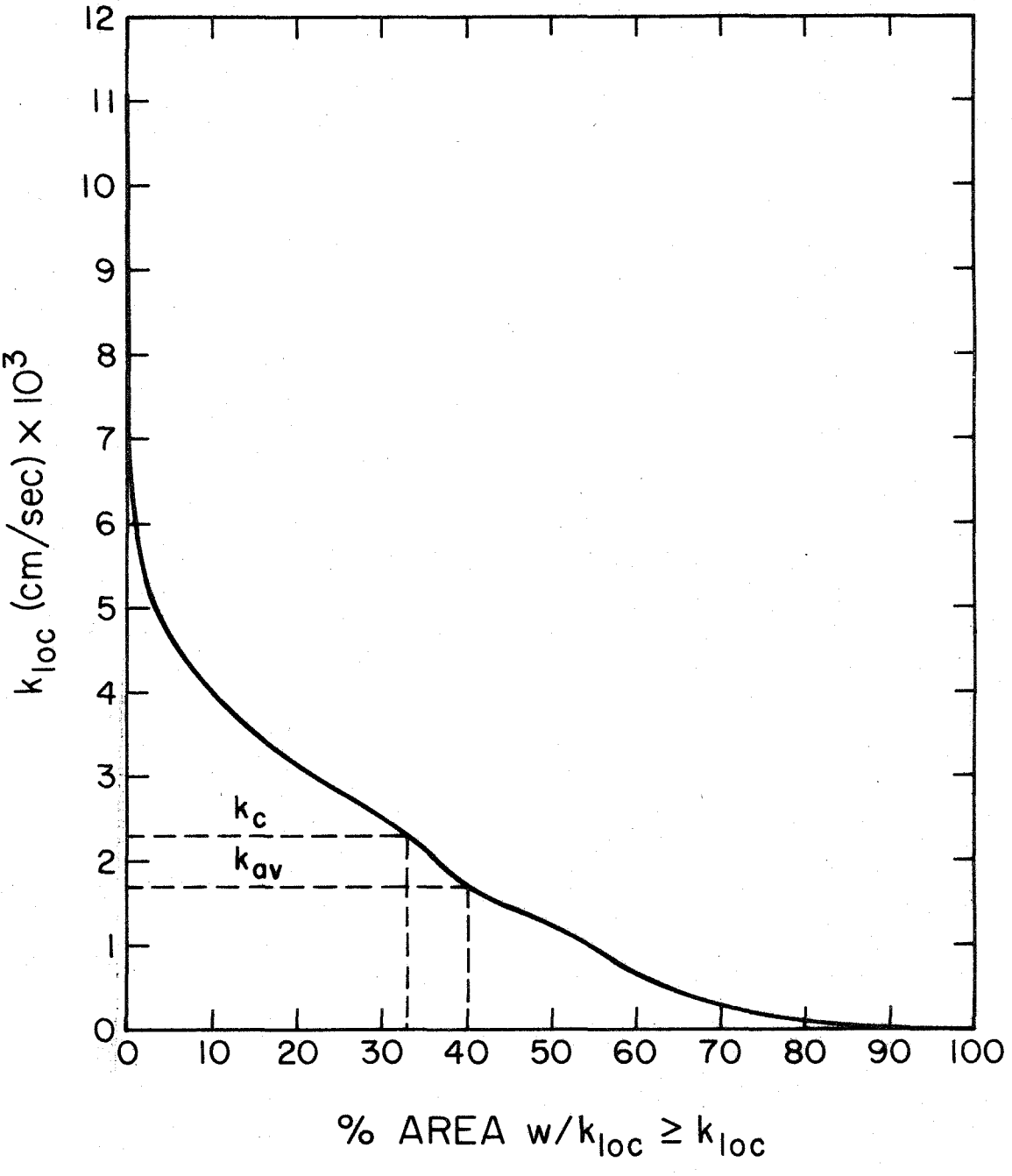

Graph 6 Cumulative Surface Area Distribution for Map 6 Showing the % of the Surface Area of the Daughter Branch with a Local Transfer Coefficient ≥ Stated Value (d_p = 1.1 μm, $\overline{U}$ = 200 cm/sec)

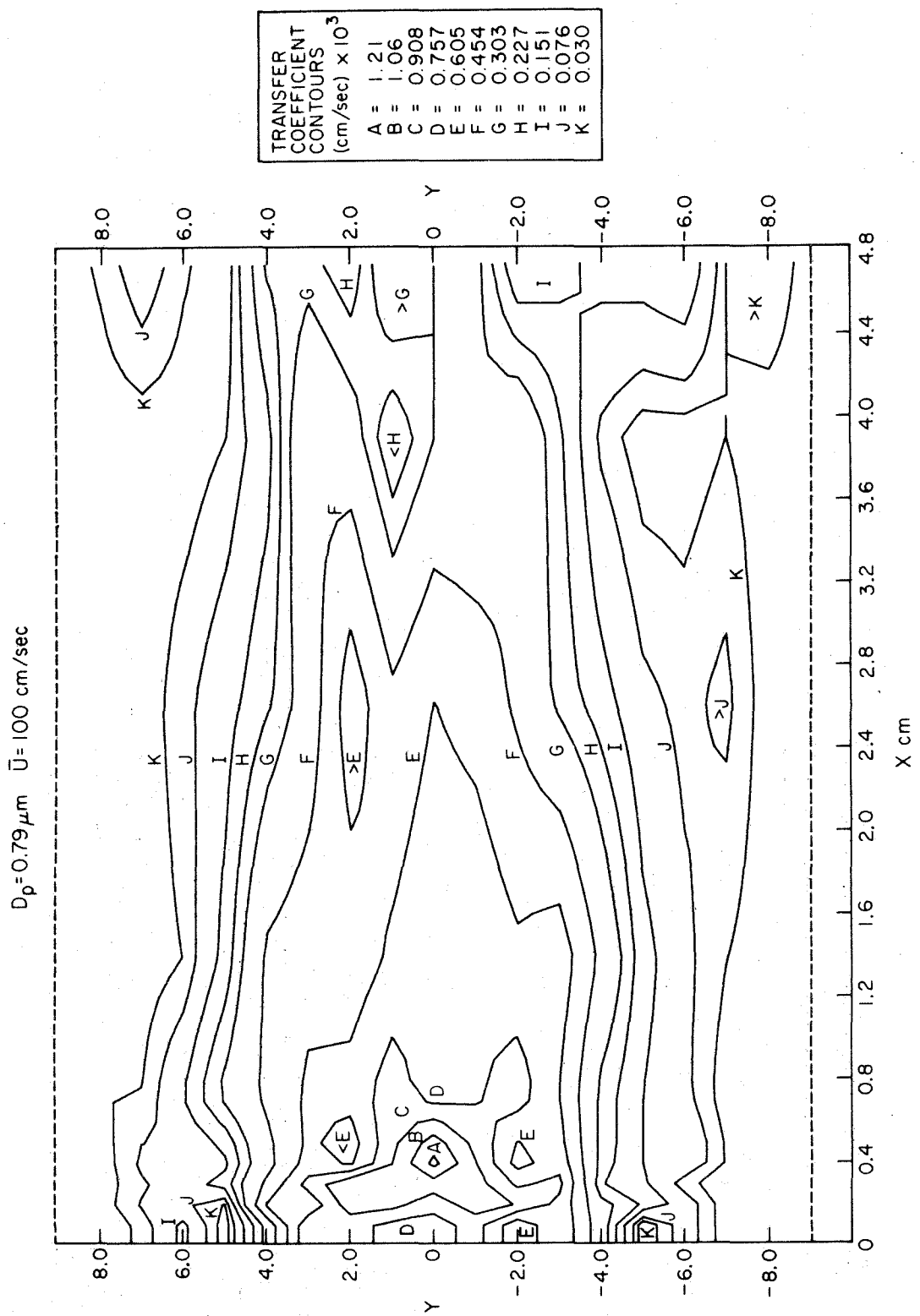

Map 7 3-D Run 13

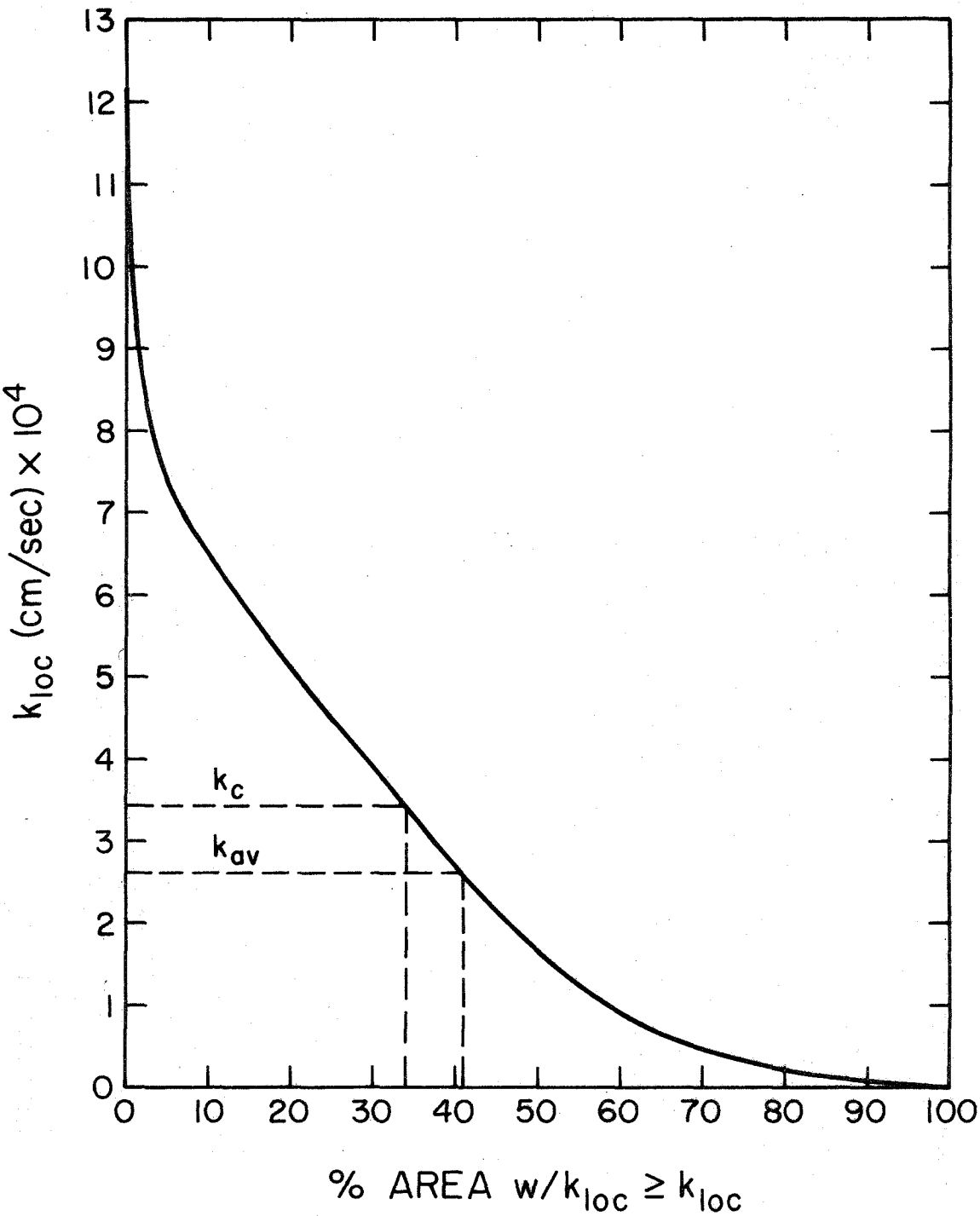

Graph 7 Cumulative Surface Area Distribution for Map 7 Showing the % of the Surface Area of the Daughter Branch with a Local Transfer Coefficient ≥ Stated Value (d_p = 0.79 μm, $\overline{U}$ = 100 cm/sec)

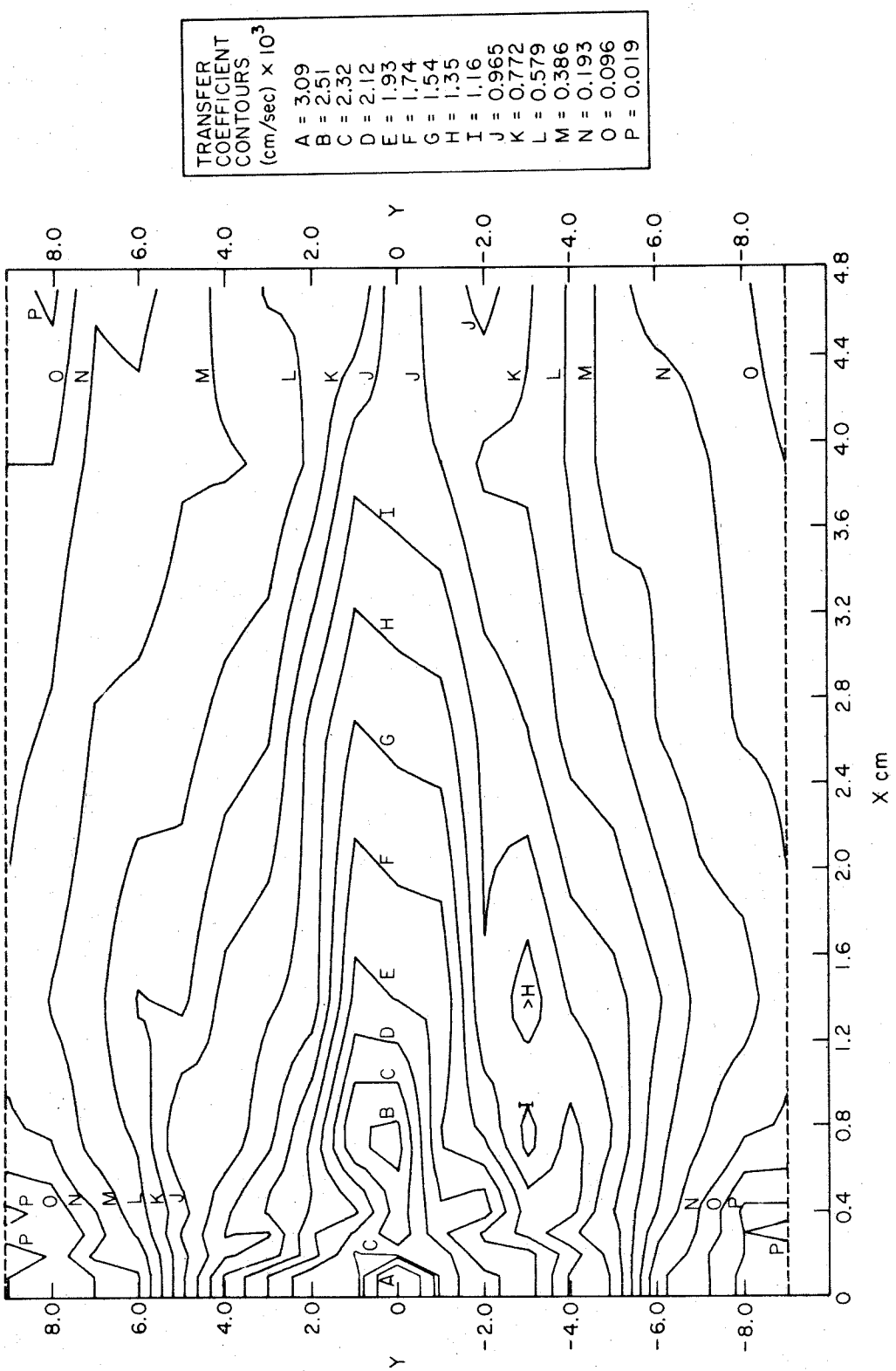

Map 8 3-D Run 26

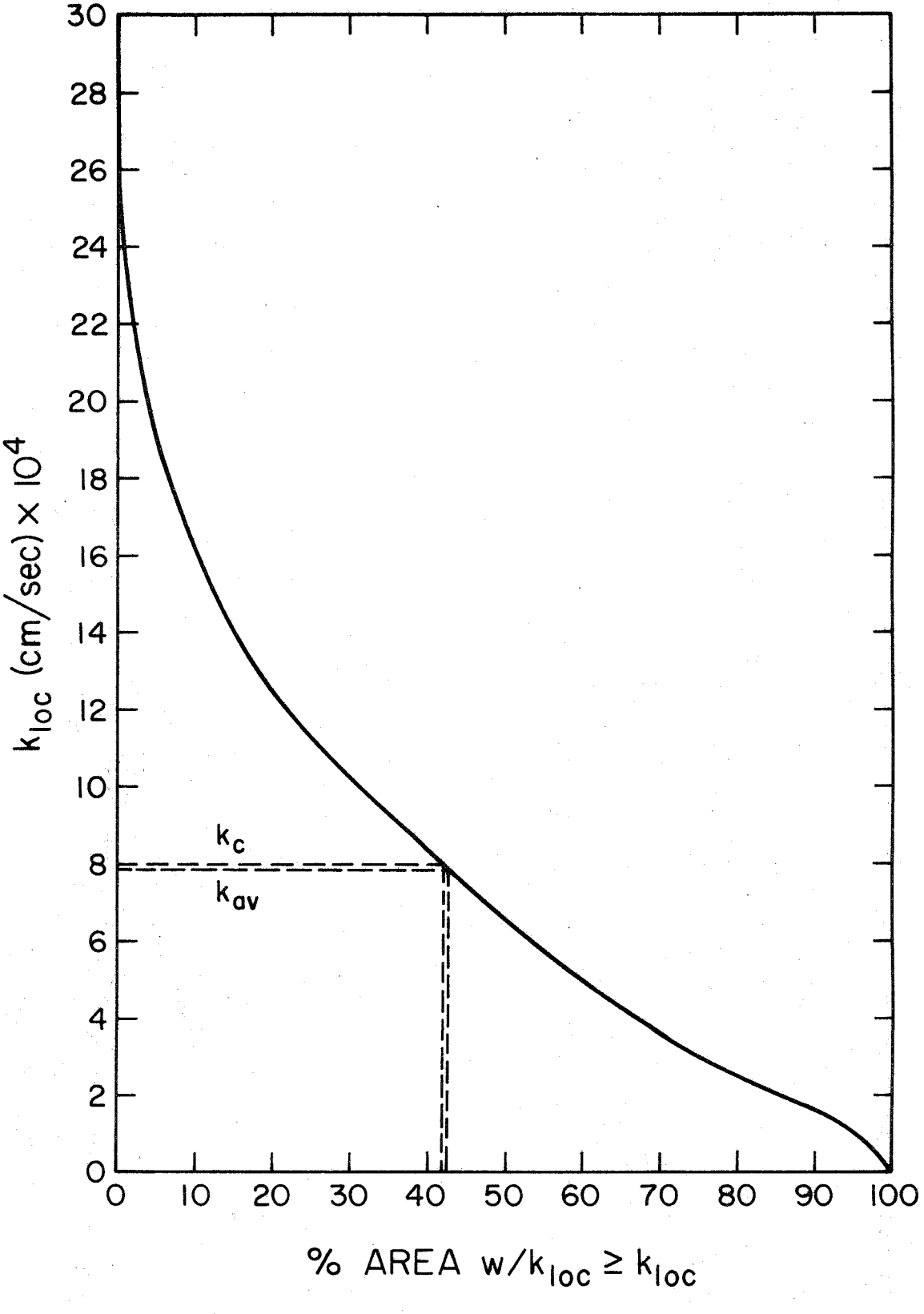

Graph 8 · Cumulative Surface Area Distribution for Map 8 Showing the % of the Surface Area of the Daughter Branch with a Local Transfer Coefficient ≥ Stated Value (d_p = 0.81 μm, $\overline{U}$ = 200 cm/sec)

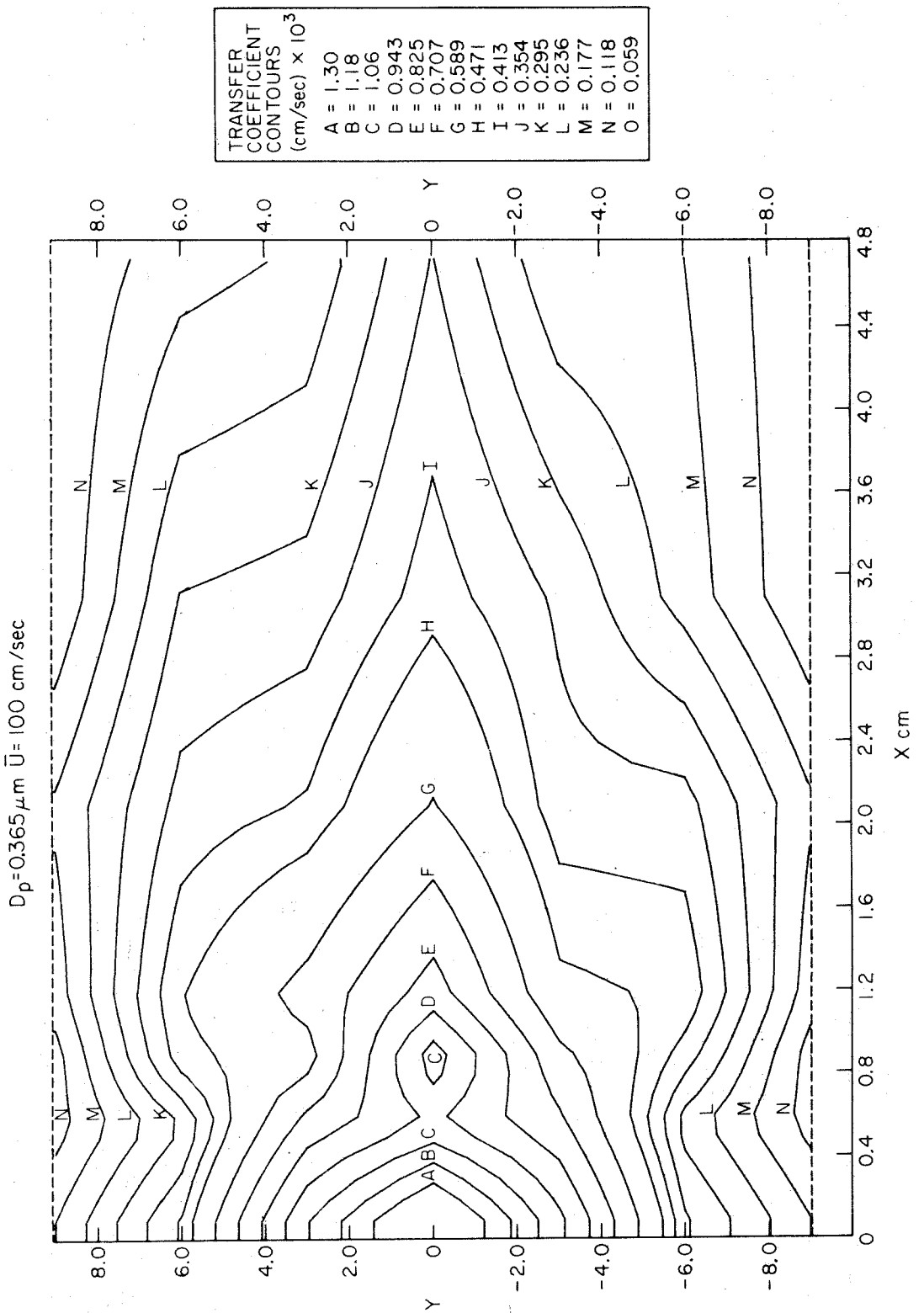

Map 9 3-D Run 28

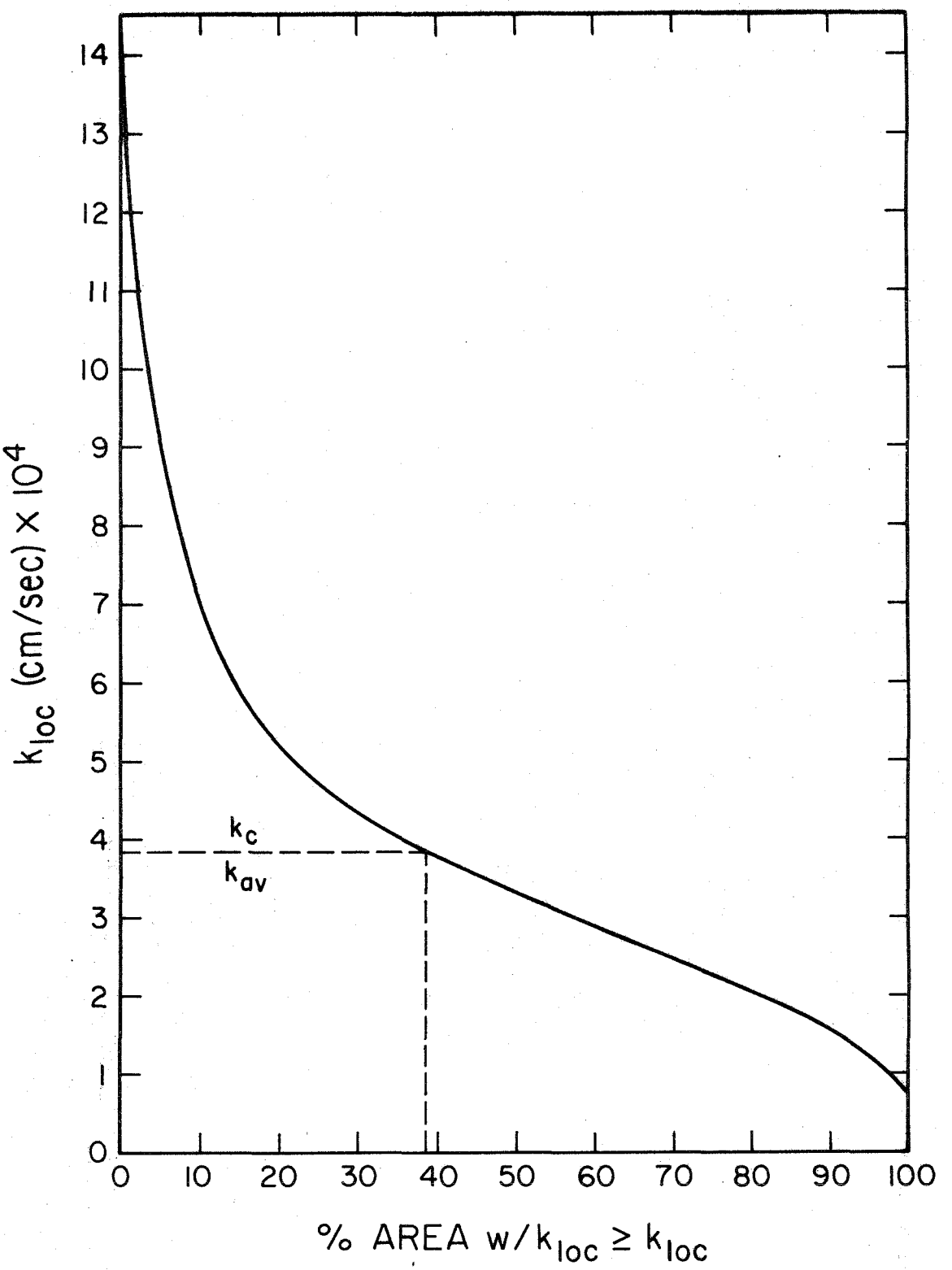

Graph 9 Cumulative Surface Area Distribution for Map 9 Showing the % of the Surface Area of the Daughter Branch with a Local Transfer Coefficient ≥ Stated Value (d_p = 0.365 μm, $\bar{U}$ = 100 cm/sec)

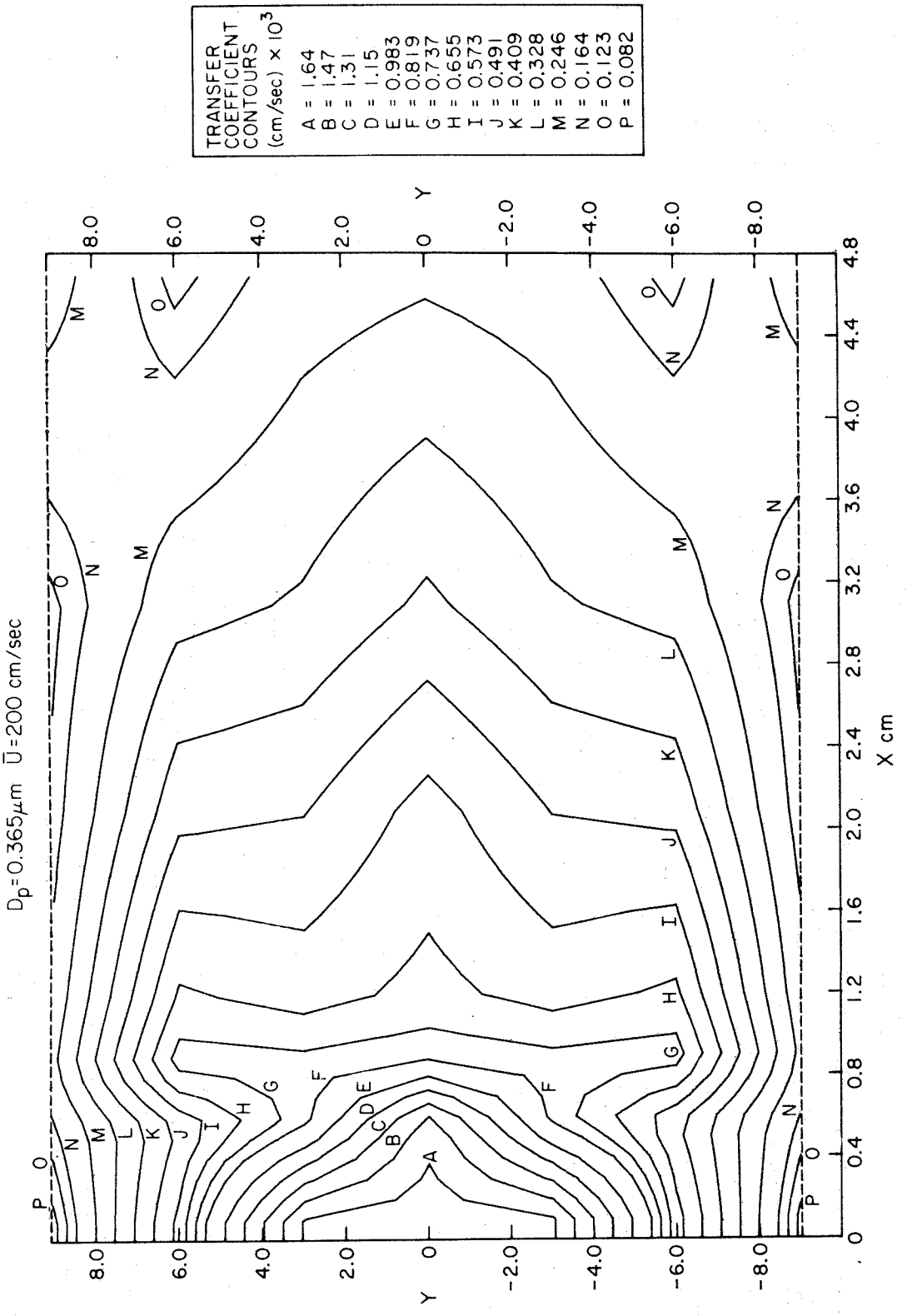

Map 10 3-D Run 32

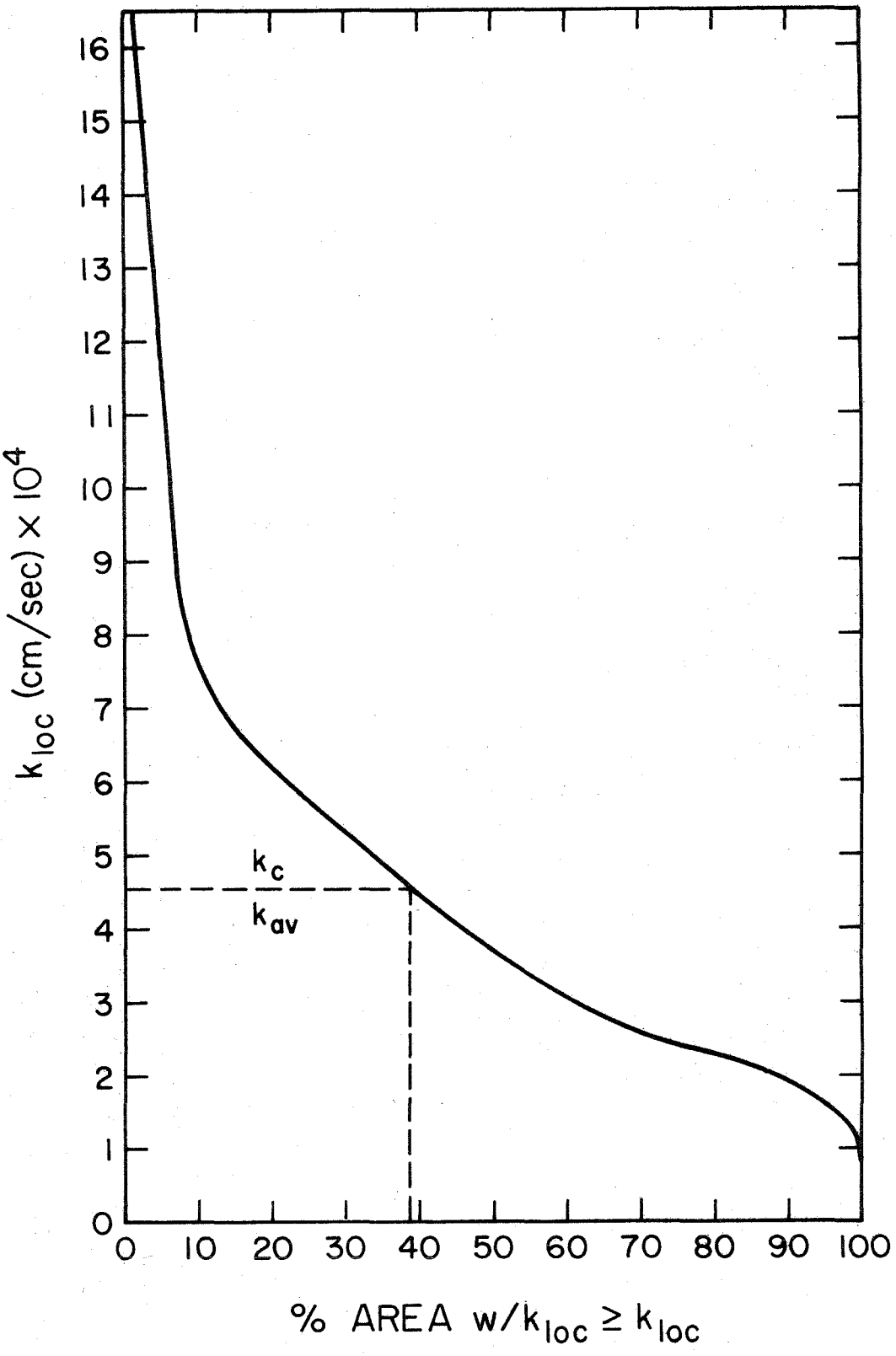

Graph 10 Cumulative Surface Area Distribution for Map 10 Showing the % of the Surface Area of the Daughter Branch with a Local Transfer Coefficient ≥ Stated Value (d_p = 0.365 μm, $\overline{U}$ = 200 cm/sec)

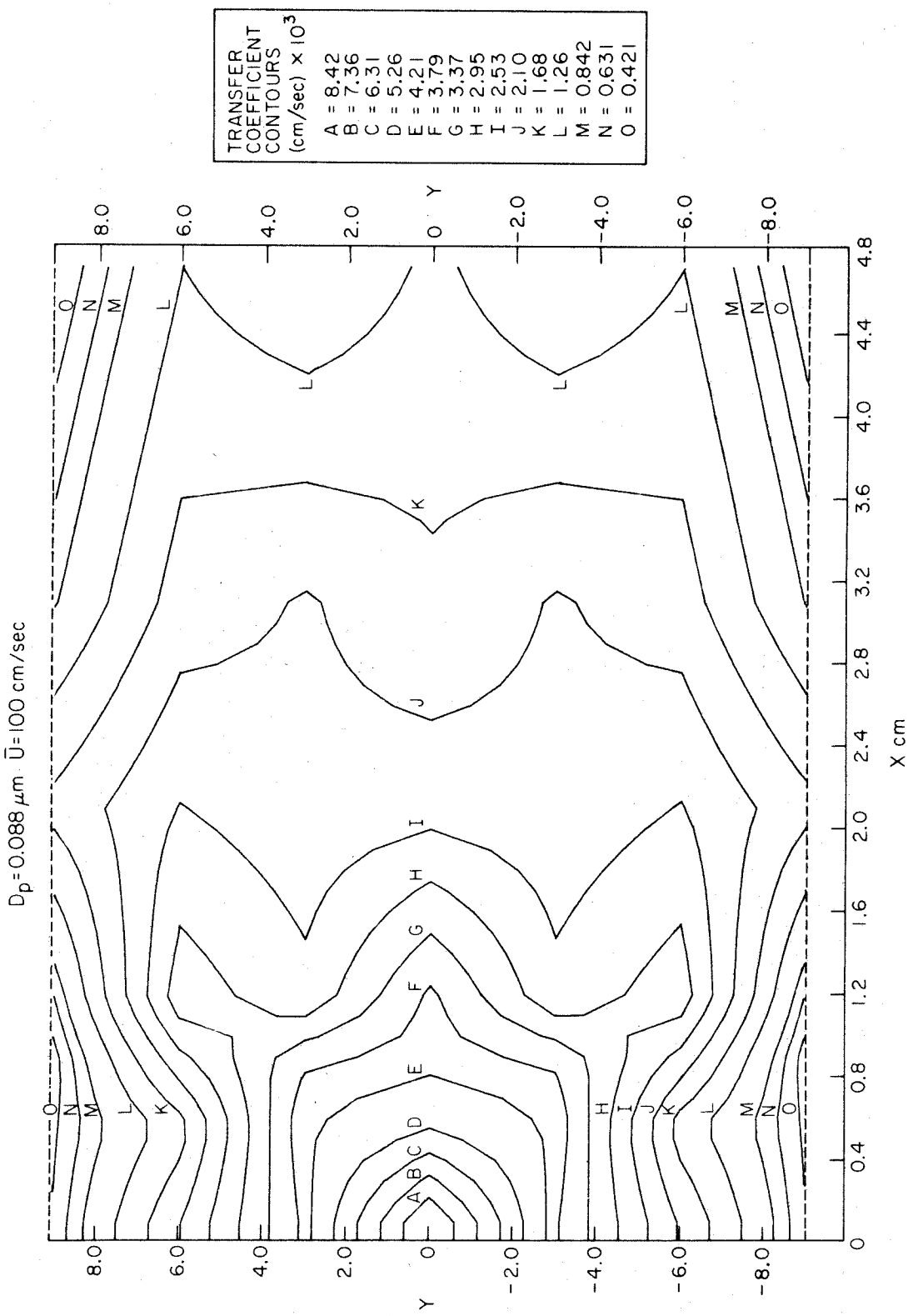

Map 11 3-D Run 31

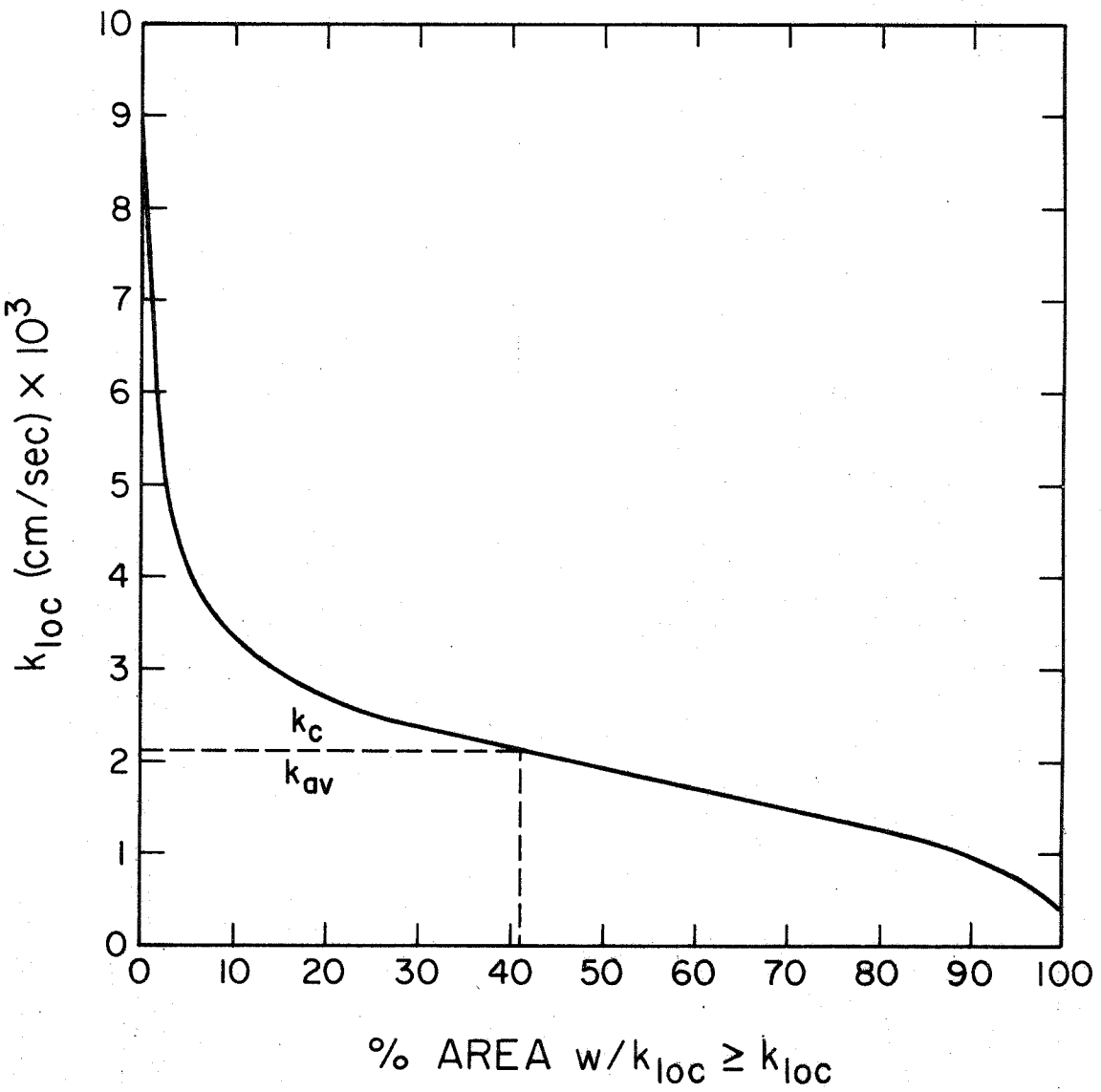

Graph 11 Cumulative Surface Area Distribution for Map 11 Showing the % of the Surface Area of the Daughter Branch with a Local Transfer Coefficient ≥ Stated Value (d_p = 0.088 μm, $\overline{U}$ = 100 cm/sec)

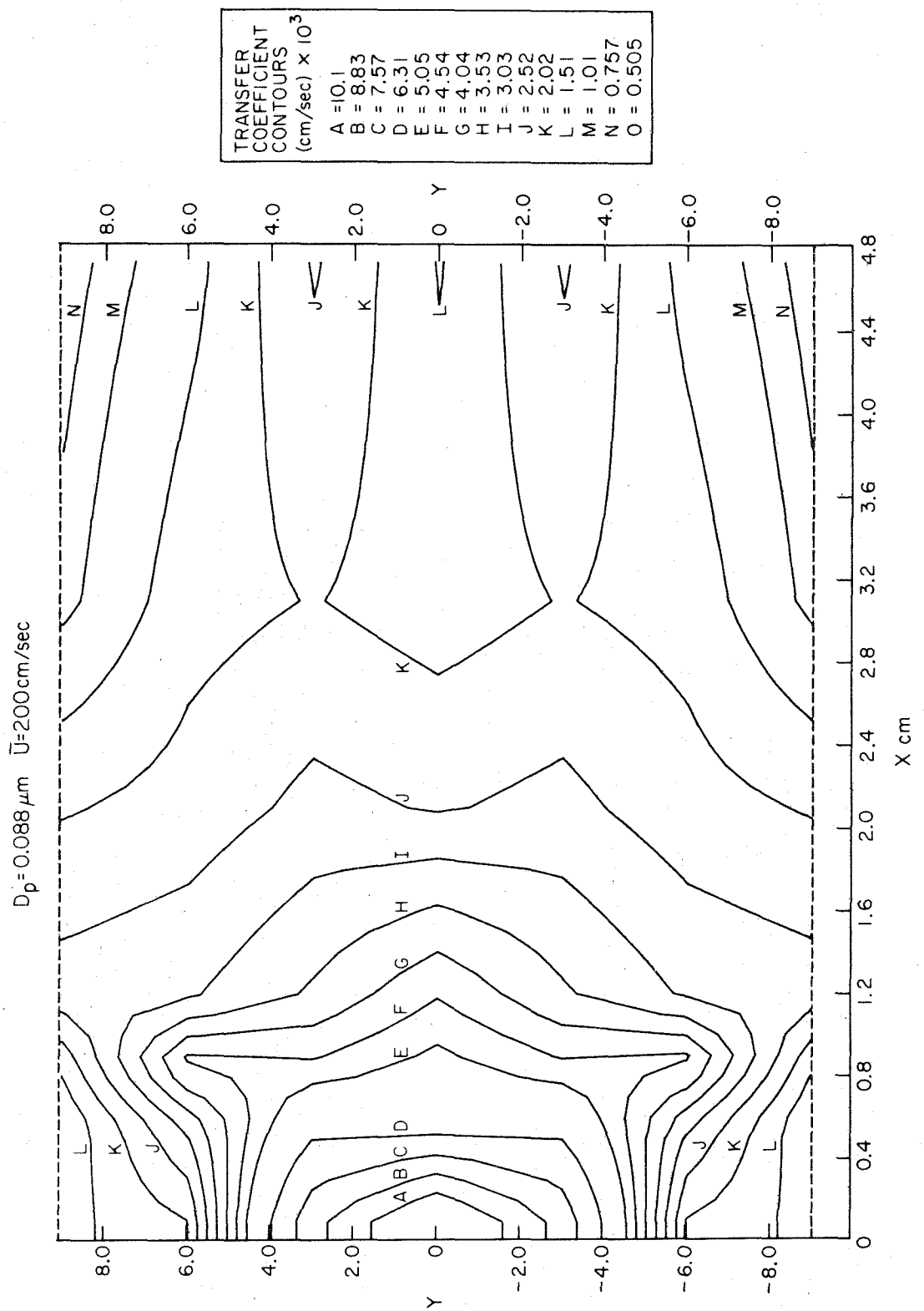

Map 12 3-D Run 33

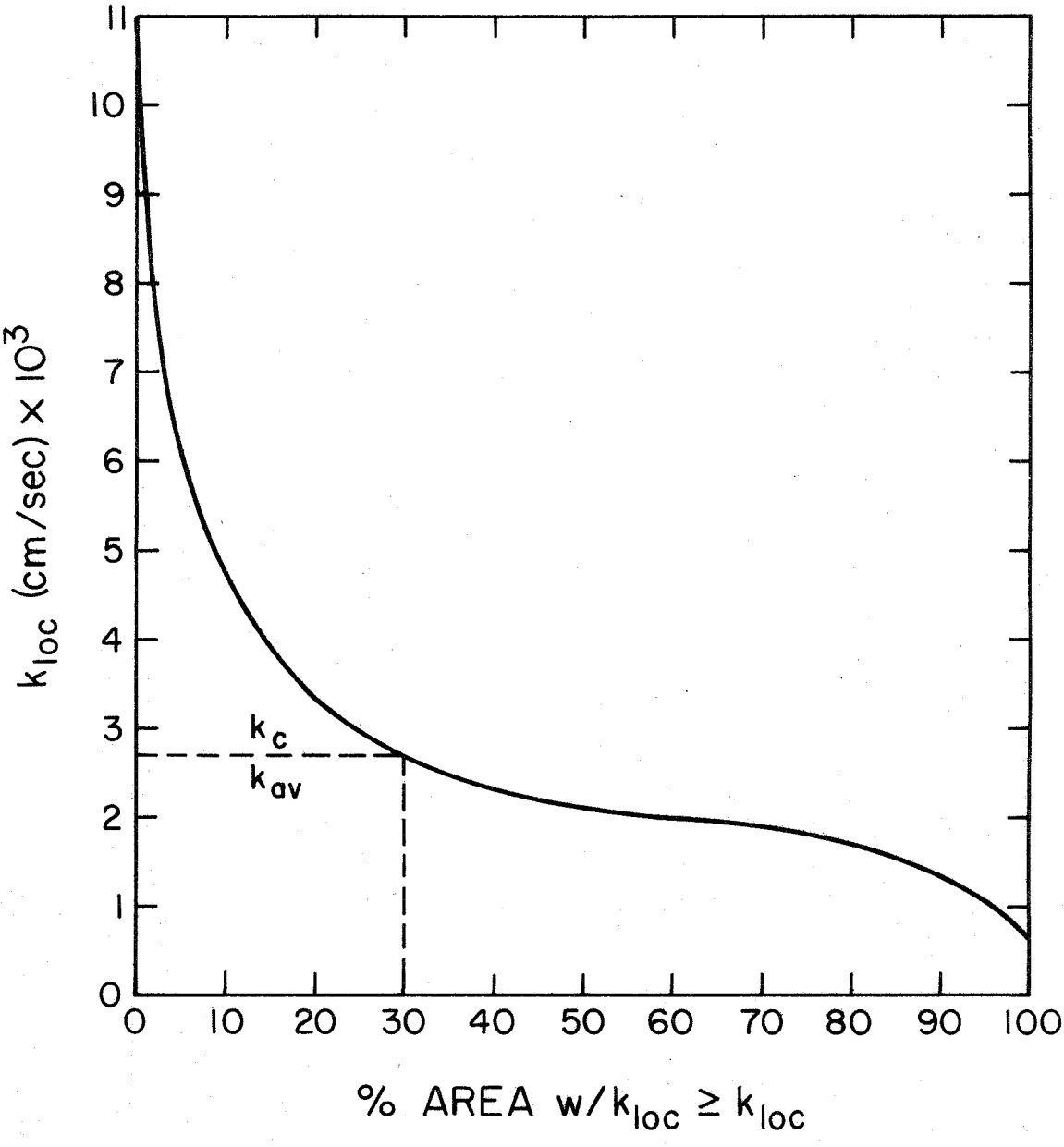

Graph 12 Cumulative Surface Area Distribution for Map 12 Showing the % of the Surface Area of the Daughter Branch with a Local Transfer Coefficient ≥ Stated Value (d_p = 0.088μm, $\overline{U}$ = 200 cm/sec)

6.2 Analysis of the Contour Maps

6.2.1 General Trends for 5.7μm and 2.02μm Contour Maps

Maps 1 - 4 show the deposition trends for large particles which are controlled by impaction, sedimentation and interception. A peak in deposition or "hot spot" occurs along the inner wall (Y = -1 to +1) at the carina in each map. A second peak occurs between 0.4 and 0.8 cm. downstream for 2.02μm particles at $\overline{U}$=100 cm./sec. The 2.02μm particles deposit in a long plateau with a minor peak between 0.4 and 2.6 cm. downstream between Y=±1 when $\overline{U}$=200 cm./sec.; they also form a secondary peak at X=0.8 cm., Y=2.0 in Map 4. Impaction causes the peak at the carina, while secondary flows may be the cause of the peaks between X=0.4 and 0.8 cm.

Beyond the distant peak between Y=±2, k_{loc} decreases along one or two ridges running to the end of the branch. The value of k_{loc} also decreases toward the outside wall for given X because the sedimentation flux decreases from Y=0 to Y=±4.5. Contours parallel to the X axis characterize deposition controlled by sedimentation. Deposition on the outside wall ($|Y|>4.5$) was probably caused by the secondary flows, since no sedimentation can occur on these surfaces with the model in the vertical orientation.

Asymmetric patterns about Y=0 are in part caused by asymmetries in the model geometry. However, the main cause in the 5.7 and 2.02 μm runs was the large statistical error in the small number of particles

counted at each location beyond the carina. The asymmetries in Maps 1 and 3 were minimized by averaging the data from multiple runs.

The cumulative surface area distribution demonstrates the uniformity of deposition. A horizontal distribution curve indicates uniform deposition over the surface, while a narrow, vertical peak demonstrates a strong nonuniformity of "hot spot". For example, Graph 2 shows that k_{av} in Map 2 is 0.0342 cm./sec. and only 32.5% of the area has a $k_{loc} \geq k_{av}$. About 50% of the surface area received no deposition. The peak "hot spot" on Map 2 (area within contour A) has a transfer coefficient more than 48.5 times larger than the integrated average value and its surface area is only 0.13% of the total or 2.4 $mm.^2$ Therefore, the approximately 20,000 epithelial cells within this region in the real lung (Altshuler, et al., 1964: Fig. 3) would receive at least 48.5 times more 5.7μm particles than predicted for uniform deposition.

6.2.2 General Trends for 1.1μm and 0.79μm Contour Maps

Maps 5 - 8 demonstrate the deposition patterns expected for particles in the 0.5 to 1.5μm range. The deposition of particles in this transition range can be influenced simultaneously, but to different degrees, by the mechanisms of inertial impaction, sedimentation, interception and Brownian diffusion.

In some ways the patterns are similar to those for larger particles (Section 6.2.1). Besides the peak at the carina each map has a second or

multiple peaks at X = 0.4 to 0.8 cm. between Y = ± 2.0. The ">" and "≫" shaped contours, demonstrating the ridge of deposition running axially between the Y = ±2.0 strips, are more obvious in these maps than in those for the 5.7 and 2.02 μm particles. The ">" shape is associated with the high axial velocity of the air near the wall in this region. The ">" and "≫" contours are associated with the pair of secondary flows imposed on the axial flow on each side of Y = 0 (Figure 3.2, Sections 1.3.2, 3.2.2, and 4.3).

In contrast to the large particles, a significant number of 1.1 and 0.79 μm particles deposit on the outside wall, and the deposition in the 200 cm./sec. runs terminated at larger Y locations than in the 100 cm./sec. runs. Contours beyond the Y = ± 2.0 region are not parallel to the X axis, like the contours for large particles, but are convex toward Y = ± 9.

Map 8 demonstrates best the expanding region of deposition for particles in this subrange. In this case the expansion proceeds outward in a diagonal direction from Y = 0, X = 0.4 - 0.8 cm. to Y = ±9, X = 0.9 - 2.0 cm. Because they can be carried farther by the helical flow before depositing, small particles have a wider deposition pattern than the large particles.

6.2.3 General Trends for 0.365 μm and 0.088 μm Contour Maps

Maps 9 - 12 demonstrate the deposition patterns for small particles

controlled by convective diffusion. Maps 10, 11, and 12 are perfectly symmetrical since strips Y = -3, and -6 were not counted. Instead, the data for Y = +3, and +6 were used. Because Map 9, in which all the grids were counted, is nearly symmetrical, this shortened the counting time with no loss of accuracy.

The peak of deposition at the carina in each map is much broader and the slope of each peak is less steep than observed in the maps of the transition and impaction subranges. A second peak is observed only for the low velocity, 0.365μm run.

Studying Maps 9 through 12 in that order shows that the strong ">" patterns in Map 9 gradually become more blunted and wider and approach straight, vertical lines in some regions of the maps. Straight, vertical contours with decreasing k_{loc} in the +X direction characterize convective diffusion downstream from the entrance to a straight tube (Levich, 1962: 112-115; Gormley and Kennedy, 1949).

In Maps 9 and 11 lobular patterns or ridges of deposition are observed from Y = 0, X = 0.4 - 0.8 cm. diagonally to Y = ± 9, X = 2.1 cm. The two ridges are more intense in Map 11 than in Map 9. In other words, the elevation of each ridge in Map 11 above the surrounding low lands is greater than in Map 9, and the crest of the ridge in Map 11 decreases in elevation less rapidly toward Y = ± 9, X = 2.1 cm. than in Map 9. In Maps 10 and 12 the ridges run diagonally from Y = 0, X = 0.4 - 0.8 cm. to Y = ± 9, X = 1.2 cm., and they are more intense for the 0.088

than the 0.365μm run. These patterns are dramatic evidence of the effect of the secondary flows which is analyzed in detail in Section 6.5. Lobular patterns can be observed in nearly all the maps in the same location; however, they become more obvious and extend farther toward the outside wall as particle size is decreased and as velocity is increased.

The cumulative surface area distributions demonstrate the sharp peaks at the carina caused by convective diffusion. They also demonstrate that the deposition covers the entire surface, but is more uniform beyond the carina for the 0.088 than for the 0.365μm particles.

Graph 12 shows that k_{av} is 0.0027 cm./sec. and that 30% of the surface area received deposition greater than or equal to the average. The peak "hot spot" on Map 12 (area within Contour A) has a transfer coefficient 3.74 times larger than k_{av}, and its surface area is only 0.61% of the total or 11.2 $mm.^2$ Accordingly, the approximately 150,000 epithelial cells in this area at the surface of a human lung receive at least 3.74 times more 0.088μm particles than predicted from uniform deposition.

6.2.4 Comparison of k_{av}, "Hot Spot" Intensity, and the Uniformity of Deposition

Figure 6.1 compares the integrated average transfer coefficient from the contour maps according to the particle diameter and the time-average flow rate. The 100 and 200 cm./sec. sets of data have the

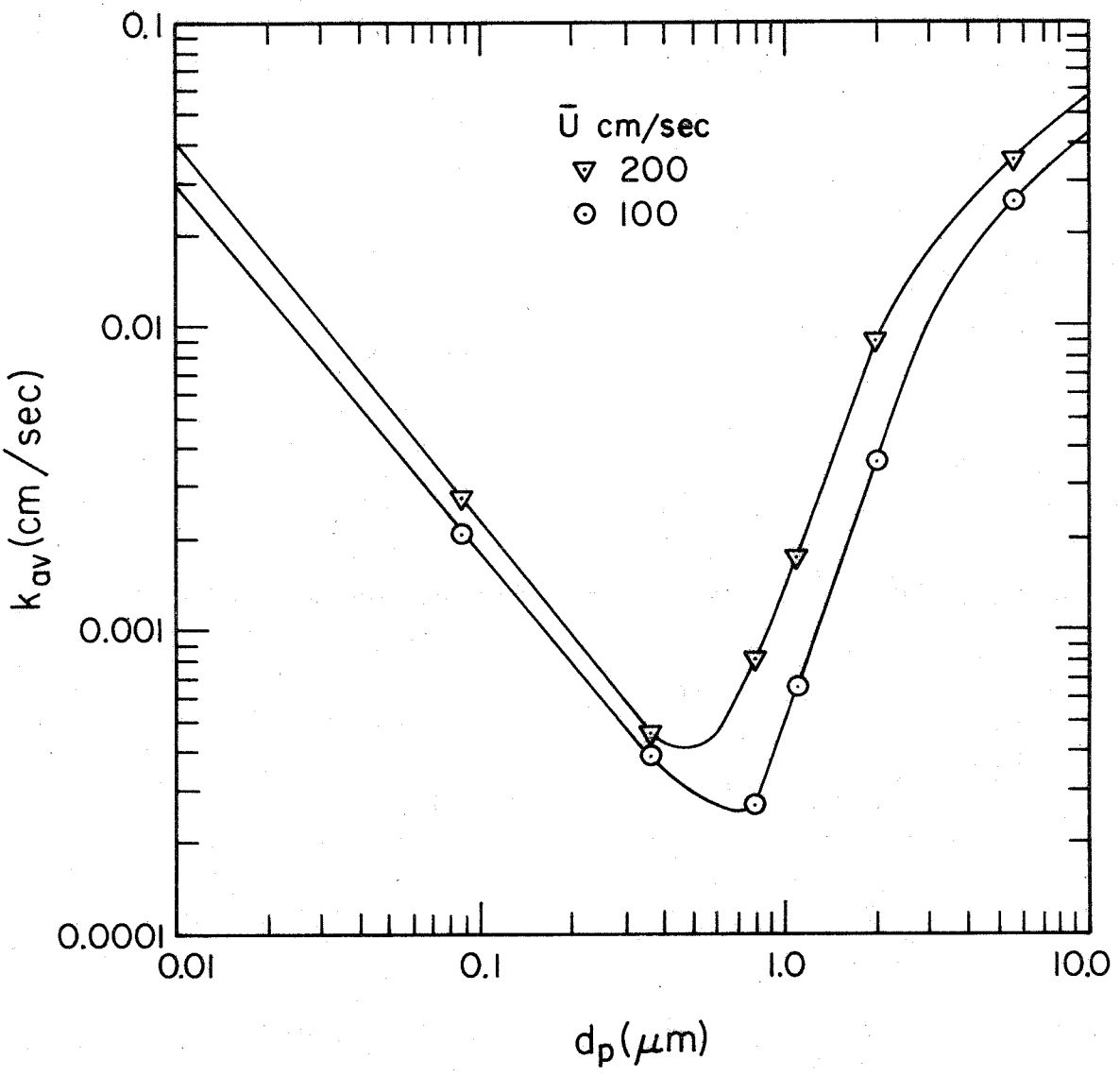

Figure 6.1 Comparison of the Integrated Average Transfer Coefficients from Maps 1-12

characteristic "V" shape observed in Figure 5.1 for the "2-D" model. Likewise, the minimum k_{loc} for the 100 cm./sec. set occurs at the same location as in Figure 5.1--between 0.5 and 1μm.

The minimum in the 200 cm./sec. set of data shifted to smaller particles--between 0.35 and 0.7μm diameter. The relatively small increase of k_{av} for the 0.365 and 0.088μm particles when the velocity increased from 100 cm./sec. to 200 cm./sec. is consistent with the theory of convective diffusion (Equation 3.8) which predicts k_{av} to increase as $U^{\frac{1}{2}}$. The larger increases of the 0.79-2.02μm particles are partially predicted from the theory of simultaneous deposition by impaction, interception, and sedimentation (Section 2.3.4). The additional enhancement of 1.1 and 0.79μm particles compared to the 2.02μm is associated with the increased deposition of the 1.1 and 0.79 μm particles on the outside wall at the higher velocity.

Figure 6.2 demonstrates the variation of the intensity of the "hot spot" effect with particle size. The parameter $\overline{k}_{0.6\%Area}/k_{av}$ was chosen as an indicator of the "hot spot" intensity. $\overline{k}_{0.6\%Area}$ is the average value of k_{loc} over 0.6% of the area having the greatest transfer coefficients on each map. k_{loc} at 0% of the area and between contours was estimated by linear extrapolation and interpolation. 0.6% of the area corresponds to roughly 150,000 epithelial cells.

The plot shows that the "hot spot" intensity varied from a high of 25.4 for the 5.7μm, 200 cm./sec. run to a low of 3.35 for the 1.1μm,

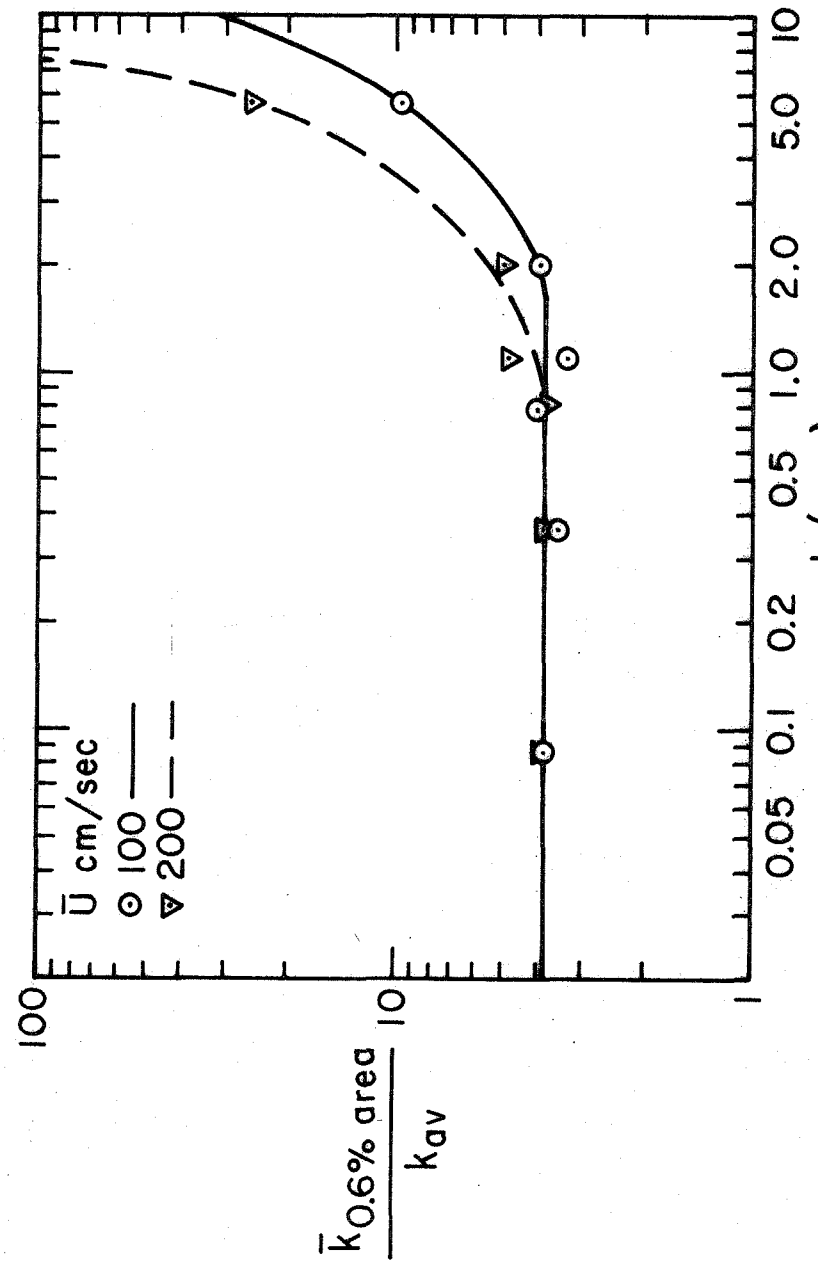

Figure 6.2 Comparison of the "Hot Spot" Intensities from Maps 1 - 12

100 cm./sec. run. The intensity is greatest for particles in the impaction and sedimentation subrange and increases rapidly with particle size. The intensity is also greater at the higher velocity for particles with $d_p > 1.0 \mu m$. Particles in the diffusion subrange have the lowest intensity (~3.8) which is essentially constant and independent of velocity.

Figures 6.3, 6.4, and 6.5 show other ways of analyzing the nonuniformity of the deposition. In Figure 6.3 the percentage of the surface area of the contour maps having $k_{loc} \leq k_{av}/10$ is compared for Maps 1 - 12. The data were obtained from Graphs 1 - 12.

The fraction of the surface receiving essentially no deposition decreases smoothly from a maximum of 49% for the 5.7μm particles to 0% for the 0.365 and 0.088μm particles. The 0.79 and 1.1μm particles covered more surface than the 2.02 and 5.7μm particles because trajectories of particles in the transition subrange deviate less from the flow streamlines. Consequently, they have a greater probability of flowing along the outside wall where they can deposit by interception and convective diffusion.

The 0.79 and 1.1μm particles covered more of the surface at 200 cm./sec. than at 100 cm./sec. because the secondary flows were more intense at the higher velocity. In other words, particle-laden air replaced the clean air along the outside wall more rapidly at the higher velocity. Also, local shear rates along the outside wall increased substantially at the higher velocity, causing increased deposition by

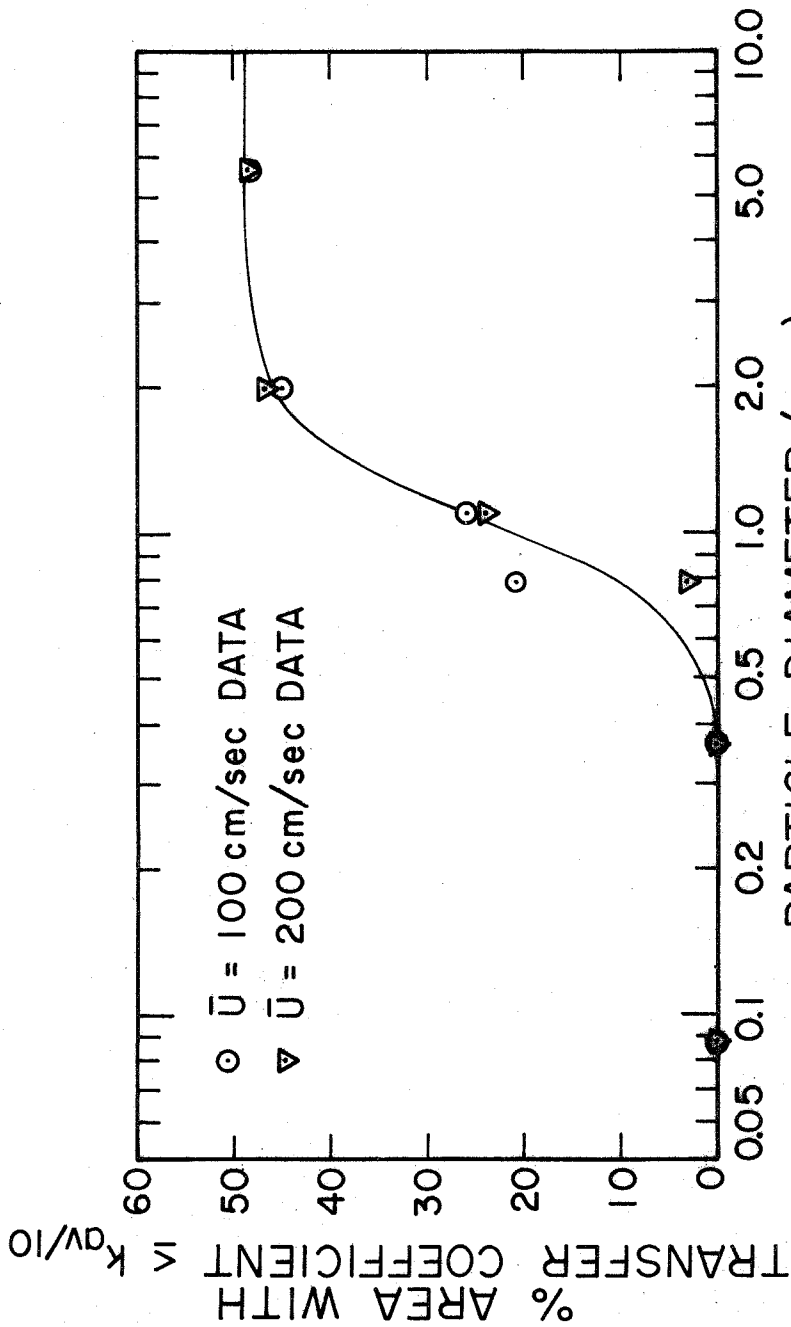

Figure 6.3 Percentage of the Surface Area Receiving Essentially No Deposition in Maps 1-12

interception and convective diffusion. The increase in the surface coverage as $\overline{U}$ increased from 100 to 200 cm./sec. was greater for the 0.79μm than for the 1.1μm. The 0.79μm particles, having a smaller relaxation time, are more effectively entrained by the helical flow and can be carried farther along the outside wall before depositing.

The surface area receiving no deposition increased slightly for the 2.02 and 5.7μm particles when the velocity increased from 100 to 200 cm./sec. Increasing axial velocity tends to localize deposition by impaction and sedimentation. This effect outweighed increases in the intensity of the secondary motions which tend to cause deposition by interception and impaction on the outside walls. The lower values and the larger increase from 100 to 200 cm./sec. for the 2.02 than for the 5.7μm particles are expected because 2.02μm particles are more effectively entrained by the helical flows.

In Figure 6.4 the percentage of the surface area with $k_{loc} \geq k_{av}$ is compared for Maps 1 - 12. The percentage for each Map is also shown by the dashed line labeled k_{av} on its corresponding Graph. A larger percentage in Figure 6.4 indicates a greater uniformity of deposition. The 0.79 and 1.1μm particles have the most uniformity while the 0.088 and 5.7μm particles at 200 cm./sec. have the least. In all cases, except for the 0.79 and 0.365μm particles, the uniformity is greater at 100 cm./sec. than at 200 cm./sec.

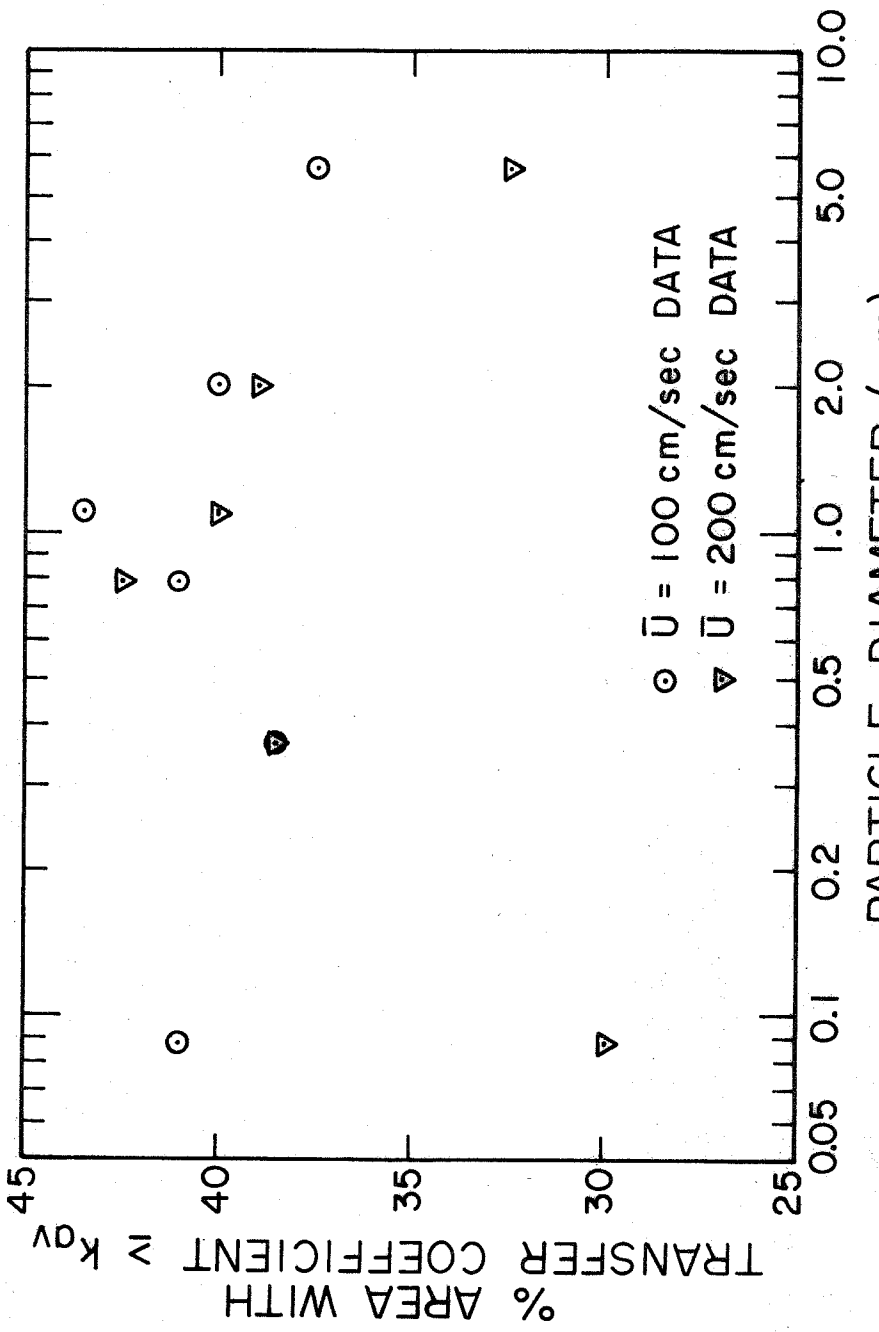

Figure 6.4 Percentage of the Surface Area Receiving More Than the Average Amount of Deposition in Each of Maps 1-12. A Larger Percentage Means More Uniform Deposition.

In Figure 6.5 the percentage of the surface area with a $k_{loc} \geq k_c$ is compared for Maps 1 - 12. The percentage for each map is also shown by the dashed line labeled k_c on its corresponding Graph. Larger percentages in Figure 6.5 indicate a greater uniformity of deposition within the area of each map in which particles are actually collected (the area receiving deposition is approximately equal to 100% minus the corresponding ordinate value in Figure 6.3). The 5.7μm particles have the least uniformity at both flow rates, and there is no flow dependent trend for the smaller particles. However, the most and similar uniformity generally occurred for 1.1, 0.79 and 0.365μm particles at either flow rate and for 0.088μm at 100 cm./sec.

Results from Figures 6.1 through 6.5 have application to inhalation therapy with medical aerosols, and to the diagnosis of lung diseases by X-ray opaque or radioactively tagged aerosols. To deliver an aerosol to the human airways which will completely cover the walls in the most uniform manner, unit density particles with diameters ≤ 0.5μm should be inhaled at low rates. Particles between 0.5 - 1.0μm can be inhaled at any flow rate for a highly uniform coating over more than 75% of the airway surface. To obtain the most nonuniform coating with the least surface coverage in the upper airways, unit density particles ≥ 5μm in diameter should be inhaled rapidly, as by panting. This will also assure a maximum accumulation at the carina of each bifurcation.

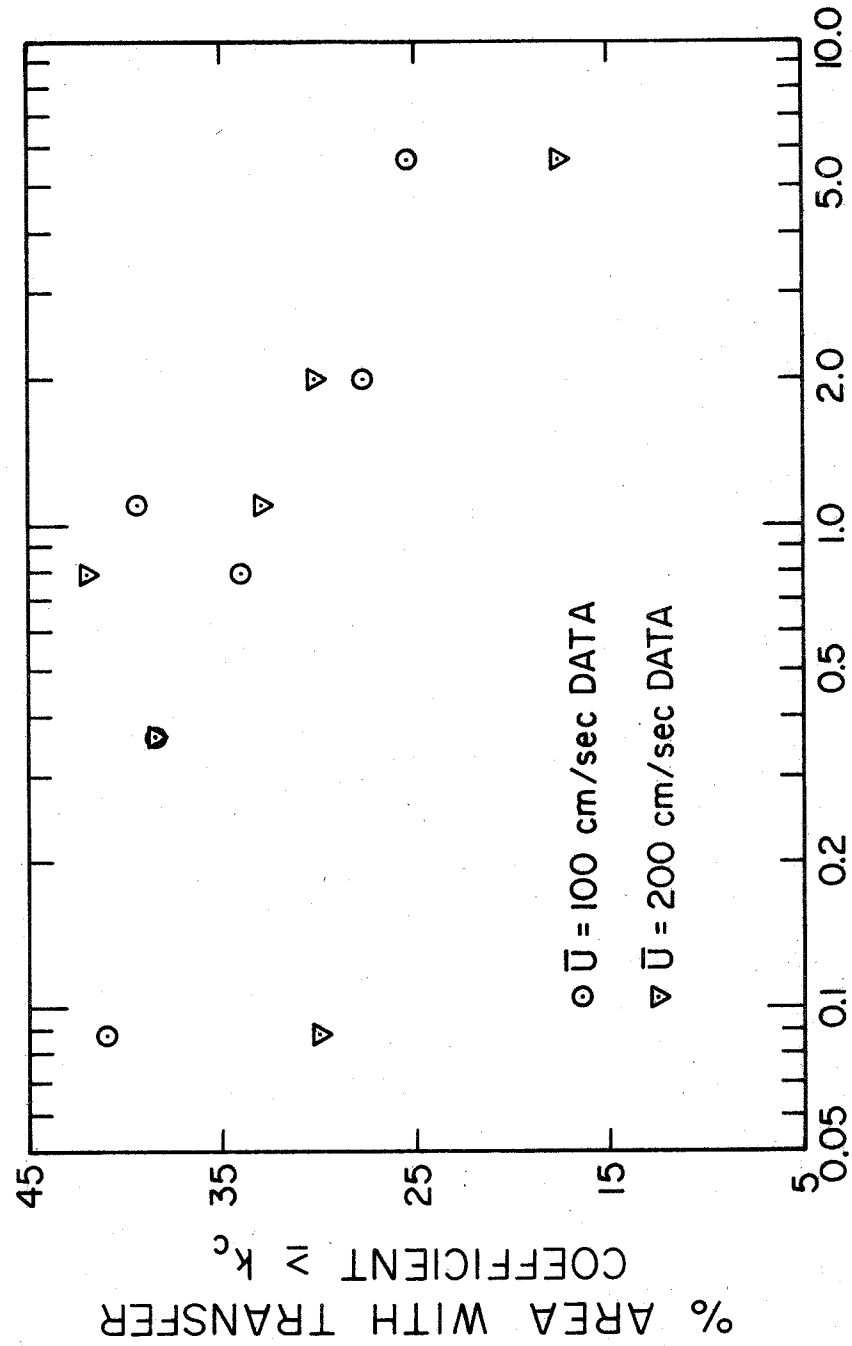

Figure 6.5 The Relative Uniformity of Particle Deposition within the Area of Each Map in which Particles are Actually Collected. Data from Maps 1-12.

6.3 Comparison of Experiment and Theory

6.3.1 5.7μm Particles

In Plots 1 and 2, the theory of deposition by inertial impaction and sedimentation of finite diameter particles (ISI theory; Section 2.3.4) and the theory of sedimentation (S theory; Section 2.3.2) are compared with data for 5.7μm particles. The transfer coefficients were measured along the Y=0 strip in the "3-D" model during 1.88 and 0.94 second inhalations respectively in Plots 1 and 2. $A=A_3S_1/S_3=1.14$ cm.$^{-7/29}$ was used in the numerical calculations in keeping with the "3-D" modification to the "2-D" theory in Equations 3.1, 3.2, and 3.3. A = 1.14 also agrees with the experimental flow conditions in the model. ISI theory does not coincide with the S theory at large X because the interception effect is not included in the S theory.

The data in Plot 1 agree well with ISI theory from X=0 to X=1.3 cm. The last three data points agree with the S theory because the unsteady boundary layers inhibit the interception expected from potential flow (Section 2.3, 5.1). Data in Plot 2 have greater scatter around the ISI theory than in Plot 1. Much of the scatter can be explained by statistical counting errors (Section C.2).

The 5.7μm particles had $\sqrt{\overline{d_p^2}}$ = 6.32μm (Table B.1); therefore if the boundary layer did not inhibit the deposition, data in Plots 1 and 2 should be greater in value than the ISI theory. Likewise, the

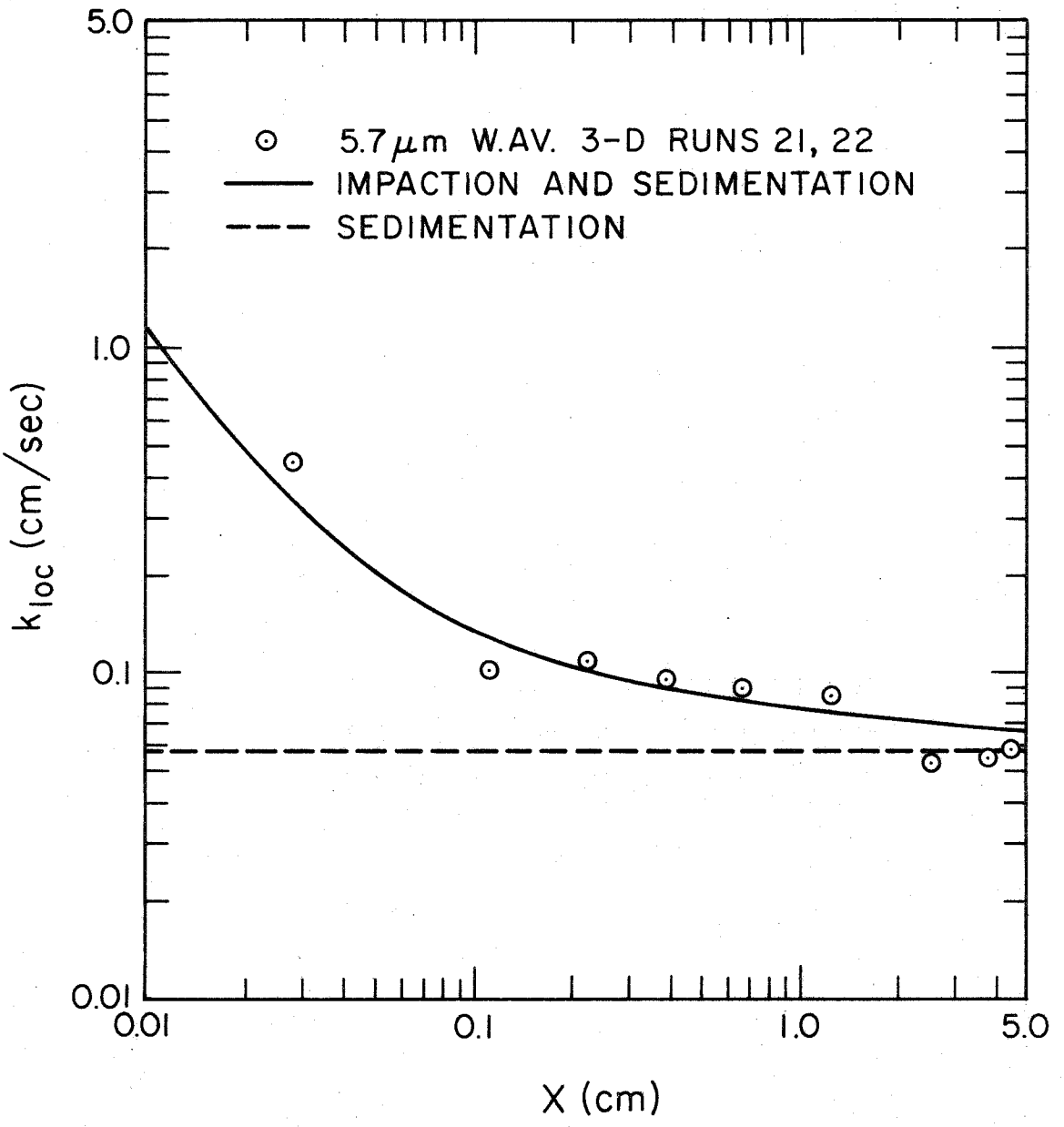

Plot 1 Comparison of Theories for 5.7 μm Particles Depositing on a Vertical 70° Wedge with Transfer Coefficients Measured Along Y=0 in the 3-D Model for 450 cc, 1.88 sec Inhalations. Impaction and Sedimentation Theory(w/ Interception) and Sedimentation Theory (w/o Interception) Use Steady Potential Flow with U=100 cm/sec and A=1.14.

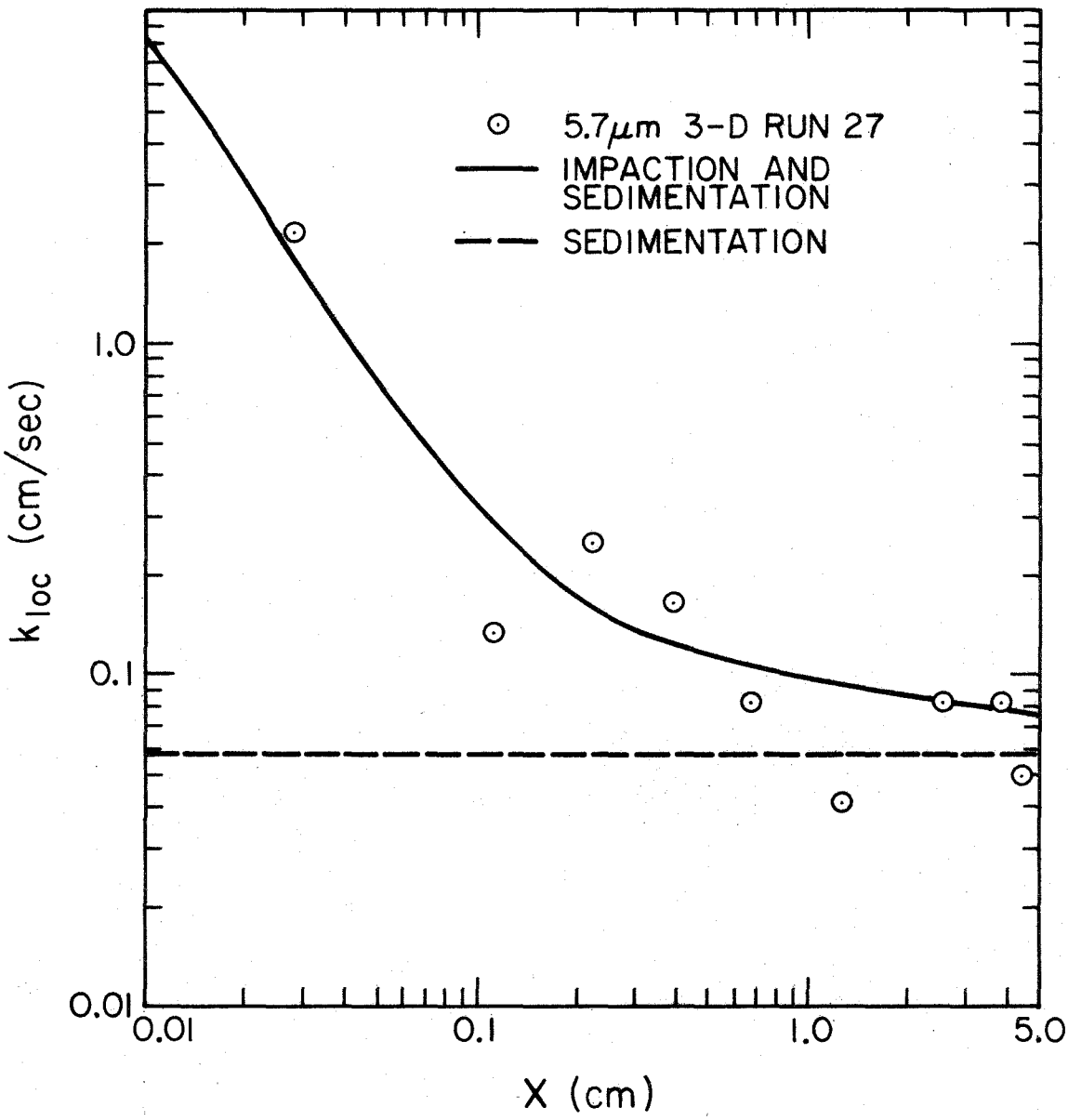

Plot 2 Comparison of Theories for 5.7 μm Particles Depositing on a Vertical 70° Wedge with Transfer Coefficients Measured Along Y=0 in the 3-D Model for 450 cc, 0.94 sec Inhalations. Impaction and Sedimentation Theory(w/ Interception) and Sedimentation Theory(w/o Interception) Use Steady Potential Flow with U=200 cm/sec and A=1.14.

200 cm./sec. data should deviate further from the theory than the 100 cm./sec. data. Some of the points in both plots agree with these predictions.

The highest axial velocity occurred along the Y=0 strip and caused the " > " shaped contours or deposition ridge in Maps 1 and 2. A declining ridge from X=0 to the end of the branch is predicted from ISI theory; however, if the theory had accounted for this higher axial velocity, data in Plots 1 and 2 would have been lower in value than the theory.

The momentum transferred to the 70° wedge of the "3-D" model was calculated for 5.7μm particles at U=200 cm./sec. They impacted at a maximum velocity of 50 cm./sec. when the trajectory coincided with the stagnation streamline; therefore, the maximum amount of momentum transferred was only 7.64×10^{-8} dyne-sec.

In conclusion, 5.7μm particles deposited along the Y=0 strip between the carina and X=2.5 cm. by simultaneous impaction, sedimentation, and interception. From 2.5 cm. to the end of the branch, sedimentation controlled the deposition. Each theory is a good approximation of the transfer coefficients in the region where it controls the deposition.

6.3.2 2.02μm Particles

Plots 3 and 4 compare the same theories used in Plots 1 and 2 with transfer coefficient data for 2.02μm particles which deposited

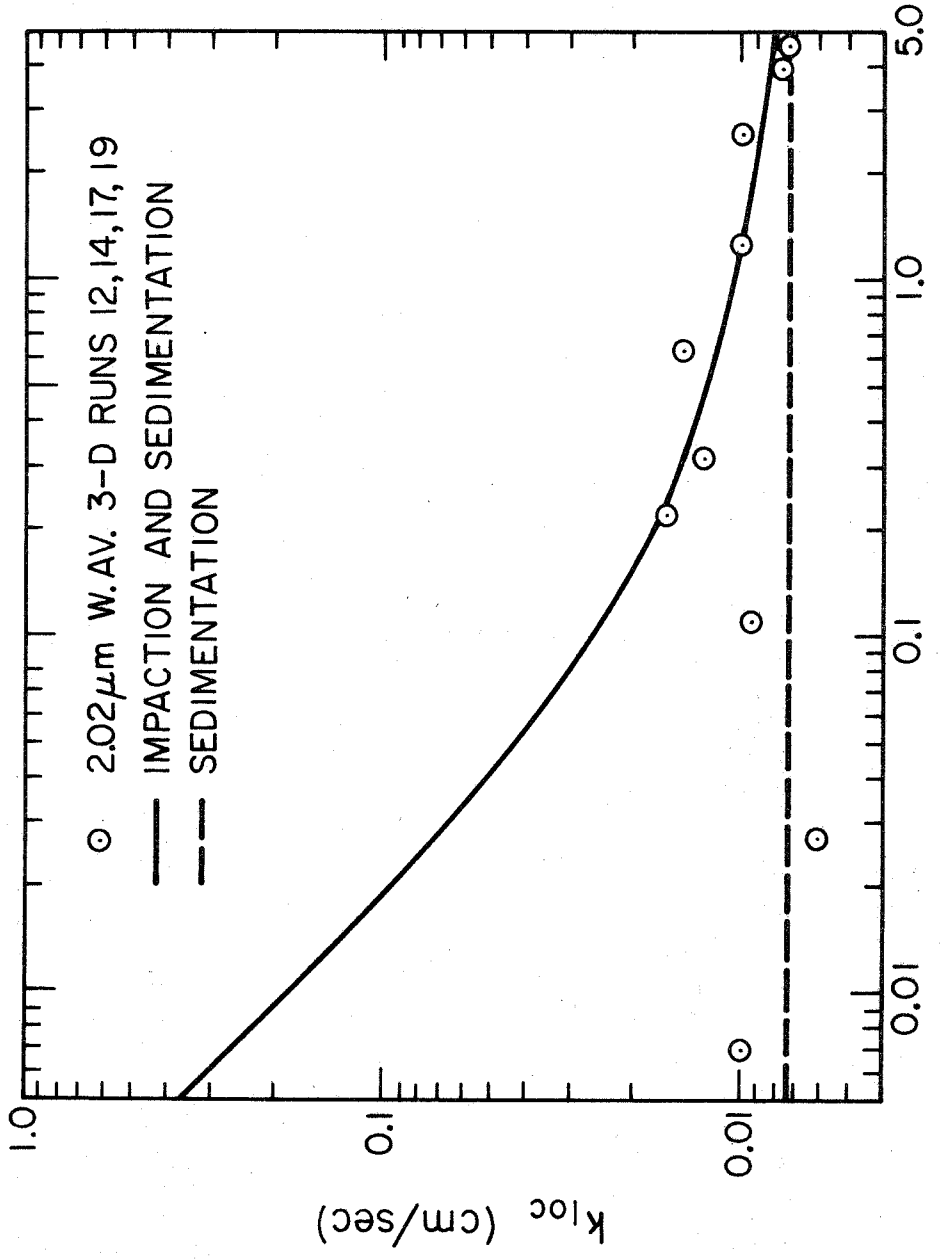

Plot 3 Comparison of Theories for 2.02 μm Particles Depositing on a Vertical 70° Wedge with Transfer Coefficients Measured Along Y=0 in the 3-D Model for 450 cc, 1.88 sec Inhalations. Impaction and Sedimentation Theory(w/ Interception) and Sedimentation Theory(w/o Interception) Use Steady Potential Flow with U=100 cm/sec and A=1.14 .

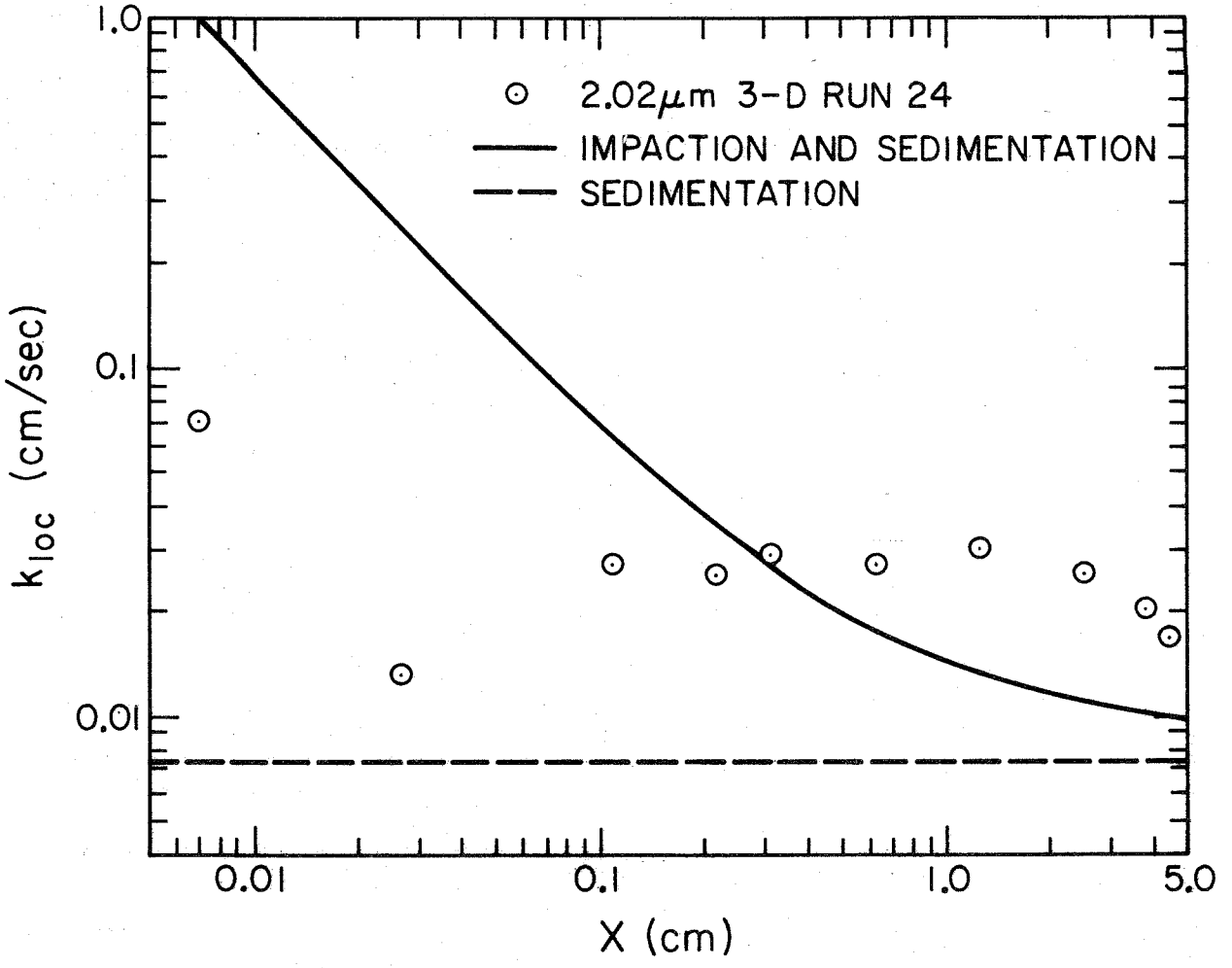

Plot 4 Comparison of Theories for 2.02 μm Particles Depositing on a Vertical 70° Wedge with Transfer Coefficients Measured Along Y=0 in the 3-D Model for 450 cc, 0.94 sec Inhalations. Impaction and Sedimentation Theory(w/ Interception) and Sedimentation Theory(w/o Interception) Use Steady Potential Flow with U=200 cm/sec and A=1.14 .

along Y=0 during 1.88 and 0.94 second inhalations, respectively. The three data points nearest the carina and the four most distant points in Plot 3 generally agree with the S theory. The points at 0.22, 0.3175 and 0.635 cm. are higher in value than the other points, and they correspond to the major peak in Map 3. Secondary flows caused this peak and the fortuitous agreement between the ISI theory and data in this region.

The trend of data in Plot 4 generally agrees with the S theory, as in Plot 3; however, the 200 cm./sec. data are approximately 2 times greater than the 100 cm./sec. data. This is expected if the deposition was controlled by interception and sedimentation in potential flow. The first three data points underestimate the ISI theory because the unsteady boundary layers inhibited the deposition. The data at 0.0275 cm. in both plots are conspicuously low, perhaps because the geometry and flow at the carina in the experimental model did not exactly match the theoretical model (Section C.1).

It is difficult to explain why data in Plot 4 greatly exceed the ISI theory, especially since the 5.7μm, 200 cm./sec. data generally agreed with the ISI theory. Thinner boundary layers and more intense secondary flows can only explain a minor rise above the theory. For some unknown reason, the measurement made of the particle concentration may have been too low.

In conclusion, 2.02μm particles deposit along most of the Y=0 strip by sedimentation and interception. Some inertial impaction took place at the carina and possibly in regions where secondary flows enhanced the deposition. Neither theory adequately represents the data because they neglect the unsteady boundary layers. Nevertheless, sedimentation theory is useful for approximating the trend of the data.

6.3.3 1.1μm Particles

Plots 5 and 6 compare the same theories used in Plots 1-4 with transfer coefficient data for 1.1μm particles which deposited along the Y=0 strip during 1.88 and 0.94 second inhalations, respectively. In Plot 5 the data are generally parallel to and slightly below the S theory for X=0 and X=1.5 cm. This shows that the unsteady boundary layer was thick enough on the average to prevent all impaction and interception predicted from a potential flow regime. But at $\overline{U}$=200 cm./sec. the boundary layer was thinner and allowed more deposition by simultaneous impaction, sedimentation and interception. This explains why data between X=0 and X=1.0 in Plot 6 are more than a factor of 2 larger than those in Plot 5.

Data in Plot 5 fall below the S theory because deposition is retarded by the clean air initially present in the model, and because sedimentation may be inhibited by boundary layer effects (Section 2.3.2). Considering the "clean air effect", the exposure time of the branch to

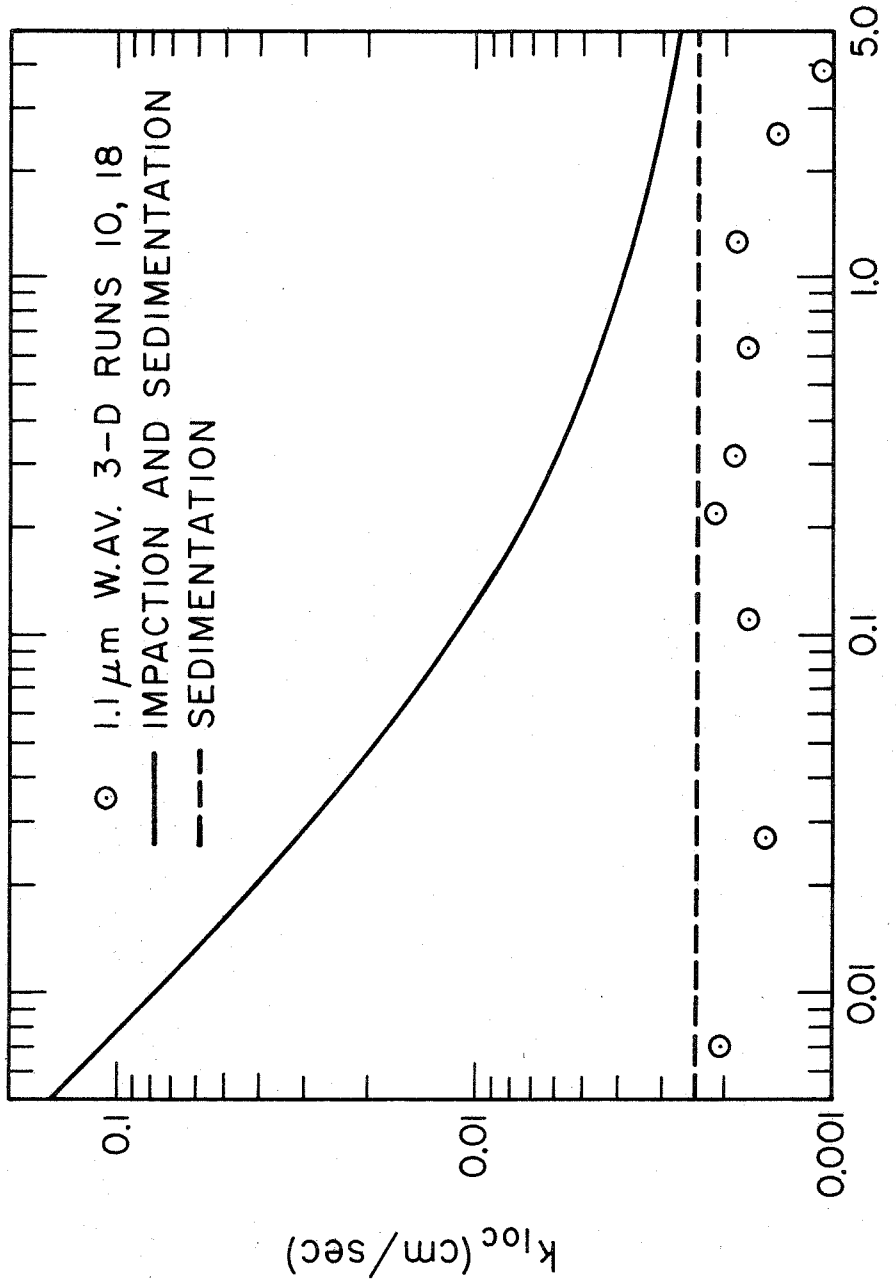

Plot 5 Comparison of Theories for 1.1 μm Particles Depositing on a Vertical 70° Wedge with Transfer Coefficients Measured Along Y=0 in the 3-D Model for 450 cc, 1.88 sec Inhalations. Impaction and Sedimentation Theory(w/ Interception) and Sedimentation Theory(w/o Interception) Use Steady Potential Flow with U=100 cm/sec and A=1.14 .

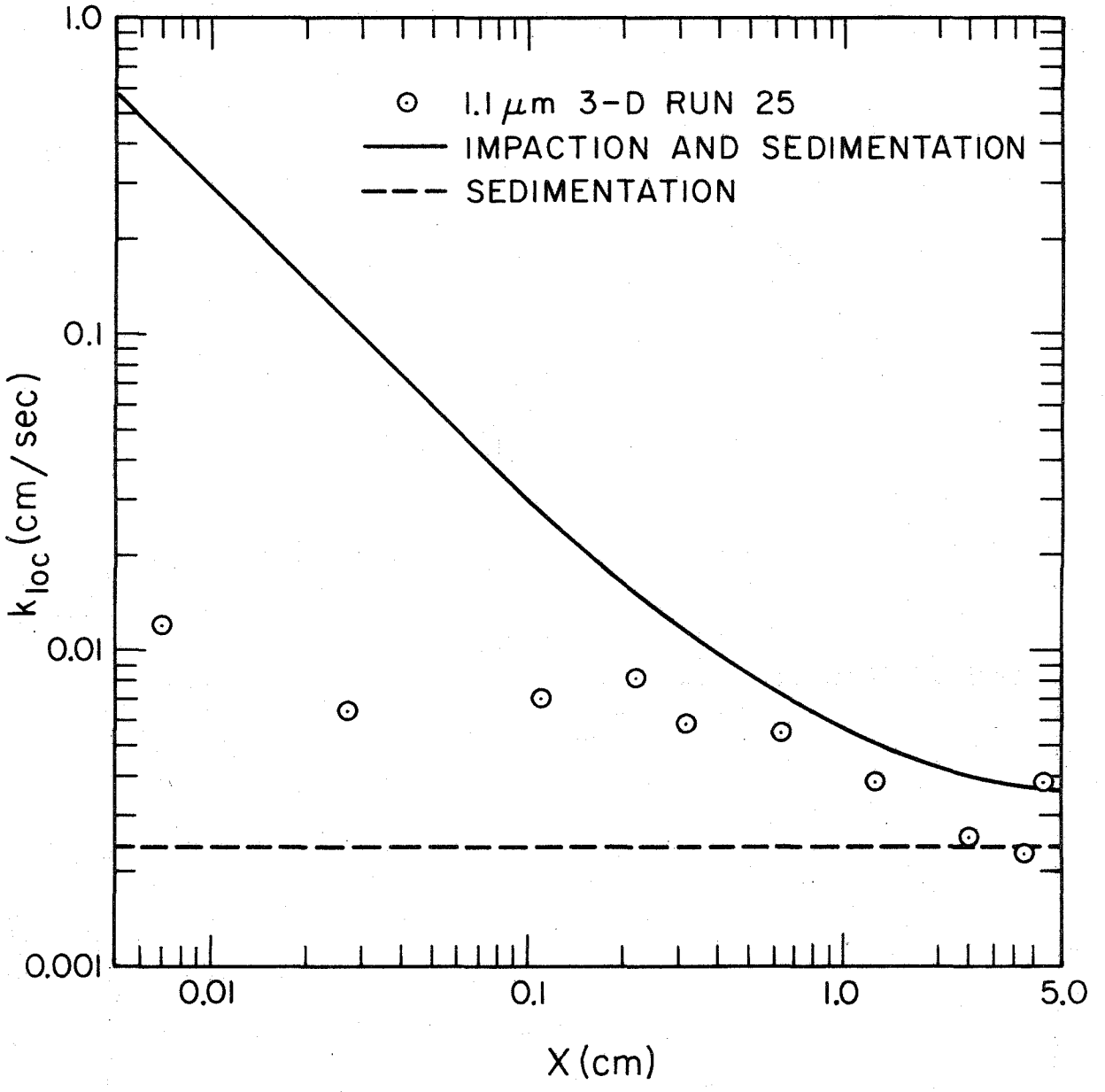

Plot 6 Comparison of Theories for 1.1 μm Particles Depositing on a Vertical 70° Wedge with Transfer Coefficients Measured Along Y=0 in the 3-D Model for 450 cc, 0.94 sec Inhalations. Impaction and Sedimentation Theory(w/ Interception) and Sedimentation Theory(w/o Interception) Use Steady Potential Flow with U=200 cm/sec and A=1.14 .

particles is shorter at the more distant locations because it takes longer for the particle-laden air to reach the core above these locations. Also, since the clean boundary layers are thicker at the more distant locations, more time is required to fill them with settling particles. Thus the exposure time at any location is less than the corrected inhalation time used to calculate k_{loc} (Section 4.8).

The "clean air effect" is even more dramatic in Plot 6 between X=0.7 and X=3.8 cm. The decrease starts closer to the carina and is more rapid than in Plot 5 because the time to fill the clean boundary layers by sedimentation is a larger fraction of the inhalation time at $\overline{U}$=200 cm./sec. than at $\overline{U}$=100 cm./sec. ($\delta(x_1)$ is proportional to $U^{-\frac{1}{2}}$ while inhalation time is proportional to U^{-1}). Another factor contributing to the decrease in Plots 5 and 6 is the greater inhibition of interception (predicted from potential flow theory) by the thicker boundary layers at the end of the branch (Section 2.3.3).

The successive ">" and "$\gtrsim$" shaped contours in Maps 5-8 show this declining ridge of depositon along the strips between Y=±2. The peak of the ridge along the ">" contours corresponds to the strip over which the highest axial velocity is found, and the sides of the ">" have progressively lower axial velocities. Deposition is highest in the region of highest axial velocity as a result of thinner boundary layers, more rapid clearance of clean air from the core, and more rapid filling of clean boundary layers with particles.

The deposition of 1.1μm particles along the Y=0 strip was controlled by sedimentation and interception over most of the branch. The theory of sedimentation accurately estimates k_{loc} over part of the strip at $\overline{U}$=100 cm./sec. Both theories inadequately approximate k_{loc} at $\overline{U}$=200 cm./sec.

6.3.4 0.79μm Particles

Plots 7 and 8 compare the data along Y=0 in Maps 7 and 8 with three different theories. The first two are the same as in Plots 1-6. The third is the quasi-steady diffusion (QD) theory or in other words the theory of convective diffusion for quasi-steady laminar boundary layer (B.L.) flow along a 70° wedge. Equation 3.9 was used to predict the local transfer coefficient, with A=1.14 cm.$^{-7/29}$ corresponding to the experimental flow conditions.

The 100 cm./sec. data in Plot 7 lie relatively farther below the S theory than the 1.1μm particles in Plot 5 because deposition by all mechanisms is more effectively retarded by the unsteady boundary layer, and because more time is needed to fill the clean boundary layers. The data decrease beyond 1.0 cm. for the reasons stated in Section 6.3.3 for Plot 5, and the peak data point at 0.3275 cm. corresponds to the peak "hot spot" in Map 7.

The 200 cm./sec. data in Plot 8 are shifted above the S theory, but not as far as the 1.1μm data were shifted in Plot 6 because the

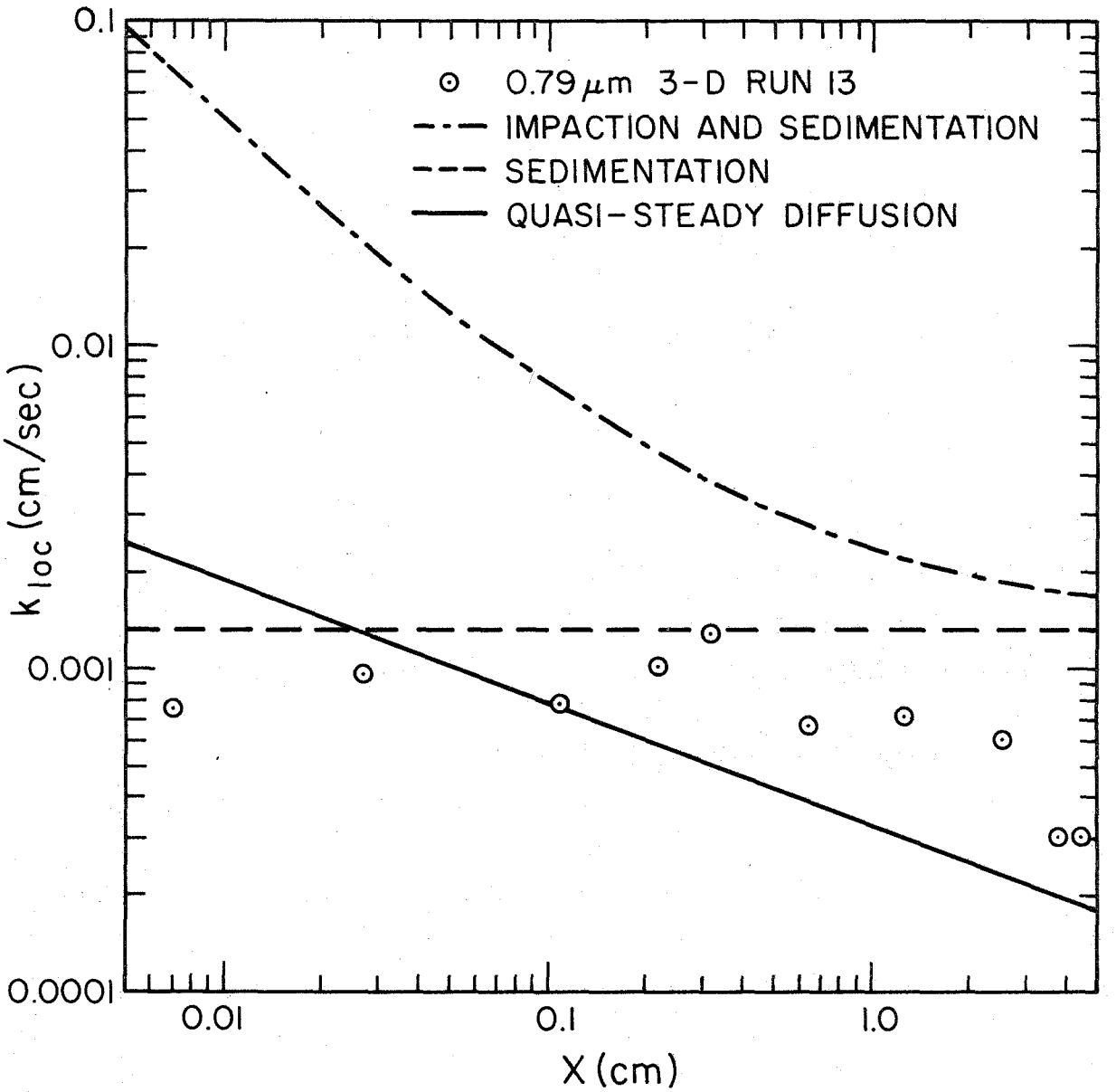

Plot 7 Comparison of Theories for 0.79 μm Particles Depositing on a Vertical 70° Wedge with Transfer Coefficients Measured Along Y=0 in the 3-D Model for 450 cc, 1.88 sec Inhalations. Impaction and Sedimentation Theory(w/ Interception) and Sedimentation(w/o Interception) Use Steady Potential Flow(U=100 cm/sec). Diffusion(Point Particles) Uses Quasi-Steady Laminar B.L. Flow($\bar{U}$=100 cm/sec). A=1.14 in the Theories.

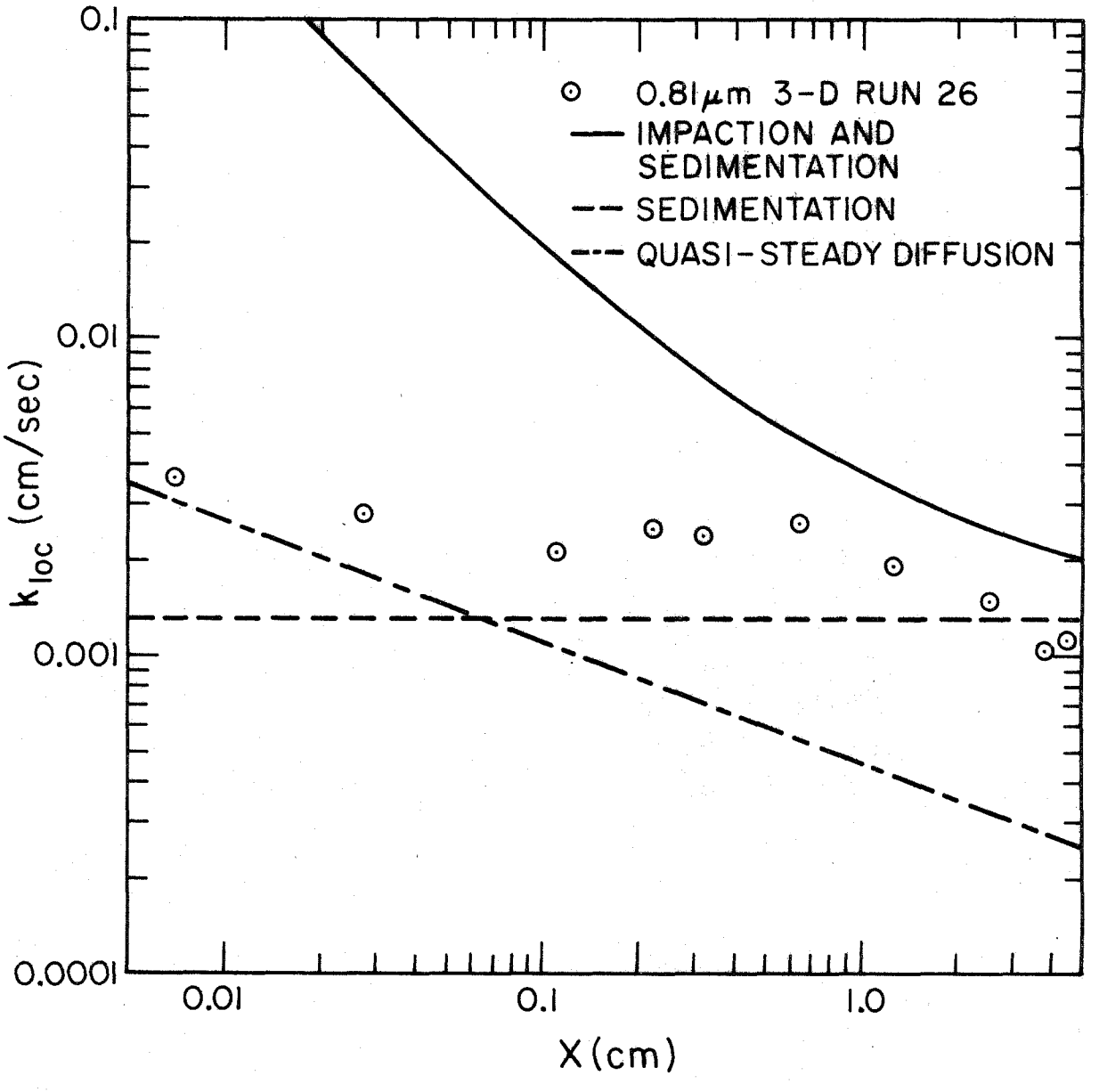

Plot 8 Comparison of Theories for 0.81 μm Particles Depositing on a Vertical 70° Wedge with Transfer Coefficients Measured Along Y=0 in the 3-D Model for 450 cc, 0.94 sec Inhalations. Impaction and Sedimentation Theory(w/ Interception) and Sedimentation(w/o Interception) Use Steady Potential Flow(U=200 cm/sec). Diffusion(Point Particles) Uses Quasi-Steady Laminar B.L. Flow($\bar{U}$=200 cm/sec). A=1.14 in the Theories.

boundary layer more effectively retards the deposition of the smaller 0.79μm particles. The decrease in the data at the end is also analogous to Plot 6 and the same explanations apply.

If convective diffusion were controlling the deposition, the clean boundary layer effect would still be present. Since the data do not fall below the QD curve along the entire length of the branch and farther below at larger X locations, convective diffusion is rejected as a significant mechanism. Sedimentation with interception was controlling and S theory can be used to approximate the local transfer coefficients along Y=0.

Comparison of results for 2.02, 1.1 and 0.79μm particles shows that the retardation of deposition by unsteady aerodynamic boundary layers was greater for smaller particles and at the lower flow rate. The "clean air effect" was also greater for smaller particles and at the lower flow rate.

6.3.5 0.365μm Particles

Plots 9 and 10 compare data along Y=0 in Maps 9 and 10 with 2 different theories for convective diffusion. Curve (1), the QD theory, is calculated from Equation 3.9 with $\sqrt{\overline{U}}$ evaluated from Figure 4.4 ($\sqrt{\overline{U}}$ = 9.62 for $\overline{U}$ = 100). Curve (2) is calculated from Levich's (1962:112-115) solution for diffusion to a tube in quasi-steady Poiseuille flow with $\sqrt[3]{\overline{V_o}}$ evaluated from Figure 4.4 ($\sqrt[3]{\overline{V_o}}$ = 5.65 for $\overline{V_o} = 2\overline{U_2} = 201.6$).

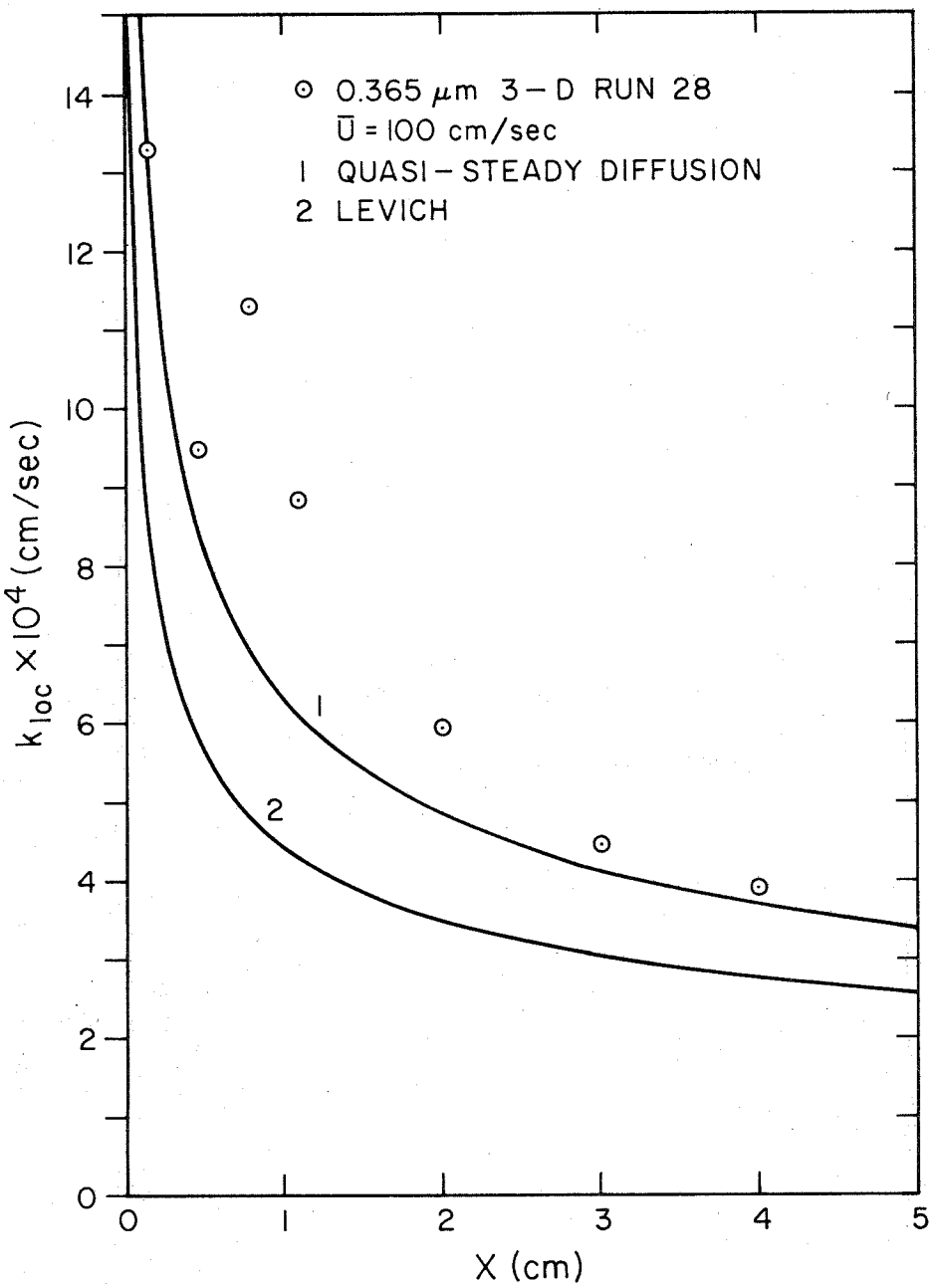

Plot 9 Comparison of Theories for Quasi-Steady Diffusion of 0.365 μm Particles with Transfer Coefficients Measured Along Y=0 in the 3-D Model for 450 cc, 1.88 sec Inhalations. Curve(1) is for Quasi-Steady Laminar B.L. Flow Along a 70° Wedge with A=1.14 . Curve(2) is for Quasi-Steady Poiseuille Flow. Theories Assume Point Particles.

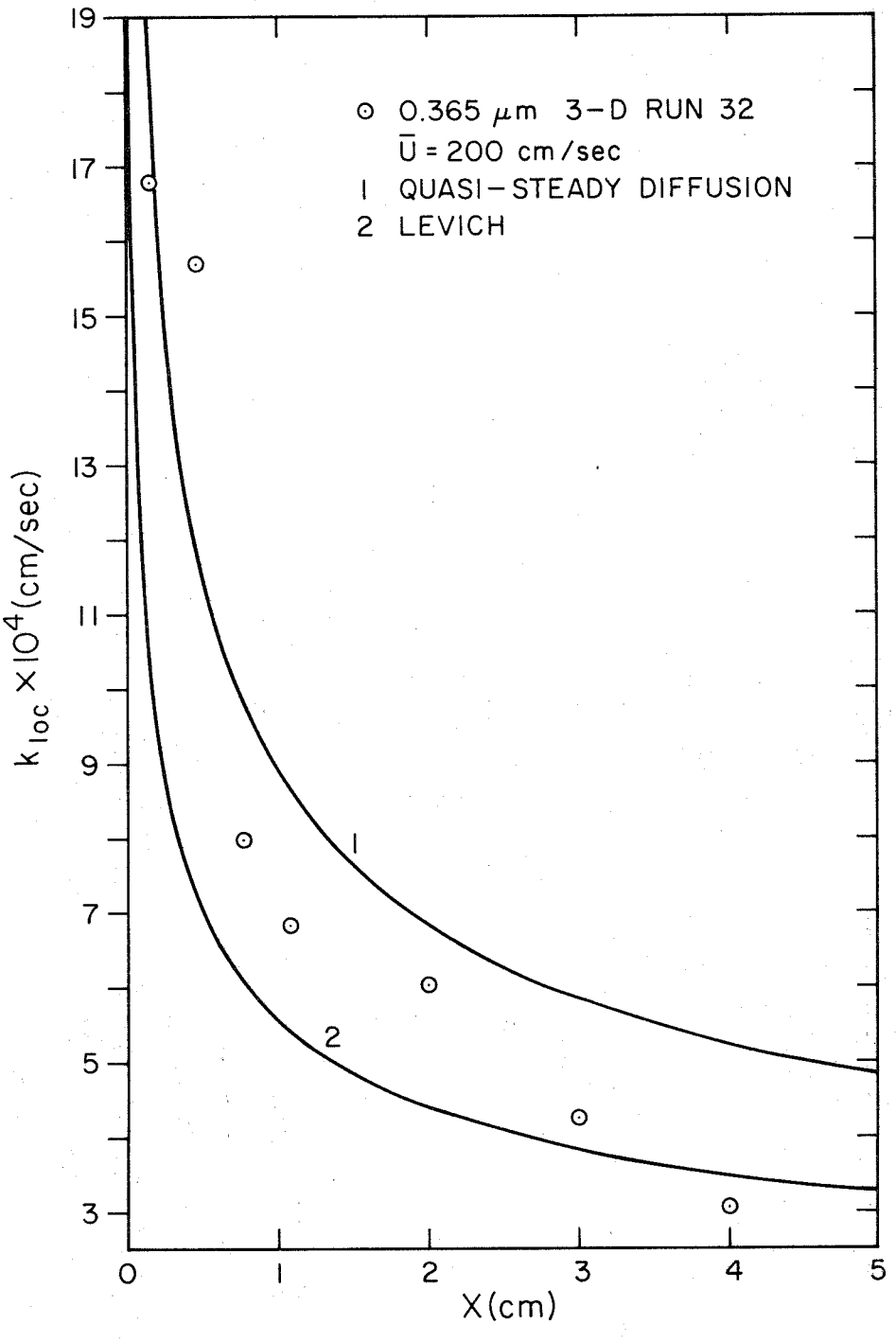

Plot 10 Comparison of Theories for Quasi-Steady Diffusion of 0.365 μm Particles with Transfer Coefficients Measured Along Y=0 in the 3-D Model for 450 cc, 0.94 sec Inhalations. Curve(1) is for Quasi-Steady Laminar B.L. Flow Along a 70° Wedge with A=1.14 . Curve(2) is for Quasi-Steady Poiseuille Flow . Theories Assume Point Particles.

The data at X = 0.155, 0.465, 3.0 and 4.0 cm. lie slightly above curve (1). The larger positive deviation of the data from curve (1) between X=0.75 and X=2.0 cm. was caused by the enhanced deposition associated with the secondary flows. The peak point at X=0.775 cm. corresponds to the secondary peak in Map 9. All data are generally higher than theory because a uniform rather than a skewed velocity profile is assumed in the daughter branch. The skewed profile in the plane of bifurcation (Figure 3.2) predicts the highest axial velocity and shear rates along Y=0. This is demonstrated most clearly by the ">" contours along the Y=0 strip in Map 9.

Curve (2) predicts lower transfer coefficients than curve (1) and generally falls below the data, as explained in Section 3.4.

In Plot 10 all except the second point fall below curve (1), and the negative deviation of the data from the theory is greater at more distant locations. The rate of decrease from X=2 to X=4 cm. is also greater than in Plot 9. This lower trend and sharper decrease in Plot 10 compared to Plot 9 were caused by the clean boundary layer effect (Section 3.4). The time period needed to develop the steady concentration distribution is greater at larger X and greater for larger particles in the diffusion range.

Wang and Friedlander (1968) derived a similarity solution for the unsteady form of the equation of convective diffusion. From

this solution they determined the time for development of the steady concentration boundary layer for 0.2 μm particles in the sixth generation of Weibel's Model "A" for a tidal volume of 450 c.c. inhaled over 2 seconds. Choosing t=0 when the particles reach the carina at X=0 in the sixth generation, 0.3 and 0.6 seconds were required respectively to develop a steady concentration distribution at X=0.221 and X=0.626 cm.

By analogy, during a 450 c.c. inhalation of 0.365 μm particles over 0.94 seconds a significant fraction of the inhalation time is required to develop steady concentration distributions beyond X=0.5 cm. along Y=0. The axial velocity is less along Y strips more distant from Y=0; hence, the concentration distribution will develop more slowly causing much less deposition toward the outside walls than along Y=0. This is observed in Maps 9 and 10, but more obviously in Map 9 where the secondary flows are less intense and less effective in replacing the clean air along the outside walls with the particle-laden air.

The peak at X=0.75 cm. in Plot 9 corresponds to the secondary peak within contour C in Map 9. In Plot 10 the enhanced deposition caused by the secondary flow shifts to X=0.5 cm.; however, the sharp decrease in deposition beyond X=0.5 cm. precludes a secondary peak in Map 10.

Convective diffusion controls the deposition of the 0.365μm particles in the "3-D" model and the QD theory (curve 1) is fairly accurate for approximating the local transfer coefficients along Y=0. The secondary flows and clean boundary layer effects must be taken into account to improve the accuracy of the estimate.

6.3.6 0.088μm Particles

Plots 11 and 12 compare data along Y=0 in Maps 11 and 12 with the same theories used in Plots 9 and 10. The trends of the data and the agreement between data and theory in Plots 11 and 12 are nearly identical to those for 0.365μm in Plots 9 and 10, respectively; hence, the same arguments and explanations apply.

The 0.088μm data at 200 cm./sec. fall off less rapidly with distance below the theory than occurred for the 0.365μm data at 200 cm./sec. because the 0.088μm particles develop steady concentration distributions more rapidly at any X location than the 0.365μm particles. The enhanced deposition caused by the secondary flows are apparent in Plots 11 and 12 between 0.4 and 1.0 cm. even though they do not form secondary peaks on Maps 11 and 12.

Comparison of data in Plots 1-12 shows that the highest local transfer coefficient measured along Y=0 is found at $X \leq 0.3$ cm. and, depending on particle size and inhalation rate, is 2 to 45 times greater than the transfer coefficient at the end of the branch. Except for the

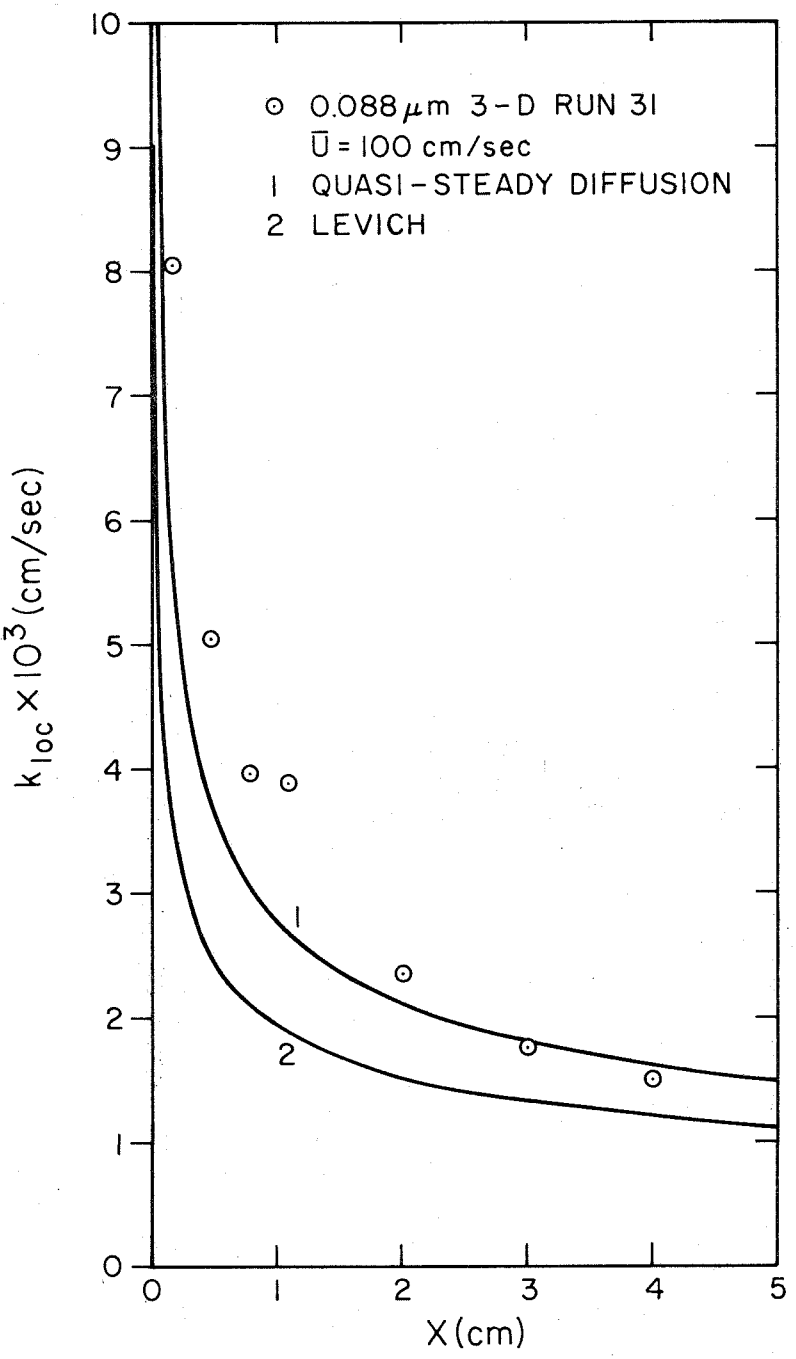

Plot 11 Comparison of Theories for Quasi-Steady Diffusion of 0.088 μm Particles with Transfer Coefficients Measured Along Y=0 in the 3-D Model for 450 cc, 1.88 sec Inhalations. Curve(1) is for Quasi-Steady Laminar B.L. Flow Along a 70° Wedge with A=1.14. Curve(2) is for Quasi-Steady Poiseuille Flow. Theories Assume Point Particles.

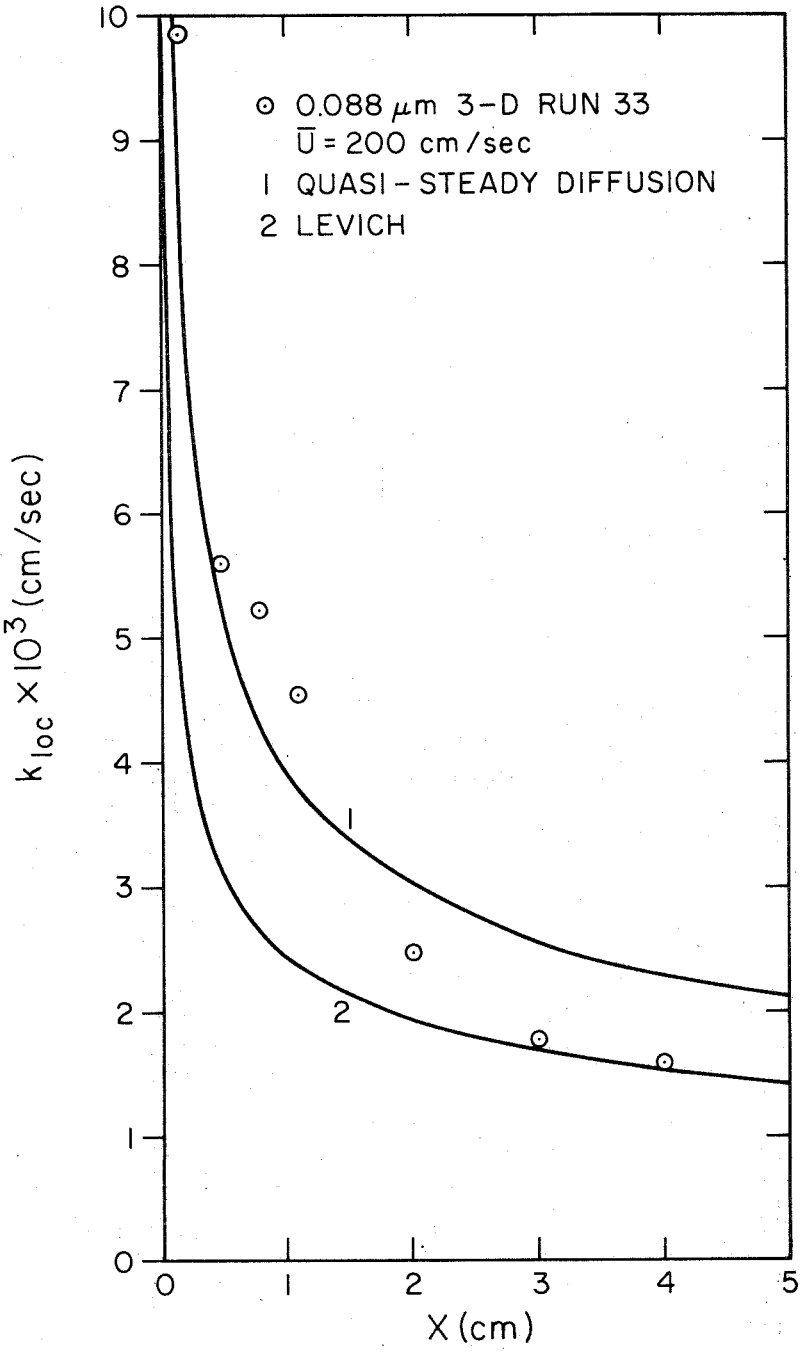

Plot 12 Comparison of Theories for Quasi-Steady Diffusion of 0.088 μm Particles with Transfer Coefficients Measured Along Y=0 in the 3-D Model for 450 cc, 0.94 sec Inhalations. Curve(1) is for Quasi-Steady Laminar B.L. Flow Along a 70° Wedge with A=1.14 . Curve(2) is for Quasi-Steady Poiseuille Flow. Theories Assume Point Particles.

effects of the secondary motions, results from all the Plots are consistent with conclusions for the "2-D" model data.

6.3.7 Comparison of Experimental Deposition Efficiency and Theory

Figures 6.6 and 6.7 compare the deposition efficiency (ϵ) measured in the daughter branch of the "3-D" model with theories from Chapter 3 and from the literature. The experimental data points were evaluated from the k_{av} data in Figure 6.1 by the following:

$$\epsilon = \frac{4k_{av}R_2L}{\overline{U}R_1^2} \quad . \tag{6.1}$$

Curve (1) represents ϵ for inhalation into the daughter branch of the "3-D" model, as calculated from Landahl's (1950a, 1963) deposition model. The probabilities for impaction and sedimentation were calculated from the 1950 article, and the diffusion probabilities were calculated from the 1963 article. The separate probabilities were combined to determine ϵ.

Curve (2) represents ϵ during inhalation, calculated from the deposition model of the International Radiological Protection Commissions's Task Group on Lung Dynamics (1966). The separate deposition probabilities were summed to determine ϵ.

Curves (4) and (5) were calculated respectively from the S and the ISI theories by using Equation 3.4. k_{av} in Equation 3.4 was the

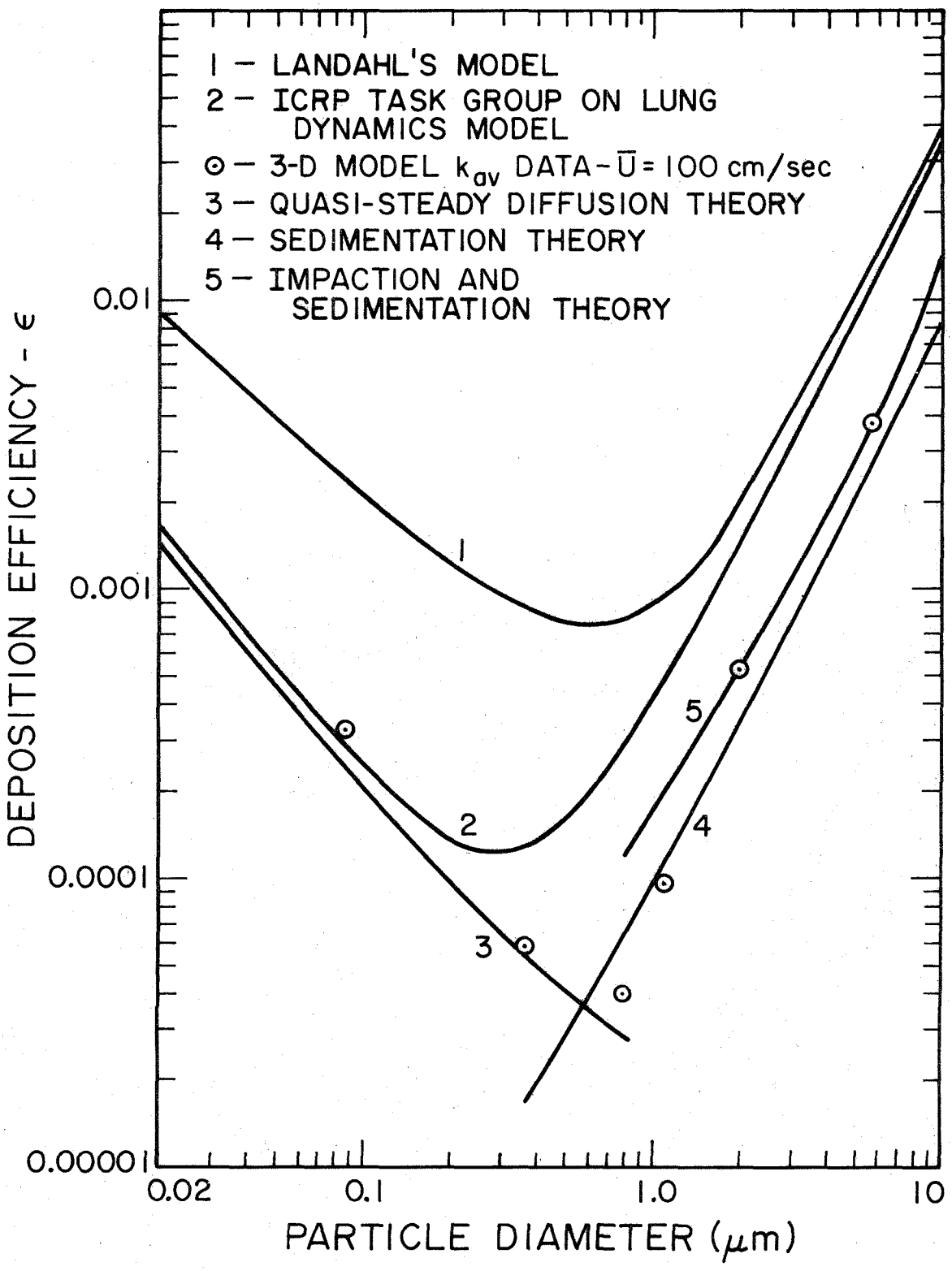

Figure 6.6 Comparison of Theoretical and Experimental Deposition Efficiencies in the Daughter Branch of the 3-D Model for 450 cc, 1.88 sec Inhalations.

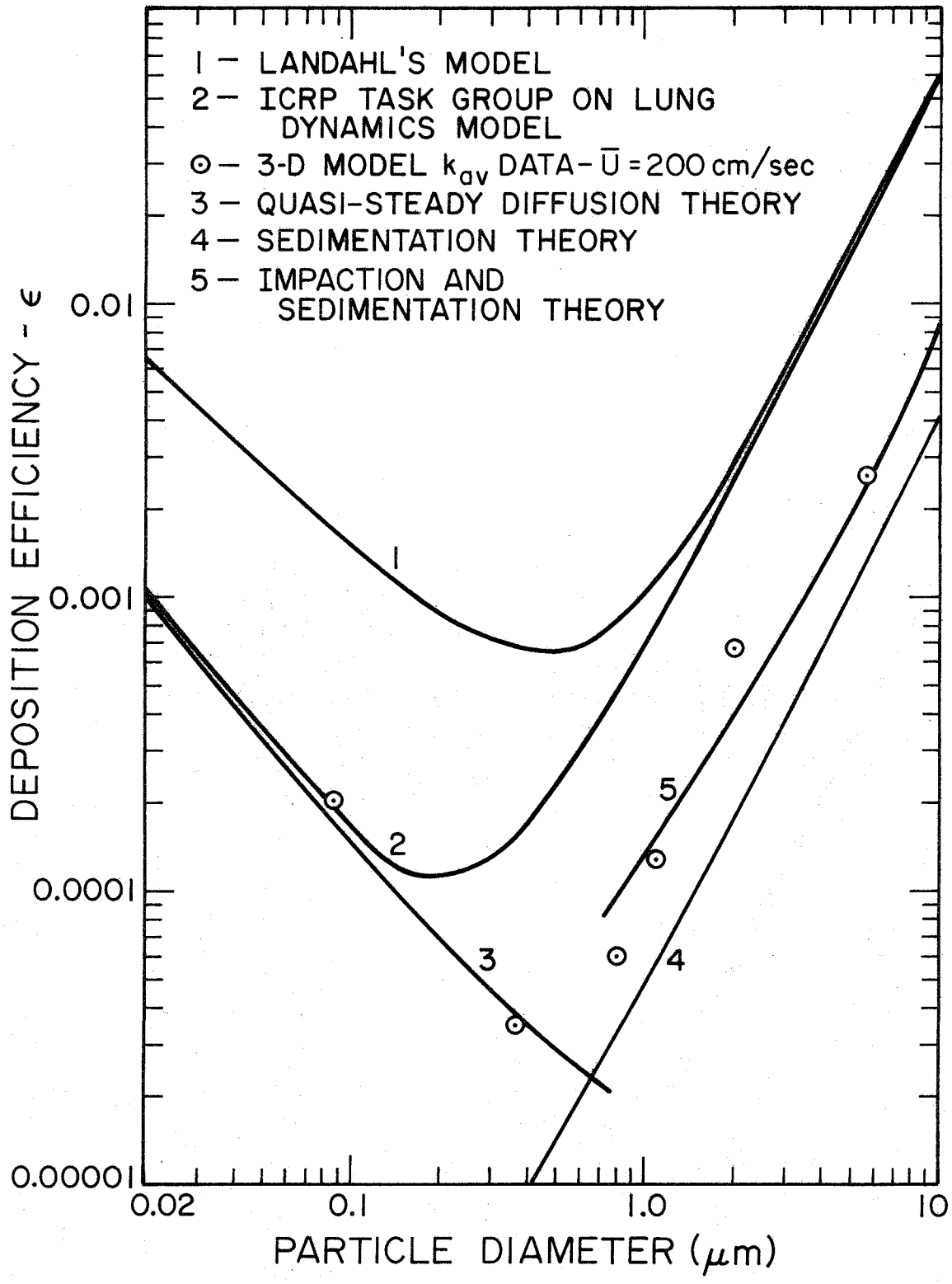

Figure 6.7 Comparison of Theoretical and Experimental Deposition Efficiencies in the Daughter Branch of the 3-D Model for 450 cc, 0.94 sec Inhalations.

average transfer coefficient over the appropriate theoretical curve in Plots 1 - 8. Curve (3) was calculated from QD theory by using the semi-empirical expression,

$$\epsilon = \frac{8k_{av}R_2L}{\pi R_1^2 \overline{U}}. \qquad (6.2)$$

k_{av} is evaluated by averaging k_{loc} in Equation 3.9 over the length of the daughter branch. Since Equation 6.2 is equivalent to multiplying Equation 6.1 by $2/\pi$, the theoretical k_{av} predicted for a two-dimensional, 70° wedge is applied over only 63.7% of the circumference or surface area of the daughter branch.

Landahl's model greatly overestimates the data at both inhalation rates because of the following: First, the formula for the diffusion probability was derived by neglecting all air flow; it assumes that diffusion occurs normal to the walls of the tube when the initial particle concentration is uniform at any cross section. Although the formula is used throughout the respiratory cycle, it is only valid for modeling deposition by diffusion during the pause between inhalation and exhalation, and for modeling turbulent diffusion (Levich, 1962: 155) from fully developed turbulent flow. Both of these mechanisms would be more effective than convective diffusion for 0.088 μm and 0.365 μm particles in the "3-D" model.

The efficiency of sedimentation predicted by Landahl's model is only slightly greater than curve (4); hence the great overestimation of

the data in the impaction and sedimentation subrange is predominantly caused by the inaccuracy of the expression for impaction. Since the expression is only a semi-empirical correlation based upon the collection efficiency of impaction range particles in a 90° elbow, it does not account for the deceleration of air at the carina and boundary layer effects which can significantly deter the impaction of all particles.

The Task Group's Model overestimates data greater than 0.1 μm in diameter, but to a lesser degree than Landahl's model for a number of reasons. The sedimentation probability of Findeisen (1935) predicts slightly less deposition than curve (4), and the impaction expression of Findeisen gives a slightly lower efficiency than Landahl's impaction expression. These two factors cause the Task Group's Model to predict a slightly lower ϵ than Landahl's model in the impaction and sedimentation subrange.

Second, Gormley and Kennedy's (1949) expression for convective diffusion in steady Poiseuille flow in a straight, cylindrical tube gives a fairly accurate estimate of the 0.365 and 0.088 μm data in both figures. Combining the sedimentation and impaction probabilities with the diffusion probability causes the disagreement between curve (2) and 0.365 μm data.

At $\overline{U}$ = 100 cm./sec. the 5.7 and 2.02 μm data agree well with the impaction and sedimentation theory. Sedimentation theory agrees well with the 0.79 and 1.1 μm data, and the 0.365 and 0.088 μm data

are in good agreement with the quasi-steady diffusion theory. The same conclusions apply at $\overline{U}$=200 cm./sec., except that the 0.81 and 1.1 μm particles lie between curves (4) and (5). This occurred because impaction and interception were retarded less by the thinner boundary layers at this higher velocity. Also, the secondary flows enhanced the deposition of these particles along the outside wall at $\overline{U}$ = 200 cm./sec. compared to $\overline{U}$ = 100 cm./sec.

Enhanced deposition by the secondary flows may be the explanation for the greater positive deviation of the 0.088 μm data from curve (3) than the 0.365 μm data. This explanation may also apply to the 2.02 μm datum at $\overline{U}$ = 200 cm./sec.

Figures 6.6 and 6.7 suggest that experimental deposition in the transition subrange between 0.1 and 1.0 μm can be more accurately modeled if one mechanism is assumed to control the deposition of each particle, than if the efficiencies from all mechanisms are combined.

The good agreement between the data and the "3-D" model theories suggests that they can be used to approximate deposition during inhalation in the large airways of humans. However, data for particles between 0.4 and 0.8 μm and less than 0.08 μm and for other inhalation rates could more accurately define the ranges of applicability of each theory.

Using the dimensionless parameters (Section 2.4) and the "3-D" modifications (Section 3.2), curve (3) in Figures 6.6 and 6.7 has the

general form

$$\epsilon = 1.6(m+1)^{-1/2}\beta^{1/3}(h_2/h)^{1/2}(A_3' S_1/S_3)^{1/2}\left(\frac{\sqrt{\bar{U}}}{\sqrt{U}}\right)Pe^{-2/3}Re^{1/6}(L/R_2)^{(m+1)/2} \tag{6.3}$$

where $A_3' = A_3 R_2^m$. This correlation of data in the diffusion subrange applies for $Pe < 2.4 \times 10^8$ at $Re = 810$ and for $Pe < 3.8 \times 10^8$ at $Re = 1620$.

Curve (4) in both figures follows from Equation 2.17b as

$$\epsilon = \frac{4R_2 L}{\pi R_1^2}\left(\frac{Stk}{Fr}\right)\sin\alpha. \tag{6.4}$$

It approximately correlates the data at $Re = 810$ for $1.4 \times 10^{-5} < Stk/Fr < 7.6 \times 10^{-5}$. At $Re = 1620$ it underestimates the data by a factor of 2 for $5 \times 10^{-6} < Stk/Fr < 2 \times 10^{-5}$.

From Equations A.26 and 3.4 and the "3-D" modifications for A in Section 3.2, curve (5) has the following parameter dependence:

$$\epsilon = \frac{4}{\pi}\frac{R_2 L}{R_1^2} f_8\left[(L/R_2), \alpha, (A_3' S_1/S_3), Stk, Fr, I\right] \tag{6.5}$$

Multiple regression analysis of curve (5) in both figures for Stk, Fr and I gives

$$\epsilon = 11.3\left(\frac{4R_2 L}{\pi R_1^2}\right) Stk^{0.36} Fr^{-0.392} I^{1.02}. \tag{6.6}$$

It approximates data at $Re = 810$ and $Fr = 16.6$ for $Stk > 1.3 \times 10^{-3}$ and $I > 2.4 \times 10^{-4}$. At $Re = 1620$ and $Fr = 66$, it approximately correlates data for $Stk > 1.3 \times 10^{-3}$ and $I > 1.6 \times 10^{-4}$.

In conclusion, data in Figures 6.6 and 6.7 demonstrate the relative, average mass dosage of each particle size expected in the daughter branch of a large airway in human lungs when equal mass concentrations of each particle size are inhaled. To show the relative "hot spot" effect, these data should be multiplied by the corresponding $\bar{k}_{0.6\%Area}/k_{av}$ value in Figure 6.2. The data demonstrate the relative number dosage of each particle size, assuming equal number concentrations of each size are inhaled.

6.4 Comparison of Deposition in Unsteady and Steady Flow

Although particle filtration theory was developed for steady flow conditions, a number of experimental studies have demonstrated that the collection efficiency measured during pulsatile flow differed from the efficiency measured during steady flow conditions at the time-average pulsatile velocity (Jordan, 1958; Stafford, et al., 1972).

By analogy, deposition during normal respiration in the lung probably cannot be accurately modeled by steady flow conditions. To test this hypothesis, deposition along Y = 0 in the "3-D" model was compared during steady and pulsatile inhalations.

The steady flow experiments were performed by Dennis Y. Loh[1]. 1.1 μm particles were inspired at steady flow rates ranging from 4.58 to 24.5 liters/min. Each corresponds to one or two points on a flow rate vs. time curve like Figure 4.4, when the time-average flow rate over the curve is 14.4 liters/min. ($\overline{U}$ = 100 cm./sec.). The transfer coefficients measured at each location from each steady flow run were time-averaged over the curve like Figure 4.4 to obtain a prediction of quasi-steady deposition for a 450 c.c., 1.88 sec. inhalation.

The velocity of Run K, U = 109.2 cm./sec. at 15.7 liters/min., was very near the time-average velocity of $\overline{U}$ = 100 cm./sec. It was the only run in which the transfer coefficients were measured over the entire surface in the manner identical to the unsteady "3-D" runs. Map 13 and Graph 13 were plotted from Run K for comparison with the 1.1 μm, $\overline{U}$ = 100 cm./sec. results in Map 5 and Graph 5.

---

[1] Former student in Chemical Engineering at the California Institute of Technology. Dennis Loh performed the experiments as an undergraduate research project in the summer of 1972 under the direction and supervision of the author. The same "3-D" model apparatus and procedure was used as in the unsteady, 1.1 μm runs described in Chapter 4, except for the following:

1. Photometer calibrations and concentration measurements were made at a sample flow rate of 8.06 liters/min.
2. Tygon tubes were attached to each daughter branch with plexiglass adapters.
3. An air pump produced the necessary volumetric flow rates within the model because the pressure head from the nebulizer was insufficient.
4. Counts were only taken along the Y = 0 strip.

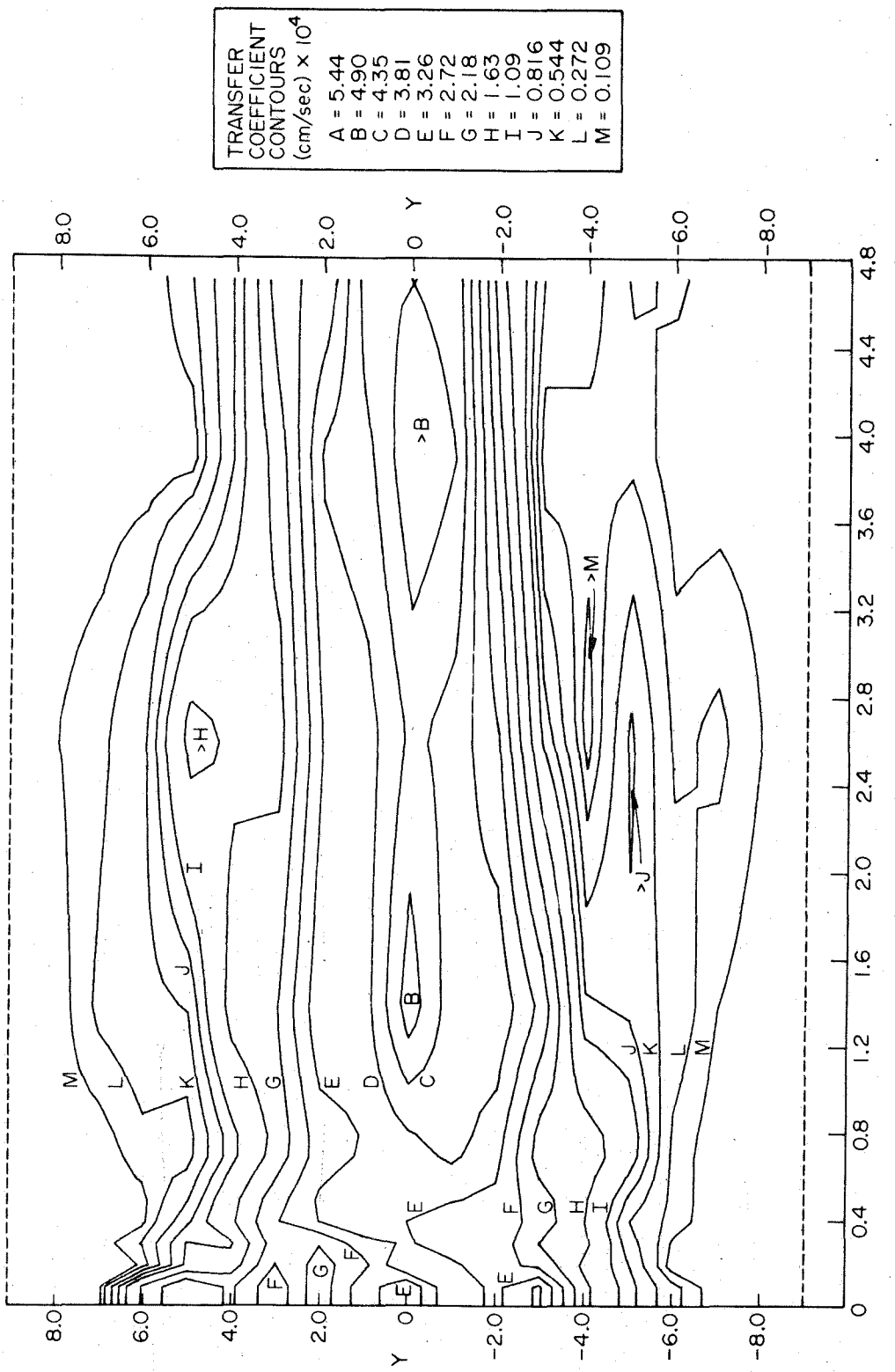

Map 13 3-D Steady Flow Run K

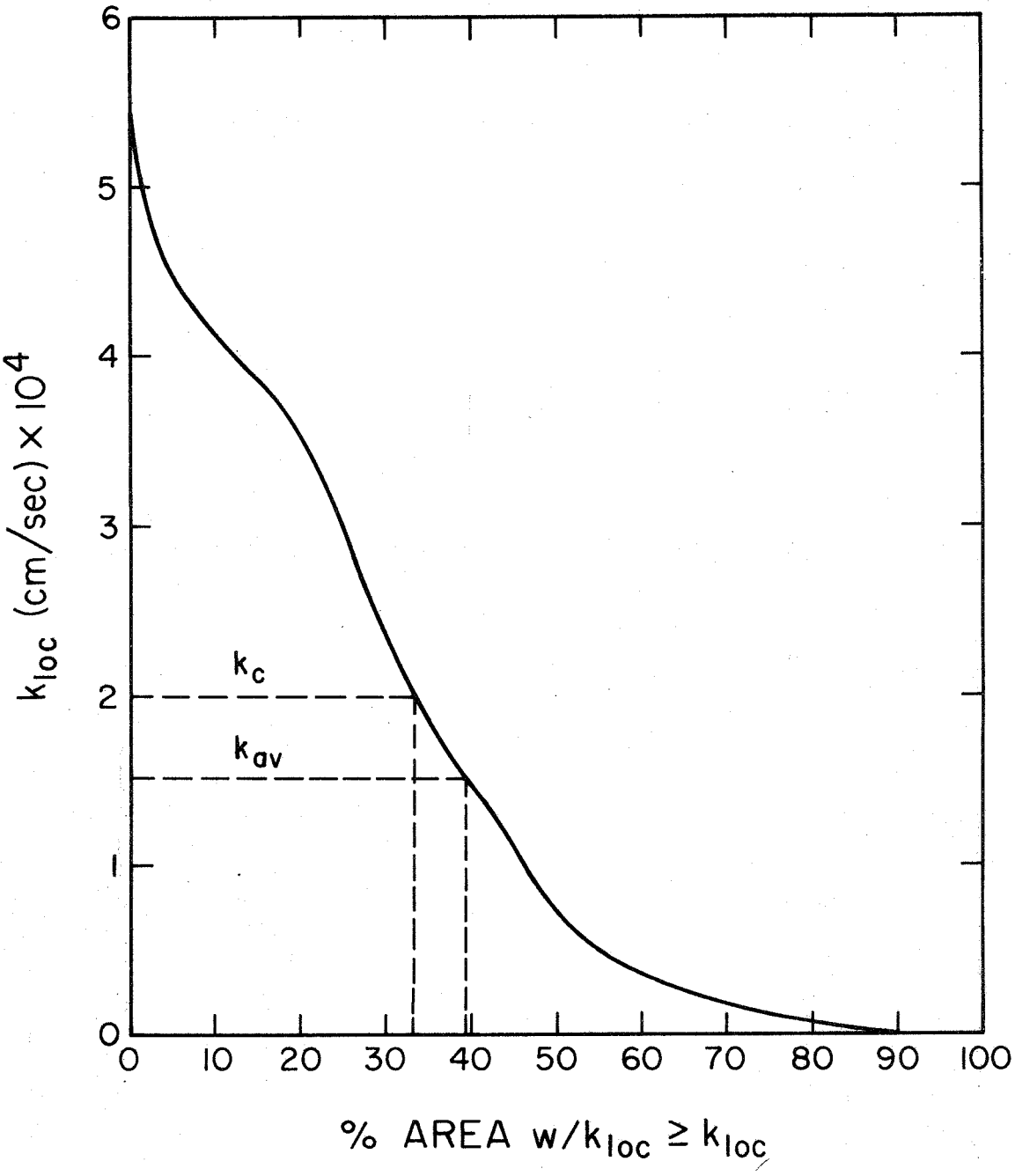

Graph 13 Cumulative Surface Area Distribution for Map 13 Showing the % of the Surface Area of the Daughter Branch with a Local Transfer Coefficient ≥ Stated Value (d_p = 1.1 μm, U = 109.2 cm/sec)

The major difference between the deposition patterns in Maps 5 and 13 occurs along the inside wall between Y = ± 2. The ">" and "≥" contours are not found in Map 13; instead, a ridge of deposition within the D contour stretches from X = 0.6 cm. to the end of the branch. A minor peak at the carina and two peaks of approximately constant elevation along the ridge at X = 1.2 - 2.0 and X = 3.2 - 4.76 in Map 13 are in contrast to the major peaks at the carina and at X = 0.2 - 0.8 cm. in Map 5.

During the steady flow runs, no "clean air effect" is expected; but the axial velocity is still highest along the Y = 0 strip. These two facts explain why there is a narrow ridge of fairly constant elevation along Y = 0 on Map 13, while a ridge of declining elevation, defined by ">" contours, occurs along Y = 0 in Map 5. The two peaks in Map 13 may have been caused by the secondary motions or by statistical errors.

Comparison of the curves in Graph 13 and Graph 5 shows that both the surface area distribution of k_{loc} and the "hot spot" intensities are similar. k_{av} and k_c in Graph 5, however, are approximately 4 times larger than k_{av} and k_c in Graph 13.

These large differences are more dramatically demonstrated in Figure 6.8. The unsteady flow data were measured along the Y = 0 strip in Map 5. The steady flow data were from the Y = 0 strip in Map 13, and the prediction of quasi-steady deposition obtained from all the steady flow runs is also shown. The unsteady flow data are explained in

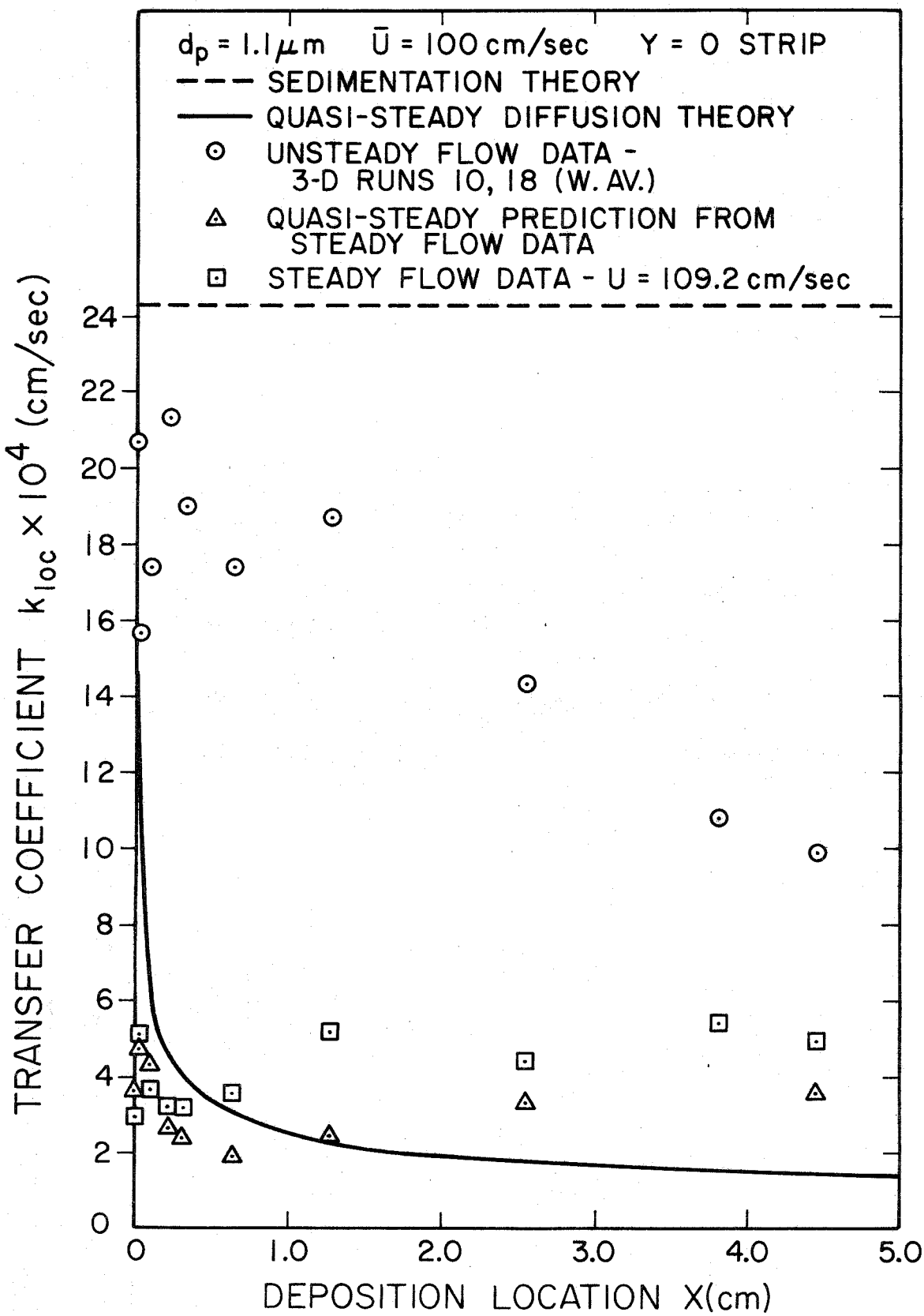

Figure 6.8 Comparison of Steady Flow Data with Unsteady Flow Data for 1.1 μm Particles in the 3-D Model

Section 6.3.3. The steady flow data have a generally uniform trend beyond the carina like the sedimentation theory, but k_{loc} for $X > 0.2$ cm. is in the range of the quasi-steady diffusion theory for point particles. Also, if steady laminar boundary layers are accounted for in sedimentation theory (Section 2.3.2), perhaps the steady flow data for $X > 0.2$ cm. can be estimated with better precision.

The disagreement between the unsteady and steady flow data may be caused by differences in the efficiency of impaction (including interception), differences in the efficiency of sedimentation and/or differences in the "clean air effect". It is also interesting to note that ϵ from Map 13 agrees well with the theoretical ϵ for convective diffusion of 1.1 μm particles.

The quasi-steady prediction from the steady flow data demonstrates a small peak at $X = 0.0275$ cm., a saddle between $X = 0.2$ and $X = 1.0$ cm., and a ridge from $X = 1.0$ cm. increasing in elevation toward the end of the branch. This is in marked contrast to the unsteady flow data which are much larger and show sharp, high peaks at the carina and at $X = 0.22$ cm. This suggests that, if secondary flows cause the peaks downstream from the carina, local intensities of secondary motions and their effects on particle deposition differ between unsteady and steady inhalations.

Thus, deposition measurements, made during steady inspiratory flow of 1.1 μm particles through the "3-D" model, cannot be used directly or in a quasi-steady calculation to approximate ϵ or the deposition patterns

occurring in the "3-D" model during simulated inhalations. This should also apply to other sizes of particles.

This conclusion is not surprising because during 450 c.c., 1.88 sec. inhalations in the "3-D" model the quasi-steady flow hypothesis is either invalid for all X or at least invalid for $X > 0.7$ cm. (From Section 1.3.5, $Freq > 1$; or $Freq' << 1$ only at $X > 0.7$ cm. According to Jaffrin and Hennessey (1972), the breathing frequency is too high and the flow rate too low to satisfy the hypothesis). Since $Freq'$ accounts for the local disturbances in the momentum boundary layer, it may be more useful than Freq for estimating where the quasi-steady deposition hypothesis holds. However, the "clean air effect" invalidates this hypothesis. Furthermore, it does not hold for 1.1μm particles because their trajectories deviate from a quasi-steady trajectory, especially during the deceleration phases of inhalation.

In multiple generation models of the lung, Section 1.3.5 suggests that quasi-steady flow is valid for all generations during normal breathing, except it may not apply to the first bifurcation if the flow rate in the trachea is less than 500 c.c./sec. It may also not be valid in regions of intense secondary flows, even though Freq and $Freq'$ indicate it should hold. Quasi-steady deposition will not hold for impaction range particles in regions having high flow rates.

In conclusion, deposition is strikingly different in lung models during steady and unsteady flow having the same time-average velocity.

Particle deposition studies done with steady flow in lung models probably cannot be used to accurately model deposition in the human lung.

6.5 The Effects of Secondary Flows on Particle Deposition

Local heat transfer coefficients measured in curved tubes suggest possible effects of secondary flows on particles in the diffusion subrange. Coefficients reported by Seban and McLaughlin (1963) varied by a factor of four from the outside bend to the inside bend around the circumference of the tube. The four-fold variation of shear rates around the daughter branch of a bifurcation (Section 1.3.2) suggests a wide variation in the transfer coefficient for particles in the diffusion subrange. However, these heat and particle transfer coefficients cannot be analogous because tube coils do not properly simulate the sharp bend between the axis of the parent tube and the inside wall of the daughter branch at bifurcations.

The best examples of the effects of the secondary flows are the lobular patterns or the two declining ridges of deposition running diagonally from Y = 0, X = 0.4 - 0.8 cm. to Y = ± 9, X = 2.1 cm. in Maps 9 and 11 and from Y = 0, X = 0.4 - 0.8 cm. to Y = ± 9, X = 1.2 cm. in Maps 10 to 12. This shift in position of the ridge from X = 2.1 to X = 1.2 cm. was caused by the doubling of the number of helical revolutions per unit distance as the flow increased from $\overline{U} = 100$ to $\overline{U} = 200$ cm./sec. These lobular patterns or diagonal ridges are observed in nearly all the

maps in the same location. They are more obvious, however, and extend farther toward the outside wall for the smaller particles and at the higher flow rate.

Other examples, which are associated with the lobular patterns, are the peaks of deposition between Y = ± 2 and X = 0.2 - 0.8 cm. in most maps and the corresponding peaks from X = 0.2 - 0.8 cm. along Y = 0 in Plots 1 - 12. Secondary flows initiate near the carina and become fully developed in this region (Sections 1.3.2, 3.2.2, and 4.3), causing enhanced deposition for all sizes of particles. In this region enhancement is greatest because the secondary flows are most intense, the boundary layers are the thinnest and the clean air is replaced most rapidly.

Major experimental evidence for the effect of secondary flows during steady flow runs is described below. Map 13 shows that 1.1 μm particles in steady flow deposit beyond Y = ± 2 toward Y = ± 9 in a pattern analogous to those produced by the unsteady helical flows in this same region in Map 5. The peaks within contour B in Map 13 between X = 3.2 and X = 4.76 cm. and at X = 0.0275 cm. also corresponds to similar peaks in Figure 6.8 for the "quasi-steady data". The enhancement of deposition at the last counting site along Y = 0 was also observed for unsteady runs in Plot 6, Plot 8, and Figure D.1. This is evidence that the helical flow, generated near the carina, completes one revolution between X = 3.2 cm. and the end of the model.

Further evidence, reported by Chua and Wang (1972) for steady flow in a similar bifurcation model, showed that 0.109μm particles peak along Y = 0 near the carina and at two diameters downstream. A peak was noted along the outside wall (Y = ±9) at one diameter downstream.

More evidence of effects and a thorough explanation of how secondary flows cause these areas of enhanced particle deposition during steady and unsteady flow are presented in Appendix D. A pictorial description of the helical flows helps to provide a clear interpretation for the diagonal ridges observed on the contour maps. The variation of the effect on different size particles is also explained in terms of deposition mechanisms.

The following summarizes the overall effect of secondary flows on particle deposition in the "3-D" model. Local enhancement of deposition of 1.1μm particles attributed to the secondary flows is greater for unsteady inhalations than for steady inspiratory flow, and locations of enhancement also differ. These differences arose because the "clean air effect" (Sections 3.2.2 and 6.3.3) is absent in steady runs, the local structure of the boundary layer differs in the two cases, and the location of the helical flows differ.

During pulsatile inhalations, overall and local enhancement of deposition by the secondary flows was greatest for diffusion range particles, intermediate for particles in the transition range, and least for particles in the impaction range; it was also greater at $\overline{U} = 200$ than

at 100 cm./sec. for all particle sizes, as expected from theory (Sections 3.3 and 3.4).

The contribution of the secondary flows to the overall deposition efficiency ϵ is small, but to estimate local nonuniformities the secondary flows must be taken into account.

Chapter 7

APPLICATION OF MODEL RESULTS TO LUNG DEPOSITION

7.1 Application to the First Bifurcation

7.1.1 Effects on Deposition of Complexities in Geometry

The lumen of the primary bonchi is enlarged at the carina causing a slightly lower axial velocity than in the "2-D" and "3-D" models. Thus, deposition by impaction and convective diffusion is probably less at the carina in the lung than estimated from the models, but the general patterns of deposition are similar.

The actual carina is usually not as sharp as in the "3-D" model. Consequently, flow around the carina is somewhat analogous to flow around the forward surface of a circular cylinder; the broader region of stagnation flow causes a broader "hot spot" at the carina.

The corrugation of the walls of the primary bonchi increases interception at the high points and reduces interception at the low points compared with smooth-walled models. Microscopic folds in the mucous membranes lining the bronchi increase deposition where the folds are not concealed by mucus.

Because the breathing frequency is low, the 5% variation in the diameter of the large bronchi during normal respiration should not disturb the boundary layer and should not cause significant radial flows.

Also, since the dimensions of the models approximate the time-averaged dimensions in the real bronchi, particle deposition should be similar.

Data obtained for air at 25° C. and 74 cm. Hg. apply to the human lung at 37° C. and 76 cm. Hg. because the differences in the absolute and kinematic viscosities are too small to affect deposition.

7.1.2 Comparison of Cyclic Flow with the Single Breath

Since clean air is drawn back through the "3-D" model during the expiratory phase, particle deposition takes place only during the inhalation phase of the respiratory cycle. There is no pause between the two phases. In the lung, particles that remain airborne after the inspiratory cycle can deposit during pauses between the two phases or during expiratory flow. Consequently the "3-D" model results approximate the deposition only during inhalation in the primary bronchi.

For certain sizes of particles the deposition in the primary bronchi during the non-inhalation periods is small compared to the deposition during inhalation. Graphs such as Figure 1.4 and the associated calculations support this generalization for particles in the diffusion subrange ($d_p < 0.1 \mu m$) and in the impaction subrange ($d_p > 2 \mu m$). For such particles k_{av} and the local transfer coefficients measured in the "3-D" model approximate deposition in the primary bronchi during normal breathing.

Particles with aerodynamic diameters between 0.1 and 2.0μm deposit with the least overall efficiency in the lungs. Accordingly, deposition in this size range during the rest of the cycle is about the same as that during inhalation.

During the pauses, particles within the 0.1 - 0.5μm range deposit uniformly throughout the primary bronchi, while those in the 0.5 - 2.0μm range deposit by sedimentation around the inside wall. Consequently, the deposition patterns in Maps 1 - 12 must not be significantly modified; the "hot spots" would also be found at the same locations with nearly the same intensity. Quantitative estimates of deposition by diffusion and sedimentation during pauses can be made from either Beeckmans' (1965) or Landahl's (1963) model.

During exhalation, the 0.1 - 0.5μm particles deposit by convective diffusion and rates can be estimated from Levich (1962: 112 - 116). Secondary flows generated at the end of the branch (Section 1.3.2) may enhance deposition. The net effect is a more uniform pattern of deposition beyond X = 1.0 cm. However, the intense "hot spots" on Maps 9 and 10 near the carina and along the diagonal ridges are not changed.

During exhalation, 0.5 - 2.0μm particles deposit along the inside wall of the branch by sedimentation, and secondary flows may enhance deposition along both walls. The net effect in Maps 3 - 8 is to convert the ">" shaped contours at the end of the branches into parallel contours. The "hot spots" remain at the same locations with

nearly the same intensity.

Particles remain suspended in the airways after exhalation in the real lungs. Figure 1.4 shows that the concentration which remains is negligible compared to the inhaled concentration for $d_p > 1\,\mu m$ and $d_p < 0.1\,\mu m$. Particles with $d_p = 0.5\,\mu m$ have a concentration about 50 to 75% of the inhaled concentration.

Suspended particles increase the deposition during inhalation by partially nullifying the "clean air effect" (Section 6.3). The following equation demonstrates this effect:

$$\frac{\#\,\text{particles}}{\text{area}} = k_{loc}\left[n_{new} t - (n_{new} - n_{old}) t_2 \right], \qquad (7.1)$$

where k_{loc} is the local transfer coefficient for one particle diameter when there is no "clean air effect", n_{new} = concentration of particles in the inhaled air, n_{old} = concentration of particles remaining suspended in the airways before inhalation, t = inhalation time period, and t_2 = the time to develop the steady concentration boundary layer or to fill the clean air with sedimenting particles to the same concentrations as the inhaled air. Equation 7.1 shows that suspended particles increase the deposition at any location above that measured in the "3-D" model runs by an amount equal to $k_{loc} n_{old} t_2$.

The net result is that the values of the last few data points along any Y strip in the 0.365, 0.79 and 1.1 μm maps should be slightly

greater to better approximate deposition in the lungs.

7.1.3 Effects of Turbulence on Deposition

The effect of turbulence (Section 1.3.3) on deposition can best be analyzed separately for each size range. For $d_p < 0.5\mu m$, turbulent diffusion is the deposition mechanism. For $d_p > 0.5\mu m$, sedimentation and impaction are the mechanisms.

An additional complication is the humidification of the air within the trachea during mouth breathing. When the inspired air is dry and cool compared to lung conditions, Hidy and Brock (1969) and Owen (1969) predict that diffusiophoresis can significantly inhibit the deposition of 0.1 to $1.0\mu m$ particles occurring by turbulent diffusion in the trachea. Turbulent deposition of particles outside this range would not be significantly deterred. Nevertheless, if the laryngeal jet is directed against the inside wall of the trachea rather than axially on account of the trachea's nonvertical orientation, a "hot spot" or streak of deposition of all particle sizes would be expected, even with the deterrence by diffusiophoresis.

Pedley, Sudlow and Shroter (1971) show that the boundary layer remains laminar in the daughter branches of the first bifurcation for $Re < 15000$. An inhalation rate greater than 260 liters/min. (near the normal maximum inspiratory flow rate) is required for $Re > 15000$ in the primary bronchi. Thus, turbulent eddies generated by the larynx

during normal breathing are probably contained in the flow outside the laminar momentum boundary layer.

For $d_p > 0.5\mu m$, these eddies can enhance deposition by projecting the particles into the laminar boundary layer at a higher local rate than when no eddies are present. The largest particles (largest τ) have the greatest probability of penetrating the boundary layer (Friedlander and Johnstone, 1957). The enhancement for $d_p > 0.5\mu m$ would be greatest in regions with the thinnest, time-averaged momentum boundary layer--the carina of each bifurcation. Enhancement by sedimentation and impaction would be greatest in the primary bronchi and decrease in subsequent generations at the same rate as the turbulence is calculated to decay (Section 1.3.3). The amount of enhancement for $d_p > 0.5\mu m$ on the carina is difficult to estimate, but it is probably not significant for $Re < 3000$.

Schlesinger (1973) recently compared the deposition rates for particles of $9\mu m$, aerodynamic diameter in a hollow cast of the trachea and the first few orders of bronchi, with and without an attached hollow cast of a larynx. At steady inhalation flows of 15, 25, 35, 45, and 55 liters/min. with a larynx, he found significant enhancement of deposition in the trachea and negligible enhancement in the primary bonchi, compared to runs without the larynx.

For $d_p < 0.5\mu m$, the concentration boundary layer is thinner than the momentum boundary layer. Because of the short branch length

and low transfer rates, the particle concentration above the concentration boundary layer is essentially constant and equal to the mainstream concentration. Turbulent eddies would keep the mainstream well mixed and might enhance their deposition compared to nonturbulent conditions.

Kestin (1966) found that free-stream turbulence with intensities of 1.0, 1.9 and 2.5% increased the local heat transfer coefficients by 35, 60 and 80% respectively over the forward surface of a cylinder having a laminar boundary layer. For laminar boundary layer flow over a flat plate at zero incidence, free-stream turbulence does not change the heat transfer coefficients measured in the absence of turbulence. When a pressure gradient was imposed on the plate to cause a linearly accelerated free stream (analogous to wedge flow with $m = 1$), an intensity of 4.5% in free-stream turbulence caused a 6.2% increase in the local heat transfer coefficients. A 1% intensity caused no measurable increase.

Kestin speculates that the eddies cause oscillations in the boundary layers, resulting in a time-averaged change in the temperature and velocity profiles. However, the change is least close to the wall where the thin concentration boundary layer lies. Therefore, free-stream turbulence in the parent branch should not enhance deposition for $d_p < 0.5 \mu m$ along the strips between $Y = \pm 2$ in the daughter branch, when the intensity is $\leq 1\%$; an increase of $< 6\%$ might occur in this region at an intensity of 4.5%.

Since the carina becomes more rounded toward the dorsal and ventral walls of the trachea (Figure 1.2, Section 1.2.2), enhancement of deposition on these surfaces by free-stream turbulence may approach the behavior of circular cylinders. The net effect would be an increase in the area and intensity of the "hot spot" at the carina. This effect would probably be greatest in the primary bronchi and decrease in subsequent generations at approximately the same rate as turbulence decays (Section 1.3.3).

In conclusion, turbulence generated during normal inhalations in the lung may slightly alter the local deposition patterns and ϵ in the primary bronchi from the results of the "3-D" model.

7.1.4 Effect of Particle Charge

In the "2-D" and "3-D" runs particles were decharged, and the theories neglect deposition by electrostatic forces. Since natural and therapeutic aerosols are charged, deposition can be enhanced in the lung by two mechanisms. One is the attractive force between the charged particles and its image in the lung surface. The electrostatic repulsion force of the surrounding particles in the air in the lung, called the "space charge effect", is the other.

Fry (1970) found that electrostatic charges on atomized PSL aerosols of 4.06 and 1.86μm diameter caused negligible enhancement of deposition in the nasopharyngeal region of humans. Experiments by

Fraser (1966) in animals suggested that only a 1 to 2% enhancement can be expected in the lungs when natural aerosols carry a normal charge (10 to 20 electrons per particle).

Calculations (Appendix B.5) were made to compare the significance of the electrostatic mechanisms with impaction, sedimentation and diffusion in the primary bronchi. They suggest that charge effects are negligible for respirable particles generated by atomization and for natural aerosols which usually carry fewer charges than particles generated by atomization.

This evidence indicates that results for the "3-D" model can be used to estimate deposition of natural and therapeutic aerosols in the primary bronchi of humans.

7.2 Application to the Second and Lower Generations

The geometry and flow behavior in the "3-D" model are more similar in some ways to lower generations of the human lung than to the first bifurcation. For example, the first three geometrical differences discussed in Section 7.1.1 do not arise or are not significant between the "3-D" model and lower generations.

The 20% variation in the diameter of the lower airways during normal respiration can generate radial flows. These are likely to be significant only in the smallest airways, and the time-averaged diameters of the airways are probably adequate for modeling deposition by diffusion

and sedimentation. Flow oscillations caused by the heart will improve the gas mixing in the airways and alveoli. Consequently, minor modifications of equations for diffusion and sedimentation may be required for the pause periods. Conclusions to Section 7.1.2, 7.1.3 and 7.1.4 also apply to lower airways.

Considerations of similarity indicate that deposition patterns and efficiency data for the "3-D" can be applied to the lower airways under certain conditions (Sections A.3 and 2.4.1). Experimental data from the "3-D" model also agree well, over a limited range of parameters, with the theories for k_{loc} and ε which were derived to apply to any bifurcation.

For the diffusion range, Equation 2.43 with $A = A_3 S_1 / S_3$ (Section 3.2.1) can be used to estimate deposition along the Y = 0 strip at bifurcations in lower airways, and Equation 6.3 can be used to estimate the deposition efficiency. Contour Maps, 9, 10, 11 and 12 can be used to approximate the distribution of the deposition estimated by Equation 6.3 and to show the "hot spots".

These maps apply to the lower airways because secondary flows occur at every branch down to $Re \approx 10$ and the axial velocity profiles are similar. Secondary flows have the same general effects on deposition as shown in the maps, but the enhancement of deposition is less in the lower airways where the flows are less intense. Although axial velocity

profiles in the parent branches of lower airways may differ from the profiles in the parent branch of the "3-D" model, profiles in the daughter branches will not differ significantly from the "3-D" model. In addition, secondary motions in one generation keep the diffusion range particles well mixed for entry into the next generation.

For $d_p > 0.5\mu m$, Maps 1-8 describe deposition trends and "hot spots" locations in vertically oriented bifurcations. For other orientations, impaction with interception will still cause a "hot spot" at the carina, but the intensity will decrease in lower airways with slower axial flow. Sedimentation will produce a pattern similar to that along the inside wall on Maps 1 - 8.

For particles with $Stk > 1.3 \times 10^{-3}$ and at $Re > 800$, the deposition efficiency in lower airways can be roughly approximated by Equation 6.6. Likewise, the local transfer coefficients can be approximated by obtaining the "2-D" numerical solution for simultaneous impaction, sedimentation and interception. It is obtained as in Section 2.3.4 except that components of the terminal settling velocity, which are consistent with the bifurcation orientation, are used in Equations 2.20 and 2.21. The solution is then applied to the daughter branch as described in Section 3.2.1.

For particles with $Stk < 1.3 \times 10^{-3}$ and $d_p > 0.5\mu m$, ϵ in lower airways can be roughly approximated by Equation 6.4. Equation 2.17b, when multiplied by $\cos\sigma$, approximates the local transfer coefficients

beyond the carina.

Alternatively the fraction of particles of any size depositing in each generation during the respiratory cycle can be approximated by the models of Landahl (1950a, 1963), Beeckmans (1965), or the Task Group on Lung Dynamics (1966). The local distribution of the fraction depositing in each branch can then be estimated from the appropriate contour maps and equations.

Another approach worth investigating is the use of the single bifurcation as a model element for calculating deposition in the lung--just as single fiber elements are used to calculate collection efficiencies in fibrous filters. The theoretical and semi-empirical relations for ϵ from the "3-D" model would be used in the calculations.

7.3 Cigarette Smoke, Atmospheric Aerosol and Lung Cancer

Schlesinger and Lippmann (1972) measured the deposition efficiency for 1.7 to 12.2 μm particles (unit density) in each lobar bronchus of silastic lung models. Good correlation was found between deposition and the frequency of occurrence of bronchial carcinoma in the lobar bronchi. Results for our "3-D" model show that particles of this size cause the most intense "hot spots" at the carina. The momentum which these particles transfer to tissue is negligible. Therefore, the hypothesis that impacting particles directly injure tissue and that such injuries subsequently play a role in carcinogenesis should be rejected.

Particles in the 2 to 10 μm subrange contain a significant part of the mass in the atmospheric aerosol of cities where pollution is dominated by the combustion of coal and fuel oil (Pasceri and Friedlander, 1965). From information on the distribution of carcinogens with respect to particle size and the deposition results from the "3-D" model, it is possible to estimate the local dosage of carcinogens along the respiratory passage.

Carcinogens are known to exist in cigarette smoke, and there is strong statistical evidence linking smoking and bronchial carcinoma. Hence it is of interest to compare the deposition efficiency in the lung for particles in cigarette smoke with the frequency of occurrence of bronchial carcinoma. Data reported by Keith and Derrick (1960) for tobacco smoke, produced by a 44 c.c., 2 sec. puff, showed a relatively stable size distribution between 0.1 to 1.0 μm which peaked between 0.2 and 0.25 μm. Harris (1960) reported a distribution which peaked at 0.16 μm with a maximum particle size of 0.54 μm for a 35 c.c., 2 sec. puff. Recent data by Porstendörfer (1971) show that the average diameter of cigarette smoke increases by a factor of 1.55 when the relative humidity increases from 40 - 50% to 100%. These data suggest that the peak in the number distribution of cigarette smoke in the human lung is between 0.25 and 0.4 μm, corresponding to a peak in the mass distribution in the 0.45 to 0.6 μm range.

Data from the "3-D" model show a minimum deposition efficiency in each branch and a minimum "hot spot" intensity at the carina for particles in the 0.25 to 0.6μm range. Consequently, if the distribution of carcinogens with respect to particle size in cigarette smoke is assumed uniform, the dosage to the carina is near a minimum for a given mass loading of smoke. In spite of this, a heavy smoker suffers large dosages in the upper airways by inhaling a large mass of smoke particles.

Convective diffusion controls the deposition of cigarette smoke in the upper airways. To compare the relative deposition with the frequency of occurrence of bronchial carcinoma, Weibel's Model "A" was used with 450 c.c., 2 sec. inhalations and the flow rate curve of Figure 4.4. Bifurcation angles were assumed to be 70°. Equations 6.2 and 3.9 were used to calculate the deposition efficiency by convective diffusion of 0.3μm particles in each branch of the first three generations. Then, the fraction of the particles exiting the trachea which deposited in each generation and the "total fraction" which deposited in generations 1, 2 and 3 were calculated.

The number of cases of carcinoma which originated in the main bronchi were summed and were referred to as the number of cases in generation #1. Likewise, the cases for the lobar and segmental bronchi were summed and were respectively referred to as cases in the #2 and #3 generation. The percentage of the "total fraction" which deposited

in each generation was compared with the frequency of occurrence of bronchial carcinoma in the corresponding generations.

The results are shown in Table 7.1. The relative average dosage of 0.3μm particles, which is predicted for the first three generation in Weibel's Model "A" of human lungs, agrees roughly with the frequency that bronchial carcinomas originate in each of these generations. It should also be noted that nearly the same relative average dosages are predicted for any particle in the diffusion subrange.

Auerbach et al. (1961) and Kotin and Falk (1959) have found histological evidence that bronchial carcinoma originates more frequently in the bifurcation regions than at other locations along the major airway. The "hot spots" shown on Maps 9 and 10 for 0.365μm particles are also located in the bifurcation region. Approximately 10 times more cigarette particles deposit in the pulmonary region than in the tracheobronchial tree. However, the average number of particles deposited per unit area in the pulmonary region is only about 1/50th of the number deposited per unit area within the "hot spots" near the carina of each bifurcation in the upper airways. The relative "hot spot" dosage of cigarette smoke to the carina in each of the first three generations of the lung, calculated from Equation 3.9, is the same as the relative dosage in Table 7.1. If the secondary flows are taken into account, the relative "hot spot" dosages do not change significantly. Thus the heavy dosage at these "hot spots" may be critical for initiating the malignancies.

Gen #	# Cases of Carcinoma per Gen	% of Cases per Gen	Relative Dosage[+] Cigarette Smoke in Each Generation
‡ Case I			
1	16	15.4	19.7
2	44	42.3	31.2
3	44	42.3	49.1
§ Case II			
1	40	17.4	19.7
2, 3	190	82.6	80.3
‖ Case III			
1	296	36.4	19.7
2, 3	518	63.6	80.3

[+] (Fraction of the particles exiting the trachea which deposited in generation i)/(Total fraction of particles exiting the trachea which deposited in the first 3 generations) x 100

‡ Garland, et. al. (1962)

§ Garland (1961)

‖ Bryson and Spencer (1951)

Table 7.1 Sites of Origin of Bronchial Carcinoma and Relative Dosages of Cigarette Smoke* During 450 c.c. 1.88 second Inhalations into Weibel's Model "A".

* Calculations for 0.3 μm diameter, unit density spheres

7.4 Tissue Dosage and Effects

A more complete model for calculating local dosage to tissue requires additional information on local transport rates of particles by the moving mucous film and on rates of transport of specific chemicals from the particles to tissue.

Several regions of stasis in the moving mucous film occur in the bronchial airways (Hilding, 1957). The carina in all airways is one such region, and it also corresponds to the location of the main "hot spot" for most particles. Particles depositing at these locations will remain, and particles carried by the mucous film can deposit at the same locations. Acidic particles, like H_2SO_4 droplets, could also cause new areas of stasis in the film if they destroy ciliated cells in the "hot spot" locations.

Afferent nerve endings, which serve as irritant or cough receptors in the tracheobronchial tree of mammals, are most concentrated at bronchial bifurcations (Widdicombe, 1954). Stimulation of these receptors in large airways by SO_2 or irritant particles causes constriction of upper and lower airways. Stimulation of similar receptors in lower airways causes constriction of lower airways (Nadel, et al., 1965; Alarie, 1973). "Hot spots" observed in the bifurcation region help explain how bronchial constriction and coughing can occur so rapidly after inhalation of irritants. This evidence also offers a teleological explanation for the high concentration of receptors at bifurcations.

Amdur and Corn (1963) studied the dose-response of guinea pigs to zinc ammonium sulfate aerosol. They found an increase in flow resistance with decreasing mass median diameter between 1.4 and 0.29 μm at a concentration of 1 mg/m^3. The calculated increase in resistance per single particle, however, was greater for the largest particles. Thus, the greater number concentration of the smaller size aerosol outweighed the greater individual irritancy of the larger particles.

To interpret these data one first notes that the upper airways of the guinea pig are approximately 9 times smaller in diameter than corresponding generations in the human lung. However, calculations indicate that the percentage of respired particles retained in the pulmonary region and the percentage retained in the tracheobronchial region, for a given particle diameter, are similar in the guinea pig and man (Kliment, Libich, and Kaudersova, 1972). Accordingly, the local deposition patterns from the "3-D" model apply approximately to bronchi in the guinea pig.

Zinc ammonium sulfate particles from 0.29 to 1.1 μm in diameter are aerodynamically equivalent to unit density spheres with diameters from 0.4 to 2.0 μm. These particles cause "hot spots" at bifurcations, but those for the larger particles are more intense. Also, the fraction of inhaled particles depositing in any bronchus is greater for the larger salt particles. This helps explain why single large particles are more

irritant than single small particles.

Two cases were considered to explain Amdur and Corn's result. First, average transfer coefficient data in Figure 6.1 were divided by the particle mass to give the number of particles of each diameter deposited per unit area when equal mass concentrations of each size are inhaled into a specific generation. k_{av}/d_p^3 vs. d_p has a trend similar to that of increasing resistance with decreasing particle size over the 0.4 to 2.0μm range. This suggests that the larger number of small particles per area can stimulate more individual receptors than a smaller number of large particles in the same area. Therefore the increase in resistance is not dependent on the mass dosage alone.

In the second case, k_{av}/d_p^2 vs. d_p was plotted from data in Figure 6.1. This weights k_{av} for each size particle by its surface area or time for dissolution. The points for $d_p < 0.8\mu$m had a trend similar to Amdur and Corn's data. The 1.1 and 2.02μm data also fall in line with the smaller sizes after the k_{av} data are corrected for the losses of large particles in the nose (guinea pigs are nose breathers). In this form k_{av} represent the relative mass of particles of each size depositing in a lower order airway when equal mass concentrations are inhaled through the nose. Thus, when equal masses of small and large particles deposit in the same area, the small particles dissolve more rapidly than the large ones and cause a greater increase in airway resistance.

The rate of dissolution is important because the moving film of mucus spreads the "hot spots" of particles and dissolved chemical over a wider area, diluting the local concentration of irritant. A higher rate of dissolution, therefore, assures a higher concentration of the irritant at the receptors. In deciliated areas, a higher rate of dissolution assures a more rapid response to the irritant.

In conclusion, factors besides average local deposition rates are important for modeling the acute dose-response of irritants in the lungs. These include the particle surface area or rate of dissolution, sites of irritant receptors, and transport rates of particles and chemical in the mucous film.

7.5 Gas and Heat Transfer and Other Applications

The local transfer rates of pollutant gases, such as SO_2, NO_2 and O_3, to the walls of the lungs can be estimated from the theoretical and experimental results for the diffusion subrange. This is based on the approximation that diffusion boundary layer theory can be extended to the case of $\nu/D \rightarrow 1$. As shown in Section 2.4.2, this approximation causes an error of only a few percent. Thus, the analysis of Section 7.2 for the diffusion subrange applies to gases. Maps 11 and 12 for 0.088μm particles approximate the local patterns of gas transfer during inhalation, and the magnitude of k_{loc} for the gas is estimated by multiplying k_{loc} for 0.088μm particles by $(D_{gas}/D_{particle})^{2/3}$. This also

applies to heat transfer in bifurcating tubes for which $Sc \approx Pr \approx 1$.

Results for the diffusion subrange can be used to estimate transfer rates of gases and suspended protein or fat molecules from blood flowing through bifurcating vessels in the human body or artificial systems. When flow and geometrical similarity are maintained, the contour maps for the 0.088μm and 0.365μm particles directly approximate the local deposition rates for fat and protein molecules because their Schmidt numbers have the same range, 10^4 to 10^5.

Local mass and heat transfer coefficients are usually more difficult to measure than the transfer coefficients for particles in the diffusion subrange. Therefore, the experimental approaches used in this study can be applied to other flow systems to approximate local and mass transfer coefficients.

Chapter 8

SUMMARY

8.1 Summary of Experiments, Results, Conclusions and Applications

Experiments on particle deposition have been conducted in two and three-dimensional models simulating the first bifurcation of the human lung (Bell and Friedlander, 1973). Local transfer coefficients were measured for monodisperse latex aerosols of unit density in the size range from 0.088 to 7.6 μm. Flow rates simulated normal inhalations at conditions of rest and moderate exercise. Particles were counted by optical and electron microscopy, and the aerosol concentration was measured either by light-scattering photometry or by gravimetry. The deposition patterns, measured in the "3-D" model for each aerosol at two flow conditions (450 c.c. tidal volume inhaled over 1.88 or 0.94 sec.), were depicted by computer-plotted maps with contours of constant transfer coefficients.

Curves of local transfer coefficients for particle deposition in both models are similar in form to those for the deposition efficiency in the entire lung and for the collection efficiency of fibrous filters. The minimum transfer coefficient occurs within the transition subrange at a diameter between 0.5 and 1.0 μm. The highest local dosage occurs near the carina and, depending on particle size, is an order of magnitude or more greater than the deposition at the end of the branch.

Larger particles (impaction subrange) produce higher local dosages near the carina, relative to the average deposition, than smaller particles (diffusion subrange).

Calculations of deposition at the bifurcation by inertial impaction, sedimentation and interception were based on a steady, two-dimensional flow over a wedge. Steady and quasi-steady laminar boundary layer flows along a wedge were employed to model the particle deposition occurring by convective diffusion. These two-dimensional theories were modified for application to the "3-D" model.

Theoretical calculations for impaction and interception of 2.68 and 7.6μ particles in the "2-D" model agree fairly well with experiment, while diffusion theory is in fair agreement with data for 0.365 and 0.79 μm particles. Data for the 1.099 and 2.02μm particles fall between the two theories because the unsteady aerodynamic boundary layers inhibit deposition. Impaction calculations with a steady laminar boundary layer predict no particle deposition beyond 0.01 cm. from the carina. Interception played a significant role in the deposition of all particles, and deposition by convective diffusion at locations $\geq$ 2.54 cm. from the carina was retarded by the clean air in the "2-D" model before each inhalation.

In the case of the "3-D" model, the minimum local and average deposition for the 450 c.c., 1.88 sec. inhalations ($\overline{U}$ = 100 cm./sec. in

the parent branch) occurs between 0.5 and 1μm, but for the 450 c.c., 0.94 sec. inhalations ($\overline{U}$ = 200 cm./sec.) the minimum occurs between 0.35 and 0.7μm. Particles in the diffusion and the impaction and sedimentation subranges may have the same average transfer coefficient, but their deposition patterns are considerably different.

Peak "hot spots" were located at the carina and between 0.2 to 0.8 cm. downstream along the inside wall of the daughter branch. The "hot spot" intensity, $\overline{k}_{0.6\%Area}/k_{av}$, varied from a high of 25.4 for the 5.7μm, 200 cm./sec. run to a low of 3.35 for the 1.1μm, 100 cm./sec. run. In other words, the 150,000 epithelial cells lining the lung wall within the small area of this "hot spot" receive 64 times more 5.7μm particles than predicted by assuming uniform deposition over the branch. The intensity is greatest for particles in the impaction and sedimentation subrange and increases rapidly with particle size. The intensity is also greater at the higher velocity for particles > 1.0μm. Particles in the diffusion subrange have the lowest intensity (~ 3.7), which is essentially constant and independent of velocity.

A "cumulative surface area distribution" curve for each contour map demonstrates the uniformity of dosage. The percentage of the surface receiving essentially no deposition decreases from a maximum of 49% for the 5.7μm particles to 0% for the 0.365 and 0.088μm particles. The 5.7 and 2.02μm particles deposited nonuniformly along the inside wall by sedimentation and impaction with interception. Deposition of

0.365 and 0.088 μm particles by convective diffusion was nonuniform and extended over the entire surface of the daughter branch in the "3-D" model. The 0.79 and 1.1 μm particles deposited nonuniformly along the inside wall by sedimentation and nonuniformly along part of the outside wall by interception and diffusion from the helical flow. The degree of nonuniformity within the area receiving deposition was greatest for the 5.7 μm particle at both flow rates; the most uniformity generally occurred for the 1.1, 0.79 and 0.365 μm particles at either flow rate.

If the secondary flows and sedimentation are accounted for, the deposition along the Y = 0 strip (inside wall) in the "3-D" model is consistent with the data from the "2-D" model. The "2-D" theory of simultaneous impaction, sedimentation and interception agrees fairly well with the 5.7 μm data. The 0.365 and 0.088 μm data are in fair agreement with the "2-D" theory of convective diffusion of point particles in quasi-steady laminar boundary layer flow. The 2.02, 1.1 and 0.79 μm data fall between the two theories; in addition, the trend of the data agrees best with sedimentation theory. To improve the agreement between the data and theory, the effects of unsteady boundary layers, secondary flows, and clean air in the model before each inhalation must be taken into account.

Deposition efficiency calculations based on the wedge flow in the "3-D" model are in better agreement with the experimental results

than the theoretical models of either Landahl or the Task Group on Lung Dynamics. Landahl's model overestimates all the data; the Task Group's model only overestimates all data > 0.1 μm and to a lesser degree than Landahl's model. The experimental deposition in the transition subrange between 0.1 and 1.0 μm can be more accurately modeled if one mechanism is assumed to control the deposition of each particle than if the efficiencies from all the mechanisms are combined.

Deposition patterns and the overall magnitude of the transfer coefficients were significantly different for unsteady and steady inhalation of 1.1 μm particles. Experimental studies with steady flow in lung models are not accurate for modeling the deposition in real lungs.

The contribution of the secondary flows to the overall deposition efficiency (ε) is small, but to estimate local nonuniformities the secondary flows must be taken into account. Secondary flows caused peaks and ridges of deposition downstream from the carina in both unsteady and steady inhalations, but the local enhancement was greater for unsteady inhalations. Locations of the enhancement by secondary motions also differed for the steady and unsteady inhalations. During unsteady inhalations, the overall and local enhancement was greatest for the diffusion subrange, intermediate for the transition subrange, and least for the impaction subrange. For all particle sizes the overall and local enhancement was also greater at $\overline{U} = 200$ cm./sec. than at $\overline{U} = 100$ cm./sec.

The "2-D" and "3-D" models (experimental and theoretical) can be used to estimate deposition in the tracheobronchial tree of normal lungs. The deposition fraction, occurring in each successive generation of the lung during the inhalation and exhalation phases, can be approximated using an airway model and the theoretical and semi-empirical correlations for ϵ, derived from the "3-D" model. The local distribution of the deposition within each branch of each generation can then be estimated from the appropriate contour maps or from the theoretical relations for k_{loc}, derived from the "2-D" model. During pauses, deposition by diffusion and sedimentation can be calculated either from Beeckmans' (1965) or Landahl's (1963) model.

The results have application to inhalation therapy with medical aerosols and to the diagnosis of lung diseases by X-ray opaque or radioactively tagged aerosols. To deliver an aerosol to the human airway which will completely cover the walls in the most uniform manner, unit density particles with diameters $\leq 0.5\mu m$ should be inhaled at low rates. Particles between 0.5 and $1.0\mu m$ can be inhaled at any flow rate for a highly uniform coating over more than 75% of the airway surface. To obtain the most nonuniform coating with the least surface coverage in the upper airways, unit density particles $\geq 5\mu m$ in diameter should be inhaled rapidly, as by panting. This will also assure a maximum accumulation at the carina of each bifurcation.

Current federal standards for atmospheric particulate pollution are stated in terms of total mass loadings per unit volume of air. For example, the current primary standard, which relates to human health, is $75 \mu m/m^3$ (annual average). Data from this study indicate that, depending on particle size, the average dosage in a generation of the lung may vary by as much as 100 times for the same mass loading of particulate matter. Although particles in the diffusion and impaction subranges may have the same average dosage, their local dosages can vary by as much as 60 times. Thus, particle size should be taken into account in setting standards for particulate pollution.

Although approximately 10 times more cigarette particles deposit in the pulmonary region than in the tracheobronchial tree, the number deposited per unit area within the "hot spots" near the carina of each bifurcation in the upper airways is 50 times greater than the average number of particles deposited per unit area in the pulmonary region. The relative intensity of the "hot spots" calculated for cigarette smoke in the first three generations of the human lung roughly agree with the frequency that bronchial carcinomas originate in each of these generations. However, a more comprehensive model for calculating the local dosage to the tissue must include the local transport rates of particles by the moving mucous film and the rates of transport of specific chemicals from the particles to the tissue. Modeling of acute effects from irritant particles and gases, like an increase in flow

resistance, must include the locations of the afferent nerve endings in the tracheobronchial tree. Specifically, it was found that if the dissolution time of soluble particles is assumed proportional to the particle surface area, their effects on flow resistance in Guinea pig lungs can be estimated by using the "3-D" model results.

Other important applications are to gas and heat transfer. Estimates of local transfer rates of pollutant gases such as O_3 and SO_2 in the lung airways and of gases and fat molecules at bifurcations in blood vessels can be made from the results of the diffusion subrange. Local mass and heat transfer coefficients are often difficult to measure. By properly taking the Schmidt number into account, local particle transfer coefficients in the diffusion subrange can be used to estimate heat and mass transfer coefficients.

8.2 Future Research

Further efforts in lung modeling should concentrate on developing a more comprehensive model to account for average and local particle deposition, particle clearance rates, local transport rates of specific chemicals to the tissue, local radiation dosages, and possible acute effects like changes in the flow resistance. The various components are currently at different stages of development. At some point they must be tied together in a dynamic model which can assess the health effects of environmental pollution.

A short experimental study should be done to determine the local deposition patterns in the parent branches of a network of branching tubes during unsteady and steady exhalations. The results would serve as an experimental check on the postulated effects of deposition during exhalation on the inhalation results of the "3-D" model.

Research is also needed to explain and model the behavior of aerosols in unsteady laminar boundary layers and in unsteady secondary flows such as those in the lungs. The effects of free-stream turbulence on particle deposition at bifurcations should be investigated.

Appendices

Appendix A

THEORETICAL DERIVATIONS

A. 1 Potential Flow Solution in the Two-Dimensional Model

Milne-Thomson (1968) gives a procedure for determining the streamlines in a canal with a side branch. Since the "2-D" model is symmetric, the streamlines can be derived by modifying Milne-Thomson's procedure for either the top or bottom half of the model--the center being determined by the stagnation streamline. The top half of the model is shown in the z-plane in Figure A. 1. The free stream velocity upstream from the branch at A_∞ is U, and the downstream velocity is U_2. $A_\infty C$ is the stagnation streamline, while the streamline $A_\infty E D_\infty$ undergoes an abrupt change of direction at E, causing an infinite velocity.

First, the branch form in the z-plane is eliminated by transforming into the Q-plane (Figure A. 1) by the transformation equation

$$Q = \log \frac{U}{\nu'} = \log \frac{U}{q} + i\theta,$$

where $\nu' = qe^{-i\theta} = u_f - iv_f$. Here, $q = \sqrt{u_f^2 + v_f^2}$, the stream speed. Along the sides of the main canal $\theta = 0$; while along the branch $\theta = \alpha$. At C $q = 0$; hence, Q is infinite. The infinite strip in the Q-plane can now be mapped into the ζ-plane (Figure A. 1) by means of the Schwarz-

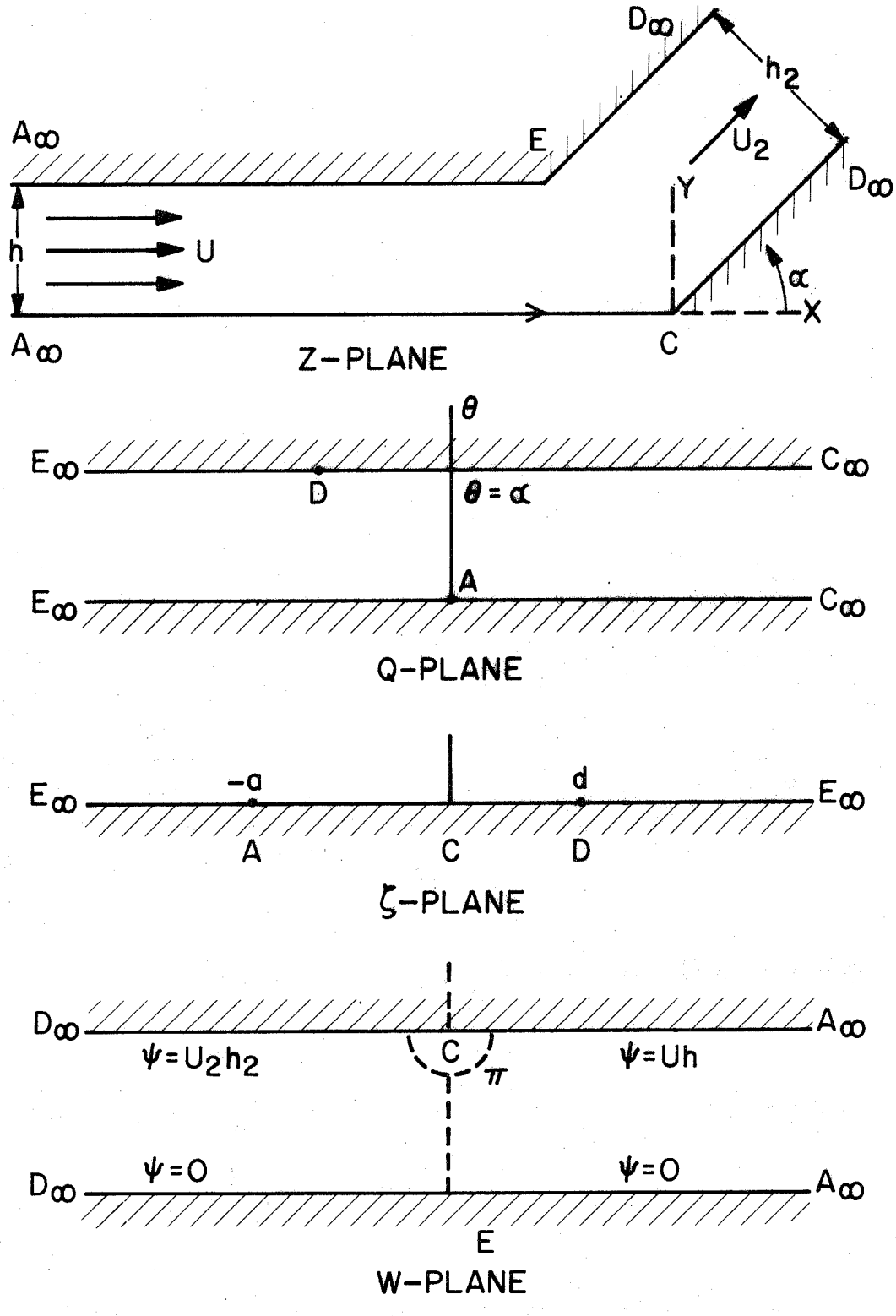

Figure A. 1 Planes Used to Determine the Potential Flow Solution for the Two-Dimensional Model

Christoffel transformation, which results in the following:

$$\zeta = e^{-Q\pi/\alpha} = -\left(\frac{\nu'}{U}\right)^{\pi/\alpha}. \tag{A.1}$$

The following values of ζ and ν' correspond by the above transformation equation:

$$\zeta = -a \qquad \nu' = U$$

and

$$\zeta = d \qquad \nu' = U_2 e^{-i\alpha}. \tag{A.2}$$

Therefore, from (A.1) $a = 1$, and $d = (U_2/U)^{\pi/\alpha}$.

The next step is to construct the complete potential plane or W-plane where $W = \phi + i\psi$. ϕ represents the potential function, while ψ represents the stream function.

Using $\psi = 0$ on $A_\infty ED_\infty$, the boundary conditions are as follows:

$$\text{on } A_\infty ED_\infty \qquad \psi = 0,$$

$$\text{on } A_\infty C \qquad \psi = Uh,$$

and

$$\text{on } CD_\infty \qquad \psi = U_2 h_2.$$

Therefore,

$$Uh = U_2 h_2, \tag{A.3}$$

which also follows from the equation of continuity.

Taking $\phi = \infty$ at A_∞ and $\phi = -\infty$ at D_∞, the result is the W-plane diagram shown in Figure A.1. To map the W-plane into the ζ-plane, the Schwarz-Christoffel transformation is used again to give

$$\frac{dW}{d\zeta} = K_1(\zeta+a)^{-1}(\zeta-d)^{-1} = \frac{K_1}{(a+d)}\left[\frac{1}{(\zeta-d)} - \frac{1}{(\zeta+a)}\right].$$

Integrating

$$W = \frac{K_1}{(a+d)} \log \frac{(\zeta-d)}{(\zeta+a)} + L_1 , \qquad (A.4)$$

where K_1 and L_1 are complex constants.

The author's original potential flow derivation was critically analyzed by Dr. Norman Malmuth and Dr. William Hall (1970). They found that Milne-Thomson's derivation and the author's derivation were in error, because K_1 and L_1 were assumed to be either real or imaginary. As indicated above, K_1 and L_1 must be assumed to be complex constants to be evaluated correctly.

Using the boundary condition that $\psi = 0$ on $D_\infty E$, $(\zeta+a)$ and $(\zeta-d)$ have the same sign. Thus, on $D_\infty E$ the logarithms are all real. Therefore, on $D_\infty E$ (Re = real, Im = imaginary)

$$\phi = \frac{\mathrm{Re}K_1}{(a+d)} \log \left|\frac{\zeta-d}{\zeta-a}\right| + \mathrm{Re}L_1$$

and

$$\psi = 0 = \frac{\mathrm{Im}K_1}{(a+d)} \log \left|\frac{\zeta-d}{\zeta+a}\right| + \mathrm{Im}L_1 .$$

Hence,

$$\mathrm{Im}L_1 = \frac{-\mathrm{Im}K_1}{(a+d)} \log \left|\frac{\zeta-d}{\zeta+a}\right| .$$

Evaluating the log in the limit as $\mathrm{Re}\zeta$ approaches ∞, $\log(1) = 0$. Therefore, $\mathrm{Im}L_1 = 0$. Thus, $0 = \frac{-\mathrm{Im}k_1}{(a+d)} \log \left|\frac{\zeta-d}{\zeta+a}\right|$.

Evaluating the log in the limit as $\zeta \to 0$, $\log \left|\frac{-d}{a}\right|$ = constant; hence $\mathrm{Im}K_1 = 0$. Applying the other boundary condition that $\psi = U_2 h_2$ at C, set $\phi = 0$ since C is a stagnation point. Thus, $\zeta = 0$ at C and substituting into (A.4)

$$W = iU_2 h_2 = \frac{i\mathrm{Re}K_1 \pi}{(a+d)} + \frac{i\mathrm{Im}K_1}{(a+d)} \log \left|\frac{d}{a}\right| + i\mathrm{Im}L_1 .$$

From the results of the first two boundary conditions above, the last two terms equal zero. Rearranging,

$$\mathrm{Re}K_1 = \frac{U_2 h_2 (a+d)}{\pi} = \frac{Uh(a+d)}{\pi} = K_1 .$$

Using $\phi = 0$,

$$0 = \frac{\mathrm{Re}K_1}{(a+d)} \log \left|\frac{d}{a}\right| + \mathrm{Re}L_1 - \pi\, \mathrm{Im}K_1 .$$

Therefore,

$$\mathrm{Re}L_1 = \frac{-Uh}{\pi} \log \left|\frac{d}{a}\right| = L_1 .$$

Substituting these values of L_1 and K_1 into (A.4) and setting $a = 1$ from (A.2), the general solution for the complex potential in the symmetric model is the following:

$$W = \frac{Uh}{\pi} \log \left[\frac{\zeta/d - 1}{\zeta + 1}\right] \qquad (A.4')$$

From (A.1)

$$\zeta = -\left(\frac{\nu'}{U}\right)^{\pi/\alpha} = \left(\frac{\nu' e^{i\alpha}}{U}\right)^{\pi/\alpha} ;$$

Rearranging,

$$\frac{-dW}{dz} = \nu' = Ue^{-i\alpha_\zeta \alpha/\pi}. \tag{A.5}$$

Differentiating (A.4′) and dividing by (A.5).

$$\frac{dz}{d\zeta} = \frac{-h}{\pi}\left[\frac{1}{(\zeta-d)} - \frac{1}{(\zeta+1)}\right]e^{i\alpha_\zeta - \alpha/\pi}.$$

Integrating with respect to ζ with $\alpha = \pi/4$ for the 90° model,

$$z = \frac{-h}{\pi} e^{i\pi/4}\left[\int\frac{\zeta^{-1/4}}{\zeta-d}\,d\zeta - \int\frac{\zeta^{-1/4}}{\zeta+1}\,d\zeta\right]$$

Transforming variables by $\zeta = x^4$, evaluating integrals from tables (Dwight, 1951) and substituting $d = (h/h_2)^4$ from (A.2) and (A.3) above,

$$z = x + iy = \frac{\sqrt{2}h}{\pi} e^{i\pi/4}\left\{1/2 \log\left|\frac{\zeta^{1/2} - \sqrt{2}\zeta^{1/4} + 1}{\zeta^{1/2} + \sqrt{2}\zeta^{1/4} + 1}\right| + \tan^{-1}\left[\frac{\sqrt{2}\,\zeta^{1/4}}{1 - \zeta^{1/2}}\right]\right\}$$

$$\frac{-h_2}{\pi} e^{i\pi/4}\left\{\log\left|\frac{\zeta^{1/4} - h/h_2}{\zeta^{1/4} + h/h_2}\right| + 2\tan^{-1}\left[\zeta^{1/4}\,\frac{h_2}{h}\right]\right\}. \tag{A.6}$$

Since $z = 0$ corresponds to $\zeta = 0$ from the transformations in Figure A.1, the integration constant $C = 0$.

Because (A.6) is not analytically invertible to give $\zeta = f(z)$, one must use (A.4′) and (A.6) as the solutions for the complex potential at location z in the z-plane in terms of the implicit variable, ζ. The stream function ψ is the complex part of W in terms of ζ at location z

in terms of ζ. Likewise, the complex velocity, $\nu' = u_f - iv_f$, is given by (A.5) in terms of ζ at location z in terms of ζ in (A.6). Therefore, derivation of an analytical expression giving the stream function or the complex velocity as a direct function of z-coordinates is not feasible.

A.2 Approximate Potential Flow Solution Along the Wedge of the "2-D" Model

Expanding each term of the complex potential function (A.4') in an infinite Maclaurin Series about $\zeta = 0$ and combining terms, the result is

$$W \simeq \frac{Uh}{\pi}\left[i\pi - (1+1/d)\zeta + 1/2(1-1/d^2)\zeta^2 - 1/3(1+1/d^3)\zeta^3 + \ldots\ldots \right]. \quad (A.7)$$

The expansion is an analytic function of ζ for $|\zeta| < d$ or 1, whichever is smaller. Neglecting the second order and higher order terms in ζ and differentiating with respect to ζ produces

$$\frac{dW}{d\zeta} \simeq \frac{Uh}{\pi}\left[-\left(\frac{1}{d}+1\right) \right]. \quad (A.8)$$

Dividing (A.8) by the negative of the complex velocity in (A.5) gives

$$\frac{dz}{d\zeta} = \frac{h}{\pi}\exp(i\alpha)\zeta^{\left(\frac{-\alpha}{\pi}\right)}\left[1 + \frac{1}{d} \right]. \quad (A.9)$$

Integrating (A.9) with respect to ζ and setting the integration constant equal to zero (since $z = 0$ at $\zeta = 0$),

$$z = \frac{h}{\pi} \exp(i\alpha) \frac{\zeta^{(1-\alpha/\pi)}}{(1-\alpha/\pi)} (1 + 1/d). \tag{A.10}$$

Solving for ζ in (A.10) and substituting $d = (h/h_2)^{\pi/\alpha}$,

$$\zeta = \left\{ \left(\frac{\pi-\alpha}{h} \right) \exp(-i\alpha)\, z \right\}^{\left(\frac{\pi}{\pi-\alpha} \right)} \left\{ \left(\frac{h_2}{h} \right)^{\pi/\alpha} + 1 \right\}^{\left(\frac{-\pi}{\pi-\alpha} \right)} \tag{A.11}$$

Substituting (A.11) into (A.7), truncated after the first order term in ζ, results in

$$W = \frac{-A}{m+1} U \exp(-m\pi)\, z^{(m+1)} + i\,Uh, \tag{A.12}$$

where $m = \alpha/(\pi-\alpha)$. The constant A is defined as

$$A = \left\{ \frac{h}{(\pi-\alpha)} \left[\left(\frac{h_2}{h} \right)^{\pi/\alpha} + 1 \right] \right\}^{-m} \tag{A.13}$$

The general equations for the potential and stream functions and the velocity components, all in terms of polar coordinates ($r = (x^2+y^2)^{1/2}$, $\theta = \arctan y/x$) with the origin at the carina and $\theta = \pi$ on the stagnation streamline, are as follows:

$$\phi = \frac{-A}{m+1} U r^{m+1} \cos[m\pi - (m+1)\theta], \tag{A.14}$$

$$\psi = \frac{A}{m+1} U r^{m+1} \sin[m\pi - (m+1)\theta] + Uh, \tag{A.15}$$

$$u_f = AU r^m \cos m[\pi - \theta], \tag{A.16}$$

and

$$v_f = AU r^m \sin m[\pi - \theta]. \tag{A.17}$$

For the "2-D" model with the 90° wedge in Figure 2.1, $m = 1/3$ and $A = 0.82$ cm.$^{-1/3}$. (A.12) through (A.17) are valid for the model

in the range $|\zeta| < d = 0.284$, which corresponds to $r < 0.7$ cm. These equations are only approximations of the general potential flow solution in this region, since the second and higher order terms of the series expansion were neglected. For $r = 0.7$ cm. and $|\zeta| = 0.284$, the sum of the second order through fourth order terms of the series is 81% of the first order term. For $|\zeta| = 0.18$ and $r = 0.5$ cm., the sum of the second order through fourth order terms is only 37.6% of the first order term. Hence, the approximate solution is most exact close to the carina.

Two tests of the accuracy of (A.12) through (A.17) are as follows:

1. Using (A.15), the stream function on the outside wall of the daughter branch ($r = 1.3$ cm., $\theta = 3\pi/4$) is 19.4 cm.^{2}/sec. A general solution for the entire channel would predict $\psi = 0$ on the outside wall.

2. From (A.15), A is calculated assuming the boundary condition $\psi = 0$ at $r = 1.3$ cm. and $\theta = 3\pi/4$. It equals 1.03 compared to 0.82 determined by (A.13).

Both results indicate that the approximate solution underestimates the total flow through the channel by 20%.

A.3 Similitude Analysis

The analysis of the deposition of aerosols in the lung can be greatly simplified by using similarity theory. The aerosol deposition data obtained in a bifurcation model of one generation of the lung can be applied to predict the aerosol deposition in other generations if the following requirements hold:

1. Geometrical similarity of the flow boundaries,
2. Similarity of the fluid flow in each generation,
3. Similarity of the trajectories of the particles in each generation.

U, h and h/U are chosen as the characteristic velocity, length, and time respectively for the parent branch. Likewise, U_2, R_2 and R_2/U_2 are the characteristic parameters for the daughter branch. R_2 is the half width of the daughter branch and U_2 is the free stream potential velocity in the daughter channel. In dimensionless form Equation 2.14 becomes

$$\frac{d\vec{u}'}{dt'} = (\vec{u}' - \vec{u}_f' - \vec{V}_s')/Stk \qquad (A.18)$$

The Stokes number ($Stk = U\tau/R_2 = h_s/R_2$) is the ratio of the particle stopping distance in the direction of the free stream flow in the parent branch to the characteristic length of the daughter branch.

$\vec{V}_s'$ is the dimensionless terminal settling velocity defined as the ratio of the Stokes Number to the Froude Number (Stk/Fr). The Froude Number = $U^2/\vec{g}R_2$ = Fr.

For a general unsteady flow field in the bifurcation model, the x and y components of the fluid velocity are

$$u_f' = f_1(x', y', t', \alpha, h_2/h, \text{Re}, \text{Freq}')$$

and $$v_f' = f_2(x', y', t', \alpha, h_2/h, \text{Re}, \text{Freq}'),$$

where α is one-half of the wedge angle, h_2/h is the ratio of the branch width to the main channel half width, $\text{Re} = 2hU/\nu$ or $2R_2U_2/\nu$ is the fluid Reynolds Number based on the channel dimensions, and $\text{Freq}' = \delta(\omega/\nu)^{1/2}$ is the frequency parameter discussed in Section 1.3.5. x' and y' are the dimensionless cartesian coordinates shown in Figure 2.1. After choosing an initial condition, (A.18) can be solved analytically or numerically for the particle velocity at any time at any position (x', y'):

$$u' = f_3(x', y', t', \alpha, h_2/h, \text{Stk}, \text{Fr}, \text{Re}, \text{Freq}')$$

and $$v' = f_4(x', y', t', \alpha, h_2/h, \text{Stk}, \text{Fr}, \text{Re}, \text{Freq}'). \qquad \text{(A.20)}$$

For particles of finite radius, r_p, the boundary condition $u' = v' = 0$ holds when $y_1' = r_p/R_2 = I$. y_1' is the dimensionless coordinate perpendicular to the wedge and I is the Interception number.

The local flux of particles to the surface of the wedge by inertial

forces, F_s, has the units of particles/cm. sec. for the "2-D" model. This can be related to the flux of particles in the main stream flow before the wedge by the continuity relation, $F_s dx_1 = F_o dy$. Here dx_1 is a differential distance along the wedge surface and dy is a differential segment perpendicular to the main stream flow. All particles flowing through segment dy in the main stream of the parent branch with flux F_o deposit on segment dx_1 of the wedge surface with a flux of F_s. $F_s = F_o dy/dx_1$ is obtained analytically from (A.20) using the boundary condition $y_1' = I$, or it can be obtained numerically by $F_s = F_o \Delta y/\Delta x_1$. In either case

$$F_s = Un_\infty f_5(x', t', \alpha, h_2/h, Stk, Fr, Re, Freq', I), \qquad (A.21)$$

where n_∞ is the particle concentration in the main stream of the parent branch.

The local particle transfer coefficient, $k_{loc}(t') = F_s(t')/n_\infty$, and the average particle transfer coefficient, $k_{av}(t') = \int_o^L k_{loc}(t')dx_1/L$, where L = the length of the wedge surface in the model. The local deposition efficiency, ϵ_{loc}, can be defined for $h \geq x_1 \sin\alpha$ as

$$\epsilon_{loc}(t') = (1/\sin\alpha) f_5(x_1', t', \alpha, h_2/h_1, Stk, Fr, Re, Freq', I). \qquad (A.22)$$

The overall efficiency, ϵ, of the wedge in the bifurcation for particle removal by inertial impaction, sedimentation and interception is the following:

$$\epsilon(t') = k_{av}(t')n_\infty L/Un_\infty h = (L/h) f_6(t', \alpha, h_2/h, Stk, Fr, Re, Freq', I). \tag{A.23}$$

When the quasi-steady flow assumption holds and when potential flow is used to approximate the steady flow regime, $Freq' < 0.1$ and $Re = \infty$. The time-averaged local transfer coefficient for a single inspiration is calculated by time-averaging the deposition results predicted by steady potential flow during each differential time interval. This is equivalent to

$$k_{loc} = \frac{1}{t}\int_o^t k_{loc}(t')dt = Uf_7(x_1', \alpha, A', Stk, Fr, I), \tag{A.24}$$

where A' is the constant in Equation (2.5) in dimensionless form. Then,

$$k_{av} = Uf_8\left(\frac{L}{R_2}, \alpha, A', Stk, Fr, I\right) \tag{A.25}$$

and

$$\epsilon = (L/h) f_8\left(\frac{L}{R_2}, \alpha, A', Stk, Fr, I\right). \tag{A.26}$$

When the deposition occurs only by inertial impaction of particles of finite diameter, the Froude number is neglected in (A.24), (A.25) and (A.26). For pure inertial deposition the Interception number is also set equal to zero. When the particles of finite diameter follow the streamlines and deposit by interception, Stk and Fr are neglected. Deposition of finite diameter particles by sedimentation depends on all

parameters in (A.24) through (A.26). If the Interception mechanism is neglected for a settling particle in the lung model, the dependence on A' and I drops out of (A.24) through (A.26). When a steady laminar boundary layer is included in the flow regime, the deposition function also depends on the Reynolds number and a dimensionless boundary layer thickness, $\delta'(x_1)$.[1]

The conclusions of the dimensionless number analysis are as follows:

1. Rigorous similarity for simultaneous inertial impaction and sedimentation of finite diameter particles in two different bifurcation models, when potential flow is valid, requires geometrically similar (α, A, L/h are equal) and equal Stokes, Froude and Interception numbers for the two models. However, assuming that air of the same temperature and particles of the same density are used in the two models, the equality of the Stokes, Froude and Interception numbers cannot be maintained.

2. If the mechanism of interception is neglected, the Froude and the Stokes number can each be held constant in the two different models when lung air and particles of fixed density are used. Hence, simultaneous inertial impaction and sedimentation of respirable

---

[1] $\delta'(x_1) = \delta(x_1)/R_2 = \text{constant } (A'Re)^{-1/2}(x_1')^{1/3}$

particles, having negligible Brownian motion, will be approximately similar in each bifurcation region in which potential flow is a valid approximation. The same conclusion holds for pure inertial or pure sedimentation deposition.

3. When the mechanism of sedimentation is negligible (for bifurcation models in certain orientations), similarity can be maintained for inertial impaction of particles having large diameters and a fixed density in lung air in bifurcation regions in which potential flow is a valid approximation.

4. In certain regions of the lung and for certain particle sizes, the laminar boundary layer along the wedge of the model is important in determining the local deposition. Assuming air at lung conditions and particles of fixed density, similitude cannot be maintained if inertial impaction, sedimentation and interception are simultaneously important. The same is true for simultaneous sedimentation and interception.

5. Where the laminar boundary layer is important and when sedimentation can be neglected, similarity can be maintained for inertial impaction and interception for bifurcation wedges approximating flat plates ($\alpha \to 0$). The same conclusion applies when either pure inertial impaction or pure interception is the controlling mechanism.

6. When the laminar boundary layer is important and interception can be neglected, similarity cannot be maintained for simultaneous inertial impaction and sedimentation deposition of fixed density particles in lung air.

7. When only sedimentation is important and interception is neglected, deposition similarity can be maintained.

A.4 Critical Stokes Number for a General Bifurcation Model

Figure 2.1 and the z-plane in Figure A.1 illustrate the shape and dimensions of the bifurcating model. The critical Stokes number, Stk_{cr}, represents the minimum value of the Stokes number needed for a particle to impact on the model carina in a finite amount of time. It neglects the effect of interception and sedimentation. From the approximate potential flow solution around the wedge (Section A.2) the velocity of the stagnation streamline is

$$u = AU r^m \cos(\pi-\theta)\Big|_{\theta=\pi} = AU r^m = AU|x|^m$$

where $m = \alpha/(\pi-\alpha)$ and $\alpha = 1/2$ the wedge angle.

$$A = \left\{\frac{h}{\pi-\alpha}\left[\left(\frac{h_2}{h}\right)^{\pi/\alpha}+1\right]\right\}^{-m}.$$

Using the x component equation of motion for a particle on the stagnation streamline (neglecting sedimentation),

$$\frac{du}{dt} = -\frac{1}{\tau}(u-u_f).$$

Letting $u = dx/dt = d|x|/dt$ and substituting for u,

$$\frac{d^2|x|}{dt^2} + \frac{1}{\tau}\frac{d|x|}{dt} + AU|x|^m = 0.$$

This non-linear, second order differential equation can only be solved analytically for the cases of $m = 1$ and $m = 0$. $m = 1$ represents the 180° wedge or perpendicular wall and $m = 0$ represents the flat plate.

For the case of $m = 1$ and with the Stokes number $= U\tau/R_2 = 2U\tau/h_2$, Stk_{cr} was derived following Fuchs (1964: 163-164):

$$Stk_{cr} = 1/(2Ah_2) = \frac{h}{h_2\pi}\left\{\left(\frac{h_2}{h}\right)^2 + 1\right\}.$$

To determine Stk_{cr} for the general case of any m, the results derived by Levin and compiled by Fuchs (1964: 164, 173) are used. The fluid velocity along the x-axis before the stagnation point in any flow regime can be expressed asymptotically by $u = -ax^m$, if the origin of coordinates is at the stagnation point. Assuming $Stk_{cr} = Da^p$, where D and p are constants, Levin has shown that $p = -1/m$. This result can be applied to viscous or potential flow.

For the case of potential flow in the bifurcation model, the stagnation stream velocity is $u = -ax^m = AU|x|^m$. Substituting, Stk_{cr} $Stk_{cr} = Da^{-1/m} = D(AU)^{-1/m} = DU^{-1/m}\left\{\frac{h}{\pi-\alpha}\left[\left(\frac{h_2}{h}\right)^{\pi/\alpha} + 1\right]\right\}$. From $Stk_{cr} = 1/(2Ah_2)$ determined for $m = 1$, D is equivalent to $U^{1/m}/2h_2$. Therefore, for the general case

$$Stk_{cr} = \frac{h}{2(\pi-\alpha)h_2}\left[\left(\frac{h_2}{h}\right)^{\pi/\alpha} + 1\right]. \qquad (A.27)$$

Evaluating Stk_{cr} for specific wedge angles in the two-dimensional bifurcation model with $h_2 = 1.3$ and $h = 0.95$:

180° wedge $\alpha = \pi/2$ $\quad Stk_{cr} = \frac{h}{\pi h_2}\left[\left(\frac{h_2}{h}\right)^2 + 1\right] = 0.668,$

90° wedge $\alpha = \pi/4$ $\quad Stk_{cr} = \frac{2h}{3\pi h_2}\left[\left(\frac{h_2}{h}\right)^4 + 1\right] = 0.698,$

30° wedge $\alpha = \pi/12$ $\quad Stk_{cr} = \frac{6h}{11\pi h_2}\left[\left(\frac{h_2}{h}\right)^{12} + 1\right] = 5.5,$

0° wedge $\alpha = 0$ $\quad Stk_{cr} = \frac{h}{2h_2\pi}\left[\left(\frac{h_2}{h}\right)^{\infty} + 1\right] = \infty.$

This analysis indicates that, when sedimentation and interception can be neglected, a 20μm particle must be carried at a free stream velocity greater than 369 cm./sec. to deposit on the carina of the two-dimensional model. For 10μm particles to deposit by pure inertial impaction, the free stream potential velocity must be greater than 1475 cm./sec.

Appendix B

EXPERIMENTAL PARAMETERS, EQUIPMENT, AND PROCEDURES

B.1 Efficiency of Deionization

The efficiency of the deionizer[1] discussed in Chapter 4 was evaluated for the aerosol of 0.365μm particles as follows. The charged and decharged aerosols were each passed through a parallel plate diffusion battery having a uniform electric field and laminar flow between the plates. From a measurement of the fraction of particles removed by the battery, the average terminal particle velocity in the field, and in turn its charge, was calculated (Fuchs, 1964: 113-115). The aerosol which bypassed the deionizer had an average electronic charge of 28, while the deionized aerosol had an average charge of only 0.4. 28 net charges compares favorably with the medians of 45+ and 15- charges measured by Whitby and Liu (1968), and 0.4 agrees with 1.4 predicted by the equilibrium Boltzmann distribution.

B.2 Effects of Impurities on Concentration

Possible errors in the concentration measurement caused by the free stabilizing agent and inorganic impurities in the hydrosol solution were also investigated. Langer and Lieberman (1960) and Langer and

---

[1] 3M Company, Model 3B4G, 3 millicuries Kr-85, 12" active length

Pierrard (1963) have documented some of the problems caused by these agents. The fraction of a filter sample composed of stabilizing agent and inorganic impurities was estimated from data on the composition of the stock, monodisperse latex suspensions (Lippie, 1965). The maximum estimate of the fraction or concentration error varied between 1 and 3% for all particles, except it was 7.4% for the 0.088μm particles.

Another possible error was the additional light scattering in the photometer caused by the small particles of hygroscopic stabilizing agent and inorganics. Size distribution measurements[1] of 2.02, 1.1, 0.79 and 0.365μm aerosols, which had been generated from a Bird Microne-bulizer at similar conditions to those reported in Section 4.4, indicated that the stabilizing agent and inorganics had a particle size ≤ 0.25μm. If all the particles formed by these impurities were 0.2μm in size, they would have caused a 5% increase in the scattering of 1.1μm particles and a 3.8% increase in the 0.79μm signal.

All experimental runs and photometer calibration runs for one particle size were made from the same stock solution. Also all exper-imental runs used the same dilution of the stock solution, and some of the points on the calibration curve were made at this same dilution. A straight line was a fairly good fit for all calibration points made at

---

[1] Measurements made by Steven L. Heisler and Rudolf Husar in 1972 at the California Institute of Technology using a single particle optical counter system including a Climet sensor and a multichannel analyzer.

different dilutions. This may not have been true if the stabilizer particles had scattered a noticeable fraction of light, in which case they would have scattered a different fraction as their size varied between different dilutions. Therefore, the only concentration error caused by the stabilizing agent and inorganics was found in the mass measurement of monodisperse particles collected on the filter.

B.3 Particle Adhesion and Shear Losses

Particle collection on the walls of the daughter branches of the experimental models was designed to simulate the real lung. Therefore, all losses of particles from their initial deposition sites and accumulations at secondary sites had to be prevented. Particles can be lost if they rebound after collision with the surface, if they are sheared loose and reentrained by the air, or if they are sheared loose and roll along the surface to secondary deposition sites.

Calculations were made to assess the probability of aerodynamic shear losses or rolling losses of the PSL particles from the cellophane or glass surfaces of the models. The calculations followed those made by Visser (1970) for measuring the force of adhesion between submicron carbon-black particles and a cellulose film in a flowing aqueous solution. A Hamacker constant of 10^{-13} ergs was chosen as a lower bound for calculating the adhesion force. The velocity profile in the boundary layer along the 90° and 70° wedge (Equation 2.10, Section 2.23) was

used to calculate the shearing force on the particle at the peak experimental flow conditions in the model. The force of adhesion was at least two orders of magnitude larger than the shearing force for all experimental particles at all locations, except within a particle diameter of the carina. There the particle diameter was larger than the displacement thickness; accordingly the potential velocity of the streamline passing through the particle center was used. The shearing force and adhesion force were then of the same order only for the 5.7μm and 7.6μm particles. These calculations predicted that approximately 50% of the 5.7μm and 7.6μm particles which deposited within 5.7μm and 7.6μm respectively from the carina could have been lost if an adhesive had not been used.

These calculations also concurred with Fuchs (1964: 348), who indicates that it is impossible to blow particles with diameters below 1.0 - 2.0μm from deposits on clean plates, even at U = 200 m./sec. Recent experimental work by Dahneke (1973) indicated that 1 m./sec. is the minimum velocity needed for rebound of 1.0μm PSL from polished quartz plates in a vacuum. The maximum impaction velocities of the experimental particles in the model were calculated to be at least an order of magnitude lower than 1 m./sec. because they decelerate with the potential flow regime and lose most of their remaining momentum in the viscous boundary layers. Rebounding, therefore, was probably not a problem in the experimental runs.

The deposition of the particles 1.0μm and larger was tested in the model with and without adhesives. Adhesives were needed to prevent losses in the "2-D" model for the 7.6μm particles and in the "3-D" model for 5.7μm at the low flow rate and for 5.7μm and 2.02μm at the high flow rate. No rolling with secondary deposition was observed for any particle size.

Calculations following Levich (1962: 659) predicted and experimental observations verified that no surface waves were initiated in the adhesive coatings at the experimental conditions of the runs.

B.4 Alternative Counting Techniques

Attempts were made to develop a less time consuming, and less tedious technique for counting the particles. In one case vibrating, piezo-electric crystals were experimentally investigated for sensing the mass of the deposited particles. However, the crystals were more sensitive to temperature flucuations caused by the flow of air than to the small mass of particles deposited during the runs.

Commercially available and automatic optical counting devices were too expensive and were not capable of distinguishing the particles from the nonuniformities, gas bubbles and other impurities found inside and on the surface of the glass plates and plastic tapes. Radioactively tagged and fluorescent particles required a much denser collection of particles on the surface than could be obtained in a

reasonable time period with the experimental apparatus. The trained human eye was more effective in distinguishing between the spherical latex particles and other spherical impurities than the other techniques, and the eye could accurately count small numbers of particles in large surface areas.

B.5 Deposition by Electrostatic Mechanisms

Although particles were decharged in the "2-D" and "3-D" runs, the deposition of charged natural and therapeutic aerosols may be enhanced in the real lung by two mechanisms (Section 7.1.4). One is the attractive force between charged particles and its image in the lung surface. The other is the electrostatic repulsion force of the surrounding particles in the air, called the "space charge effect".

To compare deposition for these mechanisms with the efficiency for impaction, sedimentation and diffusion in the primary bronchi, the following procedure was employed: Values of dimensionless force parameters for the two electrostatic mechanisms (Kraemer and Johnstone, 1955) are directly comparable to Stk and Stk/Fr because they arise from the same force balance. The Peclét number is not directly comparable. Consequently Pe for a particle in the diffusion subrange is replaced by Stk for a particle in the impaction subrange which has an equivalent experimental ϵ in Figures 6.6 and 6.7. If the parameters for the electrostatic mechanisms are much smaller than the parameter for the

mechanism controlling deposition in the "3-D" model, enhancement of deposition by charge is negligible.

The 0.365μm PSL particles, with a net charge of +30 esu. after generation by atomization (Whitby and Liu, 1968) and a concentration of 10^5 particles/c.c., have a diffusion parameter 15 times and 300,000 times larger than the parameters for electrostatic repulsion and image forces, respectively. In this case charge effects are negligible. The same conclusion holds for all respirable particles generated by atomization and for natural aerosols because they usually carry fewer charges than particles generated by atomization.

Average* Particle Diameter, μm	Standard* Deviation	% Solids	Polymer+ Type	Dilution Ratios of Stock Solutions for Runs
0.008	0.0080	10	PSL	100:1
0.365	0.0079	4	PSL	48:1
0.79	0.0044	10	PSL	24:1
0.81	0.0063	10	PSL	24:1
1.099	0.0059	10	PSL	16:1
1.1	0.0055	10	PSL	24:1
2.02	0.0135	10	PVTL	24:1, 16:1
2.68	0.0149	10	PVTL	24:1
5.7	$\sigma_g = 1.26$‡	10	SDVBL	15:1
7.6	$\sigma = 2.3\mu m$ $\sigma_g = 1.3$‡	10	SDVBL	16:1

* Average diameter and standard deviation determined by Dow Chemical Co. by sizing under an electron microscope.

+ PSL = Polystyrene latex, $\rho_p = 1.05$ gm/cc; PVTL = Polyvinyltoluene latex, $\rho_p = 1.027$ gm/cc; SDVBL = Styrene divinylbenzene latex, $\rho_p = 1.05$ gm/cc.

‡ σ_g = geometric standard deviation for log normal distributions of 5.7 and 7.6 μm particles, determined by Daniel Chang, former graduate student at California Institute of Technology.

$\sqrt{\overline{d_p^2}}$, which was evaluated for the 5.7 and 7.6 μm particles by using these values of σ_g and following Fuchs (1964:13), was respectively 6.32 and 8.72 μm. $\sqrt[3]{\overline{d_p^3}}$ likewise was 6.68 and 9.36 μm.

Table B.1 Characteristics of the Stock Hydrosols used in the Experimental Runs

Deposition Location x_1 (cm.)	Correction Factor
0.0069	0.9234
0.0275	0.9233
0.11	0.9226
0.22	0.9217
0.3175	0.9208
0.635	0.9182
1.27	0.9128
2.54	0.9022

Table B.2 Correction Factor for the Exposure Time of Deposition Sites in the "2-D" Model to the Particle-Laden Air:

$$\text{Correction Factor} = \frac{\text{Volume of Particle-Laden Air Passing During Inhalation}}{\text{Total Volume of Air Passing During Inhalation}}$$

Appendix C

EXPERIMENTAL DATA AND ERROR ANALYSIS

C.1 Error Analysis in Model Experiments

The variance of a local transfer coefficient datum is calculated from the following expression:

$$\sigma^2_{k_{loc}} = k^2_{loc}\left[\left(\frac{\sigma_{count}}{\#\ counts}\right)^2+\left(\frac{\sigma_{breath}}{\#\ breaths}\right)^2+\left(\frac{\sigma_{concentration}}{concentration}\right)^2+\left(\frac{\sigma_{c.f.}}{c.f.}\right)^2+\left(\frac{\sigma_{area}}{area}\right)^2+\left(\frac{\sigma_{time}}{time}\right)^2\right]. \quad (C.1)$$

Each of the parameters are from Equation 4.1 in Section 4.8. The probable error, P.E., of any transfer coefficient datum, assuming the data follow a Gaussian distribution, is equal to $0.6745\,\sigma_{k_{loc}}$[1]. From Equation 4.2 and Bevington (1969), the variance of a weighted average local transfer coefficient datum is calculated from the following expression:

$$\sigma^2_{W.AV.k_{loc}} = \frac{1}{\sum_i^n\left(\frac{1}{\sigma^2_{k_{loc_i}}}\right)}\ . \quad (C.2)$$

σ_x and σ_y for optical particle runs and σ_{xy} for electron microscopy runs are given in Tables C.2 and C.3. The only non-negligible error

[1] Half of the observations of an experiment are expected to fall within the boundaries denoted by $k_{loc} \pm 0.6745\,\sigma_{k_{loc}}$.

occurred at 0.0069 cm. where the P.E. was 10%. Errors in locating the Y strips and in placement of the grids are negligible.

In the "2-D" and "3-D" runs the leading edges of the cellophane tapes and the glass plate were jagged and slightly uneven on a microscopic scale of 0.001 to 0.01 cm. Air flow around this nonideal geometry probably differed from the idealized flow assumed in the deposition theories for a sharp wedge. For most runs with particles in the sedimentation and impaction subranges, the nonideal flow lowered the value of transfer coefficients at X = 0.0069 and 0.0275 cm. relative to the trend of the other data points and theory.

$\sigma_{breaths}$, σ_{area}, σ_{time}, $\sigma_{c.f.}$ and the probable errors of the time-average velocities are listed in Table C.4. Tables C.5 and C.6 list $\sigma_{concentration}$ and the particle concentration for each of the "2-D" and "3-D" runs. σ_{counts} was evaluated as described in Section C.2 from data in Sections C.3 and C.4.

In each run statistical errors in the # counts and the error in the particle concentration were the major contributors to the variance of the local transfer coefficient. In most runs a sharp decline in the number of counts beyond the carina caused the count error to dominate the variance of the transfer coefficients.

For example, sample calculations shown in Table C.7 for "2-D" Run 24 of 1.1 μm particles indicate that the probable error for the transfer

coefficient varies from 13.3% at $x_1 = 0.0069$ cm. to 32% at $x_1 = 2.54$ cm. The increase corresponded directly to a decrease of the # count from 83 to 5 over this same range.

Error bars were not placed on "2-D" and "3-D" data in the figures because they were of little use for analyzing the data to meet the goals of this thesis. The probable errors were also not great enought to invalidate any of the conclusions derived from the "2-D" and "3-D" data. Nevertheless, data needed to evaluate the probable errors for all transfer coefficients are available in Appendix C. Maximum values of the probable errors, for the "2-D" runs and for the "3-D" runs along the Y = 0 strips, generally occurred at the last point and were around 35%. Data on the outside wall of the "3-D" runs which represent only 1 count per counting area have a probable error of around 100% of the value of the transfer coefficient.

C.2 Counting Errors

In the "2-D" and "3-D" runs measured by optical microscopy, all count data in one run were taken at different locations but in regions of the same surface area. The human error involved in counting singlet particles was almost nil because the particles were easily discerned on the collecting surface. The surface density of particles was also sufficiently low to minimize misses or repeat counts.

The major source of error in the count data were the statistical

fluctuations in the counts caused by the stochastic nature of the physical processes involved in the deposition of particles from an aerosol. Within any one counting area, separate observations of the number of particles depositing in a fixed time interval are described by a Poisson distribution (Bevington, 1969) with a mean μ and a standard deviation $\sqrt{\mu}$. For one run, the count datum at each location is assumed equal to the mean of the Poisson distribution for that counting location (i.e. # counts $=\mu$).

The counting procedure for data collected from electron microscope grids is described in Section 4.7.2. As in the optical microscopy runs, the major source of error in the count data was statistical. The approximately 300 windows, on which particles were counted in the center of each grid, had the same surface area, and the particles were randomly distributed among the windows. Therefore, the standard deviation of the count data in any one window, σ_i, is a constant equal to the standard deviation for any window in the grid ($\sigma_i = \sigma$).

Defining z_i = (# singlets counted/grid window i) and N = (# windows counted on the grid), the average and mean number of singlets counted per window is given by

$$\mu \tilde{=} \bar{z} = \sum_{i}^{N} z_i / N.$$

The uncertainty in determing the mean, μ, is given by

$$\sigma_{\mu} = \frac{\sigma}{\sqrt{N}} = \sqrt{\frac{\bar{z}}{N}}.$$

Thus $\sigma_{counts} = \sqrt{\bar{z}/N}$ for "3-D" runs with 0.365 and 0.088μm particles.

C.3 "2-D" Model Data

Figure C.1 is the same as Figure 5.1, except the theories in Figure C.1 were calculated with $A = 0.82$ cm.$^{-1/3}$ instead of $A = 0.92$ cm.$^{-1/3}$. Another difference is that the diffusion theory is for steady flow conditions as predicted from Equation 2.52 for $U = 100$ cm./sec. $A = 0.82$ cm.$^{-1/3}$ is theoretically predicted from Equation 2.5 for the "2-D" experimental model. The local transfer coefficients predicted in Figure C.1 are slightly less than those in Figure 5.1, but the same conclusions are valid.

Tables C.8 - C.13 list the particle counts and the corresponding local transfer coefficients for each "2-D" run used in Figures 5.1 - 5.7 and C.1. Fractional counts mean the original counts were taken in an area one and one-half or twice as large as 0.035 cm.^{2}

C.4 "3-D" Model Data

Data from the "3-D" runs used to plot Maps 1 - 14 are tabulated in matrixes following the tables of "2-D" data. For each run a "raw count data matrix" and a "raw mass transfer coefficient data matrix" give the count data at each location and the corresponding local transfer coefficient calculated from Equation 4.1. Transfer coefficients from runs having the same size particles and flow conditions are averaged

(Equation 4.2) to form "weighted average raw mass transfer coefficient data". The 7 - 10 labeled colums are the X locations with the distance from the carina given in centimeters. In the optical runs the row labels of 1 - 19 correspond respectively to Y = +9, +8, ... +1, 0, -1, ... -8, -9. In the electron microscopy runs, row labels 1 - 7 correspond respectively to Y = +9, +6, +3, 0, -3, -6, -9.

The contours on the maps were determined by the following method. The "raw mass transfer coefficient data matrix" or the "weighted average raw mass transfer coefficient data matrix" of 19 rows by 9 or 10 columns was converted by linear interpolation into a 19 row by 48 column matrix with the columns equally spaced. Likewise, the 7 row by 7 column matrices for the electron microscopy runs were converted into 7 rows by 48 columns matrices with the columns equally spaced. From different trials, 48 was the minimum number of columns required to produce a contour plot equivalent to ones obtained from many more columns.

These enlarged matrices were automatically fed into a contour plotting program called "Contur", a library subroutine in the IBM 370 computer system at the California Institute of Technology. "Contur" determined the locations of the contours of constant k_{loc} by searching the data matrix and linearly interpolating between the points.

Matrixes of the "#windows counted/grid" and of the "average window area/grid" in the electron microscopy runs are needed to

calculate the statistical errors. Data are not listed for row 7 because it is the same as row 1. Data are not listed for rows 5 and 6 in Runs 31, 32 and 33 because these strips were not counted (Section 4.7.2).

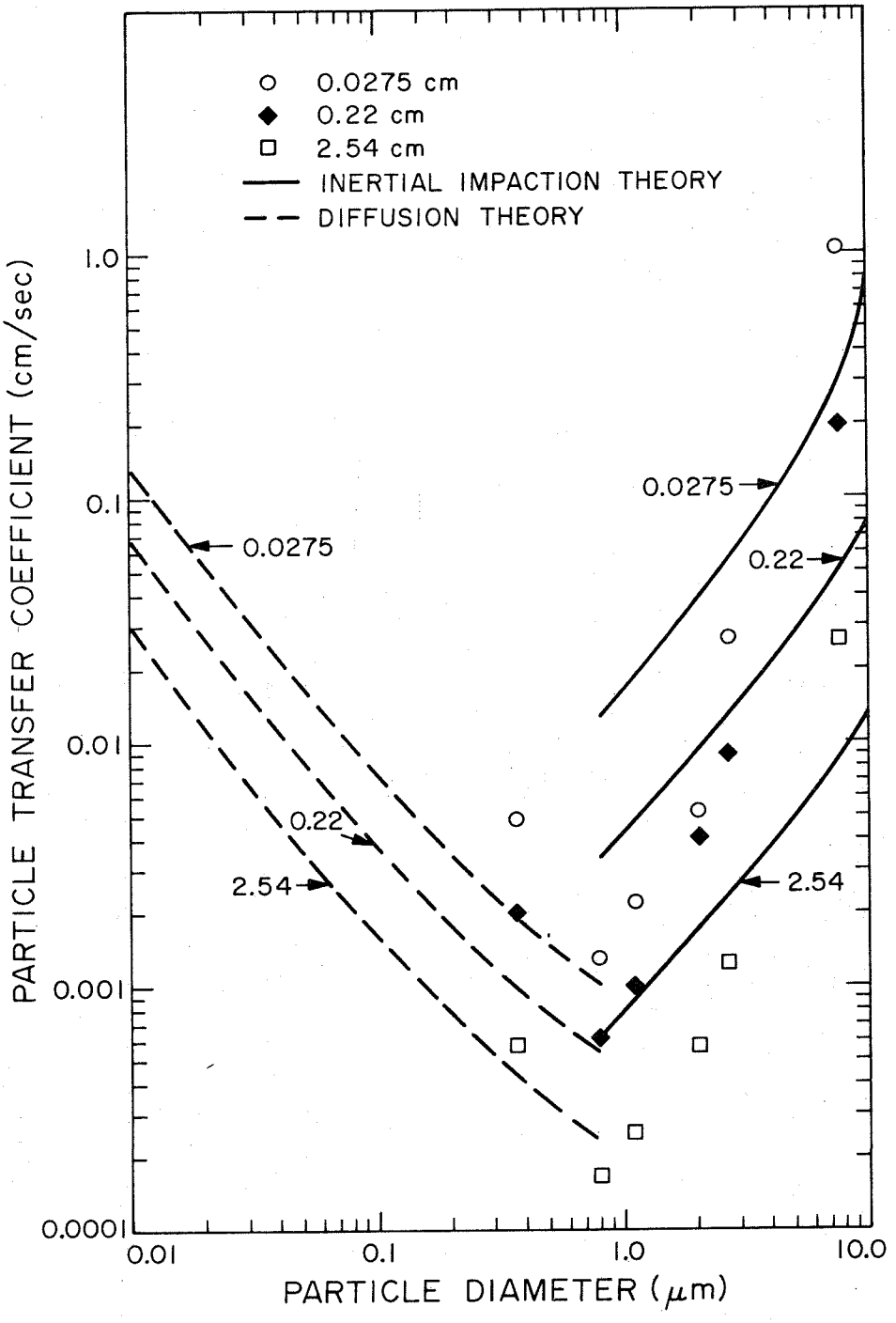

Figure C.1 Comparison of Theories with Local Transfer Coefficients Measured at 0.0275, 0.22, and 2.54 cm Downstream from the Carina in the 2-D Model for Simulated 450 cc, 1.63 sec Inhalations. Particle Diameter refers to Spheres of Unit Density. U=100 cm/sec, A=0.82 for Impaction(w/ Interception) in Steady Potential Flow and for Convective Diffusion(Point Particles) in Steady Laminar B.L. Flow.

d_p, μm	Relaxation Time-sec τ	Stopping* Distance-cm h_s	Diffusion Coefficient-$\frac{cm^2}{sec}$ D	Δy^+ - cm
20	1.23×10^{-3}	8.70×10^{-2}	1.28×10^{-8}	2×10^{-3}
10	3.08×10^{-4}	2.18×10^{-2}	2.40×10^{-8}	2×10^{-4}
7.6	1.81×10^{-4}	1.28×10^{-2}	3.24×10^{-8}	1×10^{-4}
5.7	1.03×10^{-4}	7.28×10^{-3}	4.35×10^{-8}	--
5.0	7.70×10^{-5}	5.45×10^{-3}	5.00×10^{-8}	5×10^{-5}
4.0	5.03×10^{-5}	3.56×10^{-3}	6.30×10^{-8}	4×10^{-5}
3.0	2.70×10^{-5}	1.91×10^{-3}	8.50×10^{-8}	3×10^{-5}
2.68	2.30×10^{-5}	1.65×10^{-3}	9.55×10^{-8}	2×10^{-5}
2.0	1.31×10^{-5}	9.25×10^{-4}	1.30×10^{-7}	1×10^{-5}
1.099	4.31×10^{-6}	3.05×10^{-4}	2.54×10^{-7}	4×10^{-6}
1.0	3.54×10^{-6}	2.54×10^{-4}	2.79×10^{-7}	4×10^{-6}
0.79	2.35×10^{-6}	1.66×10^{-4}	3.71×10^{-7}	--
0.365	6.20×10^{-7}	4.38×10^{-5}	9.85×10^{-7}	2.5×10^{-6}
0.088	7.90×10^{-8}	5.51×10^{-6}	9.02×10^{-6}	--

*$h_s = \tau U \sin\alpha$ where U = 100 cm/sec, $\alpha = \pi/4$

+Δy = vertical separation distance between particles at starting positions for each trajectory run for the 90° wedge. Considering only impaction and interception from potential flow.

Note: A time interval of 0.00001 seconds was used in all steady potential flow trajectory runs; a second time interval of 0.0001 or 0.0002 seconds was used inside of the boundary layer.

Table C.1 Particle Parameters

Case I : 645X magnification		Case II : 150x magnification	
X Location (cm)	σ_x (cm)	X Location (cm)	σ_x (cm)
0.0069	0.001		
0.0275	0.0011	0.028	0.001
0.11	0.0015	0.112	0.0018
0.22	0.0019	0.224	0.0026
0.3175	0.0030	0.392	0.0038
0.635	0.025	0.672	0.0058
1.27	0.025	1.27	0.025
2.54	0.025	2.54	0.025
3.81	0.025	3.81	0.025
4.45	0.025	4.45	0.025

Table C.2 Standard Deviation, σ_x, for X Locations of Data in "2-D" and "3-D" Runs Counted by Optical Microscopy

Case I - Optical Particle Runs, 645X magnification		
Y Strip	Distance of Center of* Y Strip from Y=0, cm.	σ_y, cm.
9	1.932	0.0072
8	1.717	0.0064
7	1.501	0.0056
6	1.287	0.0048
5	1.0725	0.0040
4	0.858	0.0032
3	0.6435	0.0024
2	0.429	0.0016
1	0.2145	0.0008
0	0.0	0
-1	-0.2145	0.008
-2	-0.429	0.0016
-3	-0.6435	0.0024
-4	-0.858	0.0032
-5	-1.0725	0.0040
-6	-1.287	0.0048
-7	-1.501	0.0056
-8	-1.717	0.0064
-9	-1.932	0.0072

*The error in finding the correct location for the Y=0 strip on the tape is approximately equal to the width of one viewing area =±0.01-0.02 cm. After the location for Y=0 is chosen, the locations of the other Y strips are chosen consistently from it. Each strip is 15.6 view areas wide=0.2145±0.0005 or σ_y=0.0008 cm.

Table C.3 Errors in Y Locations of Data

Continued on the following page.

Table C.3 Continued

Case II -- Electron Microscope Runs

Electron microscope girds could be accurately placed on the tape to within ±0.07 cm. of their desired position; hence, σ_{xy} = 0.1 cm. The error in placement is less than ±0.07 cm. for the 4 grids along Y=0 nearest the carina.

In all "2-D" and "3-D" runs, breaths were checked off one at a time as completed. Thus, $\sigma_{breaths} = 0$.

$\sigma_{time} = 0.0068$ sec. for 1.63 sec. inhalation (2-D).
$\sigma_{time} = 0.006$ sec. for 1.88 sec. inhalations (3-D).
$\sigma_{time} = 0.0015$ sec. for 0.94 sec. inhalations (3-D).
$\sigma_{correction\ factor} = 0.0001$ for all runs.
$\sigma_{area} = 0.00196$ cm^2 at 645X magnification (2-D).
$\sigma_{area} = 1.5 \times 10^{-5}$ cm^2 at 645X magnification (3-D).

The P.E. in the area of windows of electron microscope grids is ±3%.

The P.E. for time-average velocities in the "2-D" model for 1.63 sec., 5.6 liter inhalations are as follows:

Parent branch -- $\bar{U} = 100 \pm 2.0$ cm./sec.
Daughter branch -- $\bar{U}_2 = 73 \pm 2.0$ cm./sec.

The P.E. for time-average velocities in the "3-D" model are as follows:

1. 1.88 sec., 450 cc inhalations:
   Parent branch -- $\bar{U} = 100 \pm 1.0$ cm./sec.
   Daughter branch -- $\bar{U}_2 = 100.8 \pm 1.3$ cm./sec.
2. 0.94 sec., 450 cc inhalations:
   Parent branch -- $\bar{U} = 200 \pm 2$ cm./sec.
   Daughter branch -- $\bar{U}_2 = 201.6 \pm 2.6$ cm./sec.

Table C.4 Experimental Errors for #Breaths, Counting Area, Time, Correction Factors, and the Time-Average Velocity

D_p μm	Run #	Concentration #Particles/cc	$\sigma_{Concentration}$ #Particles/cc
7.6	19	30	10
7.6	20	66	17
2.68	7	288	45
2.68	8	253	39
2.68	11	551	86
2.02	40	322	14
2.02	41	632	28
1.099	24	6310	980
1.099	25	9200	1430
1.099	36	5800	900
0.79	30	31,900	5670
0.79	31	34,700	6170
0.365	44	76,600	6130
0.365	45	84,300	6750

Table C.5 Standard Deviations for Concentration in Each 2-D Run

D_p μm	Run #	Concentration #Particles/cc	$\sigma_{Concentration}$ #Particles/cc
5.7	21	18.4	5.2
5.7	22	14.2	4.7
5.7	27	17.7	5.9
2.02	12	840	38
2.02	14	865	39
2.02	17	1250	56
2.02	19	730	33
2.02	24	1250	56
1.1	10	5990	920
1.1	18	6790	1050
1.1	25	13900	2160
0.79	13	21200	3774
0.81	26	66500	11837
0.365	28	104400	8350
0.365	32	74400	5950
0.088	31	76000	10750
0.088	33	59500	8640

Table C.6 Standard Deviations for Concentration in Each 3-D Run

Using equation C.1 to evaluate the variance of the local transfer coefficients, each parameter within the brackets is given by

$$\sigma^2_{k_{loc}} = k^2_{loc}\left[\frac{1}{(\#counts)} + 0 + 2.42\times10^{-2} + 10^{-8} + 3.14\times10^{-3} + 1.73\times10^{-5}\right].$$

Below the standard deviation, $\sigma_{k_{loc}}$, the probable error (P.E. = $0.6745\,\sigma_{k_{loc}}$), and the % probable error, $67.45\,\sigma_{k_{loc}}/k_{loc}$, are tabulated from each of the transfer coefficient data points.

x (cm.)	$(\frac{1}{\#counts})$	$\sigma_{k_{loc}} \times 10^4$ (cm/sec)	P.E. $\times 10^4$ (cm/sec)	P.E. (%)
0.0069	0.012	8.25	5.55	13.3
0.0275	0.0227	4.94	3.33	15
0.11	0.0476	2.89	1.95	18.5
0.22	0.05	2.8	1.89	18.8
0.3175	0.05	2.8	1.89	18.8
0.635	0.0714	2.2	1.5	21
1.27	0.125	1.58	1.06	26.3
2.54	0.2	1.22	0.825	32

Table C.7 Error Analysis for 2-D Run 24 for 1.1 μm Particles

2-D Run 19

Location		Outside Slide Counts/Area	Inside Slide Counts/Area	Inside Slide k_{loc} (cm/sec)
#	x_1 (cm)			
1	0.0069	22	291	2.74
2	0.0275	5	112	1.05
3	0.11	10	40	0.376
4	0.22	8	21	0.198
5	0.3175	0	13	0.123
6	0.635	0	7	0.0660
7	1.27	0	4.44	0.0418
8	2.54	0	2.78	0.0262

2-D Run 20

1	0.0069	-	366	1.57
2	0.027	-	232	0.995
3	0.11	-	53	0.227
4	0.22	-	31.5	0.135
5	0.3175	-	27.5	0.118
6	0.635	-	19.0	0.0815
7	1.27	-	4.5	0.0193
8	2.54	-	2.0	0.0086

Table C.8 7.6 μm Data

#Breaths/Run = 60 Counting Area = 0.035cm^2

2-D Run 7

Location *	Outside Slide Counts/Area	Inside Slide Counts/Area	Inside Slide $k_{loc} \times 10^2$ (cm/sec)
1	3	32	6.31
2	2	11	2.17
3	1	5	0.986
4	0	5	0.986
5	1	5	0.986
6	0	1	0.197
7	2	2	0.394
8	1	0	-

2-D Run 8

1	7	33	7.42
2	3	13	2.93
3	0	5	1.13
4	0	2	0.450
5	0	3	0.675
6	0	2.66	0.600
7	0	0	-
8	0	0.625	0.140

2-D Run 11

1	15	147	15.16
2	3	28	2.89
3	4	13	1.34
4	6	12	1.24
5	4	6	0.618
6	3	8	0.825
7	3	2	0.206
8	8	1	0.103

* See Table C.8 for x_1 values

Table C.9 2.68 μm Data

#Breaths/Run = 30 Counting Area = 0.035 cm^2

2-D Run 40 #Breaths = 60 Counting Area = 0.035 cm^2

Location* #	Inside Slide Counts/Area	$k_{loc} \times 10^3$ (cm/sec)
1	9	8.85
2	4	3.93
3	5	4.92
4	3	2.95
5	5	4.93
6	2	1.98
7	1	0.995
8	0	-

2-D Run 41 #Breaths = 80 Counting Area = 0.035 cm^2

1	25	9.25
2	14	5.18
3	13	4.82
4	11	4.08
5	14	5.20
6	2	0.745
7	2.5	0.936
8	1.5	0.568

*See Table C.8 for x_1 values

Table C.10 2.02 μm Data

2-D Run 24 #Breaths = 60 Counting Area = 0.035cm^2

Location x_1 (cm)	Outside Slide Counts/Area	Inside Slide Counts/Area	Inside Slide $k_{loc} \times 10^3$ (cm/sec)
0.0069	10	83	4.16
0.0275	3	44	2.21
0.11	14	21	1.06
0.22	5	20	1.01
0.3175	6	20	1.01
0.635	5	14	0.706
1.27	8	8	0.405
2.54	3	5	0.257

2-D Run 25 #Breaths = 60 Counting Area = 0.035cm^2

0.0069	36	166.5	5.73
0.0275	14	60	2.06
0.11	20	29.5	1.02
0.22	18	29.5	1.02
0.3175	14	28	0.966
0.635	12	20.5	0.709
1.27	18	13	0.452
2.54	10	6	0.211

2-D Run 36 #Breaths = 50 Counting Area = 0.035cm^2

0.0069	-	-	-
0.0275	-	24.5	1.60
0.11	-	21	1.37
0.22	-	20	1.31
0.3175	-	18	1.18
0.635	-	12	0.789
1.20	-	12	0.793
2.54	-	9	0.603

Table C.11 1.099 μm Data

2-D Run 30 #Breaths = 20 Counting Area = 0.035 cm^2

Location x_1 (cm)	Inside Slide Counts/Area	$k_{loc} \times 10^4$ (cm/sec)
0.0141	32	9.54
0.0354	27	8.04
0.11	20	5.96
0.22	16.3	4.86
0.3175	13.7	4.09
0.635	10	2.99
1.27	7.3	2.20
2.54	6.7	2.04

2-D Run 31 #Breaths = 40 Counting Area = 0.035 cm^2

0.0069	214	29.2
0.0275	96	13.1
0.11	61	8.35
0.22	45	6.16
0.3175	34	4.67
0.635	25	3.44
1.27	21	2.91
2.54	12	1.68

Table C.12 0.79 μm Data

2-D Run 44 #Breaths = 50 Counting Area = 0.035 cm^2

Location* #	Inside Slide Counts/Area	$k_{loc} \times 10^3$ (cm/sec)
2	1000	4.86
3	640	3.18
4	480	2.38
5	392	1.95
6	308	1.53
7	258	1.29
8	128	0.65

2-D Run 45 #Breaths = 70 Counting Area = 0.035 cm^2

3	1440	4.65
4	512	1.66
5	388	1.25
6	342	1.11
7	172	0.562
8	152	0.502

*See Table C.8 for x_1 values

Table C.13 0.365 μm Data

MATRIX 1-A

RAW COUNT DATA MATRIX
5.7 MICRON, 3-D RUN 21

	1 0.028	2 0.112	3 0.224	4 0.392	5 0.672	6 1.270	7 2.540	8 3.810	9 4.445
1	0.0	0.0	0.0	0.0	0.0	0.0	0.0	0.0	0.0
2	0.0	0.0	0.0	0.0	0.0	0.0	0.0	0.0	0.0
3	0.0	0.0	0.0	0.0	0.0	0.0	0.0	0.0	0.0
4	0.0	0.0	0.0	0.0	0.0	0.0	0.0	0.0	0.0
5	0.0	0.0	0.0	0.0	0.0	0.0	0.0	0.0	0.0
6	3.00	3.00	1.00	2.50	2.00	2.00	3.00	1.50	3.00
7	10.00	11.00	9.50	9.00	7.00	7.00	3.00	8.00	3.50
8	13.00	13.00	9.00	14.00	12.00	13.00	10.00	10.00	5.50
9	22.00	17.00	15.50	12.50	10.50	12.50	10.50	8.50	6.50
10	76.00	17.00	17.00	16.00	10.50	12.50	6.00	9.00	7.50
11	19.00	12.00	14.00	13.50	10.50	7.00	4.50	7.50	6.00
12	11.00	10.00	10.00	11.00	7.50	8.50	11.50	8.50	6.00
13	11.00	5.00	4.00	5.50	3.00	6.50	5.50	4.00	4.00
14	2.00	1.00	1.50	2.00	3.00	1.50	0.0	2.00	2.00
15	0.0	0.0	0.0	0.0	0.0	0.0	0.0	0.0	0.0
16	0.0	0.0	0.0	0.0	0.0	0.0	0.0	0.0	0.0
17	0.0	0.0	0.0	0.0	0.0	0.0	0.0	0.0	0.0
18	0.0	0.0	0.0	0.0	0.0	0.0	0.0	0.0	0.0
19	0.0	0.0	0.0	0.0	0.0	0.0	0.0	0.0	0.0

MATRIX 1-B

RAW MASS TRANSFER COEFFICIENT DATA MATRIX
5.7 MICRON, 3-D

RUN # =21. # BREATHS = 400. TIME/BREATH, SEC = 1.88 COUNT AREA, SQ CM = 1.204E-02

	1 0.028	2 0.112	3 0.224	4 0.392	5 0.672	6 1.270	7 2.540	8 3.810	9 4.445
1	0.0	0.0	0.0	0.0	0.0	0.0	0.0	0.0	0.0
2	0.0	0.0	0.0	0.0	0.0	0.0	0.0	0.0	0.0
3	0.0	0.0	0.0	0.0	0.0	0.0	0.0	0.0	0.0
4	0.0	0.0	0.0	0.0	0.0	0.0	0.0	0.0	0.0
5	0.0	0.0	0.0	0.0	0.0	0.0	0.0	0.0	0.0
6	1.92E-02	1.92E-02	6.41E-03	1.60E-02	1.28E-02	1.28E-02	1.92E-02	9.61E-03	1.92E-02
7	6.41E-02	7.05E-02	6.09E-02	5.77E-02	4.48E-02	4.48E-02	1.92E-02	5.12E-02	2.24E-02
8	8.33E-02	8.33E-02	5.77E-02	8.97E-02	7.69E-02	8.33E-02	6.41E-02	6.41E-02	3.52E-02
9	1.41E-01	1.09E-01	9.93E-02	8.01E-02	6.73E-02	8.01E-02	6.73E-02	5.45E-02	4.16E-02
10	4.87E-01	1.09E-01	1.09E-01	1.02E-01	6.73E-02	8.01E-02	3.84E-02	5.77E-02	4.80E-02
11	1.22E-01	7.69E-02	8.97E-02	8.65E-02	6.73E-02	4.48E-02	2.88E-02	4.80E-02	3.84E-02
12	7.05E-02	6.41E-02	6.41E-02	7.05E-02	4.80E-02	5.45E-02	7.37E-02	5.45E-02	3.84E-02
13	7.05E-02	3.20E-02	2.56E-02	3.52E-02	1.92E-02	4.16E-02	3.52E-02	2.56E-02	2.56E-02
14	1.28E-02	6.41E-03	9.61E-03	1.28E-02	1.92E-02	9.61E-03	0.0	1.28E-02	1.28E-02
15	0.0	0.0	0.0	0.0	0.0	0.0	0.0	0.0	0.0
16	0.0	0.0	0.0	0.0	0.0	0.0	0.0	0.0	0.0
17	0.0	0.0	0.0	0.0	0.0	0.0	0.0	0.0	0.0
18	0.0	0.0	0.0	0.0	0.0	0.0	0.0	0.0	0.0
19	0.0	0.0	0.0	0.0	0.0	0.0	0.0	0.0	0.0

PARTICLES/CC = 1.840E 01

MATRIX 1-C

RAW COUNT DATA MATRIX
5.7 MICRON, 3-D RUN 22

	1 0.028	2 0.112	3 0.224	4 0.392	5 0.672	6 1.270	7 2.540	8 3.810	9 4.445
1	0.0	0.0	0.0	0.0	0.0	0.0	0.0	0.0	0.0
2	0.0	0.0	0.0	0.0	0.0	0.0	0.0	0.0	0.0
3	0.0	0.0	0.0	0.0	0.0	0.0	0.0	0.0	0.0
4	0.0	0.0	0.0	0.0	0.0	0.0	0.0	0.0	0.0
5	0.0	0.0	0.0	0.0	0.0	0.0	0.0	0.0	0.0
6	1.00	3.00	2.50	3.00	1.00	2.50	1.50	3.00	3.00
7	9.00	3.00	3.50	4.50	2.50	4.50	4.00	2.50	4.00
8	8.00	8.00	11.50	13.50	7.00	8.00	4.50	5.00	5.50
9	14.00	11.00	14.00	12.00	8.00	7.00	5.50	3.00	9.00
10	46.00	11.00	13.00	10.50	14.50	11.00	8.50	6.00	8.50
11	10.00	6.00	13.50	11.50	11.50	8.00	10.50	9.50	3.50
12	10.00	10.00	8.00	9.00	11.00	8.50	5.50	7.50	4.00
13	6.00	8.00	5.50	3.00	4.00	4.50	3.50	1.00	2.50
14	2.00	3.00	1.50	3.50	1.50	0.50	1.50	1.00	0.50
15	0.0	0.0	0.0	0.0	0.0	0.0	0.0	0.0	0.0
16	0.0	0.0	0.0	0.0	0.0	0.0	0.0	0.0	0.0
17	0.0	0.0	0.0	0.0	0.0	0.0	0.0	0.0	0.0
18	0.0	0.0	0.0	0.0	0.0	0.0	0.0	0.0	0.0
19	0.0	0.0	0.0	0.0	0.0	0.0	0.0	0.0	0.0

MATRIX 1-D

RAW MASS TRANSFER COEFFICIENT DATA MATRIX
5.7 MICRON, 3-D

RUN # =22. # BREATHS = 400. TIME/BREATH, SEC = 1.88 COUNT AREA, SQ CM = 1.204E-02

	1 0.028	2 0.112	3 0.224	4 0.392	5 0.672	6 1.270	7 2.540	8 3.810	9 4.445
1	0.0	0.0	0.0	0.0	0.0	0.0	0.0	0.0	0.0
2	0.0	0.0	0.0	0.0	0.0	0.0	0.0	0.0	0.0
3	0.0	0.0	0.0	0.0	0.0	0.0	0.0	0.0	0.0
4	0.0	0.0	0.0	0.0	0.0	0.0	0.0	0.0	0.0
5	0.0	0.0	0.0	0.0	0.0	0.0	0.0	0.0	0.0
6	8.33E-03	2.50E-02	2.08E-02	2.50E-02	8.33E-03	2.08E-02	1.25E-02	2.50E-02	2.50E-02
7	7.50E-02	2.50E-02	2.92E-02	3.75E-02	2.08E-02	3.75E-02	3.33E-02	2.08E-02	3.33E-02
8	6.66E-02	6.66E-02	9.58E-02	1.12E-01	5.83E-02	6.66E-02	3.75E-02	4.17E-02	4.58E-02
9	1.17E-01	9.16E-02	1.17E-01	1.00E-01	6.66E-02	5.83E-02	4.58E-02	2.50E-02	7.50E-02
10	3.83E-01	9.16E-02	1.08E-01	8.75E-02	1.21E-01	9.16E-02	7.08E-02	5.00E-02	7.08E-02
11	8.33E-02	5.00E-02	1.12E-01	9.58E-02	9.58E-02	6.66E-02	8.75E-02	7.91E-02	2.92E-02
12	8.33E-02	8.33E-02	6.66E-02	7.50E-02	9.16E-02	7.08E-02	4.58E-02	6.25E-02	3.33E-02
13	5.00E-02	6.66E-02	4.58E-02	2.50E-02	3.33E-02	3.75E-02	2.92E-02	8.33E-03	2.08E-02
14	1.67E-02	2.50E-02	1.25E-02	2.92E-02	1.25E-02	4.17E-03	1.25E-02	8.33E-03	4.17E-03
15	0.0	0.0	0.0	0.0	0.0	0.0	0.0	0.0	0.0
16	0.0	0.0	0.0	0.0	0.0	0.0	0.0	0.0	0.0
17	0.0	0.0	0.0	0.0	0.0	0.0	0.0	0.0	0.0
18	0.0	0.0	0.0	0.0	0.0	0.0	0.0	0.0	0.0
19	0.0	0.0	0.0	0.0	0.0	0.0	0.0	0.0	0.0

PARTICLES/CC = 1.415E 01

MATRIX 1-E

WEIGHTED AVERAGE RAW MASS TRANSFER COEFFICIENT DATA MATRIX
5.7 MICRON, 3-D RUNS 21, 22

	1 0.028	2 0.112	3 0.224	4 0.392	5 0.672	6 1.270	7 2.540	8 3.810	9 4.445
1	0.0	0.0	0.0	0.0	0.0	0.0	0.0	0.0	0.0
2	0.0	0.0	0.0	0.0	0.0	0.0	0.0	0.0	0.0
3	0.0	0.0	0.0	0.0	0.0	0.0	0.0	0.0	0.0
4	0.0	0.0	0.0	0.0	0.0	0.0	0.0	0.0	0.0
5	0.0	0.0	0.0	0.0	0.0	0.0	0.0	0.0	0.0
6	1.45E-02	2.17E-02	1.27E-02	1.99E-02	1.09E-02	1.63E-02	1.63E-02	1.63E-02	2.17E-02
7	6.88E-02	5.07E-02	4.71E-02	4.89E-02	3.44E-02	4.16E-02	2.53E-02	3.80E-02	2.72E-02
8	7.60E-02	7.60E-02	7.42E-02	9.96E-02	6.88E-02	7.60E-02	5.25E-02	5.43E-02	3.98E-02
9	1.30E-01	1.01E-01	1.07E-01	8.87E-02	6.70E-02	7.06E-02	5.79E-02	4.16E-02	5.61E-02
10	4.42E-01	1.01E-01	1.09E-01	9.60E-02	9.05E-02	8.51E-02	5.25E-02	5.43E-02	5.79E-02
11	1.05E-01	6.52E-02	9.96E-02	9.05E-02	7.97E-02	5.43E-02	5.43E-02	6.16E-02	3.44E-02
12	7.60E-02	7.24E-02	6.52E-02	7.24E-02	6.70E-02	6.16E-02	6.16E-02	5.79E-02	3.62E-02
13	6.16E-02	4.71E-02	3.44E-02	3.08E-02	2.53E-02	3.98E-02	3.26E-02	1.81E-02	2.35E-02
14	1.45E-02	1.45E-02	1.09E-02	1.99E-02	1.63E-02	7.24E-03	5.43E-03	1.09E-02	9.05E-03
15	0.0	0.0	0.0	0.0	0.0	0.0	0.0	0.0	0.0
16	0.0	0.0	0.0	0.0	0.0	0.0	0.0	0.0	0.0
17	0.0	0.0	0.0	0.0	0.0	0.0	0.0	0.0	0.0
18	0.0	0.0	0.0	0.0	0.0	0.0	0.0	0.0	0.0
19	0.0	0.0	0.0	0.0	0.0	0.0	0.0	0.0	0.0

MATRIX 2-A

RAW COUNT DATA MATRIX
5.7 MICRON, 3-D RUN 27

	1	2	3	4	5	6	7	8	9
	0.028	0.112	0.224	0.392	0.672	1.270	2.540	3.810	4.445
1	0.0	0.0	0.0	0.0	0.0	0.0	0.0	0.0	0.0
2	0.0	0.0	0.0	0.0	0.0	0.0	0.0	0.0	0.0
3	0.0	0.0	0.0	0.0	0.0	0.0	0.0	0.0	0.0
4	0.0	0.0	0.0	0.0	0.0	0.0	0.0	0.0	0.0
5	1.00	0.0	0.0	0.0	0.0	0.0	0.0	0.0	0.0
6	1.00	2.00	1.00	0.0	1.00	0.50	0.0	1.00	1.00
7	5.00	1.00	6.00	7.00	3.00	6.00	3.50	1.00	2.50
8	5.00	4.00	7.00	9.00	8.00	7.50	4.00	1.00	4.00
9	20.00	11.00	3.00	7.00	6.00	5.50	3.50	3.00	3.50
10	31.00	8.00	15.00	10.00	5.00	2.50	5.00	5.00	3.00
11	19.00	8.00	9.00	6.00	7.00	7.50	3.50	3.50	2.50
12	3.00	6.00	5.00	7.00	5.00	3.00	2.50	2.00	1.50
13	1.00	4.00	1.00	0.0	1.50	2.00	1.50	2.50	2.00
14	1.00	1.00	1.00	3.00	0.50	1.00	1.00	1.50	0.0
15	2.00	1.00	0.0	1.00	0.0	0.0	0.0	0.0	0.0
16	0.0	0.0	0.0	0.0	0.0	0.0	0.0	0.0	0.0
17	0.0	0.0	0.0	0.0	0.0	0.0	0.0	0.0	0.0
18	0.0	0.0	0.0	0.0	0.0	0.0	0.0	0.0	0.0
19	0.0	0.0	0.0	0.0	0.0	0.0	0.0	0.0	0.0

MATRIX 2-B

RAW MASS TRANSFER COEFFICIENT DATA MATRIX
5.7 MICRON, 3-D

RUN # =27. # BREATHS = 320. TIME/BREATH, SEC = 0.94 COUNT AREA, SQ CM = 1.204E-02

	1	2	3	4	5	6	7	8	9
	0.028	0.112	0.224	0.392	0.672	1.270	2.540	3.810	4.445
1	0.0	0.0	0.0	0.0	0.0	0.0	0.0	0.0	0.0
2	0.0	0.0	0.0	0.0	0.0	0.0	0.0	0.0	0.0
3	0.0	0.0	0.0	0.0	0.0	0.0	0.0	0.0	0.0
4	0.0	0.0	0.0	0.0	0.0	0.0	0.0	0.0	0.0
5	1.66E-02	0.0	0.0	0.0	0.0	0.0	0.0	0.0	0.0
6	1.66E-02	3.33E-02	1.66E-02	0.0	1.66E-02	8.32E-03	0.0	1.66E-02	1.66E-02
7	8.32E-02	1.66E-02	9.99E-02	1.17E-01	4.99E-02	9.99E-02	5.83E-02	1.66E-02	4.16E-02
8	8.32E-02	6.66E-02	1.17E-01	1.50E-01	1.33E-01	1.25E-01	6.66E-02	1.66E-02	6.66E-02
9	3.33E-01	1.83E-01	4.99E-02	1.17E-01	9.99E-02	9.16E-02	5.83E-02	4.99E-02	5.83E-02
10	2.18E 00	1.33E-01	2.50E-01	1.66E-01	8.32E-02	4.16E-02	8.32E-02	8.32E-02	4.99E-02
11	3.16E-01	1.33E-01	1.50E-01	9.99E-02	1.17E-01	1.25E-01	5.83E-02	5.83E-02	4.16E-02
12	4.99E-02	9.99E-02	8.32E-02	1.17E-01	8.32E-02	4.99E-02	4.16E-02	3.33E-02	2.50E-02
13	1.66E-02	6.66E-02	1.66E-02	0.0	2.50E-02	3.33E-02	2.50E-02	4.16E-02	3.33E-02
14	1.66E-02	1.66E-02	1.66E-02	4.99E-02	8.32E-03	1.66E-02	1.66E-02	2.50E-02	0.0
15	3.33E-02	1.66E-02	0.0	1.66E-02	0.0	0.0	0.0	0.0	0.0
16	0.0	0.0	0.0	0.0	0.0	0.0	0.0	0.0	0.0
17	0.0	0.0	0.0	0.0	0.0	0.0	0.0	0.0	0.0
18	0.0	0.0	0.0	0.0	0.0	0.0	0.0	0.0	0.0
19	0.0	0.0	0.0	0.0	0.0	0.0	0.0	0.0	0.0

PARTICLES/CC = 1.77E 01

MATRIX 3-A

RAW COUNT DATA MATRIX
2.02 MICRON, 3-D RUN 12

	1 0.007	2 0.027	3 0.110	4 0.220	5 0.317	6 0.635	7 1.270	8 2.540	9 3.810	10 4.450
1	0.0	1.00	0.0	0.0	1.00	0.0	0.0	0.0	0.0	1.00
2	0.0	1.00	0.0	0.0	0.0	0.0	0.0	0.0	0.0	0.0
3	0.0	0.0	0.0	0.0	0.0	0.0	0.0	0.0	0.0	0.0
4	0.0	1.00	0.0	1.00	1.00	1.00	0.0	0.0	0.0	0.0
5	0.0	2.00	0.0	2.00	1.00	0.0	1.00	0.0	0.0	2.00
6	2.00	5.50	3.00	4.00	2.50	7.00	2.50	2.00	3.50	1.50
7	5.00	8.50	12.00	11.50	10.50	8.50	8.00	10.00	7.00	5.50
8	10.00	17.00	16.00	18.50	13.50	13.00	13.50	15.50	8.50	8.50
9	13.00	13.50	15.00	19.50	14.50	15.50	19.00	17.00	7.00	15.00
10	22.00	7.00	15.50	27.00	22.00	19.00	16.50	16.50	16.00	10.00
11	19.00	9.50	13.00	21.50	16.50	15.00	12.50	15.00	11.00	12.00
12	17.00	12.50	14.50	9.50	12.00	14.50	13.00	11.00	9.50	12.00
13	7.00	14.00	10.50	10.50	11.00	8.50	10.00	5.00	5.50	10.00
14	6.00	8.50	6.00	4.50	6.50	6.00	4.50	3.50	4.50	5.50
15	0.0	1.00	1.00	2.00	1.00	0.0	0.0	0.0	0.0	2.00
16	0.0	1.00	0.0	0.0	0.0	0.0	0.0	0.0	0.0	0.0
17	0.0	1.00	0.0	0.0	0.0	0.0	0.0	0.0	0.0	0.0
18	0.0	1.00	0.0	0.0	0.0	0.0	0.0	0.0	0.0	0.0
19	0.0	1.00	0.0	0.0	1.00	0.0	0.0	0.0	0.0	1.00

MATRIX 3-B

RAW MASS TRANSFER COEFFICIENT DATA MATRIX
2.02 MICRON, 3-D

RUN # =12. # BREATHS = 300. TIME/BREATH, SEC = 1.88 COUNT AREA, SQ CM = 2.949E-03

	1 0.007	2 0.027	3 0.110	4 0.220	5 0.317	6 0.635	7 1.270	8 2.540	9 3.810	10 4.450
1	0.0	7.64E-04	0.0	0.0	7.64E-04	0.0	0.0	0.0	0.0	7.64E-04
2	0.0	7.64E-04	0.0	0.0	0.0	0.0	0.0	0.0	0.0	0.0
3	0.0	0.0	0.0	0.0	0.0	0.0	0.0	0.0	0.0	0.0
4	0.0	7.64E-04	0.0	7.64E-04	7.64E-04	7.64E-04	0.0	0.0	0.0	0.0
5	0.0	1.53E-03	0.0	1.53E-03	7.64E-04	0.0	7.64E-04	0.0	0.0	1.53E-03
6	1.53E-03	4.20E-03	2.29E-03	3.06E-03	1.91E-03	5.35E-03	1.91E-03	1.53E-03	2.67E-03	1.15E-03
7	3.82E-03	6.49E-03	9.17E-03	8.78E-03	8.02E-03	6.49E-03	6.11E-03	7.64E-03	5.35E-03	4.20E-03
8	7.64E-03	1.30E-02	1.22E-02	1.41E-02	1.03E-02	9.93E-03	1.03E-02	1.18E-02	6.49E-03	6.49E-03
9	9.93E-03	1.03E-02	1.15E-02	1.49E-02	1.11E-02	1.18E-02	1.45E-02	1.30E-02	5.35E-03	1.15E-02
10	1.08E-02	5.35E-03	1.18E-02	2.06E-02	1.68E-02	1.45E-02	1.26E-02	1.26E-02	1.22E-02	7.64E-03
11	1.45E-02	7.26E-03	9.93E-03	1.64E-02	1.26E-02	1.15E-02	9.55E-03	1.15E-02	8.40E-03	9.17E-03
12	1.30E-02	9.55E-03	1.11E-02	7.26E-03	9.17E-03	1.11E-02	9.93E-03	8.40E-03	7.26E-03	9.17E-03
13	5.35E-03	1.07E-02	8.02E-03	8.02E-03	8.40E-03	6.49E-03	7.64E-03	3.82E-03	4.20E-03	7.64E-03
14	4.58E-03	6.49E-03	4.58E-03	3.44E-03	4.97E-03	4.58E-03	3.44E-03	2.67E-03	3.44E-03	4.20E-03
15	0.0	7.64E-04	7.64E-04	1.53E-03	7.64E-04	0.0	0.0	0.0	0.0	1.53E-03
16	0.0	7.64E-04	0.0	0.0	0.0	0.0	0.0	0.0	0.0	0.0
17	0.0	7.64E-04	0.0	0.0	0.0	0.0	0.0	0.0	0.0	0.0
18	0.0	7.64E-04	0.0	0.0	0.0	0.0	0.0	0.0	0.0	0.0
19	0.0	7.64E-04	0.0	0.0	7.64E-04	0.0	0.0	0.0	0.0	7.64E-04

PARTICLES/CC = 8.400E 02

MATRIX 3-C

RAW COUNT DATA MATRIX
2.02 MICRON, 3-D RUN 14

	1 0.007	2 0.027	3 0.110	4 0.220	5 0.317	6 0.635	7 1.270	8 2.540	9 3.810	10 4.450
1	0.0	0.0	0.0	0.0	0.0	0.0	0.0	0.0	0.0	0.0
2	0.0	0.0	0.0	0.0	0.0	0.0	0.0	0.0	0.0	0.0
3	0.0	0.0	0.0	0.0	0.0	0.0	0.0	0.0	0.0	0.0
4	0.0	0.0	0.0	0.0	0.0	0.0	0.0	0.0	0.0	0.0
5	0.0	0.0	0.0	0.0	0.0	0.0	0.0	0.0	0.0	0.0
6	4.00	4.50	4.00	4.50	3.00	4.00	4.00	4.00	3.50	0.0
7	8.00	7.00	9.00	12.50	4.00	11.50	10.00	3.50	9.00	5.00
8	11.50	8.50	12.00	10.50	14.50	8.50	10.50	13.50	7.00	7.50
9	12.50	14.50	14.50	18.50	17.50	13.00	12.00	13.50	11.00	11.00
10	11.50	13.00	11.00	18.00	16.00	24.00	11.00	9.00	6.50	6.50
11	9.50	15.00	14.00	15.50	11.00	12.00	13.00	10.00	8.50	9.00
12	7.50	6.00	14.50	12.00	12.50	11.50	8.50	9.00	6.00	4.50
13	7.50	10.00	9.50	10.50	10.50	9.50	5.50	8.00	2.50	3.50
14	3.00	3.50	2.50	3.00	3.50	6.00	4.00	1.00	5.00	0.0
15	0.0	0.0	0.0	0.0	0.0	0.0	0.0	0.0	0.0	0.0
16	0.0	0.0	0.0	0.0	0.0	0.0	0.0	0.0	0.0	0.0
17	0.0	0.0	0.0	0.0	0.0	0.0	0.0	0.0	0.0	0.0
18	0.0	0.0	0.0	0.0	0.0	0.0	0.0	0.0	0.0	0.0
19	0.0	0.0	0.0	0.0	0.0	0.0	0.0	0.0	0.0	0.0

MATRIX 3-D

RAW MASS TRANSFER COEFFICIENT DATA MATRIX
2.02 MICRON, 3-D

RUN # =14. # BREATHS = 300. TIME/BREATH, SEC = 1.88 COUNT AREA, SQ CM = 2.949E-03

	1 0.007	2 0.027	3 0.110	4 0.220	5 0.317	6 0.635	7 1.270	8 2.540	9 3.810	10 4.450
1	0.0	0.0	0.0	0.0	0.0	0.0	0.0	0.0	0.0	0.0
2	0.0	0.0	0.0	0.0	0.0	0.0	0.0	0.0	0.0	0.0
3	0.0	0.0	0.0	0.0	0.0	0.0	0.0	0.0	0.0	0.0
4	0.0	0.0	0.0	0.0	0.0	0.0	0.0	0.0	0.0	0.0
5	0.0	0.0	0.0	0.0	0.0	0.0	0.0	0.0	0.0	0.0
6	2.97E-03	3.34E-03	2.97E-03	3.34E-03	2.23E-03	2.97E-03	2.97E-03	2.97E-03	2.60E-03	0.0
7	5.93E-03	5.19E-03	6.68E-03	9.27E-03	2.97E-03	8.53E-03	7.42E-03	2.60E-03	6.68E-03	3.71E-03
8	8.53E-03	6.31E-03	8.90E-03	7.79E-03	1.08E-02	6.31E-03	7.79E-03	1.00E-02	5.19E-03	5.56E-03
9	9.27E-03	1.08E-02	1.08E-02	1.37E-02	1.30E-02	9.64E-03	8.90E-03	1.00E-02	8.16E-03	8.16E-03
10	8.53E-03	9.64E-03	8.16E-03	1.34E-02	1.19E-02	1.78E-02	8.16E-03	6.68E-03	4.82E-03	4.82E-03
11	7.05E-03	1.11E-02	1.04E-02	1.15E-02	8.16E-03	8.90E-03	9.64E-03	7.42E-03	6.31E-03	6.68E-03
12	5.56E-03	4.45E-03	1.08E-02	8.90E-03	9.27E-03	8.53E-03	6.31E-03	6.68E-03	4.45E-03	3.34E-03
13	5.56E-03	7.42E-03	7.05E-03	7.79E-03	7.79E-03	7.05E-03	4.08E-03	5.93E-03	1.85E-03	2.60E-03
14	2.23E-03	2.60E-03	1.85E-03	2.23E-03	2.60E-03	4.45E-03	2.97E-03	7.42E-04	3.71E-03	0.0
15	0.0	0.0	0.0	0.0	0.0	0.0	0.0	0.0	0.0	0.0
16	0.0	0.0	0.0	0.0	0.0	0.0	0.0	0.0	0.0	0.0
17	0.0	0.0	0.0	0.0	0.0	0.0	0.0	0.0	0.0	0.0
18	0.0	0.0	0.0	0.0	0.0	0.0	0.0	0.0	0.0	0.0
19	0.0	0.0	0.0	0.0	0.0	0.0	0.0	0.0	0.0	0.0

PARTICLES/CC = 8.650E 02

MATRIX 3-E

RAW COUNT DATA MATRIX
2.02 MICRON, 3-D RUN 17

	1 0.007	2 0.027	3 0.110	4 0.220	5 0.317	6 0.635	7 1.270	8 2.540	9 3.810	10 4.450
1	0.0	0.0	0.0	0.0	0.0	0.0	0.0	0.0	0.0	0.0
2	0.0	0.0	0.0	0.0	0.0	0.0	0.0	0.0	0.0	0.0
3	0.0	0.0	0.0	0.0	0.0	0.0	0.0	0.0	0.0	0.0
4	0.0	0.0	0.0	0.0	0.0	0.0	0.0	0.0	0.0	0.0
5	0.0	0.0	0.0	0.0	0.0	0.0	0.0	0.0	0.0	0.0
6	4.00	3.00	6.00	4.00	3.00	9.00	3.00	1.00	1.00	4.00
7	7.00	20.00	9.00	14.00	7.00	8.00	10.00	9.00	10.00	10.00
8	16.00	16.00	21.00	14.00	18.00	11.00	13.00	10.00	12.00	11.00
9	17.00	8.00	20.00	13.00	30.00	28.00	23.00	16.00	12.00	8.00
10	9.00	9.00	13.00	30.00	23.00	21.00	17.00	18.00	14.00	15.00
11	15.00	8.00	16.00	19.00	14.00	19.00	10.00	18.00	14.00	16.00
12	12.00	13.00	8.00	18.00	24.00	18.00	15.00	6.00	8.00	10.00
13	12.00	11.00	8.00	16.00	12.00	9.00	3.00	14.00	4.00	8.00
14	6.00	6.00	1.00	6.00	5.00	5.00	6.00	2.00	2.00	4.00
15	0.0	0.0	0.0	0.0	0.0	0.0	0.0	0.0	0.0	0.0
16	0.0	0.0	0.0	0.0	0.0	0.0	0.0	0.0	0.0	0.0
17	0.0	0.0	0.0	0.0	0.0	0.0	0.0	0.0	0.0	0.0
18	0.0	0.0	0.0	0.0	0.0	0.0	0.0	0.0	0.0	0.0
19	0.0	0.0	0.0	0.0	0.0	0.0	0.0	0.0	0.0	0.0

MATRIX 3-F

RAW MASS TRANSFER COEFFICIENT DATA MATRIX
2.02 MICRON, 3-D

RUN # =17. # BREATHS = 300. TIME/BREATH, SEC = 1.88 COUNT AREA, SQ CM = 2.949E-03

	1 0.007	2 0.027	3 0.110	4 0.220	5 0.317	6 0.635	7 1.270	8 2.540	9 3.810	10 4.450
1	0.0	0.0	0.0	0.0	0.0	0.0	0.0	0.0	0.0	0.0
2	0.0	0.0	0.0	0.0	0.0	0.0	0.0	0.0	0.0	0.0
3	0.0	0.0	0.0	0.0	0.0	0.0	0.0	0.0	0.0	0.0
4	0.0	0.0	0.0	0.0	0.0	0.0	0.0	0.0	0.0	0.0
5	0.0	0.0	0.0	0.0	0.0	0.0	0.0	0.0	0.0	0.0
6	2.05E-03	1.54E-03	3.08E-03	2.05E-03	1.54E-03	4.62E-03	1.54E-03	5.13E-04	5.13E-04	2.05E-03
7	3.59E-03	1.03E-02	4.62E-03	7.19E-03	3.59E-03	4.11E-03	5.13E-03	4.62E-03	5.13E-03	5.13E-03
8	8.21E-03	8.21E-03	1.08E-02	7.19E-03	9.24E-03	5.65E-03	6.67E-03	5.13E-03	6.16E-03	5.65E-03
9	8.73E-03	4.11E-03	1.03E-02	6.67E-03	1.54E-02	1.44E-02	1.18E-02	8.21E-03	6.16E-03	4.11E-03
10	4.62E-03	4.62E-03	6.67E-03	1.54E-02	1.18E-02	1.08E-02	8.73E-03	9.24E-03	7.19E-03	7.70E-03
11	7.70E-03	4.11E-03	8.21E-03	9.75E-03	7.19E-03	9.75E-03	5.13E-03	9.24E-03	7.19E-03	8.21E-03
12	6.16E-03	6.67E-03	4.11E-03	9.24E-03	1.23E-02	9.24E-03	7.70E-03	3.08E-03	4.11E-03	5.13E-03
13	6.16E-03	5.65E-03	4.11E-03	8.21E-03	6.16E-03	4.62E-03	1.54E-03	7.19E-03	2.05E-03	4.11E-03
14	3.08E-03	3.08E-03	5.13E-04	3.08E-03	2.57E-03	2.57E-03	3.08E-03	1.03E-03	1.03E-03	2.05E-03
15	0.0	0.0	0.0	0.0	0.0	0.0	0.0	0.0	0.0	0.0
16	0.0	0.0	0.0	0.0	0.0	0.0	0.0	0.0	0.0	0.0
17	0.0	0.0	0.0	0.0	0.0	0.0	0.0	0.0	0.0	0.0
18	0.0	0.0	0.0	0.0	0.0	0.0	0.0	0.0	0.0	0.0
19	0.0	0.0	0.0	0.0	0.0	0.0	0.0	0.0	0.0	0.0

PARTICLES/CC = 1.250E 03

MATRIX 3-G

RAW COUNT DATA MATRIX
2.02 MICRON, 3-D RUN 19

	1 0.007	2 0.027	3 0.110	4 0.220	5 0.317	6 0.635	7 1.270	8 2.540	9 3.810	10 4.450
1	0.0	0.0	0.0	0.0	0.0	0.0	0.0	0.0	0.0	0.0
2	0.0	0.0	0.0	0.0	0.0	0.0	0.0	0.0	0.0	0.0
3	0.0	0.0	0.0	0.0	0.0	0.0	0.0	0.0	0.0	0.0
4	0.0	0.0	0.0	0.0	0.0	0.0	0.0	0.0	0.0	0.0
5	0.0	0.0	0.0	0.0	0.0	1.00	0.0	0.0	0.0	0.0
6	6.00	7.00	6.00	7.00	5.00	9.00	8.00	7.00	5.00	6.00
7	16.00	14.00	13.00	18.00	19.00	17.00	16.00	19.00	10.00	11.00
8	14.00	17.00	25.00	22.00	29.00	29.00	19.00	34.00	11.00	17.00
9	25.00	29.00	21.00	30.00	27.00	18.00	21.00	32.00	13.00	24.00
10	26.00	13.00	26.00	36.00	27.00	36.00	25.00	25.00	17.00	20.00
11	17.00	14.00	24.00	24.00	20.00	30.00	22.00	34.00	23.00	16.00
12	16.00	18.00	16.00	24.00	13.00	21.00	24.00	19.00	17.00	13.00
13	8.00	13.00	9.00	22.00	5.00	12.00	15.00	12.00	6.00	9.00
14	7.00	10.00	9.00	5.00	3.00	9.00	9.00	6.00	3.00	3.00
15	0.0	0.0	0.0	0.0	1.00	1.00	1.00	0.0	0.0	0.0
16	0.0	0.0	0.0	0.0	0.0	0.0	0.0	0.0	0.0	0.0
17	0.0	0.0	0.0	0.0	0.0	0.0	0.0	0.0	0.0	0.0
18	0.0	0.0	0.0	0.0	0.0	0.0	0.0	0.0	0.0	0.0
19	0.0	0.0	0.0	0.0	0.0	0.0	0.0	0.0	0.0	0.0

MATRIX 3-H

RAW MASS TRANSFER COEFFICIENT DATA MATRIX
2.02 MICRON, 3-D

RUN # =19. # BREATHS = 600. TIME/BREATH, SEC = 1.88 COUNT AREA, SQ CM = 2.949E-03

	1 0.007	2 0.027	3 0.110	4 0.220	5 0.317	6 0.635	7 1.270	8 2.540	9 3.810	10 4.450
1	0.0	0.0	0.0	0.0	0.0	0.0	0.0	0.0	0.0	0.0
2	0.0	0.0	0.0	0.0	0.0	0.0	0.0	0.0	0.0	0.0
3	0.0	0.0	0.0	0.0	0.0	0.0	0.0	0.0	0.0	0.0
4	0.0	0.0	0.0	0.0	0.0	0.0	0.0	0.0	0.0	0.0
5	0.0	0.0	0.0	0.0	0.0	4.39E-04	0.0	0.0	0.0	0.0
6	2.64E-03	3.08E-03	2.64E-03	3.08E-03	2.20E-03	3.96E-03	3.52E-03	3.08E-03	2.20E-03	2.64E-03
7	7.03E-03	6.15E-03	5.71E-03	7.91E-03	8.35E-03	7.47E-03	7.03E-03	8.35E-03	4.39E-03	4.83E-03
8	6.15E-03	7.47E-03	1.10E-02	9.67E-03	1.27E-02	1.27E-02	8.35E-03	1.49E-02	4.83E-03	7.47E-03
9	1.10E-02	1.27E-02	9.23E-03	1.32E-02	1.19E-02	7.91E-03	9.23E-03	1.41E-02	5.71E-03	1.05E-02
10	1.14E-02	5.71E-03	1.14E-02	1.58E-02	1.19E-02	1.58E-02	1.10E-02	1.10E-02	7.47E-03	8.79E-03
11	7.47E-03	6.15E-03	1.05E-02	1.05E-02	8.79E-03	1.32E-02	9.67E-03	1.49E-02	1.01E-02	7.03E-03
12	7.03E-03	7.91E-03	7.03E-03	1.05E-02	5.71E-03	9.23E-03	1.05E-02	8.35E-03	7.47E-03	5.71E-03
13	3.52E-03	5.71E-03	3.96E-03	9.67E-03	2.20E-03	5.27E-03	6.59E-03	5.27E-03	2.64E-03	3.96E-03
14	3.08E-03	4.39E-03	3.96E-03	2.20E-03	1.32E-03	3.96E-03	3.96E-03	2.64E-03	1.32E-03	1.32E-03
15	0.0	0.0	0.0	0.0	4.39E-04	4.39E-04	4.39E-04	0.0	0.0	0.0
16	0.0	0.0	0.0	0.0	0.0	0.0	0.0	0.0	0.0	0.0
17	0.0	0.0	0.0	0.0	0.0	0.0	0.0	0.0	0.0	0.0
18	0.0	0.0	0.0	0.0	0.0	0.0	0.0	0.0	0.0	0.0
19	0.0	0.0	0.0	0.0	0.0	0.0	0.0	0.0	0.0	0.0

PARTICLES/CC = 7.300E 02

MATRIX 3-I

WEIGHTED AVERAGE RAW MASS TRANSFER COEFFICIENT DATA MATRIX
2.02 MICRON, 3-D RUNS 12, 14, 17, 19

	1 0.007	2 0.027	3 0.110	4 0.220	5 0.317	6 0.635	7 1.270	8 2.540	9 3.810	10 4.450
1	0.0	1.45E-04	0.0	0.0	1.45E-04	0.0	0.0	0.0	0.0	1.45E-04
2	0.0	1.45E-04	0.0	0.0	0.0	0.0	0.0	0.0	0.0	0.0
3	0.0	0.0	0.0	0.0	0.0	0.0	0.0	0.0	0.0	0.0
4	0.0	1.45E-04	0.0	1.45E-04	1.45E-04	1.45E-04	0.0	0.0	0.0	0.0
5	0.0	2.91E-04	0.0	2.91E-04	1.45E-04	1.45E-04	1.45E-04	0.0	0.0	2.91E-04
6	2.33E-03	2.91E-03	2.76E-03	2.83E-03	1.96E-03	4.21E-03	2.54E-03	2.03E-03	1.89E-03	1.67E-03
7	5.23E-03	7.19E-03	6.25E-03	8.14E-03	5.89E-03	6.54E-03	6.39E-03	6.03E-03	5.23E-03	4.58E-03
8	7.48E-03	8.50E-03	1.08E-02	9.45E-03	1.09E-02	8.94E-03	8.14E-03	1.06E-02	5.60E-03	6.39E-03
9	9.81E-03	9.45E-03	1.02E-02	1.18E-02	1.29E-02	1.08E-02	1.09E-02	1.14E-02	6.25E-03	8.43E-03
10	9.96E-03	6.10E-03	9.52E-03	1.61E-02	1.28E-02	1.45E-02	1.01E-02	9.96E-03	7.78E-03	7.48E-03
11	8.79E-03	6.76E-03	9.74E-03	1.16E-02	8.94E-03	1.10E-02	8.36E-03	1.12E-02	8.21E-03	7.70E-03
12	7.63E-03	7.19E-03	7.70E-03	9.23E-03	8.94E-03	9.45E-03	8.79E-03	6.54E-03	5.89E-03	5.74E-03
13	5.01E-03	6.98E-03	5.38E-03	8.57E-03	5.60E-03	5.67E-03	4.87E-03	5.67E-03	2.62E-03	4.43E-03
14	3.20E-03	4.07E-03	2.69E-03	2.69E-03	2.62E-03	3.78E-03	3.42E-03	1.82E-03	2.11E-03	1.82E-03
15	0.0	1.45E-04	1.45E-04	2.91E-04	2.91E-04	1.45E-04	1.45E-04	0.0	0.0	2.91E-04
16	0.0	1.45E-04	0.0	0.0	0.0	0.0	0.0	0.0	0.0	0.0
17	0.0	1.45E-04	0.0	0.0	0.0	0.0	0.0	0.0	0.0	0.0
18	0.0	1.45E-04	0.0	0.0	0.0	0.0	0.0	0.0	0.0	0.0
19	0.0	1.45E-04	0.0	0.0	1.45E-04	0.0	0.0	0.0	0.0	1.45E-04

MATRIX 4-A

RAW COUNT DATA MATRIX
2.02 MICRON, 3-D RUN 24

	1	2	3	4	5	6	7	8	9	10
	0.007	0.027	0.110	0.220	0.317	0.635	1.270	2.540	3.800	4.450
1	0.0	0.0	0.0	0.0	0.0	0.0	0.0	0.0	0.0	0.0
2	0.0	0.0	0.0	0.0	0.0	0.0	0.0	0.0	0.0	0.0
3	0.0	0.0	0.0	0.0	0.0	0.0	0.0	0.0	0.0	0.0
4	0.0	0.0	0.0	0.0	0.0	0.0	0.0	0.0	0.0	0.0
5	1.00	0.0	1.00	1.00	1.00	1.00	1.00	0.0	0.0	0.0
6	13.00	8.00	11.50	5.50	3.50	4.50	6.50	3.50	3.00	2.00
7	11.00	16.00	23.00	23.00	19.00	19.50	12.00	26.00	12.00	15.00
8	20.00	17.00	20.00	18.50	24.50	31.50	23.50	27.50	23.00	18.00
9	24.00	17.00	27.00	30.00	28.00	25.50	26.00	25.50	27.50	26.00
10	80.00	15.00	31.50	29.50	33.50	31.50	36.00	30.00	24.50	19.50
11	15.00	25.00	29.00	31.00	27.50	35.00	28.50	30.50	22.00	20.00
12	16.00	15.00	16.50	19.50	20.00	24.00	24.00	26.50	25.00	22.50
13	16.00	7.00	12.50	19.50	23.50	15.50	16.00	20.50	15.00	12.00
14	8.00	3.00	6.00	7.00	7.00	5.50	5.50	4.50	1.50	1.00
15	0.0	4.00	2.00	0.0	3.00	1.00	0.0	1.00	0.0	0.0
16	0.0	1.00	0.0	0.0	0.0	0.0	0.0	0.0	0.0	0.0
17	0.0	0.0	0.0	0.0	0.0	0.0	0.0	0.0	0.0	0.0
18	0.0	0.0	0.0	0.0	0.0	0.0	0.0	0.0	0.0	0.0
19	0.0	0.0	0.0	0.0	0.0	0.0	0.0	0.0	0.0	0.0

MATRIX 4-B

RAW MASS TRANSFER COEFFICIENT DATA MATRIX
2.02 MICRON, 3-D

RUN # =24. # BREATHS = 350. TIME/BREATH, SEC = 0.94 COUNT AREA, SQ CM = 2.949E-03

	1	2	3	4	5	6	7	8	9	10
	0.007	0.027	0.110	0.220	0.317	0.635	1.270	2.540	3.800	4.450
1	0.0	0.0	0.0	0.0	0.0	0.0	0.0	0.0	0.0	0.0
2	0.0	0.0	0.0	0.0	0.0	0.0	0.0	0.0	0.0	0.0
3	0.0	0.0	0.0	0.0	0.0	0.0	0.0	0.0	0.0	0.0
4	0.0	0.0	0.0	0.0	0.0	0.0	0.0	0.0	0.0	0.0
5	8.79E-04	0.0	8.79E-04	8.79E-04	8.79E-04	8.79E-04	8.79E-04	0.0	0.0	0.0
6	1.14E-02	7.03E-03	1.01E-02	4.83E-03	3.08E-03	3.95E-03	5.71E-03	3.08E-03	2.64E-03	1.76E-03
7	9.66E-03	1.41E-02	2.02E-02	2.02E-02	1.67E-02	1.71E-02	1.05E-02	2.28E-02	1.05E-02	1.32E-02
8	1.76E-02	1.49E-02	1.76E-02	1.63E-02	2.15E-02	2.77E-02	2.06E-02	2.42E-02	2.02E-02	1.58E-02
9	2.11E-02	1.49E-02	2.37E-02	2.64E-02	2.46E-02	2.24E-02	2.28E-02	2.24E-02	2.42E-02	2.28E-02
10	7.03E-02	1.32E-02	2.77E-02	2.59E-02	2.94E-02	2.77E-02	3.16E-02	2.64E-02	2.15E-02	1.71E-02
11	1.32E-02	2.20E-02	2.55E-02	2.72E-02	2.42E-02	3.08E-02	2.50E-02	2.68E-02	1.93E-02	1.76E-02
12	1.41E-02	1.32E-02	1.45E-02	1.71E-02	1.76E-02	2.11E-02	2.11E-02	2.33E-02	2.20E-02	1.98E-02
13	1.41E-02	5.15E-03	1.10E-02	1.71E-02	2.06E-02	1.36E-02	1.41E-02	1.80E-02	1.32E-02	1.05E-02
14	7.03E-03	2.64E-03	5.27E-03	6.15E-03	6.15E-03	4.83E-03	4.83E-03	3.95E-03	1.32E-03	8.79E-04
15	0.0	3.51E-03	1.76E-03	0.0	2.64E-03	8.79E-04	0.0	8.79E-04	0.0	0.0
16	0.0	8.79E-04	0.0	0.0	0.0	0.0	0.0	0.0	0.0	0.0
17	0.0	0.0	0.0	0.0	0.0	0.0	0.0	0.0	0.0	0.0
18	0.0	0.0	0.0	0.0	0.0	0.0	0.0	0.0	0.0	0.0
19	0.0	0.0	0.0	0.0	0.0	0.0	0.0	0.0	0.0	0.0

PARTICLES/CC = 1.252E 03

MATRIX 5-A

RAW COUNT DATA MATRIX
1.1 MICRON, 3-D RUN 10

	1	2	3	4	5	6	7	8	9
	0.007	0.027	0.110	0.220	0.317	0.635	1.270	2.540	3.810
1	0.0	0.0	0.0	0.0	0.0	0.0	1.00	0.0	1.00
2	0.0	0.0	0.0	0.0	1.00	0.0	0.0	1.00	0.0
3	2.00	1.00	1.00	0.0	1.00	0.0	3.00	2.00	1.00
4	0.0	2.00	1.00	0.0	0.0	6.00	0.0	1.00	0.0
5	3.00	2.00	3.00	6.00	3.00	1.00	5.00	4.00	1.00
6	7.00	6.00	7.00	9.00	6.00	9.00	6.00	5.00	1.00
7	14.00	18.00	22.00	11.00	15.00	9.00	11.00	10.00	6.00
8	21.00	30.00	19.00	23.00	13.00	21.00	18.00	12.00	13.00
9	13.00	17.00	20.00	18.00	20.00	15.00	16.00	11.00	20.00
10	15.00	18.00	20.00	20.00	21.00	23.00	17.00	14.00	14.00
11	16.00	12.00	11.00	13.00	19.00	19.00	17.00	15.00	15.00
12	11.00	13.00	14.00	25.00	15.00	15.00	16.00	13.00	12.00
13	17.00	10.00	15.00	23.00	14.00	18.00	11.00	10.00	13.00
14	6.00	8.00	6.00	14.00	9.00	12.00	10.00	9.00	3.00
15	2.00	4.00	3.00	5.00	2.00	2.00	3.00	0.0	3.00
16	1.00	0.0	4.00	3.00	1.00	2.00	1.00	0.0	1.00
17	0.0	0.0	2.00	3.00	1.00	0.0	1.00	2.00	0.0
18	0.0	0.0	0.0	0.0	0.0	0.0	1.00	0.0	1.00
19	0.0	0.0	0.0	0.0	0.0	0.0	1.00	0.0	1.00

MATRIX 5-B

RAW MASS TRANSFER COEFFICIENT DATA MATRIX
1.1 MICRON, 3-D

RUN # =10. # BREATHS = 300. TIME/BREATH, SEC = 1.88 COUNT AREA, SQ CM = 2.949E-03

	1 0.007	2 0.027	3 0.110	4 0.220	5 0.317	6 0.635	7 1.270	8 2.540	9 3.810
1	0.0	0.0	0.0	0.0	0.0	0.0	1.07E-04	0.0	1.07E-04
2	0.0	0.0	0.0	0.0	1.07E-04	0.0	0.0	1.07E-04	0.0
3	2.14E-04	1.07E-04	1.07E-04	0.0	1.07E-04	0.0	3.21E-04	2.14E-04	1.07E-04
4	0.0	2.14E-04	1.07E-04	0.0	0.0	6.43E-04	0.0	1.07E-04	0.0
5	3.21E-04	2.14E-04	3.21E-04	6.43E-04	3.21E-04	1.07E-04	5.36E-04	4.28E-04	1.07E-04
6	7.50E-04	6.43E-04	7.50E-04	9.64E-04	6.43E-04	9.64E-04	6.43E-04	5.36E-04	1.07E-04
7	1.50E-03	1.93E-03	2.36E-03	1.18E-03	1.61E-03	9.64E-04	1.18E-03	1.07E-03	6.43E-04
8	2.25E-03	3.21E-03	2.04E-03	2.46E-03	1.39E-03	2.25E-03	1.93E-03	1.29E-03	1.39E-03
9	1.39E-03	1.82E-03	2.14E-03	1.93E-03	2.14E-03	1.61E-03	1.71E-03	1.18E-03	2.14E-03
10	1.61E-03	1.93E-03	2.14E-03	2.14E-03	2.25E-03	2.46E-03	1.82E-03	1.50E-03	1.50E-03
11	1.71E-03	1.29E-03	1.18E-03	1.39E-03	2.04E-03	2.04E-03	1.82E-03	1.61E-03	1.61E-03
12	1.18E-03	1.39E-03	1.50E-03	2.68E-03	1.61E-03	1.61E-03	1.71E-03	1.39E-03	1.29E-03
13	1.82E-03	1.07E-03	1.61E-03	2.46E-03	1.50E-03	1.93E-03	1.18E-03	1.07E-03	1.39E-03
14	6.43E-04	8.57E-04	6.43E-04	1.50E-03	9.64E-04	1.29E-03	1.07E-03	9.64E-04	3.21E-04
15	2.14E-04	4.28E-04	3.21E-04	5.36E-04	2.14E-04	2.14E-04	3.21E-04	0.0	3.21E-04
16	1.07E-04	0.0	4.28E-04	3.21E-04	1.07E-04	2.14E-04	1.07E-04	0.0	1.07E-04
17	0.0	0.0	2.14E-04	3.21E-04	1.07E-04	0.0	1.07E-04	2.14E-04	0.0
18	0.0	0.0	0.0	0.0	0.0	0.0	1.07E-04	0.0	1.07E-04
19	0.0	0.0	0.0	0.0	0.0	0.0	1.07E-04	0.0	1.07E-04

PARTICLES/CC = 5.990E 03

MATRIX 5-C

RAW COUNT DATA MATRIX
1.1 MICRON, 3-D RUN 18

	1	2	3	4	5	6	7	8	9
	0.007	0.027	0.110	0.220	0.317	0.635	1.270	2.540	3.810
1	0.0	0.0	0.0	0.0	0.0	0.0	0.0	0.0	0.0
2	0.0	0.0	0.0	0.0	0.0	0.0	1.00	0.0	0.0
3	0.0	0.0	1.00	0.0	1.00	1.00	2.00	1.00	0.0
4	2.00	7.00	1.00	3.00	4.00	4.00	4.00	3.00	1.00
5	3.00	6.00	10.00	10.00	12.00	10.00	11.00	6.00	6.00
6	20.00	16.00	29.00	20.00	20.00	21.00	20.00	14.00	8.00
7	39.00	32.00	25.00	27.00	27.00	35.00	28.00	27.00	13.00
8	32.00	32.00	44.00	45.00	48.00	47.00	25.00	17.00	18.00
9	40.00	40.00	41.00	46.00	38.00	39.00	25.00	36.00	17.00
10	48.00	30.00	33.00	45.00	37.00	30.00	40.00	30.00	19.00
11	31.00	28.00	40.00	39.00	27.00	49.00	37.00	28.00	21.00
12	34.00	31.00	38.00	42.00	31.00	44.00	35.00	23.00	23.00
13	35.00	36.00	28.00	38.00	20.00	26.00	27.00	14.00	8.00
14	17.00	21.00	22.00	20.00	19.00	21.00	17.00	11.00	8.00
15	5.00	4.00	7.00	8.00	10.00	6.00	12.00	6.00	3.00
16	3.00	1.00	5.00	0.0	3.00	3.00	5.00	3.00	1.00
17	0.0	0.0	0.0	0.0	0.0	1.00	1.00	1.00	0.0
18	0.0	0.0	0.0	0.0	0.0	0.0	0.0	0.0	0.0
19	0.0	0.0	0.0	0.0	0.0	0.0	0.0	0.0	0.0

MATRIX 5-D

RAW MASS TRANSFER COEFFICIENT DATA MATRIX
1.1 MICRON, 3-D

RUN # =18. # BREATHS = 600. TIME/BREATH, SEC = 1.88 COUNT AREA, SQ CM = 2.949E-03

	1 0.007	2 0.027	3 0.110	4 0.220	5 0.317	6 0.635	7 1.270	8 2.540	9 3.810
1	0.0	0.0	0.0	0.0	0.0	0.0	0.0	0.0	0.0
2	0.0	0.0	0.0	0.0	0.0	0.0	4.73E-05	0.0	0.0
3	0.0	0.0	4.73E-05	0.0	4.73E-05	4.73E-05	9.45E-05	4.73E-05	0.0
4	9.45E-05	3.31E-04	4.73E-05	1.42E-04	1.89E-04	1.89E-04	1.89E-04	1.42E-04	4.73E-05
5	1.42E-04	2.84E-04	4.73E-04	4.73E-04	5.67E-04	4.73E-04	5.20E-04	2.84E-04	2.84E-04
6	9.45E-04	7.56E-04	1.37E-03	9.45E-04	9.45E-04	9.92E-04	9.45E-04	6.62E-04	3.78E-04
7	1.84E-03	1.51E-03	1.18E-03	1.28E-03	1.28E-03	1.65E-03	1.32E-03	1.28E-03	6.14E-04
8	1.51E-03	1.51E-03	2.08E-03	2.13E-03	2.27E-03	2.22E-03	1.18E-03	8.03E-04	8.51E-04
9	1.89E-03	1.89E-03	1.94E-03	2.17E-03	1.80E-03	1.84E-03	1.18E-03	1.70E-03	8.03E-04
10	2.27E-03	1.42E-03	1.56E-03	2.13E-03	1.75E-03	1.42E-03	1.89E-03	1.42E-03	8.98E-04
11	1.46E-03	1.32E-03	1.89E-03	1.84E-03	1.28E-03	2.32E-03	1.75E-03	1.32E-03	9.92E-04
12	1.61E-03	1.46E-03	1.80E-03	1.98E-03	1.46E-03	2.08E-03	1.65E-03	1.09E-03	1.09E-03
13	1.65E-03	1.70E-03	1.32E-03	1.80E-03	9.45E-04	1.23E-03	1.28E-03	6.62E-04	3.78E-04
14	8.03E-04	9.92E-04	1.04E-03	9.45E-04	8.98E-04	9.92E-04	8.03E-04	5.20E-04	3.78E-04
15	2.36E-04	1.89E-04	3.31E-04	3.78E-04	4.73E-04	2.84E-04	5.67E-04	2.84E-04	1.42E-04
16	1.42E-04	4.73E-05	2.36E-04	0.0	1.42E-04	1.42E-04	2.36E-04	1.42E-04	4.73E-05
17	0.0	0.0	0.0	0.0	0.0	4.73E-05	4.73E-05	4.73E-05	0.0
18	0.0	0.0	0.0	0.0	0.0	0.0	0.0	0.0	0.0
19	0.0	0.0	0.0	0.0	0.0	0.0	0.0	0.0	0.0

PARTICLES/CC = 6.790E 03

MATRIX 5-E

WEIGHTED AVERAGE RAW MASS TRANSFER COEFFICIENT DATA MATRIX
1.1 MICRON, 3-D RUNS 10, 18

	1	2	3	4	5	6	7	8	9
	0.007	0.027	0.110	0.220	0.317	0.635	1.270	2.540	3.810
1	0.0	0.0	0.0	0.0	0.0	0.0	3.28E-05	0.0	3.28E-05
2	0.0	0.0	0.0	0.0	3.28E-05	0.0	3.28E-05	3.28E-05	0.0
3	6.56E-05	3.28E-05	6.56E-05	0.0	6.56E-05	3.28E-05	1.64E-04	9.84E-05	3.28E-05
4	6.56E-05	2.95E-04	6.56E-05	9.84E-05	1.31E-04	3.28E-04	1.31E-04	1.31E-04	3.28E-05
5	1.97E-04	2.62E-04	4.26E-04	5.25E-04	4.92E-04	3.61E-04	5.25E-04	3.28E-04	2.30E-04
6	8.85E-04	7.21E-04	1.18E-03	9.51E-04	8.52E-04	9.84E-04	8.52E-04	6.23E-04	2.95E-04
7	1.74E-03	1.64E-03	1.54E-03	1.25E-03	1.38E-03	1.44E-03	1.28E-03	1.21E-03	6.23E-04
8	1.74E-03	2.03E-03	2.07E-03	2.23E-03	2.00E-03	2.23E-03	1.41E-03	9.51E-04	1.02E-03
9	1.74E-03	1.87E-03	2.00E-03	2.10E-03	1.90E-03	1.77E-03	1.34E-03	1.54E-03	1.21E-03
10	2.07E-03	1.57E-03	1.74E-03	2.13E-03	1.90E-03	1.74E-03	1.87E-03	1.44E-03	1.08E-03
11	1.54E-03	1.31E-03	1.67E-03	1.70E-03	1.51E-03	2.23E-03	1.77E-03	1.41E-03	1.18E-03
12	1.48E-03	1.44E-03	1.70E-03	2.20E-03	1.51E-03	1.93E-03	1.67E-03	1.18E-03	1.15E-03
13	1.70E-03	1.51E-03	1.41E-03	2.00E-03	1.11E-03	1.44E-03	1.25E-03	7.87E-04	6.89E-04
14	7.54E-04	9.51E-04	9.18E-04	1.11E-03	9.18E-04	1.08E-03	8.85E-04	6.56E-04	3.61E-04
15	2.30E-04	2.62E-04	3.28E-04	4.26E-04	3.93E-04	2.62E-04	4.92E-04	1.97E-04	1.97E-04
16	1.31E-04	3.28E-05	2.95E-04	9.84E-05	1.31E-04	1.64E-04	1.97E-04	9.84E-05	6.56E-05
17	0.0	0.0	6.56E-05	9.84E-05	3.28E-05	3.28E-05	6.56E-05	9.84E-05	0.0
18	0.0	0.0	0.0	0.0	0.0	0.0	3.28E-05	0.0	3.28E-05
19	0.0	0.0	0.0	0.0	0.0	0.0	3.28E-05	0.0	3.28E-05

MATRIX 6-A

RAW COUNT DATA MATRIX
1.1 MICRON, 3-D RUN 25

	1 0.007	2 0.027	3 0.110	4 0.220	5 0.317	6 0.635	7 1.270	8 2.540	9 3.800	10 4.450
1	0.0	0.0	0.0	0.0	0.0	0.0	1.00	0.0	0.0	0.0
2	0.0	0.0	0.0	0.0	0.0	1.00	3.00	0.0	0.0	0.0
3	0.0	1.00	1.00	2.00	0.0	6.00	5.00	2.00	0.0	0.0
4	5.00	4.00	3.00	4.00	8.00	11.00	7.00	6.00	1.00	3.00
5	13.00	19.00	19.00	11.00	16.00	17.00	9.00	18.00	4.00	4.00
6	21.00	33.00	25.00	18.00	13.00	22.00	20.00	13.00	17.00	6.00
7	39.00	29.00	41.00	37.00	30.00	34.00	30.00	24.00	18.00	18.00
8	37.00	33.00	39.00	53.00	35.00	38.00	51.00	40.00	31.00	26.00
9	51.00	70.00	59.00	57.00	66.00	61.00	60.00	49.00	39.00	40.00
10	130.00	70.00	77.00	89.00	64.00	60.00	42.00	28.00	25.00	42.00
11	63.00	77.00	62.00	52.00	69.00	60.00	45.00	31.00	27.00	39.00
12	50.00	57.00	41.00	63.00	42.00	46.00	50.00	35.00	33.00	24.00
13	35.00	34.00	24.00	30.00	39.00	30.00	25.00	22.00	16.00	17.00
14	20.00	26.00	20.00	18.00	30.00	19.00	21.00	14.00	12.00	7.00
15	12.00	13.00	15.00	17.00	15.00	21.00	13.00	15.00	7.00	3.00
16	2.00	1.00	3.00	5.00	9.00	5.00	5.00	4.00	2.00	0.0
17	0.0	0.0	2.00	1.00	0.0	1.00	2.00	1.00	1.00	0.0
18	0.0	0.0	0.0	0.0	0.0	1.00	3.00	1.00	0.0	0.0
19	0.0	0.0	0.0	0.0	0.0	0.0	1.00	0.0	0.0	0.0

MATRIX 6-B

RAW MASS TRANSFER COEFFICIENT DATA MATRIX
1.1 MICRON, 3-D

RUN # =25. # BREATHS = 300. TIME/BREATH, SEC = 0.94 COUNT AREA, SQ CM = 2.949E-03 PARTICLES/CC = 1.390E 04

	1	2	3	4	5	6	7	8	9	10
	0.007	0.027	0.110	0.220	0.317	0.635	1.270	2.540	3.800	4.450
1	0.0	0.0	0.0	0.0	0.0	0.0	9.23E-05	0.0	0.0	0.0
2	0.0	0.0	0.0	0.0	0.0	9.23E-05	2.77E-04	0.0	0.0	0.0
3	0.0	9.23E-05	9.23E-05	1.85E-04	0.0	5.54E-04	4.62E-04	1.85E-04	0.0	0.0
4	4.62E-04	3.69E-04	2.77E-04	3.69E-04	7.39E-04	1.02E-03	6.46E-04	5.54E-04	9.23E-05	2.77E-04
5	1.20E-03	1.75E-03	1.75E-03	1.02E-03	1.48E-03	1.57E-03	8.31E-04	1.66E-03	3.69E-04	3.69E-04
6	1.94E-03	3.05E-03	2.31E-03	1.66E-03	1.20E-03	2.03E-03	1.85E-03	1.20E-03	1.57E-03	5.54E-04
7	3.60E-03	2.68E-03	3.79E-03	3.42E-03	2.77E-03	3.14E-03	2.77E-03	2.22E-03	1.66E-03	1.66E-03
8	3.42E-03	3.05E-03	3.60E-03	4.89E-03	3.23E-03	3.51E-03	4.71E-03	3.69E-03	2.86E-03	2.40E-03
9	4.71E-03	6.46E-03	5.45E-03	5.26E-03	6.09E-03	5.63E-03	5.54E-03	4.52E-03	3.60E-03	3.69E-03
10	1.20E-02	6.46E-03	7.11E-03	8.22E-03	5.91E-03	5.54E-03	3.88E-03	2.59E-03	2.31E-03	3.88E-03
11	5.82E-03	7.11E-03	5.72E-03	4.80E-03	6.37E-03	5.54E-03	4.15E-03	2.86E-03	2.49E-03	3.60E-03
12	4.62E-03	5.26E-03	3.79E-03	5.82E-03	3.88E-03	4.25E-03	4.62E-03	3.23E-03	3.05E-03	2.22E-03
13	3.23E-03	3.14E-03	2.22E-03	2.77E-03	3.60E-03	2.77E-03	2.31E-03	2.03E-03	1.48E-03	1.57E-03
14	1.85E-03	2.40E-03	1.85E-03	1.66E-03	2.77E-03	1.75E-03	1.94E-03	1.29E-03	1.11E-03	6.46E-04
15	1.11E-03	1.20E-03	1.38E-03	1.57E-03	1.38E-03	1.94E-03	1.20E-03	1.38E-03	6.46E-04	2.77E-04
16	1.85E-04	9.23E-05	2.77E-04	4.62E-04	8.31E-04	4.62E-04	4.62E-04	3.69E-04	1.85E-04	0.0
17	0.0	0.0	1.85E-04	9.23E-05	0.0	9.23E-05	1.85E-04	9.23E-05	9.23E-05	0.0
18	0.0	0.0	0.0	0.0	0.0	9.23E-05	2.77E-04	9.23E-05	0.0	0.0
19	0.0	0.0	0.0	0.0	0.0	0.0	9.23E-05	0.0	0.0	0.0

MATRIX 7-A

RAW COUNT DATA MATRIX
0.79 MICRON, 3-D RUN 13

	1 0.007	2 0.027	3 0.110	4 0.220	5 0.317	6 0.635	7 1.270	8 2.540	9 3.800	10 4.450
1	0.0	0.0	0.0	0.0	1.00	0.0	0.0	0.0	0.0	0.0
2	0.0	0.0	0.0	0.0	0.0	1.00	0.0	1.00	0.0	1.00
3	1.00	0.0	3.00	2.00	3.00	1.00	0.0	0.0	0.0	3.00
4	5.00	3.00	3.00	4.00	2.00	5.00	1.00	2.00	0.0	1.00
5	0.0	0.0	1.00	7.00	4.00	11.00	6.00	4.00	1.00	0.0
6	12.00	15.00	21.00	15.00	13.00	16.00	16.00	7.00	4.00	7.00
7	27.00	20.00	21.00	28.00	21.00	21.00	18.00	12.00	15.00	10.00
8	28.00	32.00	33.00	35.00	16.00	22.00	17.00	23.00	12.00	7.00
9	25.00	29.00	32.00	34.00	29.00	28.00	21.00	16.00	5.00	12.00
10	25.00	32.00	26.00	34.00	43.00	22.00	24.00	20.00	10.00	10.00
11	26.00	23.00	34.00	32.00	30.00	24.00	24.00	18.00	10.00	11.00
12	21.00	35.00	29.00	23.00	17.00	28.00	21.00	14.00	14.00	5.00
13	23.00	20.00	24.00	27.00	22.00	20.00	23.00	9.00	8.00	5.00
14	12.00	12.00	11.00	7.00	9.00	9.00	14.00	6.00	2.00	5.00
15	0.0	1.00	8.00	5.00	5.00	5.00	6.00	3.00	0.0	5.00
16	3.00	1.00	4.00	1.00	5.00	3.00	3.00	2.00	0.0	6.00
17	0.0	0.0	0.0	0.0	1.00	0.0	1.00	3.00	1.00	1.00
18	0.0	0.0	1.00	1.00	0.0	0.0	0.0	0.0	0.0	2.00
19	0.0	0.0	0.0	0.0	1.00	0.0	0.0	0.0	0.0	0.0

MATRIX 7-B

RAW MASS TRANSFER COEFFICIENT DATA MATRIX
0.79 MICRON, 3-D RUN 13

RUN # =13. # BREATHS = 300. TIME/BREATH, SEC = 1.88 COUNT AREA, SQ CM = 2.949E-03 PARTICLES/CC = 2.120E 04

	1	2	3	4	5	6	7	8	9	10
	0.007	0.027	0.110	0.220	0.317	0.635	1.270	2.540	3.800	4.450
1	0.0	0.0	0.0	0.0	3.03E-05	0.0	0.0	0.0	0.0	0.0
2	0.0	0.0	0.0	0.0	0.0	3.03E-05	0.0	3.03E-05	0.0	3.03E-05
3	3.03E-05	0.0	9.08E-05	6.05E-05	9.08E-05	3.03E-05	0.0	0.0	0.0	9.08E-05
4	1.51E-04	9.08E-05	9.08E-05	1.21E-04	6.05E-05	1.51E-04	3.03E-05	6.05E-05	0.0	3.03E-05
5	0.0	0.0	3.03E-05	2.12E-04	1.21E-04	3.33E-04	1.82E-04	1.21E-04	3.03E-05	0.0
6	3.63E-04	4.54E-04	6.36E-04	4.54E-04	3.93E-04	4.84E-04	4.84E-04	2.12E-04	1.21E-04	2.12E-04
7	8.17E-04	6.05E-04	6.36E-04	8.47E-04	6.36E-04	6.36E-04	5.45E-04	3.63E-04	4.54E-04	3.03E-04
8	8.47E-04	9.69E-04	9.99E-04	1.06E-03	4.84E-04	6.66E-04	5.15E-04	6.96E-04	3.63E-04	2.12E-04
9	7.57E-04	8.78E-04	9.69E-04	1.03E-03	8.78E-04	8.47E-04	6.36E-04	4.84E-04	1.51E-04	3.63E-04
10	7.57E-04	9.69E-04	7.87E-04	1.03E-03	1.30E-03	6.66E-04	7.26E-04	6.05E-04	3.03E-04	3.03E-04
11	7.87E-04	6.96E-04	1.03E-03	9.69E-04	9.08E-04	7.26E-04	7.26E-04	5.45E-04	3.03E-04	3.33E-04
12	6.36E-04	1.06E-03	8.78E-04	6.96E-04	5.15E-04	8.47E-04	6.36E-04	4.24E-04	4.24E-04	1.51E-04
13	6.96E-04	6.05E-04	7.26E-04	8.17E-04	6.66E-04	6.05E-04	6.96E-04	2.72E-04	2.42E-04	1.51E-04
14	3.63E-04	3.63E-04	3.33E-04	2.12E-04	2.72E-04	2.72E-04	4.24E-04	1.82E-04	6.05E-05	1.51E-04
15	0.0	3.03E-05	2.42E-04	1.51E-04	1.51E-04	1.51E-04	1.82E-04	9.08E-05	0.0	1.51E-04
16	9.08E-05	3.03E-05	1.21E-04	3.03E-05	1.51E-04	9.08E-05	9.08E-05	6.05E-05	0.0	1.82E-04
17	0.0	0.0	0.0	0.0	3.03E-05	0.0	3.03E-05	9.08E-05	3.03E-05	3.03E-05
18	0.0	0.0	3.03E-05	3.03E-05	0.0	0.0	0.0	0.0	0.0	6.05E-05
19	0.0	0.0	0.0	0.0	3.03E-05	0.0	0.0	0.0	0.0	0.0

MATRIX 8-A

RAW COUNT DATA MATRIX
0.81 MICRON, 3-D RUN 26

	1	2	3	4	5	6	7	8	9	10
	0.007	0.027	0.110	0.220	0.317	0.635	1.270	2.540	3.800	4.450
1	1.00	1.00	0.0	2.00	0.0	9.00	12.00	8.00	5.00	3.00
2	2.00	2.00	1.00	1.00	2.00	10.00	21.00	11.00	5.00	1.00
3	5.00	5.00	12.00	5.00	10.00	25.00	27.00	21.00	12.00	10.00
4	10.00	13.00	14.00	23.00	27.00	31.00	41.00	23.00	12.00	9.00
5	48.00	48.00	47.00	52.00	45.00	62.00	38.00	26.00	19.00	14.00
6	81.00	80.00	67.00	71.00	68.00	53.00	54.00	34.00	19.00	23.00
7	95.00	79.00	74.00	68.00	84.00	67.00	59.00	39.00	21.00	29.00
8	114.00	103.00	95.00	100.00	89.00	93.00	64.00	64.00	32.00	31.00
9	113.00	121.00	121.00	109.00	96.00	132.00	104.00	81.00	57.00	35.00
10	190.00	144.00	110.00	131.00	124.00	135.00	100.00	77.00	54.00	58.00
11	117.00	123.00	114.00	99.00	102.00	89.00	99.00	75.00	50.00	44.00
12	100.00	92.00	92.00	88.00	108.00	79.00	61.00	57.00	38.00	51.00
13	90.00	75.00	96.00	72.00	76.00	55.00	76.00	50.00	38.00	41.00
14	68.00	67.00	76.00	58.00	76.00	74.00	59.00	36.00	29.00	29.00
15	56.00	47.00	56.00	54.00	49.00	60.00	54.00	32.00	14.00	14.00
16	11.00	11.00	19.00	23.00	31.00	33.00	42.00	20.00	19.00	8.00
17	6.00	5.00	6.00	9.00	9.00	21.00	27.00	14.00	11.00	7.00
18	0.0	1.00	1.00	1.00	0.0	10.00	25.00	9.00	7.00	6.00
19	1.00	1.00	0.0	2.00	0.0	9.00	12.00	8.00	5.00	3.00

MATRIX 8-B

RAW MASS TRANSFER COEFFICIENT DATA MATRIX
0.81 MICRON, 3-D

RUN # =26. # BREATHS = 300. TIME/BREATH, SEC = 0.94 COUNT AREA, SQ CM = 2.949E-03 PARTICLES/CC = 6.650E 04

	1	2	3	4	5	6	7	8	9	10
	0.007	0.027	0.110	0.220	0.317	0.635	1.270	2.540	3.800	4.450
1	1.93E-05	1.93E-05	0.0	3.86E-05	0.0	1.74E-04	2.32E-04	1.54E-04	9.65E-05	5.79E-05
2	3.86E-05	3.86E-05	1.93E-05	1.93E-05	3.86E-05	1.93E-04	4.05E-04	2.12E-04	9.65E-05	1.93E-05
3	9.65E-05	9.65E-05	2.32E-04	9.65E-05	1.93E-04	4.82E-04	5.21E-04	4.05E-04	2.32E-04	1.93E-04
4	1.93E-04	2.51E-04	2.70E-04	4.44E-04	5.21E-04	5.98E-04	7.91E-04	4.44E-04	2.32E-04	1.74E-04
5	9.26E-04	9.26E-04	9.07E-04	1.00E-03	8.68E-04	1.20E-03	7.33E-04	5.02E-04	3.67E-04	2.70E-04
6	1.56E-03	1.54E-03	1.29E-03	1.37E-03	1.31E-03	1.02E-03	1.04E-03	6.56E-04	3.67E-04	4.44E-04
7	1.83E-03	1.52E-03	1.43E-03	1.31E-03	1.62E-03	1.29E-03	1.14E-03	7.53E-04	4.05E-04	5.60E-04
8	2.20E-03	1.99E-03	1.83E-03	1.93E-03	1.72E-03	1.79E-03	1.24E-03	1.24E-03	6.18E-04	5.98E-04
9	2.18E-03	2.34E-03	2.34E-03	2.10E-03	1.85E-03	2.55E-03	2.01E-03	1.56E-03	1.10E-03	6.75E-04
10	3.67E-03	2.78E-03	2.12E-03	2.53E-03	2.39E-03	2.61E-03	1.93E-03	1.49E-03	1.04E-03	1.12E-03
11	2.26E-03	2.37E-03	2.20E-03	1.91E-03	1.97E-03	1.72E-03	1.91E-03	1.45E-03	9.65E-04	8.49E-04
12	1.93E-03	1.78E-03	1.78E-03	1.70E-03	2.08E-03	1.52E-03	1.18E-03	1.10E-03	7.33E-04	9.84E-04
13	1.74E-03	1.45E-03	1.85E-03	1.39E-03	1.47E-03	1.06E-03	1.47E-03	9.65E-04	7.33E-04	7.91E-04
14	1.31E-03	1.29E-03	1.47E-03	1.12E-03	1.47E-03	1.43E-03	1.14E-03	6.95E-04	5.60E-04	5.60E-04
15	1.08E-03	9.07E-04	1.08E-03	1.04E-03	9.46E-04	1.16E-03	1.04E-03	6.18E-04	2.70E-04	2.70E-04
16	2.12E-04	2.12E-04	3.67E-04	4.44E-04	5.98E-04	6.37E-04	8.11E-04	3.86E-04	3.67E-04	1.54E-04
17	1.16E-04	9.65E-05	1.16E-04	1.74E-04	1.74E-04	4.05E-04	5.21E-04	2.70E-04	2.12E-04	1.35E-04
18	0.0	1.93E-05	1.93E-05	1.93E-05	0.0	1.93E-04	4.82E-04	1.74E-04	1.35E-04	1.16E-04
19	1.93E-05	1.93E-05	0.0	3.86E-05	0.0	1.74E-04	2.32E-04	1.54E-04	9.65E-05	5.79E-05

MATRIX 9-A

RAW COUNT DATA MATRIX
0.365 MICRON, 3-D RUN 28

	1	2	3	4	5	6	7
	0.155	0.465	0.775	1.080	2.000	3.000	4.000
1	0.2530	0.1590	0.1550	0.2460	0.3160	0.1130	0.1110
2	0.6390	0.4910	0.7480	0.7960	0.6350	0.5040	0.3530
3	1.6200	1.2800	0.9210	1.0700	0.7140	0.5410	0.4030
4	2.2500	1.6100	1.9200	1.5000	1.0100	0.7530	0.6620
5	1.5100	1.2400	1.0600	0.8370	0.6390	0.5830	0.4200
6	0.5580	0.4520	0.6470	0.7760	0.6350	0.3580	0.3230
7	0.2530	0.1590	0.1550	0.2460	0.3160	0.1130	0.1110

MATRIX 9-B

RAW MASS TRANSFER COEFFICIENT DATA MATRIX
0.365 MICRON, 3-D

RUN # =28. # BREATHS =1980. TIME/BREATH, SEC = 1.88 COUNT AREA, SQ CM = 4.660E-06

	1	2	3	4	5	6	7
	0.155	0.465	0.775	1.080	2.000	3.000	4.000
1	1.49E-04	9.37E-05	9.13E-05	1.45E-04	1.86E-04	6.66E-05	6.54E-05
2	3.77E-04	2.89E-04	4.41E-04	4.69E-04	3.74E-04	2.97E-04	2.08E-04
3	9.55E-04	7.54E-04	5.43E-04	6.31E-04	4.21E-04	3.19E-04	2.37E-04
4	1.33E-03	9.49E-04	1.13E-03	8.84E-04	5.95E-04	4.44E-04	3.90E-04
5	8.90E-04	7.31E-04	6.25E-04	4.93E-04	3.77E-04	3.44E-04	2.48E-04
6	3.29E-04	2.66E-04	3.81E-04	4.57E-04	3.74E-04	2.11E-04	1.90E-04
7	1.49E-04	9.37E-05	9.13E-05	1.45E-04	1.86E-04	6.66E-05	6.54E-05

PARTICLES/CC = 1.044E 05

MATRIX 9C #WINDOWS COUNTED/GRID
0.365 MICRON, 3-D RUN 28

	1	2	3	4	5	6	7
1	296	294	296	294	294	256	289
2	288	294	294	294	296	291	273
3	294	291	286	291	290	292	295
4	290	292	293	296	294	294	293
5	293	294	195	295	288	290	293
6	294	291	292	294	265	293	294

MATRIX 9D AVERAGE WINDOW AREA/GRID
0.365 MICRON, 3-D RUN 28 UNITS= E-06 SQ CM

	1	2	3	4	5	6	7
1	4.66	4.0	4.66	4.0	4.66	4.66	4.66
2	4.66	4.0	5.0	4.0	4.66	3.24	3.24
3	4.0	4.66	4.0	4.66	4.66	4.66	4.66
4	4.66	4.66	3.24	4.66	4.66	3.24	4.66
5	4.66	4.66	4.66	4.66	3.24	4.66	4.66
6	4.66	4.0	4.66	4.66	3.24	5.2	4.66

MATRIX 10-A

RAW COUNT DATA MATRIX
0.365 MICRON, 3-D RUN 32

	1 0.155	2 0.465	3 0.775	4 1.080	5 2.000	6 3.000	7 4.000
1	0.0598	0.0952	0.1420	0.1200	0.0830	0.0663	0.1330
2	0.3450	0.3030	0.4760	0.4120	0.2850	0.1820	0.1080
3	0.8350	0.4810	0.4660	0.3810	0.2980	0.2060	0.1550
4	1.0260	0.9580	0.4880	0.4170	0.3690	0.2600	0.1860
5	0.8350	0.4810	0.4660	0.3810	0.2980	0.2060	0.1550
6	0.3450	0.3030	0.4760	0.4120	0.2850	0.1820	0.1080
7	0.0598	0.0952	0.1420	0.1200	0.0830	0.0663	0.1330

MATRIX 10-B

RAW MASS TRANSFER COEFFICIENT DATA MATRIX
0.365 MICRON, 3-D

RUN # =32. # BREATHS =2000. TIME/BREATH, SEC = 0.94 COUNT AREA, SQ CM = 4.660E-06

	1 0.155	2 0.465	3 0.775	4 1.080	5 2.000	6 3.000	7 4.000
1	9.79E-05	1.56E-04	2.33E-04	1.97E-04	1.36E-04	1.09E-04	2.18E-04
2	5.65E-04	4.96E-04	7.80E-04	6.75E-04	4.67E-04	2.96E-04	1.77E-04
3	1.37E-03	7.88E-04	7.63E-04	6.24E-04	4.88E-04	3.37E-04	2.54E-04
4	1.68E-03	1.57E-03	7.99E-04	6.83E-04	6.04E-04	4.26E-04	3.05E-04
5	1.37E-03	7.88E-04	7.63E-04	6.24E-04	4.88E-04	3.37E-04	2.54E-04
6	5.65E-04	4.96E-04	7.80E-04	6.75E-04	4.67E-04	2.98E-04	1.77E-04
7	9.79E-05	1.56E-04	2.33E-04	1.97E-04	1.36E-04	1.09E-04	2.18E-04

PARTICLES/CC = 7.438E 04

MATRIX 10C #WINDOWS COUNTED/GRID
0.365 MICRON, 3-D RUN 32

	1	2	3	4	5	6	7
1	286	294	291	291	293	298	228
2	293	290	294	291.5	287.5	293	295
3	293.5	293	287.5	290.5	294	290.5	292.5
4	289.5	276	289	283	290	299.5	294

MATRIX 10D AVERAGE WINDOW AREA/GRID
0.365 MICRON, 3-D RUN 32 UNITS= E-06 SQ CM

	1	2	3	4	5	6	7
1	7.08	4.66	7.08	4.66	7.08	7.08	6.45
2	4.66	4.66	4.66	4.66	4.66	7.08	5.4
3	4.85	4.66	4.66	3.24	7.08	7.08	4.0
4	4.66	4.0	4.66	4.66	4.66	4.85	3.24

MATRIX 11-A

RAW COUNT DATA MATRIX
0.088 MICRON, 3-D RUN 31

	1	2	3	4	5	6	7
	0.155	0.465	0.775	1.080	2.000	3.000	4.000
1	0.2000	0.1800	0.1400	0.2900	0.8600	0.3900	0.2100
2	0.8900	0.7000	1.1100	1.5200	1.2100	0.8900	0.7100
3	1.8700	1.9400	1.7800	1.2600	1.0700	1.0200	0.6400
4	3.8300	2.4000	1.8900	1.8500	1.1200	0.8400	0.7200
5	1.8700	1.9400	1.7800	1.2600	1.0700	1.0200	0.6400
6	0.8900	0.7000	1.1100	1.5200	1.2100	0.8900	0.7100
7	0.2000	0.1800	0.1400	0.2900	0.8600	0.3900	0.2100

MATRIX 11-B

RAW MASS TRANSFER COEFFICIENT DATA MATRIX
0.088 MICRON, 3-D

RUN # =31. # BREATHS = 500. TIME/BREATH, SEC = 1.38 COUNT AREA, SQ CM = 7.100E-06

	1	2	3	4	5	6	7
	0.155	0.465	0.775	1.080	2.000	3.000	4.000
1	4.21E-04	3.79E-04	2.95E-04	6.10E-04	1.81E-03	8.21E-04	4.42E-04
2	1.87E-03	1.47E-03	2.34E-03	3.20E-03	2.55E-03	1.87E-03	1.49E-03
3	3.93E-03	4.08E-03	3.75E-03	2.65E-03	2.25E-03	2.15E-03	1.35E-03
4	8.06E-03	5.05E-03	3.98E-03	3.89E-03	2.36E-03	1.77E-03	1.51E-03
5	3.93E-03	4.08E-03	3.75E-03	2.65E-03	2.25E-03	2.15E-03	1.35E-03
6	1.87E-03	1.47E-03	2.34E-03	3.20E-03	2.55E-03	1.87E-03	1.49E-03
7	4.21E-04	3.79E-04	2.95E-04	6.10E-04	1.81E-03	8.21E-04	4.42E-04

PARTICLES/CC = 7.600E 04

MATRIX 11C #WINDOWS COUNTED/GRID
0.088 MICRON, 3-D RUN 31

	1	2	3	4	5	6	7
1	89.5	89.5	90	89	88.5	89	88.5
2	57	87.5	88	88	88	88	88.5
3	60	89	89	88.5	95	120	90
4	125	120	111.5	94	88.5	89.5	89

MATRIX 11D AVERAGE WINDOW AREA/GRID
0.088 MICRON, 3-D RUN 31 UNITS= E-06 SQ CM

	1	2	3	4	5	6	7
1	6.76	7.5	7.08	7.5	5.76	7.5	6.76
2	6.45	7.08	6.45	7.08	6.45	7.08	8.0
3	7.08	7.08	7.08	7.5	7.08	7.5	7.5
4	7.08	6.45	7.08	6.76	6.45	7.5	6.45

MATRIX 12-A

RAW COUNT DATA MATRIX
0.088 MICRON, 3-D RUN 33

	1	2	3	4	5	6	7
	0.155	0.465	0.775	1.080	2.000	3.000	4.000
1	0.4900	0.4100	0.6600	1.1000	0.7800	0.3500	0.2800
2	0.9400	1.2400	1.8800	1.1800	0.8800	0.7200	0.6000
3	3.0000	2.3600	1.8100	1.4400	1.0600	0.8100	0.9400
4	3.9100	2.2200	2.0700	1.8000	0.9800	0.7000	0.6300
5	3.0000	2.3600	1.8100	1.4400	1.0600	0.8100	0.9400
6	0.9400	1.2400	1.8800	1.1800	0.8800	0.7200	0.6000
7	0.4900	0.4100	0.6600	1.1000	0.7800	0.3500	0.2800

MATRIX 12-B

RAW MASS TRANSFER COEFFICIENT DATA MATRIX
0.088 MICRON, 3-D

RUN # =33. # BREATHS =1400. TIME/BREATH, SEC = 0.94 COUNT AREA, SQ CM = 5.400E-06

	1	2	3	4	5	6	7
	0.155	0.465	0.775	1.080	2.000	3.000	4.000
1	1.24E-03	1.03E-03	1.67E-03	2.78E-03	1.97E-03	8.83E-04	7.07E-04
2	2.37E-03	3.13E-03	4.75E-03	2.98E-03	2.22E-03	1.82E-03	1.51E-03
3	7.57E-03	5.96E-03	4.57E-03	3.63E-03	2.68E-03	2.04E-03	2.37E-03
4	9.87E-03	5.60E-03	5.22E-03	4.54E-03	2.47E-03	1.77E-03	1.59E-03
5	7.57E-03	5.96E-03	4.57E-03	3.63E-03	2.68E-03	2.04E-03	2.37E-03
6	2.37E-03	3.13E-03	4.75E-03	2.98E-03	2.22E-03	1.82E-03	1.51E-03
7	1.24E-03	1.03E-03	1.67E-03	2.78E-03	1.97E-03	8.83E-04	7.07E-04

PARTICLES/CC = 5.950E 04

MATRIX 12C #WINDOWS COUNTED/GRID
0.088 MICRON, 3-D RUN 33

	1	2	3	4	5	6	7
1	88	88.5	88	88	88	90	90
2	88	88.5	89.5	88	88.5	89.5	89.5
3	86.5	88.5	88.5	90	88.5	88.5	90
4	88.5	87.5	88.5	90	90	88.5	88

MATRIX 12D AVERAGE WINDOW AREA/GRID
0.088 MICRON, 3-D RUN 33 UNITS= E-06 SQ CM

	1	2	3	4	5	6	7
1	5.4	3.24	3.24	4.0	4.0	4.0	4.0
2	5.4	5.76	5.4	5.2	5.4	5.2	4.0
3	4.66	4.0	4.66	4.0	5.4	5.4	5.76
4	5.4	4.0	5.4	4.66	4.66	5.4	5.76

MATRIX 13-A

RAW COUNT DATA MATRIX
1.1 MICRON, 3-D STEADY FLOW RUN K

	1	2	3	4	5	6	7	8	9	10
	0.007	0.027	0.110	0.220	0.317	0.635	1.270	2.540	3.810	4.445
1	0.0	0.0	0.0	0.0	0.0	0.0	0.0	0.0	0.0	0.0
2	0.0	0.0	0.0	0.0	0.0	0.0	0.0	1.00	0.0	0.0
3	0.0	0.0	0.0	0.0	0.0	0.0	3.00	2.00	0.0	0.0
4	12.00	2.00	1.00	3.00	0.0	2.00	4.00	5.00	0.0	0.0
5	21.00	8.00	11.00	10.00	6.00	1.00	5.00	17.00	0.0	2.00
6	19.00	19.00	11.00	9.00	15.00	8.00	17.00	14.00	8.00	8.00
7	28.00	26.00	25.00	22.00	25.00	16.00	20.00	13.00	18.00	23.00
8	19.00	26.00	17.00	21.00	32.00	27.00	34.00	30.00	36.00	28.00
9	29.00	32.00	22.00	29.00	36.00	30.00	33.00	33.00	39.00	43.00
10	27.00	47.00	34.00	30.00	30.00	33.00	48.00	41.00	50.00	46.00
11	34.00	33.00	31.00	26.00	28.00	37.00	37.00	38.00	45.00	43.00
12	29.00	30.00	26.00	29.00	28.00	32.00	39.00	30.00	21.00	17.00
13	33.00	24.00	24.00	19.00	24.00	17.00	29.00	9.00	1.00	4.00
14	16.00	15.00	14.00	17.00	15.00	18.00	8.00	0.0	2.00	3.00
15	8.00	6.00	8.00	6.00	5.00	13.00	7.00	8.00	2.00	1.00
16	3.00	2.00	0.0	1.00	2.00	2.00	4.00	2.00	0.0	1.00
17	0.0	0.0	0.0	0.0	0.0	0.0	1.00	3.00	0.0	0.0
18	0.0	0.0	0.0	0.0	0.0	0.0	0.0	1.00	0.0	0.0
19	0.0	0.0	0.0	0.0	0.0	0.0	0.0	0.0	0.0	0.0

MATRIX 13-B

RAW MASS TRANSFER COEFFICIENT DATA MATRIX
1.1 MICRON, 3-D STEADY FLOW

RUN # = K # BREATHS =5400. TIME/BREATH, SEC = 1.00 COUNT AREA, SQ CM = 2.949E-03 PARTICLES/CC = 6.160E 03

	1	2	3	4	5	6	7	8	9	10
	0.007	0.027	0.110	0.220	0.317	0.635	1.270	2.540	3.810	4.445
1	0.0	0.0	0.0	0.0	0.0	0.0	0.0	0.0	0.0	0.0
2	0.0	0.0	0.0	0.0	0.0	0.0	0.0	1.09E-05	0.0	0.0
3	0.0	0.0	0.0	0.0	0.0	0.0	3.26E-05	2.18E-05	0.0	0.0
4	1.31E-04	2.18E-05	1.09E-05	3.26E-05	0.0	2.18E-05	4.35E-05	5.44E-05	0.0	0.0
5	2.28E-04	8.70E-05	1.20E-04	1.09E-04	6.53E-05	1.09E-05	5.44E-05	1.85E-04	0.0	2.18E-05
6	2.07E-04	2.07E-04	1.20E-04	9.79E-05	1.63E-04	8.70E-05	1.85E-04	1.52E-04	8.70E-05	8.70E-05
7	3.05E-04	2.83E-04	2.72E-04	2.39E-04	2.72E-04	1.74E-04	2.18E-04	1.41E-04	1.96E-04	2.50E-04
8	2.07E-04	2.83E-04	1.85E-04	2.28E-04	3.48E-04	2.94E-04	3.70E-04	3.26E-04	3.92E-04	3.05E-04
9	3.16E-04	3.48E-04	2.39E-04	3.16E-04	3.92E-04	3.26E-04	3.59E-04	3.59E-04	4.24E-04	4.68E-04
10	2.94E-04	5.11E-04	3.70E-04	3.26E-04	3.26E-04	3.59E-04	5.22E-04	4.46E-04	5.44E-04	5.00E-04
11	3.70E-04	3.59E-04	3.37E-04	2.83E-04	3.05E-04	4.03E-04	4.03E-04	4.13E-04	4.90E-04	4.68E-04
12	3.16E-04	3.26E-04	2.83E-04	3.16E-04	3.05E-04	3.48E-04	4.24E-04	3.26E-04	2.28E-04	1.85E-04
13	3.59E-04	2.61E-04	2.61E-04	2.07E-04	2.61E-04	1.85E-04	3.16E-04	9.79E-05	1.09E-05	4.35E-05
14	1.74E-04	1.63E-04	1.52E-04	1.85E-04	1.63E-04	1.96E-04	8.70E-05	0.0	2.18E-05	3.26E-05
15	8.70E-05	6.53E-05	8.70E-05	6.53E-05	5.44E-05	1.41E-04	7.62E-05	8.70E-05	2.18E-05	1.09E-05
16	3.26E-05	2.18E-05	0.0	1.09E-05	2.18E-05	2.18E-05	4.35E-05	2.18E-05	0.0	1.09E-05
17	0.0	0.0	0.0	0.0	0.0	0.0	1.09E-05	3.26E-05	0.0	0.0
18	0.0	0.0	0.0	0.0	0.0	0.0	0.0	1.09E-05	0.0	0.0
19	0.0	0.0	0.0	0.0	0.0	0.0	0.0	0.0	0.0	0.0

MATRIX 14-A

RAW COUNT DATA MATRIX
1.1 MICRON, 3-D RUN 20

	1	2	3	4	5	6	7	8	9	10
	0.007	0.027	0.110	0.220	0.317	0.635	1.270	2.540	3.800	4.450
1	0.0	1.00	3.00	2.00	1.00	1.00	7.00	3.00	1.00	3.00
2	1.00	3.00	4.00	4.00	3.00	4.00	7.00	5.00	4.00	3.00
3	13.00	13.00	16.00	11.00	10.00	7.00	16.00	22.00	10.00	8.00
4	16.00	25.00	10.00	21.00	18.00	22.00	30.00	20.00	13.00	12.00
5	20.00	34.00	26.00	22.00	27.00	26.00	23.00	11.00	16.00	15.00
6	28.00	21.00	14.00	31.00	23.00	19.00	25.00	10.00	9.00	19.00
7	24.00	24.00	28.00	26.00	28.00	23.00	26.00	16.00	18.00	15.00
8	15.00	15.00	17.00	20.00	18.00	17.00	21.00	12.00	14.00	11.00
9	10.00	8.00	14.00	13.00	17.00	14.00	7.00	4.00	3.00	8.00
10	10.00	8.00	10.00	9.00	5.00	7.00	3.00	3.00	3.00	5.00
11	5.00	11.00	9.00	10.00	11.00	2.00	3.00	8.00	5.00	4.00
12	9.00	14.00	8.00	16.00	21.00	10.00	10.00	8.00	8.00	4.00
13	22.00	16.00	22.00	24.00	24.00	15.00	17.00	15.00	8.00	1.00
14	20.00	21.00	13.00	14.00	28.00	20.00	9.00	13.00	11.00	3.00
15	17.00	16.00	16.00	18.00	17.00	27.00	15.00	16.00	8.00	10.00
16	10.00	17.00	18.00	9.00	15.00	17.00	13.00	13.00	13.00	10.00
17	5.00	9.00	8.00	5.00	7.00	8.00	10.00	5.00	9.00	6.00
18	3.00	0.0	6.00	1.00	4.00	3.00	11.00	6.00	5.00	0.0
19	0.0	1.00	3.00	2.00	1.00	1.00	7.00	3.00	1.00	3.00

MATRIX 14-B

RAW MASS TRANSFER COEFFICIENT DATA MATRIX
1.1 MICRON, 3-D

RUN #=20. # BREATHS = 400. TIME/BREATH, SEC = 1.88 COUNT AREA, SQ CM = 2.949E-03 PARTICLES/CC = 1.017E 04

	1	2	3	4	5	6	7	8	9	10
	0.007	0.027	0.110	0.220	0.317	0.635	1.270	2.540	3.800	4.450
1	0.0	4.73E-05	1.42E-04	9.46E-05	4.73E-05	4.73E-05	3.31E-04	1.42E-04	4.73E-05	1.42E-04
2	4.73E-05	1.42E-04	1.89E-04	1.89E-04	1.42E-04	1.89E-04	3.31E-04	2.37E-04	1.89E-04	1.42E-04
3	6.15E-04	6.15E-04	7.57E-04	5.21E-04	4.73E-04	3.31E-04	7.57E-04	1.04E-03	4.73E-04	3.79E-04
4	7.57E-04	1.18E-03	4.73E-04	9.94E-04	8.52E-04	1.04E-03	1.42E-03	9.46E-04	6.15E-04	5.68E-04
5	9.46E-04	1.61E-03	1.23E-03	1.04E-03	1.28E-03	1.23E-03	1.09E-03	5.21E-04	7.57E-04	7.10E-04
6	1.32E-03	9.94E-04	6.62E-04	1.47E-03	1.09E-03	8.99E-04	1.18E-03	4.73E-04	4.26E-04	8.99E-04
7	1.14E-03	1.14E-03	1.32E-03	1.23E-03	1.32E-03	1.09E-03	1.23E-03	7.57E-04	8.52E-04	7.10E-04
8	7.10E-04	7.10E-04	8.04E-04	9.46E-04	8.52E-04	8.04E-04	9.94E-04	5.68E-04	6.62E-04	5.21E-04
9	4.73E-04	3.79E-04	6.62E-04	6.15E-04	8.04E-04	6.62E-04	3.31E-04	1.89E-04	1.42E-04	3.79E-04
10	4.73E-04	3.79E-04	4.73E-04	4.26E-04	2.37E-04	3.31E-04	1.42E-04	1.42E-04	1.42E-04	2.37E-04
11	2.37E-04	5.21E-04	4.26E-04	4.73E-04	5.21E-04	9.46E-05	1.42E-04	3.79E-04	2.37E-04	1.89E-04
12	4.26E-04	6.62E-04	3.79E-04	7.57E-04	9.94E-04	4.73E-04	4.73E-04	3.79E-04	3.79E-04	1.89E-04
13	1.04E-03	7.57E-04	1.04E-03	1.14E-03	1.14E-03	7.10E-04	8.04E-04	7.10E-04	3.79E-04	4.73E-05
14	9.46E-04	9.94E-04	6.15E-04	6.62E-04	1.32E-03	9.46E-04	4.26E-04	6.15E-04	5.21E-04	1.42E-04
15	8.04E-04	7.57E-04	7.57E-04	8.52E-04	8.04E-04	1.28E-03	7.10E-04	7.57E-04	3.79E-04	4.73E-04
16	4.73E-04	8.04E-04	8.52E-04	4.26E-04	7.10E-04	8.04E-04	6.15E-04	6.15E-04	6.15E-04	4.73E-04
17	2.37E-04	4.26E-04	3.79E-04	2.37E-04	3.31E-04	3.79E-04	4.73E-04	2.37E-04	4.26E-04	2.84E-04
18	1.42E-04	0.0	2.84E-04	4.73E-05	1.89E-04	1.42E-04	5.21E-04	2.84E-04	2.37E-04	0.0
19	0.0	4.73E-05	1.42E-04	9.46E-05	4.73E-05	4.73E-05	3.31E-04	1.42E-04	4.73E-05	1.42E-04

Appendix D

DEPOSITION FROM HELICAL FLOWS

D.1 Unsteady Flow

The major experimental evidence for the effect of secondary flows on particle deposition is discussed in Section 6.5. Further evidence is presented in Map 14 and Figure D.1. Map 14 shows the deposition patterns for 1.1 μm particles for 450 cc., 1.88 sec. inhalations when the plane of the bifurcation was horizontally oriented. The Y = +4.5 strip was the preferred site for sedimentation during 200 of the 400 breaths. During the last 200 breaths the model was rotated 180° so Y = -4.5 was the preferred site. Asymmetries in the contours around Y = 0 were primarily caused by unequal concentrations of particles during each set of 200 breaths.

Regions of enhanced deposition run diagonally on Map 14 from Y = 0, X = 0.2 to Y = ± 9, X = 1.6 cm. The major peaks or "hot spots" for the entire map occur along these two diagonal regions of enhanced deposition, and generally correspond to the Y strips receiving the maximum sedimentation. These diagonal regions also correspond well to those suspected of being caused by secondary motions in the vertical runs.

It is interesting to note that the ">" shaped contours in Map 5 between Y = ± 2 shifted to locations in Map 14 between Y = +5 and +7 and

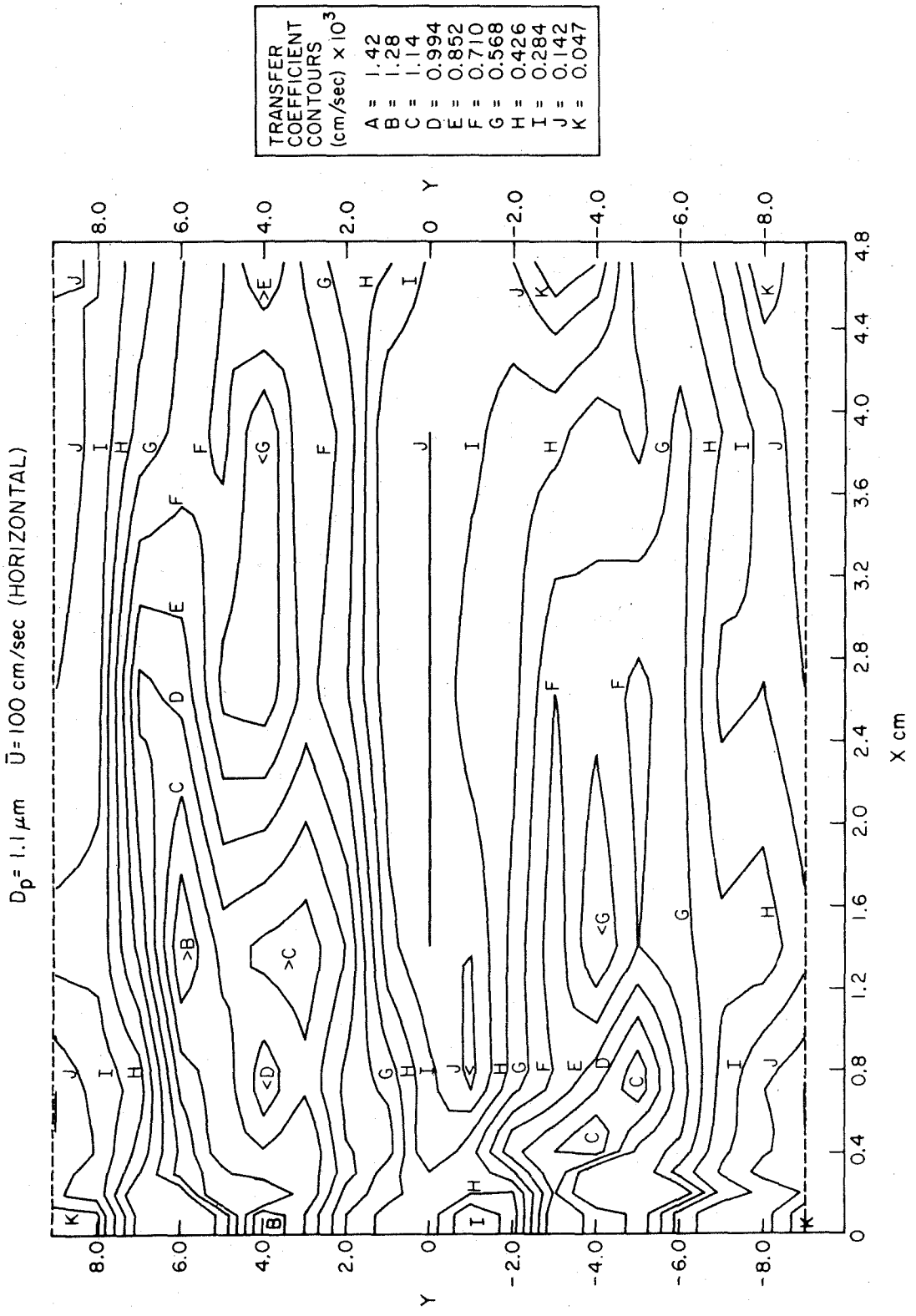

Map 14 3-D Run 20

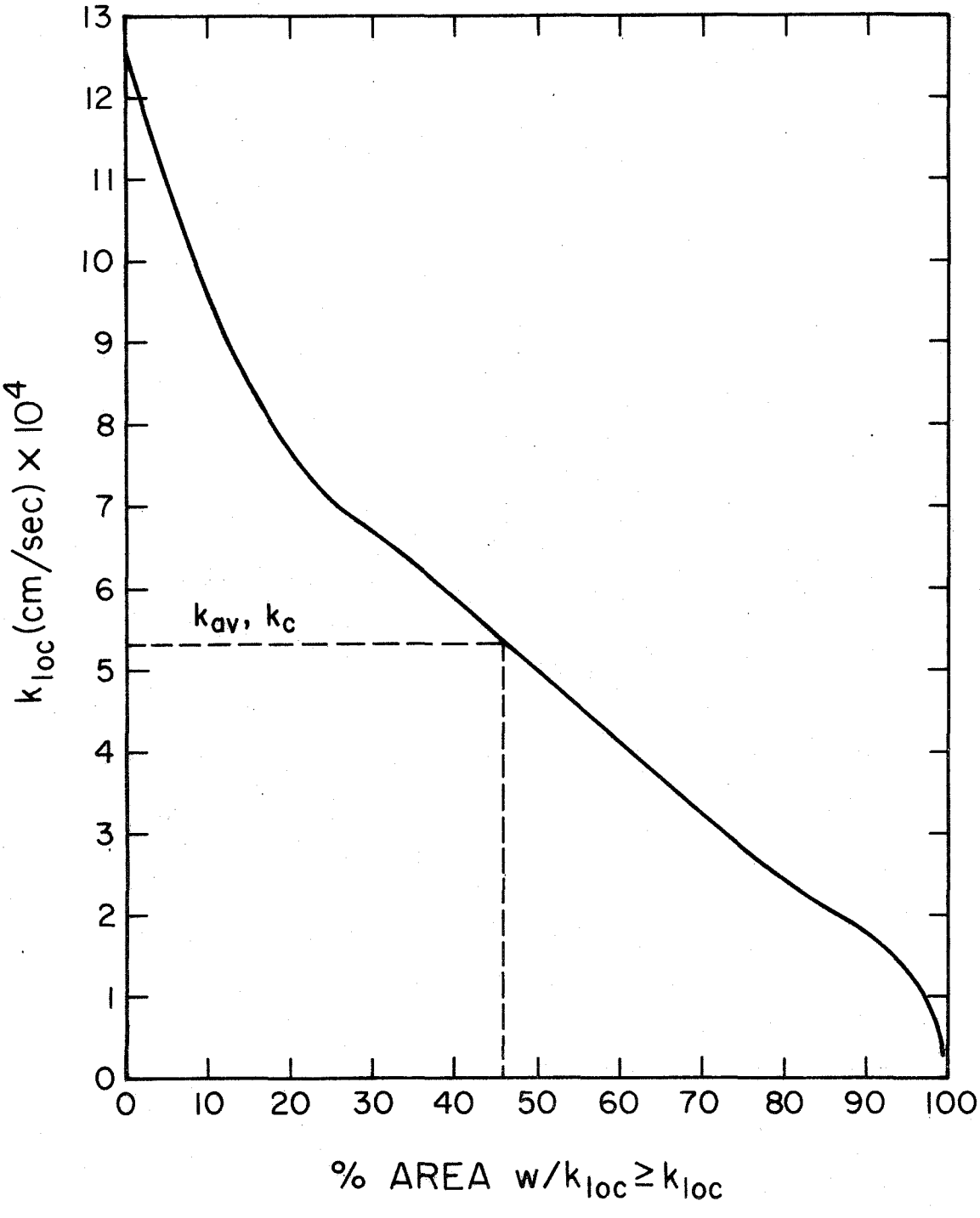

Graph 14 Cumulative Surface Area Distribution for Map 14 Showing the % of the Surface Area of the Daughter Branch with a Local Transfer Coefficient ≥ Stated Value (d_p = 1.1 μm, $\overline{U}$ = 100 cm/sec)

between Y = - 5 and - 7. This is further evidence of the effect of the clean air on sedimentation and of the effect of the secondary flows on the clean air.

Figure D. 1 shows that the peak at X = 0. 2 cm. in the vertical run, which was attributed to the secondary flows, corresponds to a relatively less intense peak from X = 0. 1 - 0. 2 cm. in the horizontal run. The last data point in the horizontal run may have been enhanced by the secondary motions, but this is not apparent in the vertical run because sedimentation predominates along Y = 0.

The diagonal ridges of deposition in the vertical, unsteady flow runs are caused by secondary flows in the manner described below. The explanation is easier to understand by referring to Figure D. 2. The helical paths of particles entrained in steady flow in Figure D. 2 approximate best the flow patterns at the instant U = 100 cm. /sec. during pulsatile inhalations.

Particle-laden air, having the highest axial velocity from the core of the trachea, initially impinges on the carina between the Y = ± 2 strips, causing the highest local shear rates between X = 0 and X = 0. 8 cm. Secondary flows are initiated between Y ± 2 and X = 0. 2 - 0. 8 cm., on account of the imbalance between local centrifugal forces on the air and the local lateral pressure gradients. The resultant helical flows carry the particle-laden air diagonally from Y = 0, X = 0. 1 - 0. 8 cm.

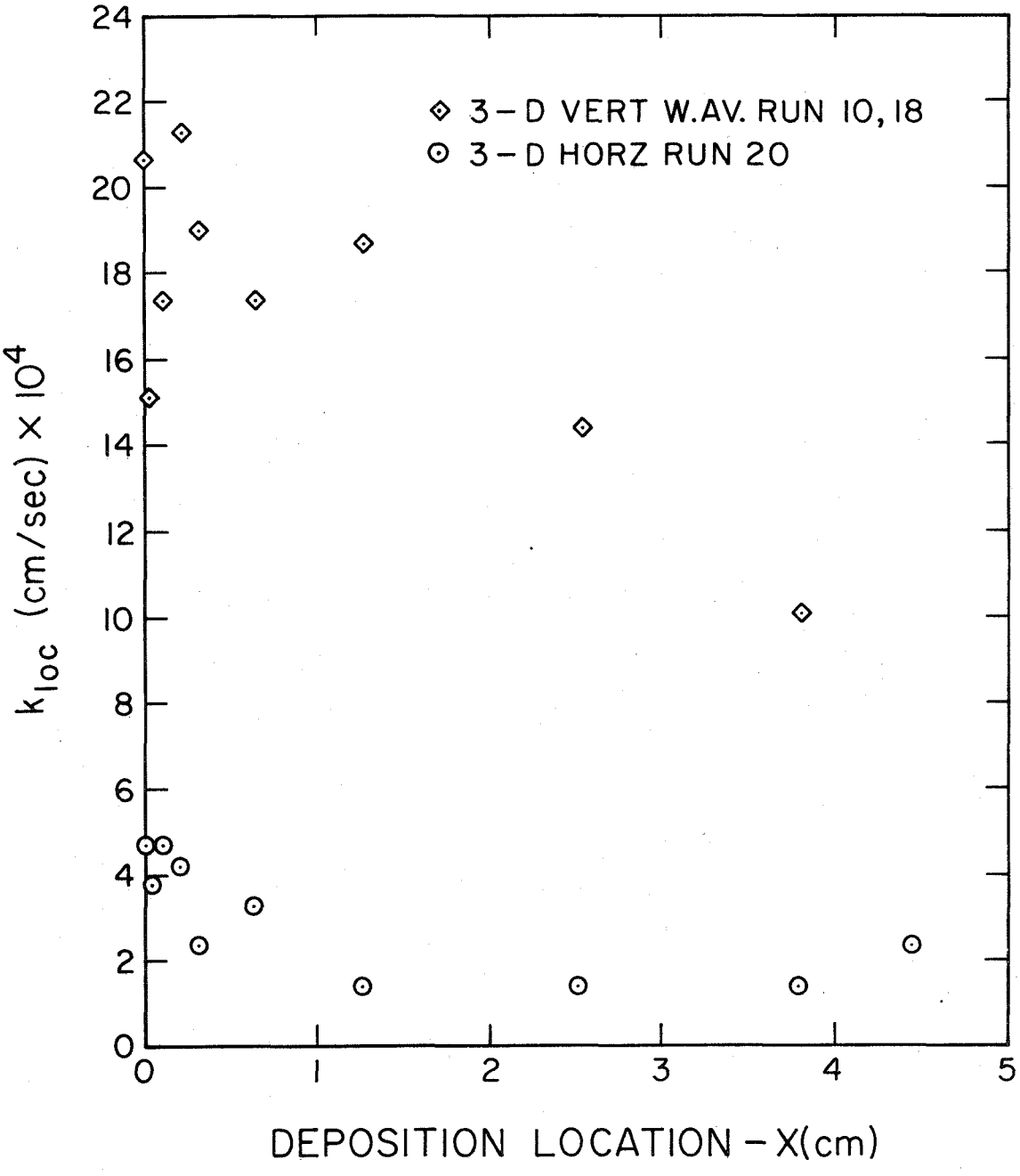

Figure D.1 Comparison of Data Along the Y=0 Strip for 1.1 μm Runs with the 3-D Model in a Horizontal and Vertical Orientation. ($\bar{U}$ = 100 cm/sec).

toward the outside wall and returns to the inside wall along Y = 0 near the end of the branch.

The helical flows rapidly replace the clean air initially present along the walls beyond the Y = ± 2 strips. The clean air would be removed much more slowly if secondary motions were not present. Consequently particles in the diffusion and transition subrange, which are readily entrained by the helical flows, are carried rapidly into these regions. While the helical flows replace the clean air, they also cause higher local shear rates or thinner boundary layers in these diagonal regions. The boundary layer along the diagonal path increases in thickness toward the outside wall, but it remains relatively thinner than the surrounding X locations on the same Y strip.

Theories in Sections 3.3 and 3.4 help to explain the enhanced deposition of each particle size caused by secondary flows. The theory also correctly predicts a greater enhancement for $\overline{U} = 200$ cm./sec. compared to $\overline{U} = 100$ cm./sec.

The 0.088μm and 0.365μm particles deposit very effectively by convective diffusion in regions of the thinnest boundary layer caused by the helical flows. The 0.088μm particles diffuse more effectively to the walls and into the clean air regions than the 0.365μm particles; hence, a greater local enhancement occurs over a larger area.

The 0.79μm and 1.1μm particles, having small settling velocities, are partially entrained by the helical flows. In the diagonal regions along

the inside wall, where the boundary layer is thin and centrifugal forces are strong, their deposition is enhanced by impaction and interception. Along the outside wall, they deposit most effectively in the diagonal regions by either impaction with interception or convective diffusion with interception. Since the most rapid replacement of the clean air occurs along the diagonal regions, these areas also have the greatest exposure time to the particles. The enhancement of deposition is relatively less for the 1.1 and 0.79μm particles than for the 0.365 and 0.088μm particles because impaction, interception and convective diffusion are weak mechanisms for the 1.1 and 0.79μm particles compared to convective diffusion for the 0.088 and 0.365μm particles.

The effects of secondary flows on 2.02 and 5.7μm particles are weak and only occur along the inside wall. The large settling velocities of these particles cause them to fall away from the outside wall before they can deposit by interception, if carried there by the secondary motions. The high local shear rates associated with the helical flows along the inside wall allows enhanced deposition by impaction with interception.

Secondary flows at $\overline{U} = 200$ cm./sec. are more intense than at $\overline{U} = 100$ cm./sec., and they complete approximately twice as many helical revolutions in the same distance. Consequently, at $\overline{U} = 200$ cm./sec. they cause more rapid replacement of the clean air and mixing of the particles with the clean air along the outside wall. Doubling of the number of helical revolutions per distance shifted the position of the

diagonal ridge of deposition from X = 2.1 cm. to X = 1.2 cm. in Maps 9, 10, 11, and 12 along the Y = ± 9 strip.

From the principle of continuity of flow, the helical flows are expected throughout the branch (Figure D.2). Enhancement of deposition by the secondary motions, however, is apparent only in the diagonal ridge starting at X = 0.1 - 0.8 cm. within Y = ± 2 on the maps of the unsteady runs for the following reasons: First, local shear rates are lower or boundary layers are thicker at any X location downstream from the diagonal ridge along any Y strip. Since the helical flows occur outside of the boundary layers (Pedley et al., 1971), thicker, local boundary layers more effectively inhibit the deposition of particles transferred into them from the helical flows. Secondary motions are also less intense at the downstream location on account of energy dissipation. Because of the clean air initially in the model and the associated clean boundary layers, the exposure times of the downstream locations to particles transferred from the helical flows are less than locations nearer the carina. Finally, the air carried by the helical flows which pass near the wall between Y = ± 2 from X = 1.5 to X = 4.0 cm. originated from relatively particle-free air along the outside wall between X = 0 and X = 1.0 cm. (Figure D.2).

D.2 Steady Flow

The explanations of the effects of secondary motions on deposition

during unsteady flow apply to steady flow, except for the following differences:

1. The thickness of the steady momentum boundary layer at any location is greater than the corresponding time-averaged, local thickness in the unsteady runs. Therefore, 1.1 μm particles which are transferred into the boundary layer by the secondary flows have a smaller chance of depositing by impaction and interception than in the unsteady runs. This is part of the explanation for the lack of peaks on Map 13 from X = 0.2 to X = 0.8 cm. within Y = ± 2 which were observed on Map 5.

2. The clean air, which is initially present in the model during the unsteady runs, is absent during the steady flow runs. Consequently, regions having secondary flows of high intensity in the steady flow runs cause less enhancement of local deposition than occurs in the unsteady flow runs.

3. Since particles in the transition range are easily entrained by the steady helical flows, they follow helical trajectories along the daughter branch. Some of the helical paths are expected to be relatively particle-free and some to be particle-laden, depending on the exact position from which they originated at the entrance to the daughter branch. Naturally, the relatively particle-free paths can cause less enhancement of deposition than the particle-laden paths.

Experimental observations in Section 4.3 found that the helical flows complete one revolution in approximately three diameters down-

stream when U = 100 cm./sec. Figure D.2 sketches the helical paths in the region of one of the two symmetrical vortices in the daughter branch when U = 100 cm./sec. Particles on Path #1 follow the stagnation streamline in the axial center of the trachea and deposit near X = 0 simultaneously by inertial impaction, sedimentation and interception.

Particles on Path #2 originate in the region of high velocity within the particle-laden core of the parent branch. They are carried near the inside wall within Y = 0 to Y = +2 and X = 0 to X = 0.8 cm., where the helical flow originates. 1.1 μm particles can deposit in this region if they are projected by the helical flow with a sufficient velocity to penetrate the boundary layer. The helical path carries the particles along the outside wall to Y = +9 between X = 1.8 and X = 2.6 cm. While traveling along the wall from Y = 0 to Y = 4.5 deposition occurs mainly by sedimentation from the helical flow through the boundary layer. Between Y = 4.5 and Y = 9, deposition occurs by convective diffusion with interception. The helical path then returns to the inside wall at Y = 0 between X = 3.2 and X = 4.76 cm. after crossing the center of the branch. Here the helical flow makes a sharp bend to start its return to the outside wall. Because of the high axial velocity next to the wall along Y = 0, a more intense helical motion and a thinner boundary layer is found than along the other positions where Path #2 passed near the wall. Centrifugal forces imposed on the particles by the secondary motions may be sufficient to cause the enhancement of deposition observed in this region

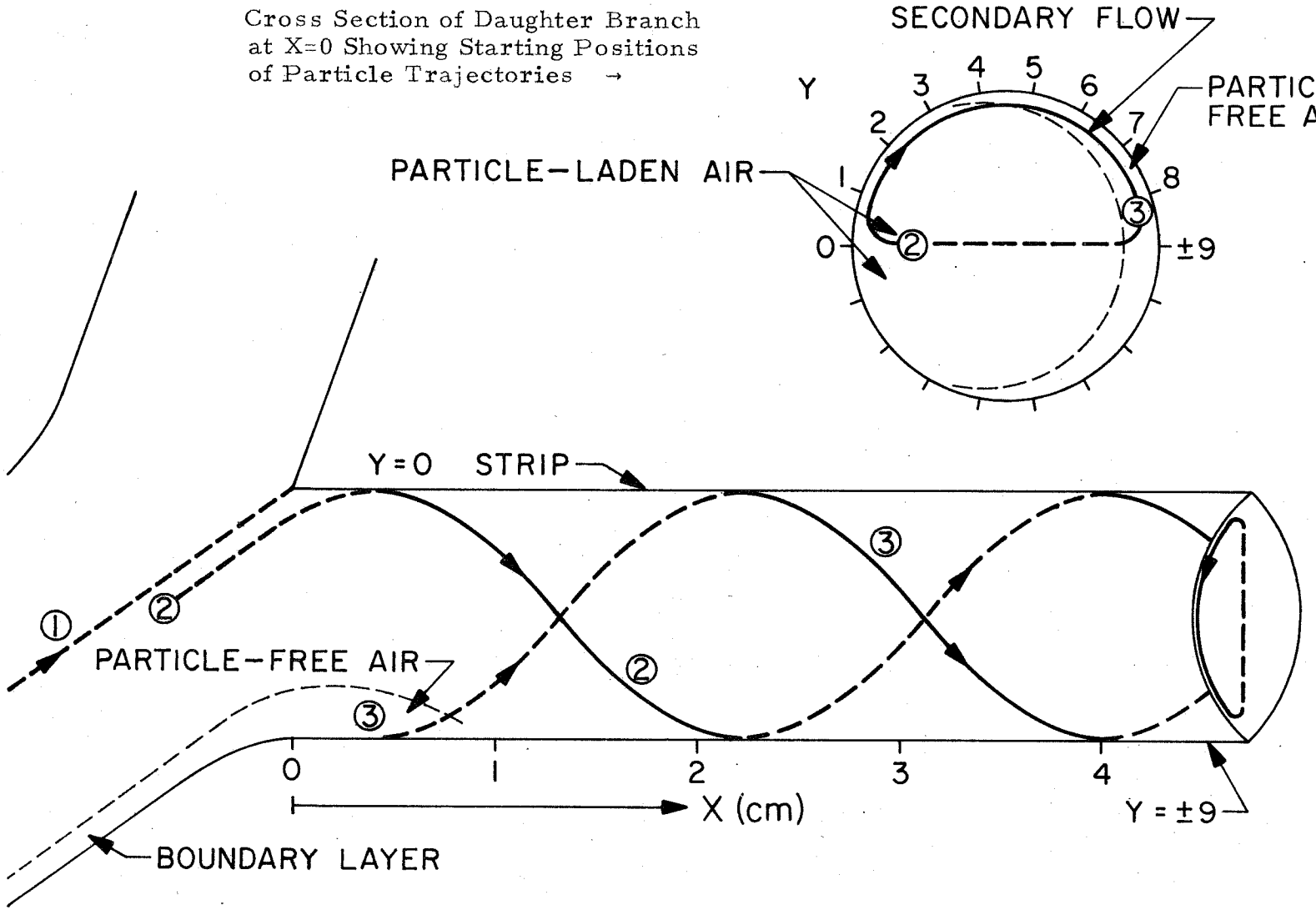

Figure D.2 Trajectories of Particles Carried by the Steady Helical Flow in the Daughter Branch when U = 100 cm/sec

on Map 13 and in the "quasi-steady data" in Figure 6.8.

Particles on Path #3 in Figure D.2 originate near X = 0 at any Y position along the outside wall. Here the air is relatively clean on account of losses from the boundary layer in the parent branch. The relatively particle-free air is carried in a helical path from the outside wall across the center of the branch to the inside wall at Y = 0 between X = 1.0 and X = 3.0 cm. The path then returns to the outside wall. In regions where the relatively clean air passes near the wall, secondary motions enhance the deposition negligibly in comparison to regions touched by the paths carrying particles. This explains the relatively low deposition on Map 13 between X = 3.6 and X = 4.76 cm. along the outside wall. It also explains the points with low deposition in the "quasi-steady data" in Figure 6.8.

This scheme of clean and particle-laden helical paths may also explain the enhancement of the last data point in Figure D.1, Plot 6, and Plot 8.

Appendix E

COMPUTER PROGRAM LISTINGS

```
E.1  PROGRAM TO CALCULATE THE LOCAL TRANSFER COEFFICIENTS FOR AEROSOL
     DEPOSITION ALONG THE WEDGE OF A VERTICAL 2-D BIFURCATION LUNG
     MODEL BY INERTIAL IMPACTION, SEDIMENTATION, AND INTERCEPTION
     SIMULTANEOUSLY:  STEADY POTENTIAL FLOW

C DEFINITION OF VARIABLES
C
C      XO,YO= PARTICLE COORDINATES AT STARTING POSITION
C      X1,Y1,X2,Y2= PARTICLE COORDINATES AT BEGINNING AND END OF EACH
C      TRAJECTORY SEGMENT
C      UX,UY= PARTICLE AND STREAM VELOCITY COMPONENTS AT STARTING POSITION
C      UX1,UY1= STREAM VELOCITY COMPONENT AT BEGINNING OF EACH SEGMENT
C      VX1,VY1,VX2,VY2= PARTICLE VELOCITY COMPONENT AT BEGINNING AND END
C      OF EACH SEGMENT
C      LIM= MAXIMUM NUMBER OF STARTING POSITIONS
C      DELZ= VERTICAL DISTANCE BETWEEN STARTING POSITIONS
C      TAU= PARTICLE RELAXATION TIME
C      R= PARTICLE RADIUS
C      C=MAXIMUM DISTANCE OF TRAVEL ALLOWABLE ALONG WEDGE
C      DT= TIME INTERVAL FOR EACH SEGMENT
C      U= STREAM VELOCITY AT INFINITY
C      U1= STREAM VELOCITY AT ONE CENTIMETER BEFORE THE WEDGE ON THE
C      STAGNATION STREAMLINE
C      XL= PARTICLE DEPOSITION LOCATION ALONG WEDGE FOR ONE RUN
C      ZL= AVERAGE DEPOSITION LOCATION FOR TWO XL LOCATIONS
C      FSC= DEPOSITION FLUX/PARTICLE CONCENTRATION IN STREAM
C      VS= PARTICLE SETTLING VELOCITY
C      ZG= ZG*DELZ=YO LOCATION FOR FIRST TRAJECTORY CALCULATION
C      H= HALF WIDTH OF PARENT BRANCH, CM
C      H2=WIDTH OF DAUGHTER BRANCH IN MODEL, CM
C      2-D MODEL       H= 0.95          H2= 1.3
C      3-D MODEL       H= 0.873         H2= 1.23
C
C MAIN PROGRAM TO DETERMINE PARTICLE TRAJECTORIES
C
```

```
      COMMON UX(40),UY(40),XL(40),DELZ,N
     0DOUBLE PRECISION DELZ,X0,Y0,THETA,DIST6,DIST,ZANGLE,VX1,VY1,X1,Y1,
     1UX1,UY1,RELX,T,X2,Y2,VX2,VY2,Z,XL,UX,UY,SLOEP,U1,PI,ALPHA,ALPHAM,V
     2S,TALPHA,CALPHA
      DIST6(A,B,C)=U1*(A*A+B*B)**(C/2)
    5 READ(5,10) LIM,DELZ,X0,TAU,R,C,DT,ANGLE,H,H2
   10 FORMAT(I10,2D10.5,4E10.5,F10.2/2F10.3)
      IF(LIM .LT. 1) STOP
      READ(5,11) IVS,U,ZG
   11 FORMAT(I10,2E10.5)
      IF(IVS .LT. 1) GO TO 101
      G=981.
      VS=TAU*G
      GO TO 13
  101 VS=0.0
   13 WRITE(6,12) LIM,DELZ,X0,TAU,R,C,DT,U,VS,ANGLE
  120FORMAT(6H1LIM =,I5,5X,6HDELZ =,D10.3,10X,4HXC =,D10.3,10X,5HTAU =,
     1E10.4,10X,3HR =,E10.3//4H C =,E10.3,10X,4HDT =,E10.3,10X,3HU =,E10
     2.4,10X,4HVS =,D10.4,3X,7HANGLE =,F10.2/////)
      DT2=DT
      PI=3.14159265358979 32
      ALPHA=ANGLE*PI/360.
      ALPHAM=ALPHA/(PI-ALPHA)
      TALPHA=DTAN(ALPHA)
      CALPHA=DCOS(ALPHA)



      A1=((H/(PI-ALPHA))*((H2/H)**(PI/ALPHA)+1.))**ALPHAM
      U1=U/A1
C
C     START OF MAIN DO LOOP FOR EACH NEW STARTING POSITION
C
      DO 69 I=1,LIM
      T=(-DT2)/TAU
```

```
      RELX=1.0-DEXP(T)
      RUN=FLOAT(I)
      XRUN=FLOAT(I)+ZG
C
C     CALC OF INITIAL PARTICLE VELOCITIES
C
      YO=DELZ*(XRUN-1.0)+.CCCCCCCCCCCCCC01
      THETA=DATAN2(YO,XO)
      ZANGLE=ALPHAM*(PI-THETA)
      DIST=DIST6(XO,YO,ALPHAM)
      UX(I)=DIST*DCOS(ZANGLE)
      UY(I)=DIST*DSIN(ZANGLE)
      WRITE(6,15)I,XO,YO,UX(I),UY(I)
   15OFORMAT(12HORUN NUMBER=,I4,3X,3HXO=,D13.5,4X,3HYO=,D13.5,5X,7HUX(I)
     1 =,D13.5,5X,7HUY(I) =,D13.5//)
      VX1=UX(I)
      VY1=UY(I)
      X1=XO
      Y1=YO
      J=1
C
C     PARTICLE VELOCITIES AND POSITIONS CALC IN POTENTIAL FLOW REGIME
C
   20 THETA=DATAN2(Y1,X1)
      ZANGLE=ALPHAM*(PI-THETA)
      DIST=DIST6(X1,Y1,ALPHAM)
      UX1=DIST*DCOS(ZANGLE)
      UY1=DIST*DSIN(ZANGLE)
      VX2=VX1+((UX1+VS)-VX1)*RELX
      VY2=VY1+(UY1-VY1)*RELX
      X2=X1+(UX1+VS)*DT+TAU*(VX1-(UX1+VS))*RELX
      Y2=Y1+UY1*DT+TAU*(VY1-UY1)*RELX
      Z=DSQRT(X2*X2+Y2*Y2)
```

```
C
C     CHECK IF PARTICLES HAVE IMPACTED ON THE WEDGE WALL
C
      IF(X2 .LT. -.01) GO TO 23
      IF(Z .LE. R) GO TO 30
      IF(X2 .GE. 0.0 .AND. Y2 .LE. R) GO TO 30
      IF(Y2 .LE. (X2*TALPHA+R/CALPHA)) GO TO 40
      IF(X2 .GE. 0.0 .AND. Z .GT. C) GO TO 50
   23 X1=X2
      Y1=Y2
      VX1=VX2
      VY1=VY2
      GO TO 20
C
C     CALCULATION OF EXACT DEPOSITION LOCATIONS
C
   30 XL(I)=0.0
      GO TO 69
   40 SLOEP=(Y2-Y1)/(X2-X1)
      XL(I)=((R/CALPHA)-Y1+X1*SLOEP)/((CALPHA)*(SLOEP-TALPHA))*R*TALPHA
      IF(XL(I) .LT. 0.0) XL(I)=0.0
   69 CONTINUE



      N=IFIX(RUN-.9)
      M=N
      GO TO 54
   50 N=IFIX(RUN-1.9)
      M=N+1
   54 WRITE(6,51)
   51 FORMAT(1H1,15X,2HUX,18X,2HUY,18X,2HXL//)
      WRITE(6,52) (UX(I),UY(I),XL(I), I=1,M)
   52 FORMAT(1HO,3D20.8)
      WRITE(6,53)
```

```
   53 FORMAT(1H1)
      CALL DEPOST
      GO TO 5
      END
C SUBROUTINE TO CALCULATE THE DEPOSITION RATES AND LOCATIONS
      SUBROUTINE DEPOST
      COMMON UX(40),UY(40),XL(40),DELZ,N
      DOUBLE PRECISION AVUX,AVUY,AVEL,ANGL,ZL,FSC,DELZ,UX,UY,XL,ZLL,FLSC
      WRITE(6,5)
    5 FORMAT(1HO,20X,17HAVER DEP LOCATION,26X,13HDEP FLUX/CONC//)
      DO 15 K=1,N
      AVUX=(UX(K)+UX(K+1))/2.0
      AVUY=(UY(K)+UY(K+1))/2.0
      AVEL=DSQRT(AVUX*AVUX+AVUY*AVUY)
      ANGL=DATAN2(AVUY,AVUX)
      ZL=(XL(K)+XL(K+1))/2.0
      IF(ZL .LE. 0.0) GO TO 7
      FSC=AVEL*DELZ*DCOS(ANGL)/(XL(K+1)-XL(K))
      FLSC=DLOG10(FSC)
      ZLL=DLOG10(ZL)
      GO TO 9
    7 FSC=AVEL*DELZ*DCOS(ANGL)/(.0001)
      FLSC=DLOG10(FSC)
      ZLL=0.0
    9 WRITE(6,25) ZL,ZLL,FSC,FLSC
   25 FORMAT(1HO,D20.8,10X,F10.5,20X,D20.8,10X,F10.5)
   15 CONTINUE
      RETURN
      END
```

E.2 PROGRAM TO ANALYTICALLY CALCULATE LOCAL TRANSFER COEFFICIENTS ON A 90 DEGREE WEDGE IN A 2-D BIFURCATION MODEL: STEADY POTENTIAL FLOW

```
C DEFINITION OF VARIABLES
C
C      PHI= STREAM FUNCTION IN EQ. 2.6
C      U1= AU IN EQ. 2.6
C      R,THETA= POLAR COORDINATES OF PARTICLES ALONG A STREAMLINE
C      DELR= SMALL R INCREMENT
C      RP= PARTICLE RADIUS
C      XO= X DISTANCE FROM WEDGE= -1.0 CM.
C      UX,UY= POTENTIAL VELOCITY COMPONENTS IN EQS. 2.7 AND 2.8
C      XL= DEPOSITION LOCATION ALONG WEDGE
C      DELX= DISTANCE BETWEEN DEPOSITION LOCATIONS
C      FSC= DEPOSITION FLUX/PARTICLE CONCENTRATION IN STREAM
C
      ODOUBLE PRECISION DELX,DELR,RP,XO,XMIN,U,THETA,CC,CC,PI,PHI,C,THETA
     11,XARG,X,XL,R,S,Y,UX,UY,ARG,FI
      COMMON UX(50),UY(50),XL(50),Y(50),PHI(50),DELX,N
    5 READ(5,10) LIM,DELX,DELR,RP,XO,XMIN,U
   10 FORMAT(I10,6D10.5)
      IF(LIM .LT. 1) STOP
      WRITE(6,60) LIM,DELX,DELR,RP,XO,XMIN,U
   60 FORMAT(5H1DATA,3X,4HLIM=,I3,5X,5HDELX=,E10.4,5X,5HDELR=,E10.4,5X,3
     1HRP=,E10.4,5X,3HXO=,E10.4,5X,5HXMIN=,E10.4,5X,2HU=,E10.4////)
      U1=U/1.22
      PI=3.1415926535897932
      CC=4./3.
      DO 50 I=1,LIM
      FI=DFLOAT(I-1)
```

```
      XL(I)=DELX*FI
      R=DSQRT(XL(I)*XL(I)+RP*RP)
      THETA=PI+DATAN2(RP,XL(I))
      CD=PI/3.-CC*THETA
      PHI(I)=.75*U1*R**CC*DSIN(CD)
      IF(I .LE. 1) GO TO 7
      IF((PHI(I)-PHI(I-1)) .LE. 0.0) GO TO 51
    7 Q=DELR
      R=1.01
   29 ARG=(CC*PHI(I)/U1*R**CC)
   30 THETA1=PI/4.+.75*(PI-DARSIN(ARG))
      X=R*DCOS(THETA1)
      IF(DABS(X-X0) .LE. XMIN) GO TO 25
      IF(DABS(X-X0) .GT. Q) GO TO 9
      GO TO 11
    9 R=R-Q
      GO TO 29
   11 S=.5*Q
      IF((X-X0) .GT. 0.0) GO TO 12
      R=R+S
      Q=.5*Q
      GO TO 30
   12 R=R-S
      Q=.5*Q
      GO TO 30
   25 Y(I)=R*DSIN(THETA1)
      XARG=(PI-THETA1)/3.
      UX(I)=U1*R**(1./3.)*DCOS(XARG)
      UY(I)=U1*R**(1./3.)*DSIN(XARG)
      N=I
```

```
   50 CONTINUE
      WRITE(6,39)
   39 FORMAT(1H0,15X,2HXL,15X,2HUX,18X,2HUY,18X,1HY//)
      WRITE(6,40) (XL(I),UX(I),UY(I),Y(I),I=1,N)
   40 FORMAT(1H0,4D20.8)
   51 CALL FLUX
      GO TO 5
      END
C     SUBROUTINE TO CALCULATE THE DEPOSITION FLUXES
      SUBROUTINE FLUX
      DOUBLE PRECISION AVUX,AVUY,AVEL,ANGL,ZL,DELY,UX,UY,XL,ZLL,FLSC,FSC
     1,Y,DELX,PHI
      COMMON UX(50),UY(50),XL(50),Y(50),PHI(50),DELX,N
      WRITE(6,4)
    4 FORMAT(1H1,5X,15HSTREAM FUNCTION,9X,17HAVER DEP LOCATION,29X,13HDE
     1P FLUX/CONC//)
      M=N-1
      DO 15 K=1,M
      AVUX=(UX(K)+UX(K+1))/2.0
      AVUY=(UY(K)+UY(K+1))/2.0
      AVEL=DSQRT(AVUX*AVUX+AVUY*AVUY)
      ANGL=DATAN2(AVUY,AVUX)
      ZL=(XL(K)+XL(K+1))/2.0
      DELY=Y(K+1)-Y(K)
      FSC=AVEL*DELY*DCOS(ANGL)/DELX
      ZLL=DLOG10(ZL)
      FLSC=DLOG10(FSC)
      WRITE(6,25) PHI(K),ZL,ZLL,FSC,FLSC
   25 FORMAT(1H0,D12.5,3X,D20.8,10X,F10.5,10X,D20.8,10X,F10.5)
   15 CONTINUE
      RETURN
      END
```

NOMENCLATURE

Arabic Notation

A = potential flow constant, $cm.^{-m}$ -- see Equation 2.5

A_1 = dimensionless form of A or A_3

A_3 = constant defined by Equation 3.1

C = slip flow correction factor - see Equation 2.14

D = particle diffusion coefficient, $cm.^2/sec.$

F_o = particle flux in the main stream before the wedge in the direction parallel to the stagnation streamline, $particles/cm^2$ sec.

F_s = particle deposition flux on the wedge, $particles/cm^2$ sec.

G = average speed of two particles at their starting positions cm./sec.

I = Interception number = r_p/R_2

L = length of the daughter branches in the models, cm.

Fr = Froude number = U^2/gR_2

$Freq$ = frequency parameter = $R(\omega/\nu)^{\frac{1}{2}}$

$Freq'$ = modified frequency parameter = $\delta(\omega/\nu)^{\frac{1}{2}}$

Pe = Peclét number = $2R_2U_2/D$

R = radius of lung branch, cm.

R_1 = radius of the parent branch in the "3-D" model, cm.

R_2 = radius or half width of the daughter branches in the models

R_p = particle radius, cm.

Re = Reynolds number for fluid flow in branch = $2hU/\nu$ or $2R_2U_2/\nu$

Re_{crit} = Reynolds number at which turbulence initiates

Re_p = particle Reynolds number = $2r_p|\vec{u} - \vec{u}_f|/\nu$

Re_x = Reynolds number based on distance along wedge = Ux_1/ν

Re_{xcrit} = Re_x for which turbulence initiates at x_1

S_1 = cross-sectional area of parent branch in "3-D" model, cm^2.

S_2 = cross-sectional area of daughter branch in "3-D" model, cm^2.

S_3 = cross-sectional area at narrowest region in junction before the carina, in "3-D" model, cm^2.

Sc = Schmidt number = ν/D

Stk = Stokes number = $U\tau/R_2$

Stk_{cr} = critical Stokes number -- see Equation 2.25

U = free stream velocity in the parent branch, cm./sec.

$\overline{U}$ = time-average free stream velocity in parent branch

U_2 = free stream velocity in daughter branch

$\overline{U}_2$ = time-average free stream velocity in daughter branch

V_s = terminal settling velocity, cm./sec.

V_s' = Stk/Fr = dimensionless terminal settling velocity

W = complex potential

d_p, D_p = particle diameter, cm.

g = gravitational acceleration constant, cm^2./sec.

h = half width of the main channel in "2-D" model, cm.

h_2 = width of the daughter branches in the "2-D" model, cm.

h_3 = half width of the narrowest region of the main channel in the models, cm.

h_s = stopping distance, cm.

k_{av} = integrated average transfer coefficient, cm./sec.

k_{loc} = local transfer coefficient, cm./sec.

k_c = average transfer coefficient within area in which deposition occurs in the "3-D" model, cm./sec.

m = constant, dependent on the wedge angle = $\alpha/(\pi - \alpha)$

n = local particle concentration, particles/cc

n_∞ = particle concentration in the free stream, particles/cc

q = stream speed, cm/sec.

r = polar coordinate, cm.

r_p = particle radius, cm.

t = time, sec.

u = particle velocity component in x direction, cm./sec.

v = particle velocity component in y direction, cm./sec.

u_1 = particle velocity component parallel to the wedge, cm./sec.

v_1 = particle velocity component perpendicular to the wedge, cm./sec.

u_f, v_f = x, y components of the stream velocity, cm./sec.

u_{f1}, v_{f1} = x_1, y_1 components of the stream velocity, cm./sec.

x, y = Cartesian coordinates in z-plane of model, cm.

x_1 = Cartesian coordinate parallel to the wedge, cm.

y_1 = Cartesian coordinate perpendicular to the wedge, cm.

z = complex coordinate = $x + iy$

Greek Notation

ϕ	=	potential function
ψ	=	stream function
α	=	bisected wedge angle, radians
β	=	constant from laminar boundary layer solution for each wedge angle
$\delta, \delta(x_1)$	=	momentum boundary layer thickness, cm.
$\delta_1(x_1)$	=	displacement thickness, cm.
$\delta_c, \delta_c(x_1)$	=	concentration boundary layer thickness, cm.
ϵ	=	overall deposition or collection efficiency of model
ϵ_{loc}	=	local deposition or collection efficiency in model
ζ	=	transformation variable -- see equation (A.1)
η	=	dimensionless similarity variable used in boundary layer solutions
θ	=	polar coordinate
μ	=	absolute viscosity of air, gm/(cm. sec.)
ν, ν	=	kinematic viscosity of air, $cm.^2/sec.$
ν^*	=	complex velocity
ρ, ρ_g	=	density of air, g/cc
ρ_p	=	density of the particle, g/cc
σ	=	angle between a normal to the wall of the daughter branch and the diameter of the branch in the plane of the bifurcation, radians
τ	=	relaxation time of the particle, sec.
Φ	=	angle between the average velocity vector and the stagnation streamline
ω	=	angular frequency of breathing, sec^{-1}.

REFERENCES CITED

1. Alarie, Y. (1973). "Sensory Irritation by Airborne Chemicals," CRC Critical Reviews in Toxicology, 2:299-363.

2. Alavi, S. M., T. E. Keats, and W. M. O'Brien (1970). "The Angle of Tracheal Bifurcation: Its Normal Measuration," Amer. J. Roentgenol., 108:546-549.

3. Altshuler, B. (1959). "Calculation of Regional Deposition of Aerosol in the Respiratory Tract," Bull. Math Biophys., 21:257-270.

4. Altshuler, B., N. Nelson and M. Kuschner (1964). "Estimation of Lung Tissue Dose from the Inhalation of Radon and Daughters," Health Phys., 10:1137-1161.

5. Amdur, M. C. and M. Corn (1963). "The Irritant Potency of Zinc Ammonium Sulfate of Different Particle Sizes," Am. Ind. Hyg. Assoc. J., 24:326-333.

6. Auerbach, O., A. P. Stout, E. C. Hammond and L. Garfinkel (1961). "Changes in Bronchial Epithelium in Relation to Cigarette Smoking and in Relation to Lung Cancer," New. Eng. J. Med., 265:253-267.

7. Basset, A. B. (1888). A Treatise on Hydrodynamics, 1st Edition, Cambridge, England:Deighton, Bell and Co., Chapter XXII. Cited by Basset, A. B. (1961). A Treatise on Hydrodynamics, Vol. II, New York:Dover, Chapter XXII.

8. Batchelor, G. K. (1953). The Theory of Homogeneous Turbulence, London:Cambridge University, 74.

9. Beeckmans, J. M. (1965). "The Deposition of Aerosols in the Respiratory Tract: I. Mathematical Analysis and Comparison with Experimental Data," Canadian J. Physiol. Phar. 43:157-172.

10. Bell, K. A. and S. K. Friedlander (1973). "Aerosol Deposition in Models of a Human Lung Bifurcation," Staub-Reinhalt. Luft, 33:178-182.

11. Bevington, P. R. (1969). Data Reduction and Error Analysis for the Physical Sciences, New York:McGraw-Hill, Chapter 5.

12. Bryson, C. C. and H. Spencer (1951). "Carcinoma of the Bronchus," Quarterly Journal of Medicine, New Series XX, No. 78:173-187.

13. Chandrasekhar, S. (1943). "Stochastic Problems in Physics and Astronomy," Review of Modern Physics, 15:16-20.

14. Chua, J. H. and C. Wang (1972). "Particle Deposition in a Y-Shaped Branching Tube," J. Res. Assoc. Powder Tech. (Japan), 9:37-45.

15. Dahneke, B. (1973). Information presented at informal research seminar at California Institute of Technology, May, 1973.

16. Davies, C. N. (1945). "Definitive Equations for the Fluid Resistance of Spheres, " Proc. Phys. Soc., 57:259-270.

17. Davies, C. N. (1961). "A Formalized Anatomy of the Human Respiratory Tract," Inhaled Particles and Vapours, Ed. by C. N. Davies, London: Pergamon, 82-87.

18. Dekker, E. (1961). "Transition Between Laminar and Turbulent Flow in Human Trachea, " J. Appl. Physiol., 16:1060-1064.

19. Dwight, H. B. (1951). Tables of Integrals and Other Mathematical Data, New York:Macmillan, Equation 170.2.

20. Engel, S. (1962). Lung Structure, Springfield, Illinois:Charles C. Thomas, 215-224.

21. Ermala, P. and L. R. Holsti (1955). "Distribution and Absorption of Tobacco Tar in the Organs of the Respiratory Tract," Cancer, 8:673-678.

22. Falkner, V. M. and S. W. Skan (1931). "Solutions of the Boundary-Layer Equations," Phil. Mag., Ser. 7, 12:865-873.

23. Findeisen, W. (1935). "Über das Absetzen kleiner, in der Luft suspendierter Teilchen in der menschlichen Lunge bei der Atmung," Pflüger Arch. f.d. ges. Physiol., 236:367-379.

24. Fraser, D. A. (1966). "The Deposition of Unipolar Charged Particles of the Lungs of Animals," Arch. Environ. Health, 13:152-157.

25. Friedlander, S. K. and H. F. Johnstone (1957). "Deposition of Suspended Particles from Turbulent Gas Streams," Ind. Engr. Chem., 49:1151-1156.

26. Friedlander, S. K. (1959). "Principles of Gas-Solids Separations in Dry Systems," Chemical Engineering Progress Symposium Series, Vol. 55, No. 25, 135-149.

27. Friedlander, S. K. (1964). "Particle Deposition by Diffusion in the Lower Lung: Application of Dimensional Analysis," Amer. Ind. Hyg. Assn. J., 25:37-42.

28. Friedlander, S. K. (1967). "Particle Diffusion in Low-Speed Flows," J. Colloid Interface Sci., 23:157-164.

29. Fry, F. A. (1970). "Charge Distribution on Polystyrene Aerosols and Deposition in the Human Nose," Aerosol Science, 1:135-146.

30. Fuchs, N. A. (1964). Mechanics of Aerosols, New York:Pergamon, 408 pp.

31. Garland, H. L. (1961). "Bronchial Carcinoma: Lobar Distribution of Lesions in 250 Cases," Calif. Medicine, 94:7-8.

32. Garland, H. L., et al. (1962). "The Apparent Sites of Origin of Carcinomas of the Lung," Radiology, 78:1-11.

33. Gormley, P. G. and M. Kennedy (1949). "Diffusion from a Stream Flowing through a Cyclindrical Tube," Proc. Royal Irish Acad., 52A:163-169.

34. Gussman, R. A. and Beeckmans, J. M. (1971). "Theoretical Consideration for Pulmonary Deposition in High Pressure Environments: A Model," Inhaled Particles III. Vol. 1, Ed. by W. H. Walton, Surrey, England:Unwin Brothers, 33-41.

35. Hacker, P. T., R. J. Brun, and B. Boyd (1953). "Impingement of Droplets in 90° Elbows with Potential Flow," National Advisory Committee for Aeronautics, Technical Note 2999.

36. Ham, A. W. (1968). Histology, 5th Ed., Philadelphia:J. B. Lippincott Co., 746-750.

37. Harris, W. J. (1960). "Size Distribution of Tobacco Smoke Droplets by a Replica Method," Nature, 186:537-538.

38. Hayek, H. von (1960). The Human Lung (translated by V. E. Krahl), New York:Hafner, 372 pp.

39. Hilding, A. C. (1957). "Ciliary Streaming in the Bronchial Tree and the Time Element in Carcinogenesis," New. Eng. J. Med., 256:634-640.

40. Hidy, G. M. and J. R. Brock (1969). "Lung Deposition of Aerosols--A Footnote on the Role of Diffusiophoresis," Env. Sci. Tech., 3:563-567.

41. Horsfield, K. and G. Cumming (1967). "Angles of Branching and Diameters of Branches in the Human Bronchial Tree," Bull. Math. Biophys., 29:245-159.

42. Horsfield, K. and G. Cumming (1968). "Morphology of the Bronchial Tree in Man," J. Appl. Physiol., 24:273-283.

43. Jaffrin, M. Y. and T. V. Hennessey, Jr. (1972). "Pressure Distribution in a Model of the Central Airways for Sinusoidal Flow," Bull. Physio-Path. Resp., 8:375-390.

44. Jordan, H. S. (1958). "The Effect of Pulsating Stream Flow on the Efficiency of Filtration by a Fibrous Mat," M. E. Dissertation, Harvard University. Cited by Silverman, L. and C. E. Billings (1961). "Pattern of Airflow in the Respiratory Tract," Inhaled Particles and Vapours, Ed. by C. N. Davies, London:Pergamon, 42.

45. Kays, W. M. (1966). Convective Heat and Mass Transfer, New York:McGraw-Hill, 209-210.

46. Keith, C. H. and J. C. Derrick (1960). "Measurement of the Particle Size Distribution and Concentration of Cigarette Smoke by the Conifuge," J. Colloid Sci., 15:340-356.

47. Kestin, J. (1966). "The Effect of Free-Stream Turbulence on Heat Transfer Rates," Advances in Heat Transfer, Vol. 3, Ed. T. F. Irvine, Jr. and J. P. Hartnett, New York:Academic, 1-31.

48. Kliment, V., J. Libich, and V. Kaudersova (1972). "Geometry of Guinea Pig Respiratory Tract and Application of Landahl's Model of Deposition of Aerosol Particles," J. Hyg. Epidem., Microbiol. and Immun., 16:107-114.

49. Kotin, P., and H. L. Falk (1959). "The Role and Action of Environmental Agents in the Pathogenesis of Lung Cancer: I. Air Pollutants," Cancer, 12:147-163.

50. Kraemer, H. F. and H. F. Johnstone (1955). "Collection of Aerosol Particles in Presence of Electrostatic Fields," Ind. Eng. Chem., 47:2426-2434.

51. Landahl, H. D. (1950a). "On the Removal of Air-Borne Droplets by the Human Respiratory Tract: I. The Lung," Bull. Math. Biophys., 12:43-56.

52. Landahl, H. D. (1950b). "On the Removal of Air-Borne Droplets by the Human Respiratory Tract: II. The Nasal Passages," Bull. Math. Biophys., 12:161-169.

53. Landahl, H. D., T. N. Tracewell, and W. H. Lassen (1951). "On the Retention of Airborne Particulates in the Human Lung: II," A.M.A. Arch. Ind. Hyg. Occup. Med., 3:359.

54. Landahl, H. D., T. N. Tracewell, and W. H. Lassen (1952). "Retention of Airborne Particulates in the Human Lung: III," A.M.A. Arch. Ind. Hyg. Occup. Med., 6:508.

55. Landahl, H. D. (1963). "Particle Removal by the Respiratory System: Note on the Removal of Airborne Particulates by the Human Respiratory Tract with Particular Reference to the Role of Diffusion," A. M. A. Arch. Ind. Hyg. Occup. Med., 25:29-39.

56. Landau, L. D. and E. M. Lifshitz (1959). Fluid Mechanics, London:Pergamon Press, 88-97.

57. Langer, G. and A. Lieberman (1960). "Anomalous Behavior of Aerosol Produced by Atomization of Monodisperse Polystyrene Latex," J. Colloid Sci., 15:357-360.

58. Langer, G. and J. M. Pierrard (1963). "Anomalous Behavior of Aerosol Produced by Atomization of Monodisperse Polystyrene Latex," J. Colloid Sci., 18:95-97.

59. Langhaar, H. L. (1942). "Steady Flow in the Transition Length of a Straight Tube," J. Appl. Mech., 9:A55-A58.

60. Levich, V. G. (1962). Physicochemical Hydrodynamics, Englewood Cliffs, N. J.:Prentice Hall, 700 pp.

61. Lippie, L. H. (1965). Bioproducts Dept., The Dow Chemical Company, Midland, Michigan, Private Communication. Cited by Black, A. P. and M. R. Vilaret (1969). "Effect of Particle Size on Turbidity Removal," J. Am. Water., 61:209-214.

62. Lippmann, M. and R. Albert (1969). "The Effect of Particle Size in the Regional Deposition of Inhaled Aerosols in the Human Respiratory Tract," Amer. Ind. Hyg. Assn. J., 30:257-275.

63. Malmuth, N. and W. Hall (1970). Personal Communication with Author, June 1970, from North American Rockwell Science Center, Thousand Oaks, California.

64. Marshall, R. and W. S. Holden (1963). "Changes in the Calibre of the Smaller Airways in Man," Thorax, 18:54.

65. Martin, D. and W. Jacobi (1972). "Diffusion Deposition of Small-Sized Particles in the Bronchial Tree," Health Physics, 23:23-29.

66. Milne-Thomson, L. M. (1968). Theoretical Hydrodynamics, 5th ed., New York: MacMillan 743 pp.

67. Mitchell, R. I. (1971). Aerosol Retention in the Lungs as a Function of Respiration Rate and Particle Size, Ph. D. Thesis, The Ohio State University.

68. Nadel, J. A., et al. (1965). "Location and Mechanism of Airway Constriction After Inhalation of Histamine Aerosol and Inorganic Sulfate Aerosol," Inhaled Particles and Vapours: II, Ed. by C. N. Davies, London: Pergamon, 55-67.

69. Nadel, J. A., et al. (1970). "A New Contrast Medium for Roentgenographic Examination of Human Airways," New Eng. J. Med., 283: 281-286.

70. Owen, P. R. (1969). "Turbulent Flow and Particle Deposition in the Trachea," CIBA Symposium on Circulatory and Respiratory Mass Transport, New York: Pergamon, 236-254.

71. Pasceri, R. E. and S. K. Friedlander (1965). "Measurement of the Particle Size Distribution of the Atmospheric Aerosol: II. Experimental Results and Discussion," J. Atmos. Sci., 22: 577-584.

72. Pedley, T. J., R. C. Schroter, and M. F. Sudlow (1970). "The Prediction of Pressure Drop and Variation of Resistance Within the Human Bronchial Airways," Respir. Physiol., 9: 387-405.

73. Pedley, T. J., R. C. Schroter, and M. F. Sudlow (1971). "Flow and Pressure Drop in Systems of Repeatedly Branching Tubes," J. Fluid Mech., 46 (2): 365-383.

74. Porstendörfer, J. (1971). "Untersuchungen zur Frage Des Wachstuns von Inhalierten Aerosol Teilchen in Atemtrakt," Aerosol Science, 2: 73-79.

75. Scherer, P. W. (1972). "A Model for High Reynolds Number Flow in a Human Bronchial Bifurcation," J. Biomechanics, 5: 223-229.

76. Schlesinger, R. B. and M. Lippmann (1972). "Particle Deposition in Casts of the Human Tracheobronchial Tree," Amer. Ind. Hyg. Assoc. J., 33: 237-251.

77. Schlesinger, R. B.(1973). Personal Communication with Author, May 1973, fron Institute of Environmental Medicine, New York University Medical Center.

78. Schlichting, H. (1968). Boundary Layer Theory, 6th ed., New York: McGraw Hill, 747 pp.

79. Schreck, R. M. and L. F. Mockros (1970). "Fluid Dynamics in the Upper Pulmonary Airways," American Institute of Aeronautics and Astronautics, Paper No. 70-788.

80. Schroter, R. C. and M. R. Sudlow (1969). "Flow Patterns in Models of the Human Bronchial Airways," Respir. Physiol., 7: 341-355.

81. Seban, R. A. and E. F. McLaughlin (1963). "Heat Transfer in Tube Coils with Laminar and Turbulent Flow," Int. J. Heat Mass Transfer, 6: 387-395.

82. Silverman, L. and C. Billings (1961). "Pattern of Airflow in the Respiratory Tract," Inhaled Particles and Vapours, Ed. C. N. Davies, London: Pergamon, 9-45.

83. Stafford, R. G., H. J. Ettinger, and T. J. Rowland (1972). "Respirator-Cartridge Filter Efficiency Under Cyclic and Steady-Flow Conditions," Los Alamos Scientific Laboratory Report, LA-5022, November.

84. Stuart, J. T. (1963). "Unsteady Boundary Layers," Laminar Boundary Layer Theory, Ed. L. Rosenhead, London: Oxford, 361-362.

85. Task Group on Lung Dynamics (1966). "Deposition and Retention Models for Internal Dosimetry of the Human Respiratory Tract," Health Physics, 12: 173-207.

86. Thomas, J. W. and R. E. Yoder (1956). "Aerosol Size for Maximum Penetration Through Fiberglass and Sand Filters," A. M. A. Arch. Ind. Health., 13: 545-549.

87. Visser, J. (1970). "Measurement of the Force of Adhesion Between Submicron Carbon-Black Particles and a Cellulose Film in Aqueous Solution," J. Colloid Interface Sci., 34: 26-31.

88. Walton, W. H. and A. Woolcock (1960). "The Suppression of Airborne Dust by Water Spray," Aerodynamic Capture of Particles, Ed. by E. G. Richardson, New York: Pergamon, 140.

89. Wang, C. S. and S. K. Friedlander (1968). "Theory of Particle Deposition by Convective Diffusion in the Upper Respiratory Tract," Unpublished Report, California Institute of Technology, July 1968.

90. Weibel, E. R. (1963). Morphometry of the Human Lung, New York: Academic, 151 pp.

91. Weibel, E. R. and D. H. Gomez (1962). "Architecture of the Human Lung," Science, 137: 577-585.

92. West, J. B. (1961). "Observations on Gas Flow in the Human Bronchial Tree," Inhaled Particles and Vapours, Ed. C. N. Davies, New York: Pergamon, 3-7.

93. Whitby, K. T. and Y. H. Liu (1966). "The Electrical Behavior of Aerosol," Aerosol Science, Ed. C. N. Davies, New York: Academic, 59-86.

94. Whitby, K. T. and Y. H. Liu (1968). "Polystyrene Aerosols -- Electrical Charge and Residue Size Distribution," Atmos. Environ., 2: 103-116.

95. Widdicombe, J. G. (1954). "Receptors in the Trachea and Bronchi of the Cat," J. Physiol., 123: 71-104.

96. Wormersley, J. R. (1955). "Oscillatory Motion of a Viscous Liquid in a Thin Walled Elastic Tube," Phil. Mag., Ser. 7, 46: 199-221.

97. Yeh, H. C. (1972). "Use of a Heat Transfer Analogy for the Mathematical Model of Respiratory Tract Deposition," Annual Report of the Fission Product Inhalation Program, Lovelace Foundation for Medical Education and Research, Albuquerque, New Mexico, 310-314.

98. Zamel, N., et al. (1970). "Powdered Tantalum as a Medium for Human Laryngography," Radiology, 94: 547-553.

Proposition: A More Precise Method for Measuring the Degradation Rates of Benzo(a)pyrene and Other Carcinogenic Polycyclic Aromatic Hydrocarbons Exposed to Simulated Atmospheric Conditions

Abstract

Knowledge of the rate of degradation of BaP and other carcinogenic polycyclic aromatic hydrocarbons in the atmosphere is important for estimating health hazards and for developing control strategies. Since current evidence for the degradation rates are conflicting and scanty, this proposition suggests a different and more accurate method for measuring the degradation rates.

Calculations based on a spherical shell model for a particle in a stagnant gas show that the degradation of polycyclic aromatic hydrocarbons on particles in the atmosphere is controlled by the rate of chemical reaction. To accurately measure the chemical and photooxidation reaction rate constants, an experimental system is proposed which includes a rotating disk coated with a PAH and spinning in a large volume batch reactor containing smog gases and irradiated by artificial sunlight. Equations and techniques are propounded for determining the rate constants, reaction orders, and diffusion coefficients of gases in this system.

I. Introduction

In the 18th century Percivall Pott(1775) implicated chimney soot as the cause of the high incidence of cancer of the scrotum in chimney sweeps. Subsequent studies of people occupationally exposed to products from the burning, refining and distillation of fossil fuels showed a higher incidence of skin and lung cancer compared to workers not contacting these products. In 1933 benzo(a)pyrene, a polycyclic aromatic hydrocarbon(PAH), was isolated from coal tar. Experiments in which benzo(a)pyrene(BaP) and other distillates of coal tar were applied to the skins of animals showed that skin cancer could be artificially induced by certain polycyclic aromatic hydrocarbons(PAHs). Lung cancer in rats and primates could not be induced by BaP alone, but carcinomas occurred when the BaP was absorbed onto carbon particles or ferric oxide(Pylev, 1967; Crocker, 1970).

PAHs in cigarette smoke are an important factor in the dominant relation between cigarette smoking and lung cancer in man. However, after accounting for the effect of cigarette smoking, epidemiologic studies show that the incidence of lung cancer among urban dwellers is twice that of those living in rural areas; the incidence is even greater within urban areas having a high level of air pollution composed of PAHs and other fossil-fuel products from industrial sources(Committee on Biologic Effects of Atmospheric Pollutants, 1972). The Committee estimated that, based on epidemiological data, an increase of 1μg of BaP per 1000 m^3 of air could result in a

5 percent increase in the lung cancer death rate(rural concentrations are typically 0.01 to 2.0μg BaP/1000 m^3 while urban concentrations are 8 to 60 μg BaP/1000 m^3). However, for a complete evaluation of the health hazards to man of PAHs in the air, they recommended further research in many areas. One was that more information is needed on the chemical half-lives of the various PAHs in the atmosphere. This proposition suggests a method for measuring the degradation rate of PAHs exposed to simulated atmospheric conditions which is more accurate than techniques used in previous studies.

The methods and results of previous studies are described below. Falk et al.(1956) exposed pure PAHs(BaP, chrysene, coronene, benzo(ghi)perylene, fluoranthene, and pyrene) in crystalline form on filter surfaces to pure air and to synthetic smog. Filter samples of soot from auto exhaust were similarly exposed. The pure PAHs showed a wide range of stability, but BaP belonged to the group with the maximum stability. An exposure for one hour to synthetic smog($\simeq$100 hrs. of Los Angeles smog) in lighted conditions degraded the BaP on the filter by only 50 percent. Synthetic smog enhanced the rate and degree of degradation of all PAHs compared to pure air, but in pure air only BaP showed a significantly higher degradation rate in light than in dark conditions. Therefore, it is difficult to choose one PAH as an index of the stability of the others. The rate of reaction depends on the physical state of the PAH because, when similarly exposed, PAHs absorbed on soot degraded less than the unabsorbed filter

samples of pure PAH. Overall, Falk's results suggested half-lives of several days for PAHs in a clean or smoggy atmosphere.

Tebbens et al.(1966) studied the chemical modification of airborne arenes under fluorescent irradiation by passing diluted smoke through a dynamic flow chamber(22 ft. length). Samples collected before and after irradiation were analyzed for their BaP and perylene content, and also for their particle size. Irradiation alone of soot in pure air for 1 to 1½ hrs. reduced the BaP and perylene concentration in all particle size ranges by 35 to 65 percent. 50 to 80 ppm of SO_2 with irradiation also greatly decreased BaP, and BaP was fairly equally distributed on a weight percent basis throughout all particle sizes of freshly generated soot. These results agree qualitatively with Falk's, however the degradation rates are 25 to 50 times higher than Falk's reported rates(i.e., half-lives for PAHs in a clean or smoggy stmosphere are expected to be several hours instead of several days). This large variation may have been caused by differences in the intensity of irradiation because Tebbens controlled irradiation up to one-fourth of the intensity of noon sunlight, while Falk reported no data on the intensity of irradiation.

Subsequent work by Thomas et al.(1968) using the same procedure as Tebbens et al.(1966) demonstrated that ozone, oxygen, or air under light or dark conditions degrades BaP to a complex mixture of acidic compounds. Since a 40 minute exposure of soot to one-fourth the intensity of noon sunlight in air resulted in a 60 percent degradation of BaP, half-lives

on the order of 1 hour are predicted for the atmosphere during daylight.

These conflicting and scanty results clearly suggest that a more accurate, efficient, and repeatable method is needed for measuring the half-lives of PAHs exposed to simulated atmospheric conditions.

II. Possible Reactions of BaP in the Atmosphere

In the development of this proposition, BaP is chosen for analysis; however, the scheme presented below applies to any PAH.

BaP has the following structure and is known to react in solutions by addition and substitution reactions at the locations shown(Clar, 1964):

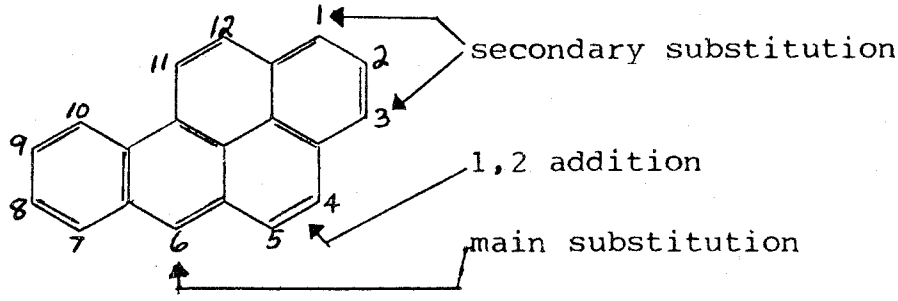

Reactions of BaP in solutions have been extensively studied, but little comparable work has been done in vapor and adsorbed phases. The few studies of the adsorbed state suggest that PAHs react readily. Reactions should be similar in all phases; however, their rates will vary greatly under different atmospheric conditions. Reactions in solution, vapor, or adsorbed phase which may occur by similar mechanisms in the adsorbed phase in the atmosphere are listed below.

Photooxidation(Masuda and Kuratsune, 1966; Inscoe, 1964):

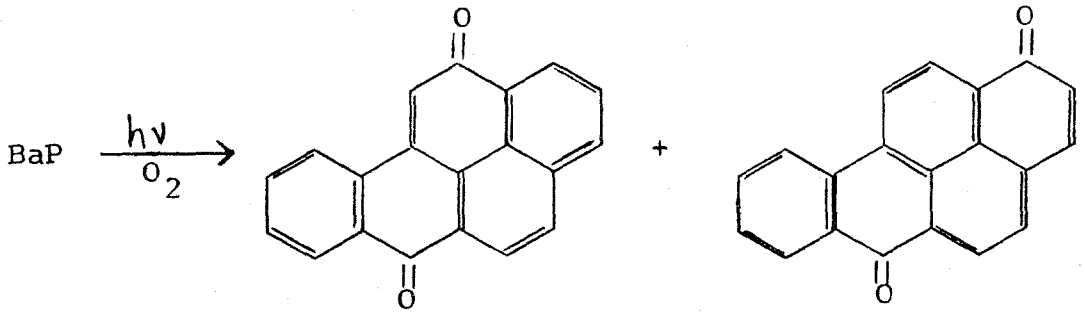

6,12 dione

1,6 dione

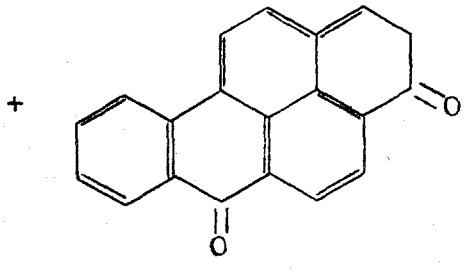

3,6 dione

The mechanism of reaction may involve energy transfer(Foote, 1968):

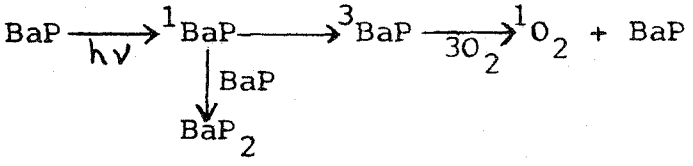

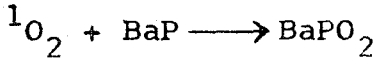

Ozonalysis(Moriconi et al., 1961):

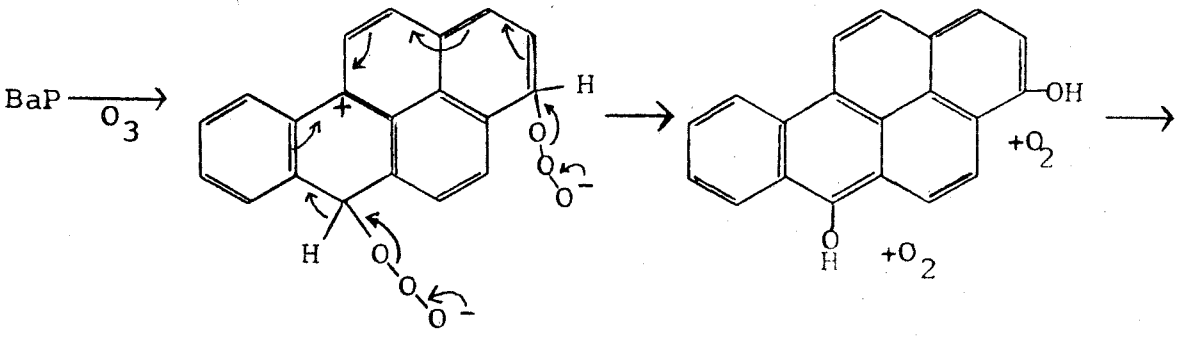

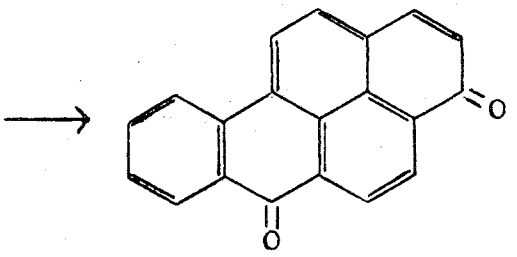

$\frac{\text{3,6 dione}}{\text{1,6 dione}} = \frac{3}{1}$ ratio

3,6 dione or 1,6 dione

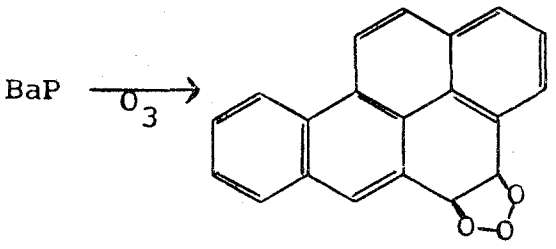

4,5 dione(trace amounts)

molozonide

One-Electron Oxidations(Adams, 1969):

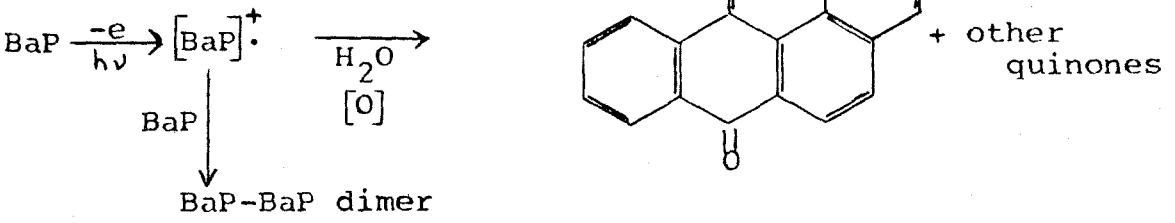

Peroxides(Roitt and Waters,1952):

$$BaP + (C_6H_5CO_2)_2 \xrightarrow[N_2]{80^{\circ}} BaP\text{-}O_2CC_6H_5 + C_6H_5COOH$$

(at the main substitution site)

NO_x(Fieser and Herschberg, 1939):

$$BaP + HNO_3 \longrightarrow BaP\text{-}NO_2 + H_2O$$ (at main substitution site)

SO_x(Vollmann et al.,1937):

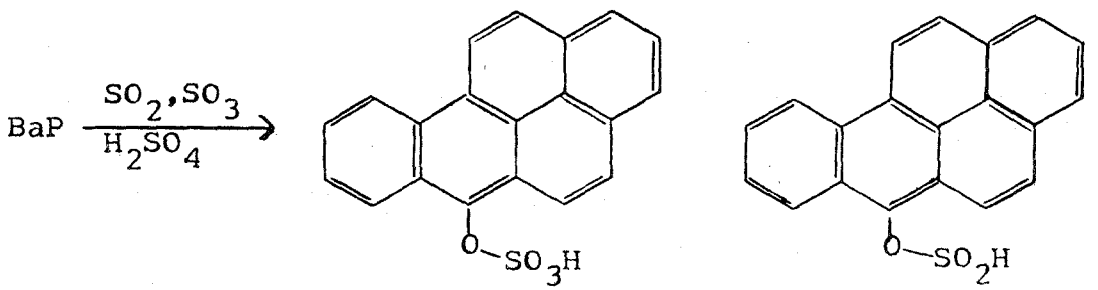

III. Spherical Shell Model

The rate of degradation of BaP on airborne soot can be analyzed most simply by a nonporous, spherical shell model, using classical techniques for noncatalytic fluid-solid reactions. A sketch of the model is as follows:

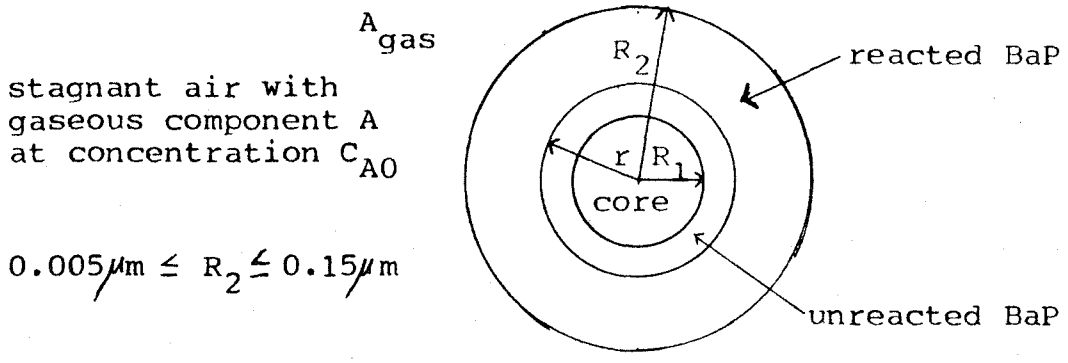

This model is justified by the following evidence. Polycyclic organic matter is mainly associated with airborne soot having a unit density, aerodynamic equivalent diameter between 0.1 and 5μm(Tebbens et al., 1966; Committee on Biologic Effects of Atmospheric Pollutants, 1972:Chapter 4). Thomas et al.(1968) reports that the soot has considerable chain structure because it is formed by agglomeration of many small spherical soot particles ranging from 0.01 to 0.3μm in diameter. Under X-ray diffraction analysis each spherical particle possesses hexagonal symmetry similar to graphite crystals and can be viewed as an agglomerate of pericondensed PAHs. The spherical particles lack open channel porosity, hydrogen covers 1 to 3 percent of the surface, and 5 to 10 percent oxygen covers 30 percent of the surface area. All the reactive PAHs like BaP are adsorbed to the surface primarily by hydrogen bonding. Chemisorption of BaP is discounted because the rapid rates of photomodification require lose bonding of BaP at exposed sites on the surface.

Depending on the type of fuel, incomplete combustion can produce soot that is 1 to 10 percent extractable by benzene.

Assuming all the extract is in the form of BaP and using X-ray diffraction data describing the dimensions of the approximately 3000 crystallites present in a 250 A. particle, calculations show that from 15 to 70 percent of the surface of a 250 A. particle will be covered with a monolayer of BaP.

In the atmosphere the agglomerate form of soot having an equivalent diameter between 0.1 and 5μm lies in the slip flow regime($\sim 0.15 \leq d_p \leq 10\mu m$; Hidy and Brock, 1970:16). Since their particle Reynolds numbers based on their terminal settling velocities in the atmosphere are $\leq 10^{-4}$, the soot particles can be assumed surrounded by a stagnant fluid when modeling gas transfer to their surfaces.

The general degradation reaction of BaP is as follows: $\alpha A_{gas} + \beta BaP_{solid} \longrightarrow$ gaseous and solid products. It applies to each chemical reaction described in Section II. Also, it applies to the photooxidation reaction because singlet oxygen must diffuse to the surface sites or nonactivated oxygen must diffuse to the surface to be activated by BaP.

The steps for gaseous reactions with BaP are the following:

1. Diffusion of gaseous reactant A through the stagnant air surrounding the particle to the surface of the solid particle.

2. Diffusion of A through a blanket of reacted BaP to the layer of unreacted BaP.

3. Chemical reaction of A with solid BaP.

4. Diffusion of gaseous products through the reacted

layer back to the surface of the solid.

5. Diffusion of gaseous products from the surface into the stagnant air.

All the reactions in Section II are irreversible because BaP is more unstable than its oxidized forms; therefore, steps 4 and 5 can be neglected. Since the first three steps occur in series, the rate of reaction will be controlled by the step having the greatest resistance--the rate controlling step.

Case (1) Control by Gas Diffusion to the Particle

Assuming a constant external surface area of reacted BaP($4\pi R_2^2$) and a decreasing thickness with time of unreacted BaP, the following equation applies:

$$\frac{-1}{4\pi R_2^2}\ \frac{dN_B}{dt} = \left(\frac{\beta}{\alpha}\right) k_g C_{AO}$$

where $N_B = \rho_B(4\pi(r^3 - R_1^3)/3)$ = moles of BaP present. ρ_B is the molar density of BaP condensed on the surface of the sphere. ρ_B = 0.00713 moles BaP/cc. for soot with a density of 1.8 g/cc.(Thomas et al., 1968). C_{AO} is the concentration of gas A in the stagnant air, and k_g is the mass transfer coefficient. Solving for the time of partial reaction,

$$t_1 = \frac{\alpha \rho_B R_2}{3 \beta k_g C_{AO}} \left[1 - \left(\frac{r}{R_2}\right)^3\right]. \qquad (1)$$

The time for complete reaction is given by

$$\tau_1 = \frac{\alpha \rho_B R_2}{3 \beta k_g C_{AO}} \left[1 - \left(\frac{R_1}{R_2}\right)^3\right]. \qquad (2)$$

Likewise, the degree of degradation of BaP is given by

$$X_B = t_1/\tau_1 \tag{3}$$

When the particle's surface is partially coated by a monolayer of BaP,

$$t_2 = \frac{\rho_{BSO} - \rho_{BS}(t)}{(\beta\alpha)\, k_g C_{AO}}, \tag{4}$$

and

$$\tau_2 = \frac{\alpha \rho_{BSO}}{\beta k_g C_{AO}} = \frac{\alpha N_{BO}}{\beta 4\pi R_2^2 k_g C_{AO}}. \tag{5}$$

ρ_{BSO}, the initial surface density of BaP, is calculated to be 4.44×10^{-10} moles/cm^2 by assuming 70 percent coverage of the surface with a monolayer($\approx$7 A^o thick).

The mass transfer coefficient for condensation on a spherical particle in the slip flow regime in stagnant air is given by(Hidy and Brock, 1970:Eqn. 6.16)

$$k_g = \frac{D_A}{R_2(1 + \epsilon \lambda_g/R_2)}. \tag{6}$$

D_A is the mutual diffusion coefficient of component A in air, λ_g is the mean free path of air, and the coefficient ϵ has an experimental value of approximately 1.2.

τ_1 and τ_2 in Equations 2 and 5 were evaluated for R_2=0.025μm and R_2=0.25μm for O_3, SO_2, and NO_2 at concentrations typically found in Los Angeles smog. For the calculations, the diffusion coefficient was assumed equal for each gas(D = 0.1 cm^2/sec), $\lambda_g = 6 \times 10^{-6}$cm, and $R_1 = 0$ for τ_1. The results are tabulated in Table 1.

Table 1

Time for Complete Degradation of BaP on Soot in the Atmosphere when Diffusion of the Pollutant Gas to the Surface is Controlling the Rate of Reaction.

R_2= 0.025μm, k_g= 1.03 x 10^4 cm/sec

gas*	τ_1(sec)	τ_2(sec)
O_3	0.262	0.0195
SO_2	0.65	0.048
NO_2	0.21	0.016

R_2= 0.25μm, k_g= 3.11 x 10^3 cm/sec

gas*	τ_1(sec)	τ_2(sec)
O_3	8.68	0.046
SO_2	21.5	0.16
NO_2	7.07	0.053

*C_{O_3}= 0.05 ppm = 2.2 x 10^{-12} moles/cc.
C_{SO_2}= 0.02 ppm = 8.9 x 10^{-13} moles/cc.
C_{NO_2}= 0.06 ppm = 2.7 x 10^{-12} moles/cc.

Case (2) Control by Gas Diffusion through the Reacted Layer

When the stagnant air is composed of inerts, I, and a reactant gas, A, and when no gaseous products are formed, gas A must diffuse through a stagnant layer of inert gas and reacted BaP to reach the unreacted layer of BaP. Quasi-steady diffusion is assumed because the rate of diffusion of gas A through the reacted layer is much greater than the rate of shrinkage of the unreacted layer.

The time for complete conversion in the atmosphere is given by

$$\tau = \frac{\alpha \rho_B R_2^2 P_I}{6 \beta P_T D_{AI} C_{AO}} \left[1 - 3\left(\frac{R_1}{R_2}\right)^2 + 2\left(\frac{R_1}{R_2}\right)^3 \right] \qquad (7)$$

D_{AI} is the mutual diffusion coefficient of component A in the inert gas within the reacted layer. P_T is the atmospheric pressure and P_I is the partial pressure of inerts. The degree of conversion of BaP is found at any time by

$$\frac{t}{\tau} = 1 + \frac{3R_2\left\{R_1^2 - \left[R_2^3(1-X_B) + R_1^3 X_B\right]^{2/3}\right\} + 2(1-X_B)(R_2^3 - R_1^3)}{R_2^3 - 3R_2R_1^2 + 2R_1^3} \qquad (8)$$

In this case $k_d = 2P_T D_{AI}/P_I R_2$ is the controlling rate constant. D_{AI} can be determined experimentally as described in Section IV or can be estimated from the Chapman-Enskog theory.

Assuming $D_{AI} = 0.1$ cm^2/sec and $R_1 = 0$, τ was calculated for the same gas concentrations as in Table 1. For $R_2 = 0.025\mu$m, $\tau = 0.034$ sec, 0.083 sec, and 0.028 sec respectively for O_3, SO_2 and NO_2. Likewise for $R_2 = 0.25\mu$m, $\tau = 3.4$, 8.3, and 2.8 sec respectively.

Comparing these results with those in Table 1, diffusion through the reacted layer is most rapid. In both cases times

for complete reaction are around 0.03 to 20 seconds. Since experimental observations of half-lives discussed in the Introduction were on the order of hours to days, the degradation of PAHs are therefore controlled by the rate of chemical reaction of the gaseous components with the adsorbed PAH.

Case (3) Control by Chemical Reaction

In this case a reaction of any order, m, is assumed, and the time for completion of the reaction is obtained from

$$\tau_1 = \frac{\alpha \rho_B (R_2 - R_1)}{\beta k_S C_{AO}^m}, \tag{9}$$

where k_s is the surface reaction rate constant with units of $(cm/sec)(cm^3/moles)^{m-1}$. The degree of conversion, X_B, at any time is given by

$$\frac{t}{\tau_1} = 1 - \frac{\left[R_2^3 (1-X_B) + R_1^3 X_B\right]^{1/3} - R_1}{R_2 - R_1}. \tag{10}$$

For the case of a monolayer of BaP covering the surface,

$$\tau_2 = \frac{\alpha N_{BO}}{\beta 4\pi R_2^2 k_S C_{AO}^m} \tag{11}$$

where N_{BO} = the initial number of moles of BaP covering the surface at R_2. The degree of conversion is then given by

$$\frac{t}{\tau_2} = \frac{N_{BO} - N_B(t)}{N_{BO}} = X_B \tag{12}$$

Case (4) Control by the Photooxidation Reaction

In this case the rate of reaction is controlled by the intensity and wavelength of the irradiation. For example, in the first reaction in Section II the intensity of irradiation in the atmosphere determines the rate of activation of BaP and subsequently the steady state concentration of singlet

oxygen which is available for reaction with BaP. The rate equals $I_a\phi$ where I_a is the intensity of the absorbed light and ϕ is the primary quantum yield of the wavelength of irradiation. The time for complete reaction is given by

$$\tau = \frac{N_{BO}}{4\pi R_2^2 I_a \phi} \tag{13}$$

because the light activates only the monolayer of BaP on the surface of the particle. When chemical reaction is controlling, when a limited concentration of reactant is available, and when the reaction rate is also enhanced by irradiation, the pre-exponential coefficient of the Arrhenius rate law includes the intensity and wavelength dependence.

IV. Experimental System for Measurement of the Chemical and Photooxidation Reaction Rate Constants

A. Apparatus

A more precise technique than used by Falk, Thomas, or Tebbens is proposed for measuring k_s and m for Cases (3) and (4). A rotating disk coated with BaP is operated in a batch reactor filled with gases of the desired type. The reactor is a large volume, transparent flask having a system for uniform irradiation at a controlled intensity such that negligible convection currents are established. The temperature and pressure in the reactor are also rigorously controlled. The volume of gas is sufficiently large such that the concentration of the reactive component far from the surface of the disk is essentially constant during the time period of a run. The rotating disk is operated with

$\omega R^2/\nu < 10^4$-10^5 to assure undisturbed laminar flow of the gas toward the rotating disk(ω = angular velocity, R = radius of the disk, and ν = kinematic viscosity of the gas), but at a high enough speed to maintain conditions where the degradation rate is controlled by the rate of chemical reaction (Levich, 1962:76).

The major advantage of the rotating disk is that its surface is uniformly accessible to the reactive gaseous component because the diffusion boundary layer has a constant thickness over almost the entire disk. The only exception is the zone at the edge of the disk having a width of the order of the thickness of the momentum boundary layer, δ_0. The effect of this zone is negligible when $R \gg \delta_0$(Levich,1962: 70). Choosing $R \cong 1$ to 2 cm satisfies this criterion when $\omega = 10^2$- 10^3 radians/sec.

Separate measurements should be made of the rate constants for each possible reaction in the atmosphere of each possible polycyclic aromatic hydrocarbon.

B. Analytical Technique

Before each run the polished and nonreactive glass surface of the rotating disk and an identical reference disk are coated with a monolayer or a uniform thin layer of BaP. (The coating must remain thin to assure that the resistance of the reacted layers are negligible). The BaP, obtained commercially as a pure solid, sublimes and condenses onto the disk under N_2. The thickness of the layer on both disks can be calculated from gravimetric measurements or by measuring

the number of moles of BaP condensed on the reference disk by chemical analysis. A multilayer may more accurately simulate the bonding of BaP onto soot because the top molecular layer will be hydrogen bonded to the subsurface layers on the disk rather than adsorbed on glass.

After each run the moles of BaP remaining in nondegraded form on the disk are measured by following a technique used by Thomas et al.(1968). The reference disk is soaked in benzene and the extract is analyzed by infrared spectroscopy to obtain a base intensity spectrum for BaP. The reacted disk is also extracted with benzene, but the extract is chromatographed through alumina using 20 percent ether in pentane to separate the polar degraded fractions from the pure BaP. From infrared spectrographs of each fraction specific degradation products can be identified and the moles of BaP which did not react can be calculated.

Infrared spectroscopy is a sensitive technique for analyzing changes in BaP and other polycyclic aromatics. PAHs show intense absorption bands between 900 and 700 cm^{-1} which are caused by the out of plane C-H bending vibrations of these molecules. BaP specifically shows spectral responses in 4 separate subdivisions of this regime. The hydrogens in the 1, 2, and 3 carbons are referred to as trio hydrogens and give a response in the 810-750 cm^{-1} region. The 4,5 and 11,12 hydrogens are duos which give a spectral response between 860-800 cm^{-1}. 6 is a mono hydrogen responding between 900-860 cm^{-1}, while 7,8,9,10 are quartet hydrogens

responding between 770-735 cm^{-1}.

If analysis of degradation products is not desired, mass spectrometry is faster than infrared spectroscopy for measuring concentration changes in pure PAHs. Universal Oil Products(Padrta et al., 1971) has developed a technique for analysis of PAHs in auto exhaust by mass spectrometry. BaP, pyrene, perylene, benzoperylene, coronene, and phenanthrene and/or anthracene can each be quantitatively analyzed by measuring respectively the peak heights at mass to charge ratios of 228, 202, 252, 276, 300, and 178.

C. Calculation of D, k_s and m

For the diffusion of gases like SO_2, O_3, NO_2 or O_2 in the atmosphere, $\nu/D_A \gtrsim 1$. Therefore, higher order terms in the expansion of v_y, the velocity component normal to the disk, are required to accurately estimate the diffusion boundary layer thickness(Levich,1962:Eqn 11.36),

$$\delta = 1.61 \left(\frac{D_A}{\nu}\right)^{1/3} \sqrt{\frac{\nu}{\omega}} \left[1 + 0.35 \left(\frac{D_A}{\nu}\right)^{0.36}\right]. \qquad (14)$$

Case (1) Control by Diffusion to the Surface of the Disk

The diffusion coefficient of the reactant gas may be measured by rotating the disk at low values of ω, where the degradation rate may be controlled by the rate of diffusion to the surface of the disk. The mass flux to the disk surface is given by(Levich, 1962:Eqns 11.30, 11.36)

$$j = \frac{D_A C_{A0}}{\delta} = \frac{-\alpha}{\beta \pi} \frac{dN_B}{dt}, \qquad (15)$$

and the time for complete degradation of the BaP is given by

$$\tau = \frac{\alpha N_{BO} \delta}{\beta \pi R^2 D_A C_{AO}} . \qquad (16)$$

Since $N_B(t) = N_{BO}(1-(t/\tau))$, N_{BO}/τ can be evaluated from the slope of data of $N_B(t)$ vs. t, and D_A can be calculated by trial and error from Equation 16 with Equation 14.

Case (2) Control by the Rate of Chemical Reaction or Photooxidation

The rate of degradation can be controlled by the rate of chemical reaction($j = k_s C_{AO}^m = k_0 \exp(-U/RT) C_{AO}^m$) if $D_A/k_s >> \delta$ at large values of ω. If this relation holds for $\omega R^2/\nu < 10^4$, m, the order of the reaction, is evaluated from

$$m = \log \left[\frac{(N_{BO}/\tau)_1}{(N_{BO}/\tau)_2} \right] \Big/ \log \left(\frac{C_{AO1}}{C_{AO2}} \right) , \qquad (17)$$

and k_s is given by

$$k_s = \frac{\alpha N_{BO}}{\beta \pi R^2 \tau C_{AO}^m} . \qquad (18)$$

$(N_{BO}/\tau)_1$ and $(N_{BO}/\tau)_2$ are the slopes of data of $N_B(t)$ vs. t obtained respectively for C_{AO1} and C_{AO2}. The preexponential constant, k_0, and the activation energy, U, are evaluated from a plot of data of log k_s vs. 1/T, where T is the absolute temperature.

For photooxidation reactions, $j = I_a\phi = N_{BO}\alpha/\tau\pi R^2\beta$. For photooxidation reactions which also depend on C_{AO}, Equations 17 and 18 apply, but k_0 is a function of $I_a\phi$.

Case (3) Joint Control by Diffusion and Chemical Reaction

When the condition, $D_A/k_s >> \delta$, can not be met, the mass flux is given by

$$j = \frac{D_A(C_{AO} - C_{AI})}{\delta} = k_s C_{AI}^m, \tag{19}$$

and k_s is given by

$$k_s = \frac{j}{(C_{AO} - j\,\delta/D_A)^m} \tag{20}$$

When m = 1,

$$k_s = \frac{D_A}{\left[(\beta \pi R^2 D_A C_{AO} \tau/\alpha N_{BO}) - \delta\right]} \tag{21}$$

From data at two different values of ω, m is calculated from(Levich, 1962:76)

$$m \log \frac{\left[1 - (j_1 \delta_1/C_{AO} D_A)\right]}{\left[1 - (j_2 \delta_2/C_{AO} D_A)\right]} = \log \frac{j_1}{j_2} \tag{22}$$

$j_1 = (-\alpha/\beta\pi R^2)(N_{BO}/\tau)_1$ is obtained from data at constant C_{AO}, ω, and T. k_0 and U are approximated over the narrow range of temperature of interest in an urban atmosphere by plotting data of log k_s from Equation 20 vs. 1/T. Over wide ranges of T, the temperature dependence of D and ν cannot be neglected.

Case (4) Evaluation of D_{AI}

The diffusion coefficient, D_{AI}, of gas within the reacted outer layer of the spherical shell model(Case (2),Section III) can be estimated from the rotating disk system. The disk is initially coated with multilayers of BaP. These degrade until only a monolayer of pure BaP remains under the reacted layer having a thickness L. Alternatively, it may be possible to cover a monolayer of BaP with a coating of the

reacted product. The disk is rotated at large ω such that the rate of degradation is controlled by the rate of diffusion through the reacted layer and the rate of chemical reaction in the monolayer of BaP. Measurements of the mass flux ($j = (-\alpha/\beta\pi R^2)(\Delta N_B/\Delta t) = (-\alpha/\beta\pi R^2)(N_{BO}/\tau)$) at conditions for which k_s and m are known allows calculation of D_{AI} from

$$D_{AI} = \frac{jL}{\left[C_{AO} - (j/k_s)^{1/m}\right]}. \qquad (23)$$

V. Possible Techniques for Estimating the Residence Time of Polycyclic Aromatic Hydrocarbons in the Atmosphere from Kinetic Data and Particle Residence Time Data

Esmen and Corn(1971) suggested residence times of 4-40 days for submicron particles in urban air and 0.4-4 days for 1-10μm diameter particles. Since airborne soot has an aerodynamic diameter between 0.1 and 5μm, the residence time in urban air could vary from 0.5 to 10 days. However, air has a residence time of only 1 day in the Los Angeles Basin as estimated by the Committee on Biologic Effects of Atmospheric Pollutants(1972:60). If the results of Falk et al.(1956), Tebbens et al.(1966), and Thomas et al.(1968) are used, the time for chemical degradation of primary PAHs can be considerably less or somewhat longer than the residence time of soot in the Los Angeles Basin. Thus, suburban and rural areas could also be exposed to PAHs generated in urban areas.

In conclusion, imprecise data currently available for the chemical half-lives and for particle residence times

precludes more accurate estimates of the health effects of PAHs. One deficiency can be eliminated by performing the detailed kinetic studies suggested in this proposition. To improve estimates of the regional and local residence times of soot particles, tracer particles(e.g. zinc sulfide) having an equivalent aerodynamic diameter could be used in controlled dispersion experiments in specific air basins. Results from these studies may be applied to the atmosphere by one of the techniques described below.

First, a rough estimate may be obtained by exposing each PAH on the rotating disk to gaseous mixtures of synthetic smog while simulating the light intensity for specific times of day. The degradation rates for specific conditions are then time-averaged over the period in which particles of soot remain suspended in the air basin. Similarly one might be able to estimate the shortest exposure time of the population to a specific PAH by measuring the degradation rate in the presence of the peak daily concentration of a reactant gas. Alternatively, if the degradation product is more carcinogenic than the original PAH, this technique would give the maximum exposure time.

In the second technique, rate constants determined in experiments proposed in Section IV are applied to atmospheric models which follow the average behavior of gases and particles(Friedlander and Seinfeld,1969; Eschenroeder and Martinez, 1970). If one assumes that the soot particles are agglomerates of equal size spheres and that the concentrations of

reactant gases surrounding each particle as it moves through the atmosphere are essentially constant over time, one can apply the equations developed in Section III. Since calculations suggest that the rate of chemical reaction or photooxidation should control the rate of degradation, the dominant reactions must be determined at specific atmospheric conditions. The t/τ relationship for the chemical reaction controlling case then describes the degradation rate of all particles for which the above assumptions are valid, and $t/\tau = X_B$ when

$$\tau = \frac{\alpha N_{BO}}{\beta 4\pi R_2^2 \left(k_1 C_{A1}^{m_1} + k_2 C_{A2}^{m_2} + I_{a3}\phi_3 + \cdots\right)} \quad (24)$$

Alternatively, if the coating of PAH is greater than a monolayer,

$$\frac{t}{\tau} = 1 - \frac{\left[R_2^3(1-X_B) + R_1^3 X_B\right]^{1/3} - R_1}{R_2 - R_1} \quad (25)$$

and

$$\tau = \frac{\alpha \rho_B (R_2 - R_1)}{\beta\left(k_1 C_{A1}^{m_1} + k_2 C_{A2}^{m_2} + I_{a3}\phi_3 + \cdots\right)} \quad (26)$$

The time for a desired degree of conversion, X_B, is then calculated for the average radius, R_2(0.005-0.15μm), of the components of the atmospheric soot. These relations apply to large volumes of the atmosphere if the concentration of each reactant gas is essentially constant in that volume.

An accurate dynamic analysis of the behavior of PAHs in the atmosphere requires solution of a series of coupled differential equations for the time varying concentration of each reactant gas and the time varying concentration of BaP

and other PAHs on the soot in a given cell in the atmosphere. Convection, source, and loss terms to account for inputs of gases and particles and the settling, diffusion, coagulation, and scavenging of soot particles must also be included. In this approach the dominant chemical and photooxidation reactions dictate the form of the PAH degradation rate expressions. Although this is the ideal approach, implementation on a large scale is many year away.

Other information needed to improve the estimates of health effects of PAHs includes the carcinogenic properties of degradation products of primary PAHs, the distribution of PAHs according to particle size, and the manner of distribution and absorption of PAHs within single particles.

References

Adams, R.N. (1969). "Anodic Oxidation Pathways of Aromatic Hydrocarbons and Amines," Accounts Chem. Res., 2:175-180.

Clar, E. (1964). Polycyclic Hydrocarbons, London: Academic Press, 974 pp.

Committee on Biologic Effects of Atmospheric Pollutants (1972). Particulate Polycyclic Organic Matter, Washington D.C.: National Academy of Sciences, 361 pp.

Crocker, T.T., et al. (1970). "Preliminary Report on Experimental Squamous Carcinoma of the Lung in Hamsters and in a Primate(Galago crassicaudatus)," pp. 317-328. In P. Nettesheim, M.G. Hanna, Jr., and J.W. Deatherage, Jr., Eds. Morphology of Experimental Respiratory Carcinogenesis, AEC Symposium Series 21, Oak Ridge Tenn: U.S. Atomic Energy Commission, Division of Technical Information.

Eschenroeder, A. and J.R. Martinez (1970) "Mathematical Modeling of Photochemical Smog," AIAA Paper 70-116. Presented to the American Institute of Aeronautics and Astronautics 8th Aerospace Science Meeting, New York.

Esmen, N.A. and M. Corn (1971). "Residence Time of Particles in Urban Air," Atmos. Environ., 5: 571-578.

Falk, H.L., I. Markul, P. Kotin (1956). "Aromatic Hydrocarbons: Their Fate Following Emission into the Atmosphere and Experimental Exposure to Washed Air and Synthetic Smog," A.M.A. Arch. Ind. Health, 13: 13-17.

Fieser, L.F. and E.B. Herschberg (1939). "The Orientation of 3,4-Benzpyrene in Substitution Reactions," J. Amer. Chem. Soc., 61: 1565-1574.

Foote, C.S. (1968). "Photosensitized Oxygenations and the Role of Singlet Oxygen," Accounts Chem. Res., 1:104-110.

Friedlander, S.K. and J.H. Seinfeld (1969). "A Dynamic Model of Photochemical Smog," Environ. Sci. Technol., 3: 1175-1181.

Hidy, G.M. and J.R. Brock (1970). The Dynamics of Aerocolloidal Systems, New York: Pergamon Press, 379 pp.

Inscoe, M.N. (1964). "Photochemical Changes in Thin-Layer Chromatograms of Polycyclic Aromatic Hydrocarbons," Anal. Chem., 36: 2505-2506.

Levich, V.G. (1962). Physicochemical Hydrodynamics, Englewood Cliffs, N.J.: Prentice Hall, 700 pp.

Masuda, Y. and M. Kuratsume (1966). "Photochemical Oxidation of Benzo(a)pyrene," Air Water Pollut., 10: 805-811.

Moriconi, E.J., B. Rakoczy, and W.F. O'Connor (1961). "Ozonolysis of Polycyclic Aromatics. VIII. Benzo(a)-pytene," J. Amer. Chem. Soc., 83: 4618-4623.

Padrta, F.G. et al. (1971). "Polynuclear Aromatics in Automobile Exhausts," Amer. Chem. Soc. Symposium on Current Approaches to Automotive Emissions Control I. Exhaust Control. Los Angeles, April 1971.

Pott, P. (1775). Chirurgical Observations Relative to the Cataract, the Polypus of the Nose, the Cancer of the Scrotum, the Different Kinds of Ruptures, and the Mortification of the Toes and Feet, London: L. Hawes, W. Clarke, and R. Collins, 208pp.

Pylev, L.N. (1967). "Effect of the Dispersion of Soot in Deposition of 3,4-Benzpyrene in Lung Tissue of Rats," Hyg. Sanit., 32: 174-179.

Roitt, I.M. and W.A. Waters (1952). "Action of Benzoyl Peroxide on Polycyclic Aromatic Hydrocarbons," J. Chem. Soc., 2695-2705.

Tebbens, B.D., J.F. Thomas, and M. Mukai (1966). "Fate of Arenes Incorporated with Airborne Soot," Amer. Ind. Hyg. Assoc. J., 27: 415-422.

Thomas, J.F., M. Mukai, and B.D. Tebbens (1968). "Fate of Airborne Benzo(a)pyrene," Environ. Sci. Tech., 2: 33-39.

Vollmann, H. et al. (1937). "Beitrage zur Kenntnis des Pyrens und seiner Derivate," Justus Liebigs Ann. Chem., 531: 1-159.